Outflows from Young Stellar Objects: The Case of DG Tauri

Marc C. White

A thesis submitted for the degree of

Doctor of Philosophy

of the Australian National University

Australian National University

Research School of Astronomy & Astrophysics

Submitted 19th May 2014

Accepted 30th October 2014

Outflows from Young Stellar Objects: The Case of DG Tauri

Marc C. White

Supervisors:	Dr Raquel Salmeron (Chair), ANU
	Professor Peter McGregor, ANU
	Professor Geoff Bicknell, ANU
Advisors:	Dr Alex Wagner, Tsukuba University
Collaborators:	Dr Ralph Sutherland, ANU
	Dr Tracy Beck, Space Telescope Science Institute

Declaration and Author's Notes

I hereby declare that the work in this thesis is that of the candidate alone, except where indicated below or in the text of the thesis. The work was undertaken between March 2009 and May 2014 at The Australian National University, Canberra. It has not been submitted in whole or in part for any other degree at this or any other university.

Chapters 2, 3 and 4 have been submitted, accepted or published as papers in *Monthly Notices of the Royal Astronomical Society* (*MNRAS*). No permission is required to include these articles in a thesis, provided the thesis is not published commercially (`http://www.oxfordjournals.org/access_purchase/publication_rights.html`). Therefore, commercial publication of any part of this thesis is strictly prohibited.

The initial reduction of the NIFS data used in this project was performed by Professor Peter McGregor prior to the start of the candidature. Subsequent re-reductions were conducted jointly by the candidate and Professor McGregor, but did not constitute major changes to the reduction procedure, and used pre-existing reduction scripts written by Professor McGregor. The data reduction sections of Chapters 2 (§2.2) and 4 (§4.2) were written by the candidate, based on notes provided by Professor McGregor.

The MAPPINGS IV shock models used in Chapter 3 were computed by Dr Ralph Sutherland of The Research School of Astronomy and Astrophysics, The Australian National University. The text detailing the models (§3.3.1) was written by the candidate, based on notes provided by Dr Sutherland. The application of the results of these models to the mixing layer calculation in §3.3 was performed by the candidate.

The kinetic models presented in Chapter §4, §4.4, were constructed by the candidate by adapting a FORTRAN script written by Professor McGregor.

Appendix B was prepared by the candidate, based on a set of notes written by Professor Geoff Bicknell. The calculations based on this Appendix regarding the DG Tau jet (§2.4.1.5) were conducted by Professor Bicknell, based on data provided by the candidate.

For stylistic reasons, and as an acknowledgement of the status of Chapters 2, 3 and 4 as collaborative papers, this thesis retains the use of the pronoun 'we'. The text of each chapter was written solely by the candidate, with input and review by the supervisory panel and collaborators.

Due to the nature of published papers, there is some unavoidable duplication between the main chapters. I have endeavoured, as far as is possible, to avoid unnecessary duplication between the main chapters and the thesis introduction.

This thesis was examined by a three-member panel, who unanimously recommended that it be accepted in September 2014. This version of the thesis incorporates minor suggestions and corrections provided by the examination panel. The refereeing status of Chapter 3

(White et al. 2014b), and some of the references that have been formally published since the thesis was first submitted, have also been updated. This online, open-access version includes further reference updates, coloured links and references to aid in navigation, and additional reproduction permissions that were not available at the time of submission.

Marc C. White
October 2014

Acknowledgements

Although University rules state that only one name gets to go on the spine of a thesis, calling a PhD an entirely solo effort is about as truthful as claiming a Formula 1 driver operates entirely on his/her own. Whilst they are the one physically in the driver's seat (and get in to the most trouble should the car slide into a wall), no driver can finish, let alone win, without a huge team of people providing encouragement, support and expertise behind the scenes. Doing a PhD is no different, so I'd like to briefly thank those people who have contributed the most to the creation of this thesis.

First and foremost, I should thank my wonderful supervisory panel — Dr Raquel Salmeron, Professor Peter McGregor, and Professor Geoff Bicknell — for their unwavering guidance, tutelage and support over the last few years. I most definitely could not have done any of the work in this thesis without your expert knowledge and skill, so thank you, thank you, thank you. Also, a big vote of thanks to my other collaborators, Dr Ralph Sutherland (RSAA), Dr Tracy Beck (STScI) and Dr Alex Wagner (RSAA/Tsukuba) for your input and suggestions. I look forward to continuing to work with all of you in the future.

To the rest of the cast and crew of The Research School of Astronomy & Astrophysics, thank you for making turning up to work each day an enjoyable and rewarding experience. Your collective ability to calm stressed-out students, give constructive feedback, and simply create a supportive environment for nascent researchers is unbelievable. In particular, thanks to Bill Roberts and the RSAA Computer Section for the outstanding technical support they provide, as well as giving me a means of supporting myself towards the end of my thesis.

Throughout my time in Canberra, I've lived in three great sharehouses. Thank you to everyone who's put up with living with me during my thesis. I know I wasn't always the most attentive housemate whenever thesis milestones reared their heads, so I appreciate your collective ability to let some home matters slide, in the sure knowledge that I would make time to clean that bathroom... eventually.

As my main non-astronomy outlet, I must, of course, acknowledge the role that my friends in the Floorball ACT community have played in keeping me moderately sane throughout my thesis. In particular, thanks to my fellow organisers of Canberra floorball — Damien, Merrin, Dave and Rob — for giving me something to do when I needed a break from astronomy, and for picking up my slack when astronomy took over. Big thanks too to all the players of floorball in the ACT, who make it a pleasure to compete with them each week.

During the first few years of my thesis, I was privileged to be a member of the Australian Army Reserve. Although, sadly, I was unable to complete my training due to my being medically discharged, it was an honour to have served nearly four years with Canberra

Detachment, Sydney University Regiment. I'd like to thank the Officers, Other Ranks and Officer Cadets of SUR for making my time with Army so enjoyable, and such a welcome change from the world of academia.

To my family back home in Perth, Western Australia, thank you for your constant love and support, and particularly for being nice enough not to ask too many astronomy/PhD questions whenever I showed up for Christmas. Since I was an astronomy-obsessed child, you guys have always been supportive, and have lead me to where I am today. To Mum: you are the single biggest reason why I am who I am. I wish you could have been here to see this.

I would like to acknowledge the financial support of an *Australian Postgraduate Award*, a *Joan Duffield Research Scholarship*, and an *ANU Miscellaneous Scholarship* during my thesis.

Marc White
May 2014

Abstract

Protostellar jets and winds play a crucial role in the dynamics and evolution of the star-formation process. They may effectively regulate mass accretion by removing angular momentum from the circumstellar disc. Despite their importance, the physical processes driving the outflow phenomena remain poorly understood. This thesis presents a consistent model for the outflow structure and dynamics of the young stellar object DG Tauri, using data of unprecedented spatial and spectral resolution from the Near-infrared Integral Field Spectrograph (NIFS) on Gemini North.

The approaching outflow shows two components in [Fe II] 1.644 μm emission. A stationary recollimation shock is observed in the high-velocity jet, in agreement with previous X-ray and FUV observations. The pre-shock jet velocity, and inferred jet launch point (400–700 km s^{-1} and 0.02–0.07 AU, respectively), are significantly different from previous estimates. Jet 'acceleration' beyond the shock is interpreted as intrinsic velocity variability. Careful analysis reveals no evidence of jet rotation, contrary to previous work. A wide-angle, low-velocity blueshifted molecular outflow is observed in H_2 1-0 S(1) 2.1218 μm emission. Both outflows are consistent with a magnetocentrifugal disc wind origin, although an X-wind origin for the jet cannot be excluded.

The lower-velocity [Fe II] component surrounds the jet, and is interpreted as a turbulent mixing layer generated by lateral jet entrainment of molecular wind material. An analytical model of an entrainment layer is constructed, based on Riemann decomposition of directly observable outflow parameters. The model reproduces the velocity field of the entrained material without invoking an arbitrary 'entrainment efficiency' parameter. The luminosity and mass entrainment rate estimated using the model are in agreement with observations. Such lateral entrainment requires a magnetic field strength of order a few mG at hundreds of AU above the disc surface; independent arguments are advanced to support this conclusion.

The receding outflow of DG Tau takes on a bubble-shaped morphology. Kinetic models indicate this structure is a quasi-static bubble with an internal velocity field describing expansion. It is proposed that this bubble forms because the receding counterjet from DG Tau is obstructed by a clumpy ambient medium. There is evidence of interaction between the counterjet and ambient material, which is attributed to the large molecular envelope around the DG Tau system. An analytical model of a momentum-driven bubble is shown to be consistent with observations. It is concluded that the bipolar outflow from DG Tau is intrinsically symmetric; the observed asymmetries are due to environmental effects.

The observational interpretations and comprehensive modelling of the DG Tau outflows presented in this thesis constitute a significant step forward in gaining a full physical understanding of how stars accrete their mass. The complex nature of the approaching jet provides the first clear indications of the diverse phenomena associated with protostellar

mass loss. The different morphology of the receding outflow has highlighted the role of environmental factors in defining outflow characteristics. Together this work presents a new and more detailed view of the complex mechanisms associated with the formation of a low-mass star.

Contents

List of Figures

List of Tables

Glossary and Acronyms

2MASS	Two Micron All-Sky Survey
AGN	active galactic nuclei
ALMA	Atacama Large Millimeter/Sub-millimeter Array
ALTAIR	ALTtitude conjugate Adaptive optics for the InfraRed (Gemini North AO system)
AO	adaptive optics
BE99	Bacciotti & Eislöffel (1999) method for determining gas parameters from optical line ratios (see footnote 40, p. 34)
CTTS	classical T Tauri star (§1.1.2.1)
FEL	forbidden emission line
FHSC	first hydrostatic stellar core
FUV	far-ultraviolet
FWHM	full width at half-maximum
GMC	giant molecular cloud
GMT	Giant Magellan Telescope
GMTIFS	Giant Magellan Telescope Integral Field Spectrograph
HH	Herbig-Haro, e.g. Herbig-Haro object
HST	*Hubble Space Telescope*
HVC/I	high-velocity component/interval
IFS	integral-field spectrograph (IFU plus spectrograph; §1.4)
IFU	integral-field unit (§1.4)
IR	infrared
IUE	*International Ultraviolet Explorer*
IVC	intermediate-velocity component
KH	Kelvin-Helmholtz, e.g. Kelvin-Helmholtz instability
LVC/I	low-velocity component/interval

MHD	magnetohydrodynamic(s)
MRI	magnetorotational instability (§1.1.3)
MVC/I	medium-velocity component/interval
NICMOS	Near Infrared Camera and Multi-Object Spectrometer (*HST* instrument)
NIFS	Near-infrared Integral Field Spectrograph (Gemini North instrument; §1.4)
NIR	near-infrared
PACS	Photoconductor Array Camera and Spectrometer (*Herschel* instrument)
PBRS	PACS bright red source (Fig. 1.2)
PSF	point spread function
SED	spectral energy distribution (§1.1.2.2)
STIS	Space Telescope Imaging Spectrograph (*HST* instrument)
TTS	T Tauri star (§1.1.2.1)
UV	ultraviolet
VeLLO	very low-luminosity object (Fig. 1.2)
WFPC2	Wide Field and Planetary Camera 2 (*HST* instrument)
WTTS	weak-lined T Tauri star (§1.1.2.1)
YSO	young stellar object
ZAMS	zero-age main sequence

For the distinction between *outflows*, *jets* and *winds* used in this thesis, see footnote 2, p. 1.

CHAPTER 1

Introduction

> But if the matter were evenly disposed throughout an infinite space, it could never convene into one mass; but some of it would convene into one mass and some into another, so as to make an infinite number of great masses, scattered great distances from one to another throughout all of that infinite space. And thus might the sun and fixed stars be formed...
>
> – Isaac Newton[1]

Collimated outflows are ubiquitous components of accreting astrophysical objects across a wide range of masses and energies. The masses of outflow-driving systems range from supermassive black holes in active galactic nuclei to sub-solar mass protostellar cores and white dwarfs. The wide range of objects that are capable of launching jets, winds and related outflow types[2] suggest that some universal underlying mechanism is at work. This mechanism is believed to be tied to the gravitational accretion of material and the need for an efficient method of removing angular momentum (Smith 2012). Although it is generally accepted that these outflows are launched via magnetohydrodynamic processes (e.g. Livio 1999), the exact details of this mechanism or mechanisms remain elusive.

Outflows are thought to play a particularly important role in the process of star formation. They are the means by which young stars clear their environment, allowing them to become optically revealed to observers. The outflows are also used as a signature to ascertain the

[1] Letter to Richard Bentley (Jeans 1929; Larson 2003).

[2] Throughout this thesis we use the following nomenclature. *Outflows* encompass all types of collimated flows driven by protostellar objects. *Jets* refer to the highest-velocity, well-collimated central components of the outflows. *Winds* refer to the less-collimated, lower-velocity outflow components (e.g. Fig. 1.7). Note that this use of winds is distinct from the MHD disc wind (§1.2.2.1), which is a candidate mechanism for driving both *jets* and *winds* as defined here.

presence of forming stars before they are revealed. Outflows may modify the structure of protostellar discs (Combet & Ferreira 2008), affect the penetration of ionizing particles and stellar radiation into the disc (Desch et al. 2004; Cleeves et al. 2013), lead to the formation of a disc corona (Fleming & Stone 2003), lift and process dust particles (Safier 1993; Salmeron & Ireland 2012), accelerate disc dispersal (Suzuki & Inutsuka 2009), and limit the extent of infalling gas via feedback (Arce & Sargent 2004). Finally, and perhaps most importantly, outflows are thought to aid in overcoming the angular momentum problem (§1.1.3) which would otherwise impede the ability of a protostar to accrete matter. Therefore, a thorough understanding of the structure of outflows, and how they are launched, is vital to unravelling the mystery of how stars like the Sun, and potentially solar systems like our own, form.

Protostellar outflows have been studied extensively in the literature (§1.2) using spectroscopic and imaging techniques. However, spectroimaging techniques (e.g. §1.4) remain relatively underutilized. The combination of structural and kinematic information that may be obtained using an integral-field spectrograph allows for a highly-detailed analysis of the structure, kinematics and, with the inclusion of multi-epoch data, variability in protostellar outflows. The use of adaptive-optics systems allows the outflows to be resolved within tens to hundreds of AU of the driving source.

In this thesis, we present the deepest spectroimaging observations to date of the protostellar outflows associated with the actively-accreting young star DG Tauri. These data (§2) allow us to rigourously separate the emission from blended outflow components for the first time, and probe the parameters and structure of each in exquisite detail. We leverage these data to investigate critical questions in the field of protostellar outflows, such as the presence of rotation, the launch radii of the outflow components, the interactions between outflow components and ambient media, the generation of periodic and time-variable structures, and the self-similarity of the outflow components. The data motivate us to develop original analytical models of the processes by which the outflow components may interact with each other (§3), and with the ambient medium surrounding the protostar (§4). We demonstrate that the intermediate-velocity component of the approaching outflow is consistent with the formation of a turbulent mixing layer, and that the receding outflow 'bubble' structure is a sign of jet-ambient medium interaction. These models represent fundamental progress in the field of protostellar outflows, and have wide implications in the study of outflows from other young stellar objects.

In the balance of this chapter, we provide an overview of the star formation process, and the basic properties of low-mass protostars. We then discuss the role that outflows may play in star formation, as well as some key observations of these beautiful systems. We provide a summary of our object of interest, DG Tauri, as well as the instrument we used to examine it, the Near-infrared Integral Field Spectrograph (NIFS). Finally, we provide a brief outline of the remainder of this thesis.

1.1. Star Formation

Star formation is one of the most important processes in astrophysics. Stars are the fundamental units, indeed, 'atoms' of the Universe. They determine the structure and evolution of galaxies, play a dominant role in the generation of almost all observed luminosity, and possibly led to the reionization of the Universe. All elements beyond hydrogen and helium are formed in stars, and the process of star formation is inextricably linked to the formation of planetary systems (McKee & Ostriker 2007). Therefore, determining the exact nature of star formation is of central importance (Shu et al. 1987). Whilst the general picture of star formation is thought to be fairly well-understood (§1.1.1), there remain several outstanding problems (e.g. §1.1.3).

1.1.1. Overview of the Star Formation Process

The overarching picture of the process of star formation as the accumulation and collapse of overdensities in the interstellar medium has been around since at least the times of Newton (Larson 2003). However, further significant advances in the theory of star formation were not made until the middle of the 20$^{\text{th}}$ century, when it was realized by Ambartsumian (1947) that star formation was ongoing nearby in the Milky Way, and that contemporary telescope technology allowed for the detailed analysis of these objects. Subsequently, millimetre-wave CO observations in the 1970s provided direct detection of the seed material for star formation in clouds, clumps and cores (e.g. Lada 1987). The core concepts of the star formation process were reasonably well-understood by the 1980s, and are encapsulated in the review of Shu et al. (1987). However, many details of the star formation process remain unclear, and the search for a complete model of star formation remains one of the most fundamental outstanding questions of astrophysics.

The remainder of §1.1.1 provides a brief outline of the basic concepts of star formation. It is not intended to address all the outstanding questions the field; the reader is invited to consult the reviews of Lada (1987), Shu et al. (1987), Larson (2003) and McKee & Ostriker (2007), as well as the recent textbook of Bodenheimer (2011), for a more comprehensive account.

1.1.1.1. Molecular Clouds, Clumps and Cores

Massive ($\sim 10^7$ M$_\odot$) bound structures condense from the diffuse interstellar medium in galactic spiral arms due to large-scale gravitational instabilities (Larson 2003; Ballesteros-Paredes et al. 2007). These structures inherit a large amount of turbulence from the diffuse ISM which, along with self-gravity, causes them to fragment into giant molecular clouds (GMCs) with a wide range of masses (McKee & Ostriker 2007). Smaller molecular

Table 1.1 Properties of molecular clouds, clumps and cores. Adapted from Bodenheimer (2011).

	Giant molecular cloud	Molecular cloud	Molecular clump	Cloud core
Mean radius[a] (pc)	20	5	2	0.08 ($\sim 10^4$ AU)
Number density,[a] n_{H_2} (cm^{-3})	10^2	3×10^2	10^3	10^5
Mass[a] ($M_\odot$)	10^5	10^4	10^3	10^1
Linewidth (km s^{-1})	7	4	2	0.3
Temperature (K)	15	10	10	10

[a] Values quoted are indicative only; a wide range of masses and sizes are possible.

clouds may be formed by ram pressure from supersonic flows, which are potentially driven by an ensemble of supernova explosions, superbubbles and expanding HII regions (Ballesteros-Paredes et al. 2007).

Molecular clouds are strongly structured, being dominated by density enhancements referred to as clumps that are the progenitors of star clusters (McKee & Ostriker 2007). Two basic processes may be involved in the fragmentation of molecular clouds. Fragmentation may result from small inhomogeneities in the original molecular cloud distribution that are amplified by self-gravity. Alternatively, the relationship of increasing linewidth, and inferred velocity dispersion, to increasing cloud size (Table 1.1) suggests the presence of a hierarchy of supersonic turbulence within the clouds. Such supersonic turbulence would compress the gas in shocks, creating a hierarchy of compressed clumps. Both processes almost certainly play a role in fragmenting clouds down to the clump regime (Larson 2003). The same processes lead the clumps to further fragment into molecular cores (§1.1.1.2), which are the progenitors of single- or multiple-star systems. Typical bulk properties of molecular clouds, clumps and cores are listed in Table 1.1.[3]

1.1.1.2. Protostellar Collapse

The evolutionary steps by which a region of a molecular clump collapses to form an optically-revealed, low-to-intermediate mass young stellar object (YSO) was first summarized in the review of Shu et al. (1987), and is shown in Fig. 1.1. Our understanding of this overarching process has not changed significantly since then, although many of the underlying processes are still actively investigated.

Two main models to explain molecular cloud core collapse exist (Fig. 1.1a). The first, based on analyses of the stability of molecular clouds and the fragmentation process, suggests that an unstable or marginally stable clump of gas, in which gravity overcomes pressure,

[3] It is important to note that while this fragmentation process is expressed in terms of discrete stages, it has been long understood that it involves a cascade of turbulence and collapse on all scales (Hoyle 1953).

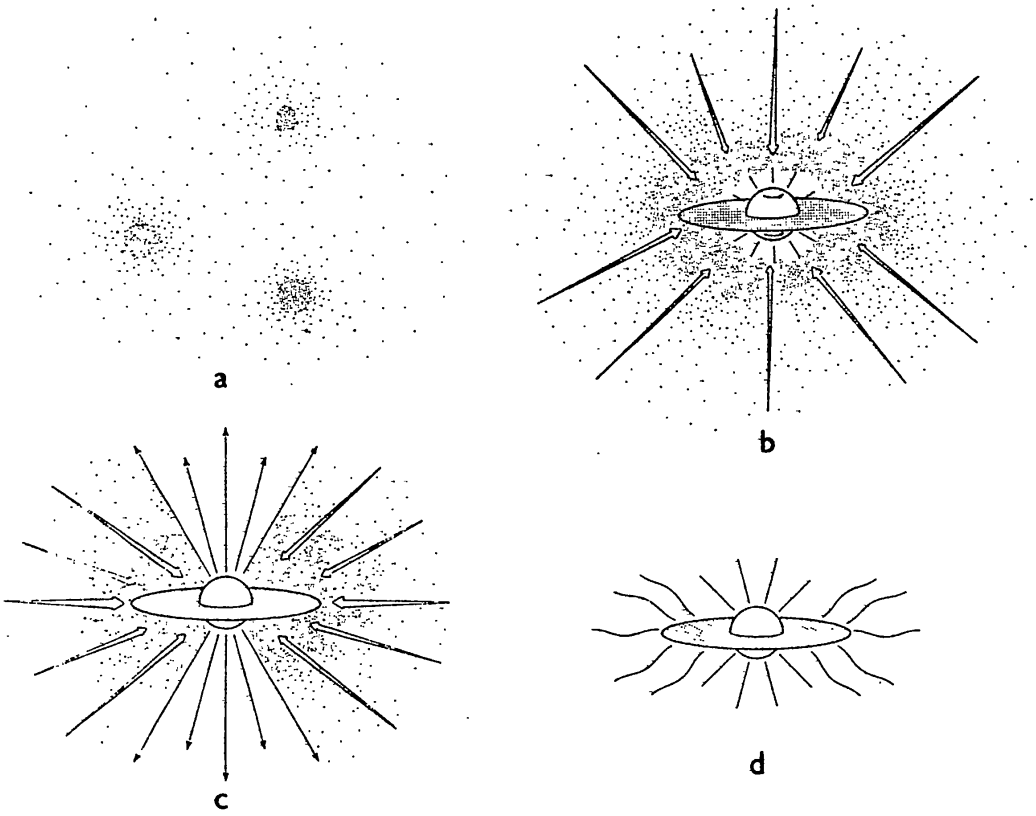

Figure 1.1 The evolution of forming stars (Shu et al. 1987). (a) Regions of molecular clouds become unstable, and begin to collapse to form protostellar cores. (b) The core develops a central density peak, which forms a protostar surrounded by a circumstellar disc. Material from the core continues to fall on to the circumstellar disc. (c) Disc accretion begins to drive bipolar outflows, which start to clear out the remnant protostellar envelope. (d) Infall from the envelope to the disc ceases, and the subsequent disc accretion then stops. The related outflows also terminate, leading to a pre-main-sequence protostar surrounding by a passive protostellar disc. *Reproduced with the permission of Annual Reviews.*

initiates a rapid runaway collapse (fast-collapse model; Hayashi 1966; Ward-Thompson 2002). The unstable clumps are formed as the result of supersonic turbulence within the molecular cloud complex (Larson 1981; Ballesteros-Paredes et al. 2007; Bodenheimer 2011). The second model states that cloud cores are initially magnetically supported, and condense slowly as magnetic support is leaked away via ambipolar diffusion (slow-collapse model; Shu 1977; Shu et al. 1987, 2004; Bodenheimer 2011; Li et al. 2014). In a magnetized plasma, the magnetic field is coupled to the charged particles, which are in turn coupled to the neutral particles via collisions. For weakly ionized plasmas, the neutrals and charged particles become decoupled as the collision rate becomes negligible, removing the support of the magnetic field from the neutrals and leaving them subject to gravitational collapse (Mestel & Spitzer 1956). Both of these models represent unphysical extremes; more realistic models are expected to be intermediate to the above scenarios (Larson 2003).

Irrespective of the trigger mechanism, as the cores collapse they become internally stratified, with a central density concentration (Bodenheimer & Sweigart 1968; Larson 1969). This concentration will eventually render the core unstable, and initiate a runaway ‘inside-out’

collapse (Shu 1977; Shu et al. 1987; Larson 2003). In the slow-collapse model of Shu et al. (1987), the surface at which gas begins to fall quickly inwards propagates outwards through the quasi-static core at the sound speed (Shu 1977). In the fast-collapse scenario (Hayashi 1966), the mass infall rate on to the nascent protostar is much higher, and material falls in at a few times the sound speed from an already-infalling core (e.g. Larson 1969). Again, reality is likely to exist somewhere between these two extremes (Larson 2003). Regardless, the net result of this collapse is the formation of a very low-mass ($\lesssim 10^{-2}$ $M_{\odot}$; Larson 2003) protostar in the centre of the cloud core (Figure 1.1b; McKee & Ostriker 2007).[4] The remainder of the cloud core continues to collapse inwards.

Most star-forming cores are rotating (Goodman et al. 1993), as would be expected for turbulent molecular clouds (Burkert & Bodenheimer 2000). Material is present with sufficient angular momentum to prevent it from falling directly onto the protostar, instead forming a circumstellar accretion disc (Figure 1.1b; Larson 2003; McKee & Ostriker 2007). As the collapse proceeds, material will fall preferentially onto the disc as opposed to the star (Shu et al. 1987). This occurs because material at greater distances from the star, with greater angular momentum, begins to undergo infall (Terebey et al. 1984; Hartmann 1998). Subsequently, material accretes through the disc onto the central star, although the method by which the material sheds excess angular momentum remains unclear (§1.1.3).[5]

Throughout the initial accretion phase, the central star remains heavily obscured by the cloud core, making direct observation of this process difficult. Indeed, the star is typically not optically revealed until the majority of mass accretion has already occurred (Larson 2003).[6] During this phase, the main contribution to the luminosity of the system comes from accretion shocks on the central star and circumstellar disc, which gives rise to the

[4] This actually takes the form of a two-phase collapse process. The first collapse ceases when the gas in the central density peak becomes hot enough to support the central hydrostatic core against further collapse. Once this gas reaches temperatures capable of dissociating molecular hydrogen, the value of the adiabatic index in the core drops below the critical value of 4/3 required for stability (Larson 2003), leading to the second collapse and the formation of the protostar (McKee & Ostriker 2007). The majority of the first hydrostatic core has collapsed into the second core within ~ 10 years (Larson 2003).

[5] It should be noted that, in the last decade, it has been realized that the strong magnetic fields of protostellar cores may effectively brake the core rotation as it collapses. This *magnetic braking* occurs when the magnetic field lines threading the disc are twisted by the disc's rotational motion, loading up the tension in the field lines. Alfvén waves then transfer angular momentum from the disc to the external medium, not unlike waves travelling along a taut, plucked rubber band (Königl & Salmeron 2011). This would solve the angular momentum problem, but prevent the formation of Keplerian rotation discs. Given the fact that such discs are ubiquitous throughout star formation, and are even starting to be detected in Class 0 objects (e.g. Tobin et al. 2012, 2013; Murillo et al. 2013), this is an outstanding issue, referred to as the 'magnetic braking catastrophe'. Although ambipolar diffusion and the Hall effect have a significant effect on the collapse process (Li et al. 2011; Braiding & Wardle 2012a,b), it is currently thought that turbulence and Ohmic dissipation are the key physical mechanisms for limiting the effectiveness of magnetic braking, and allowing the formation of rotationally-supported discs around forming stars (Li et al. 2014, and references therein). Recent simulations using multiple levels of spatial refinement suggest a two-phase core collapse process; an initial efficient shedding of angular momentum until approximately half the initial protostellar mass is accreted, followed by the formation of a rotationally-supported protoplanetary disc at later stages (Nordlund et al. 2014).

[6] The advent of the Atacama Large Millimeter/Sub-millimeter Array (ALMA) is expected to begin to address this issue directly (Shirley 2012; Li et al. 2014), but at the time of writing the first results of the array are only just beginning to appear (e.g. Pineda et al. 2012; Kristensen et al. 2013).

spectral energy distributions (SEDs) used to classify low-mass protostars (§1.1.2).

As the protostar continues to accrete matter, deuterium ignition will occur in the core when the required temperature is reached (approximately 1×10^6 K; Shu et al. 1987), approximately when the protostar reaches a mass ~ 0.2 $M_\odot$. This is a significant source of heat, which greatly slows protostellar contraction as accretion continues (Larson 2003). Furthermore, differential rotation, coupled with the convection driven by deuterium burning, can produce dynamo action and generate strong magnetic activity. The energy released may power the intense stellar surface activity observed in YSOs (Shu et al. 1987). As material preferentially falls on the circumstellar disc as opposed to the star, the ram pressure of the direct infall weakens above the rotational poles (Shu et al. 1987). This allows the outflows from the central star/inner disc to break clear of the circumstellar envelope and begin clearing it (Fig. 1.1(c)). In the original paradigm of Shu et al. (1987), these outflows were thought to be stellar winds, but it has been realized since that they are far more likely to be magnetohydrodynamic winds launched from the disc surface (§1.2; Li et al. 2014). As the envelope material is swept away, the star becomes optically revealed for the first time, and is observed as a T Tauri star (TTS) or Herbig Ae/Be star, depending on the protostar mass and spectral properties (§1.1.2). These stars emerge on the 'birthline' of the Hertzsprung-Russell diagram, and descend steep Hayashi tracks towards the zero-age main sequence (ZAMS; Stahler 1983). After the envelope around the protostar is dispersed, and full hydrostatic equilibrium is reached, the protostar contracts on a Kelvin-Helmholtz timescale until hydrogen fusion begins, and the star enters the main sequence.

1.1.2. The Classification of Protostars

1.1.2.1. By Mass and Spectral Features

The primary discriminant for the classification of YSOs is mass. High-mass YSOs, with masses $\gtrsim$ 8–10 $M_\odot$, make up the 'massive YSOs'. These objects may form via a scaled-up version of the process described in §1.1.1.2, or via the so-called 'competitive accretion' process in dense clusters (Tan et al. 2014; Krumholz 2014).[7] The low-mass YSOs are split into two further classes; the low-mass T Tauri stars, and the intermediate-mass Herbig Ae/Be stars. Conceptually, T Tauri and Herbig Ae/Be stars are differentiated by mass, with the mass cut between the two classes at $\sim$ 2–3 $M_\odot$.[8] However, the formal separation

[7] A detailed discussion of the process of massive star formation is beyond the scope of this thesis. The interested reader is directed to the reviews of Hoare et al. (2007), Tan et al. (2014) and Krumholz (2014) for details.

[8] The exact mass break between the two classes varies between authors. Appenzeller & Mundt (1989) place the cutoff at 3 $M_\odot$, Feigelson & Montmerle (1999) adopt a value of 2 $M_\odot$, and both Hillenbrand et al. (1992) and Alecian et al. (2007) allow Herbig Ae/Be stars to have masses as low as 1.5 $M_\odot$. Therefore, there is likely to be an overlap in masses between the two classes; however, this does not affect the classification of T Tauri and Herbig Ae/Be stars, which is based on spectroscopic properties (Herbig 1962; Bastian et al. 1983; Bertout 1984, 1989).

is made via spectroscopic properties. The balance of this section focuses on the T Tauri class of protostars.

T Tauri stars (TTS) were first identified from the prototype object T Tauri by Joy (1945), who proposed a set of relatively tightly-defined spectral and light-variation characteristics for the class. Herbig (1958), whilst noting their near-universal variability, determined that the classification of TTS should be made on spectroscopic properties alone, and provided a broadened, but highly-prescriptive definition (Herbig 1962). Bastian et al. (1983) realized that this definition was unnecessarily dependent on transient spectral features, and also excluded some TTS which were lacking one or two typical attributes of the class. Therefore, they determined a simplified definition of a T Tauri star:

> Stellar objects associated with a region of obscuration; in their spectrum they exhibit Balmer lines of hydrogen and the Ca II H and K lines in emission, the equivalent width of Hα being at least 5Å. There is no supergiant or early-type (earlier than late F) photospheric absorption spectrum.[9]

This definition, whilst still frequently used, is not complete; e.g. the Balmer emission lines of TTS are known to vary significantly with time (Appenzeller & Mundt 1989). Presently, the term TTS is synonymous with low-mass pre-main-sequence stars, irrespective of their emission characteristics (Hartmann 1998); these objects are identified by a range of techniques such as objective prism surveys, X-ray surveys, proper motion, photometry and variability studies, and their classification is confirmed spectroscopically (Briceño et al. 2007). Identification of young stars by comparison to theoretical stellar evolution models using colour-magnitude diagrams is the most common approach (e.g. Bouvier & Appenzeller 1992; Hughes et al. 1994; Luhman et al. 2003).

TTS typically have late spectral classes (late F to M, Petrov 2003), with strong excess IR and UV emission. In some cases, the IR excess is so pronounced that the peak of the spectral energy distribution is shifted into the far-infrared (§1.1.2.2; Rydgren et al. 1984; Bertout 1989), and the presence of hot dust, at an inferred temperature of hundreds of K, must be invoked. The UV/blue excess is radiation released by free-free and free-bound transitions in a hot hydrogen plasma, most likely formed in the accretion process (Petrov 2003).

More specifically, the spectrum of a TTS may be broken into four components — a stellar continuum, a stellar absorption line spectrum, a superimposed non-photospheric continuum, and an emission-line spectrum. The stellar absorption line spectrum is similar to that of a late-type (K to M) dwarf, with strongly enhanced Li I 6708 Å absorption (Appenzeller & Mundt 1989), which is indicative of the youth of the star (Skumanich 1972; Bertout 1989;

[9] The Bastian et al. (1983) definition of a Herbig Ae/Be star is similar, but the stellar object is earlier than F0, is associated with a reflection nebula in addition to obscuration, and does not require Ca II H and K lines in emission.

Petrov 2003). The absorption spectrum lines are often shallower than expected, being 'veiled' by the non-photospheric continuum (e.g. Greene & Lada 1996; Doppmann et al. 2005).[10] Approximately two-thirds of TTS show double-peaked Balmer lines (Appenzeller & Mundt 1989), which provide evidence for complex and time-varying gaseous flows in the envelopes of these stars (Bertout 1989). The emission-line profiles are broadened, and the forbidden lines enhanced (§1.2).

TTS are further classified by their spectra into *classical* (CTTS) and *weak-lined* (WTTS)[11] T Tauri stars. CTTS are those objects that broadly conform to the characteristics described above. As the name suggests, WTTS exhibit weaker line emission, particularly in the Balmer and forbidden lines (Appenzeller & Mundt 1989; Bertout 1989; Cieza et al. 2007). They also show little to no UV and IR excess in their spectral energy distributions. The physical reasons behind these differences are elaborated in §1.1.2.2.

1.1.2.2. By Spectral Energy Distribution

Starting in the 1980s, a classification scheme for YSOs was developed based upon the spectral energy distribution (SED, the product of wavelength, λ, and intensity at that wavelength, F_λ, as a function of λ) of the objects.[12] This classification scheme was based both on the observed SEDs and on theoretical modelling, and was hence perceived to be more meaningful as a measure of the evolutionary state of the YSO. Lada (1987) was the first to introduce a three-tier class system, and Adams et al. (1987) proposed a similar classification scheme. The hallmark of both systems is the classification of stellar objects using the slope of their SED in log-log space,

$$\alpha \equiv \frac{\mathrm{d}\log(\lambda F_\lambda)}{\mathrm{d}\log\lambda}, \tag{1.1}$$

over the wavelength range 2.2 μm to 10–25 μm (e.g. McKee & Ostriker 2007). André et al. (1993) added an additional class, Class 0, based on the sub-millimetre luminosity of deeply-embedded objects. Examples of the SEDs used to classify protostars are shown in Figs 1.2 and 1.3. The resulting classification leads to an evolutionary track, where protostars begin as Class 0 objects, and move through Classes I, II and III as they evolve (André et al. 2000). This system may be summarized thus (McKee & Ostriker 2007):[13]

[10] This veiling was first noted by Joy (1945). The term is now understood to refer to two distinct phenomena that cannot be easily differentiated in observations: (a) selective filling in of spectral lines, and (b) overlying continuum emission (Bertout 1989). Veiling in classical TTS can be so strong that it can only be explained by the presence of a non-photospheric continuum, which may exceed the photospheric continuum by a factor of several (Petrov 2003).

[11] These objects are occasionally referred to as *naked* T Tauri stars (e.g. Walter et al. 1988).

[12] SEDs may also be expressed in terms of frequency, ν vs. $F_\nu\nu$ (Adams et al. 1990). λF_λ and νF_ν are units of energy, not energy density; SEDs are determined in these units to remove any dependence on the size of the wavelength/frequency bins used.

[13] There are variations on this classification scheme. For example, Allen et al. (2007), Williams & Cieza (2011) and Dunham et al. (2014) use the classification system of Greene et al. (1994), where the cut-off

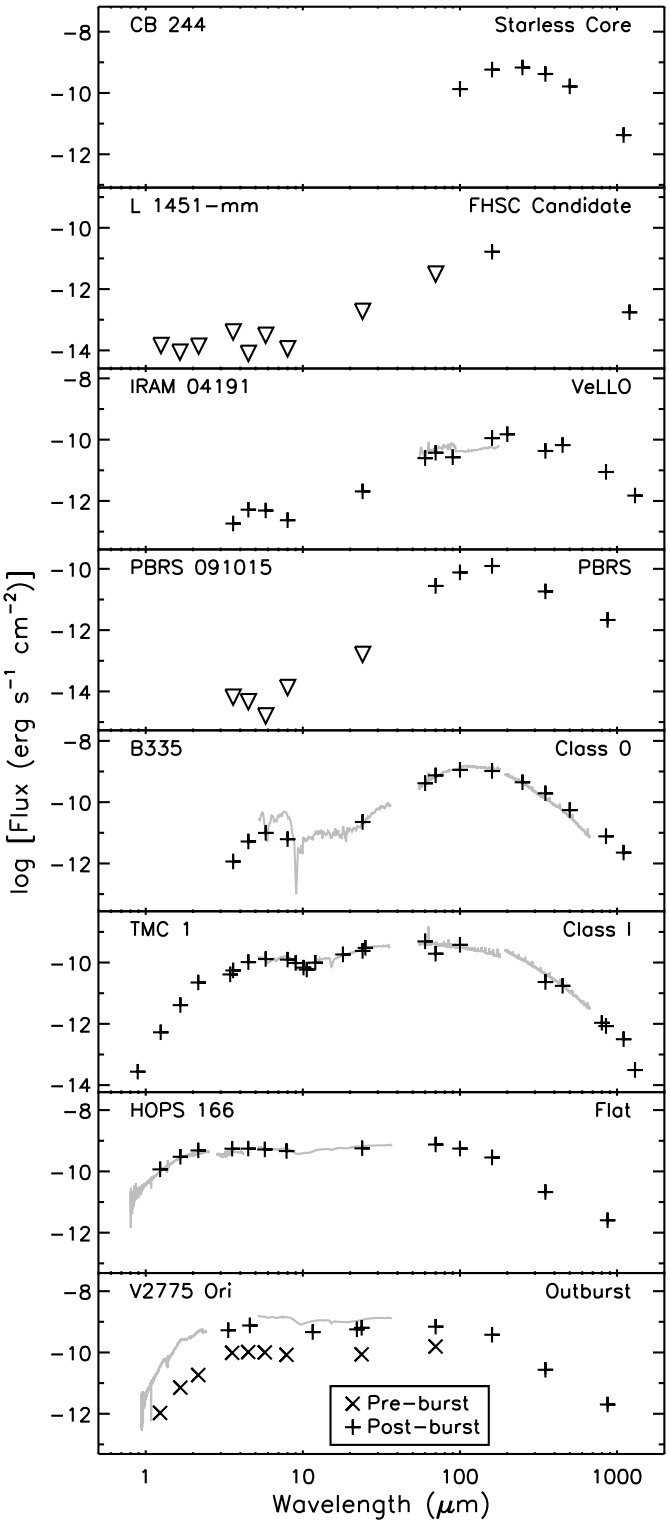

Figure 1.2 Example spectral energy distributions (SEDs) of pre-stellar molecular cores, and cores with embedded protostars (Dunham et al. 2014). *Top to bottom*: starless core (§1.1.1.2).; first hydrostatic core (FHSC) candidate (§1.1.1.2; footnote 4, p. 6); very low-luminosity object (VeLLO)[a]; PACS[b] bright red source (PBRS)[c]; Class 0 protostar; Class I protostar; flat-SED protostar; outbursting Class I protostar (e.g. Hartmann & Kenyon 1996). + and × symbols show photometric measurements, triangle symbols denote upper limits, and grey lines show spectra. *Sourced from* http://arxiv.org/abs/1401.1809. *Reproduced with the permission of M. Dunham.*

Data sources. *Starless core — Stutz et al. (2010); Launhardt et al. (2013). FHSC candidate — Pineda et al. (2011). VeLLO — Dunham et al. (2008); Green et al. (2013). PBRS — Stutz et al. (2013). Class 0 — Stutz et al. (2008); Launhardt et al. (2013); Green et al. (2013). Class I — Green et al. (2013). Flat-SED & outbursting Class I — Fischer et al. (2012).*

[a]Protostars embedded in dense cores with internal luminosities $L_{\rm int} \leq 0.1$ L$_\odot$. These objects were thought to be starless prior to the launch of the *Spitzer* space telescope (Dunham et al. 2014).

[b]The Photoconductor Array Camera and Spectrometer aboard *Herschel*.

[c]Protostars with very red colours, such that $\log\left[\lambda F_\lambda(70\ \mu{\rm m})/\lambda F_\lambda(24\ \mu{\rm m})\right] > 1.65$. Thought to be 'extreme' Class 0 protostars with higher-than-typical envelope masses and mass infall rates (Stutz et al. 2013).

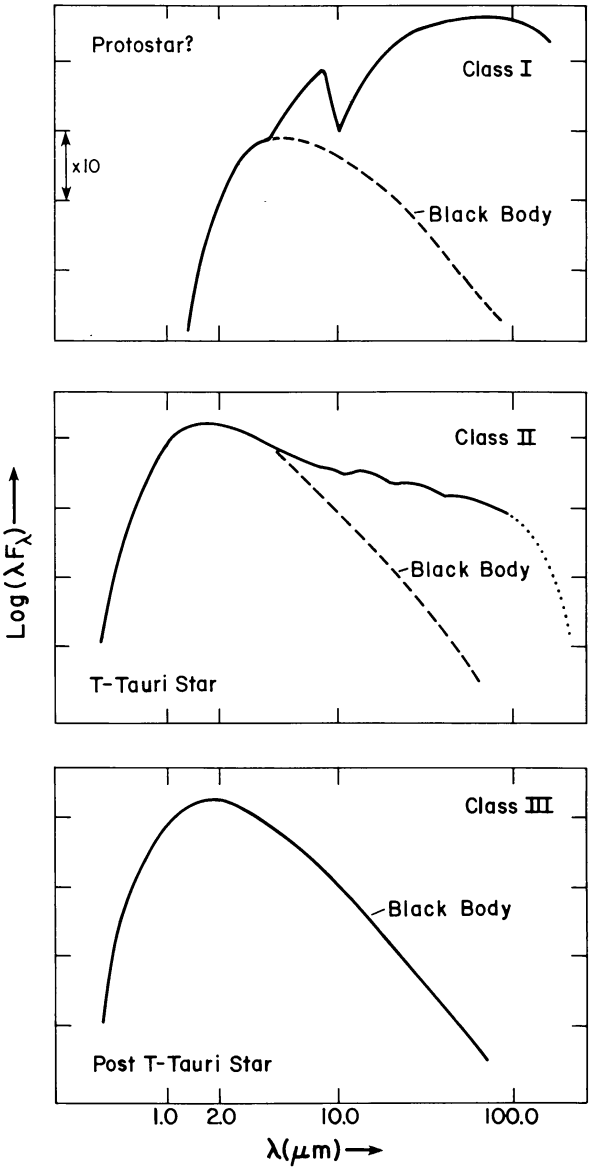

Figure 1.3 Typical spectral energy distributions (SEDs) for Class I, II and III protostars (Lada 1987). **Class I:** SED broader than a blackbody, with positive spectral indices redward of 2 μm. **Class II:** SED broader than a blackbody, with flat or negative spectral indices redward of 2 μm. **Class III:** Well-fit by a reddened blackbody function. The continued decrease of the infrared excess in the SED from Class I to Class III indicates the accretion and dissipation of the protostellar envelope (Class I to Class II) and circumstellar disc (Class II to Class III; Dunham et al. 2014). *Reproduced with the permission of C. Lada.*

Class 0: Sources with a central protostar that is very faint in the optical/near-IR[14], and a significant sub-millimetre luminosity[15], $L_{\rm smm}$, such that $L_{\rm smm}/L_{\rm bol} > 0.5\%$, where $L_{\rm bol}$ is the bolometric luminosity. Their SEDs resemble a single-temperature blackbody with $T \sim 15$–30 K. Class 0 sources are condensations in molecular cores that appear to be associated with formed, hydrostatic YSOs (André et al. 1993, 2000). These objects are just beginning the process of star formation, with the central object starting with significantly less mass than the final stellar mass (§1.1.1.2; André et al. 2000; White et al. 2007). A significant fraction of the stellar mass is accreted during

between Classes II and III is at $\alpha = -1.6$, Class I has $\alpha \geq 0.3$, and a new class, termed 'flat-SED' sources, is inserted between Classes I and II for sources with $-0.3 \leq \alpha < 0.3$. Other reviews choose not to incorporate flat-SED sources in their classification system (McKee & Ostriker 2007), although some do note them as an interesting sub-class of objects (e.g. White et al. 2007). Flat-SED sources are discussed further at the end of §1.1.2.2.

[14] That is, effectively undetectable in these regimes using 1990s-era technology (McKee & Ostriker 2007).

[15] $L_{\rm smm}$ is measured longward of 350 μm (André et al. 2000).

this stage (McKee & Ostriker 2007). These objects roughly correspond to Fig. 1.1(a).

Class I: Sources with $\alpha > 0$. In this phase, material from the envelope is infalling on to the circumstellar disc (Dunham et al. 2014). The central protostar is relatively evolved, having accreted most of its mass during its Class 0 phase (McKee & Ostriker 2007; White et al. 2007). This stage corresponds to Fig. 1.1(b) and (c).

Class II: Sources with $-1.5 < \alpha < 0$. These are pre-main sequence stars with significant circumstellar discs (classical TTS; §1.1.2.1). Both circumstellar discs and large-scale outflows are easily observable at this stage, whilst some accretion ($\lesssim 10^{-8}$ $M_\odot$ yr^{-1}) is ongoing (Hartigan et al. 1995; McKee & Ostriker 2007). This stage corresponds to somewhere between Figs 1.1(c) and (d).

Class III: Sources with $\alpha < -1.5$. This stage is reached when accretion onto the central star, and the resulting outflow activity, has largely ceased (weak-lined TTS; McKee & Ostriker 2007). This results in the disappearance of the SED emission excesses and forbidden emission lines. Class III SEDs are well-fit with a reddened blackbody function, indicative of a star close to the zero-age main sequence surrounded by a 'passive' protoplanetary disc which re-radiates stellar light (Petrov 2003). There may also be a complete lack of circumstellar material (Dunham et al. 2014). This stage corresponds to Fig. 1.1(d).

It should be noted that the above classification scheme is a binning of the continuous evolution of SED spectral index (Lada 1987), and by extension the continuous star formation process. Indeed, some authors cite an additional evolutionary stage, the transitional Class I/Class II objects (also called the flat-SED objects, see footnote 13, p. 11; Greene et al. 1994; Allen et al. 2007; Dunham et al. 2014). These objects have characteristics of Class II objects, such as well-collimated microjet-scale outflows (§1.2.1.3), but are more heavily obscured, or have higher mass accretion rates, or large remnant protostellar envelopes, like Class I objects.

The linkage between the IR and UV excesses in YSO spectra is of particular importance. It has been observed that YSOs with IR excesses almost invariably have strong optical/UV excess emission; conversely, all objects which display signs of active accretion also show IR excesses associated with the presence of an accretion disk (Hartigan et al. 1995). This correlation reveals that the powering of excess emission, and the driving of jets and winds[16], comes from the energy released in the accretion process (Cabrit 2007b). This motivates the development of models which link the accretion process with the launch of collimated outflows (§1.2.2).

[16] Hartigan et al. (1995) found a strong correlation between mid-infrared excess emission and [O I] 6300 Å jet emission.

Table 1.2 Characteristic values of specfic angular momemtum, J/M, through the process of star formation. There is a clear need for the loss of angular momentum throughout protostellar collapse and mass accretion. Adapted from Bodenheimer (2011).

Object	Scale	J/M (cm^2 s^{-1})
Molecular clump	1 pc	10^{23}
Cloud core	0.1 pc	1.5×10^{21}
Typical disc around 1 $M_\odot$ protostar	100 AU	4.5×10^{20}
T Tauri star (rotation)	few $R_\odot$	5.0×10^{17}
Sun (rotation)	$R_\odot$	10^{15}
Jupiter (orbit)	5.2 AU[a]	10^{20}

[a] Young & Freedman (2004)

Much like the realization that different types of active galactic nuclei (AGN) represent different viewing angles on to the same kind of object (Antonucci 1993; Urry & Padovani 1995), the geometry of a particular YSO, including inclination, aspherical geometry and foreground reddening effects, can confuse this classification system (McKee & Ostriker 2007; Dunham et al. 2014). For example, the simulations of protostellar collapse performed by Masunaga & Inutsuka (2000) showed that objects that would be assigned to Class I conceptually based on their evolutionary state may have SEDs characteristic of Class 0 sources if the system is viewed 'edge-on' to the nascent circumstellar disc. White et al. (2007) also point out that the properties of many Class I and Class II sources, such as effective temperature, photospheric luminosity and stellar mass, are similar, further suggesting that inclination effects may be confusing the classification system. There was much discussion at the recent *Protostars & Planets VI* meeting on the need for a more robust and meaningful classification system. It is hoped sub-millimetre instruments such as ALMA will be able to penetrate protostellar cores and reveal their true nature, allowing a classification system based on precise position on the star formation sequence to be developed.

1.1.3. Disc Accretion and the Angular Momentum Problem

The mechanism of accretion on to the central protostar remains poorly understood. This is due in large part to the accretion process being a complex interplay of magnetohydrodynamics, radiative transfer, chemistry, and possibly solid-state physics (McKee & Ostriker 2007). One clear constraint is that throughout the process of star formation, there is a continued need to remove angular momentum from the collapsing protostellar system. Observations show that at each stage of the star formation process, from core to ZAMS, the system must lose angular momentum (Table 1.2). In the earliest stages of star formation, magnetic fields may provide efficient extraction of angular momentum by magnetic braking (§1.1.1.2, particularly footnote 5, p. 6). However, irrespective of this braking, discs are observed to

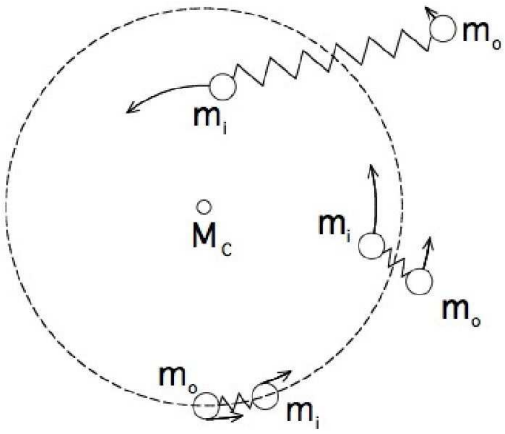

Figure 1.4 The magnetorotational instablility (MRI, Balbus 2011). Disc magnetic fields bind fluid elements in the same fashion as springs may bind masses in orbit. As the inner element, m_i, orbits the central mass, M_c, faster than the outer element, m_o, the magnetic field 'spring' causes a net transfer of angular momentum from m_i to m_o. This forces m_i to move inwards, and m_o to move further out in an unstable, runaway process. *Original figure courtesy H. Ji; sourced from Scholarpedia* (http://www.scholarpedia.org/article/Magnetorotational_instability). *Reproduced with the permission of S. Balbus.*

form around deeply embedded protostars (e.g. Tobin et al. 2012, 2013; Murillo et al. 2013). In more evolved objects (Class I and II), envelope material falls on to the circumstellar disc, through which the majority of it is accreted onto the central protostar. This process, referred to as disc accretion, must involve some mechanism for angular momentum transfer out of the disc in order to allow material to fall towards the protostar.

Angular momentum transport processes can be classified in to the following three broad categories: purely hydrodynamic, gravitational, or magnetic mechanisms (Larson 2003; McKee & Ostriker 2007). Hydrodynamic turbulence, once thought to be a possible analogue for molecular viscosity, has been largely ruled out as a possible mechanism. A large body of work has demonstrated that it is difficult to generate sustained hydrodynamic angular momentum transport, as discs are self-stabilised against the perturbations and vortices that provide the transport by epicyclic motion (McKee & Ostriker 2007; Turner et al. 2014, and references therein).[17] Furthermore, hydrodynamic mechanisms that rely on convection tend to transport angular momentum inwards (e.g. Ryu & Goodman 1992). On the other hand, self-gravitating transport mechanisms, such as gravitational Newton stresses, may be plausible, but are limited to disc regions of high surface density[18] (McKee & Ostriker 2007). This mechanism is most readily triggered in the outer reaches of the circumstellar disc, and may be important during the early Class I phase when material is rapidly fed onto the disc from the envelope (Turner et al. 2014). However, both of these types of mechanism remain poor explanations for angular momentum shedding by the inner regions of the discs of evolved Class I/Class II objects.

The most promising candidate (e.g. Salmeron 2009) for the outward radial transport of angular momentum in low-mass protostellar discs is the magnetorotational instability (MRI; Balbus & Hawley 1991, 1992; Hawley & Balbus 1991, 1992). The MRI operates

[17] More recently, some other classes of hydrodynamic disc instability, such as the Rossby wave instability, the Goldreich-Schubert-Fricket instability, and baroclinic vortex formation, have been investigated for their ability to transport angular momentum, but they are dependent upon radiative driving, which has yet to be adequately calculated (Turner et al. 2014).

[18] Formally, for a disc with surface density Σ, thermal speed (equivalent to the sound speed in an isothermal gas) $\sigma_{\rm th}$, and epicyclic frequency κ, gravitational Newton stresses are suppressed when the Toomre stability parameter $Q = \kappa\sigma_{\rm th}/\pi G\Sigma$ exceeds unity (Larson 2003, 2010; McKee & Ostriker 2007).

when matter is well-coupled[19] to a weak magnetic field[20] in the disc interior, and the disc is differentially rotating, such that angular velocity decreases outwards[21] (Balbus 2011; Königl & Salmeron 2011; Turner et al. 2014). MRI perturbations result from the action of magnetic fields in the disc connecting fluid elements located at different radii like a spring.[22] Consider, in a differentially rotating disc, two masses orbiting a central body M_c, one (m_i) inside the other (m_o), connected by a spring. As the mass m_i orbits faster than m_o, the spring stretches, pulling backwards on m_i and forward on m_o. The negative torque on m_i extracts angular momentum from it and forces it to move radially inward, whilst the positive torque on m_o causes it to gain angular momentum and move radially outward (Fig. 1.4). This process increases the tension in the spring, which in turn increases the torque on the fluid elements, leading to a runaway process. The MRI results from an entirely analogous mechanism, where the magnetic tension force between the two fluid elements acts like a spring (Balbus 2011).

As mentioned above, MRI requires that the disc magnetic field be weak, and well-coupled to the material in the disc interior, and is likely most important in the thermally-ionized gas within 0.1–1 AU of the central protostar, and beyond 10 AU in the less-dense material where non-thermal ionization is efficient (Turner et al. 2014). If these conditions are not met, then the MRI is suppressed. Angular momentum may alternatively be extracted vertically in outflows (§1.2).[23]

1.2. Protostellar Outflows

Outflows are a ubiquitous component of young stellar objects (McKee & Ostriker 2007). They are observed in young stellar objects at every stage of evolution, until the circumstellar disc activity tapers off in Class III sources (§1.2.1). These outflows can be immense, some having greater mass than the related protostar (§1.2.1.1), and others extending up to a few parsecs from the outflow source (§1.2.1.2). Modern telescopes, such as the *Hubble Space Telescope* (*HST*), and ground-based telescopes equipped with adaptive-optics systems have been able to resolve these outflows to within tens to hundreds of AU of the driving source (§1.2.1.3). A summary of various observations of protostellar outflows, and suggested

[19] The degree of this coupling is parametrized by the Elsasser number, $\Lambda \equiv v_{\rm A,0}^2/\eta_\perp \Omega_{\rm K}$, where $v_{\rm A,0}$ is the initial disc midplane Alfvén speed, $\eta_\perp \equiv c^2/(4\pi\sqrt{\sigma_{\rm H}^2+\sigma_{\rm P}^2})$ is the 'perpendicular' diffusivity, $\sigma_{\rm H}$ and $\sigma_{\rm P}$ are the Hall and Pedersen conductivities respectively, and $\Omega_{\rm K}$ is the disc Keplerian angular velocity. For MRI to radially transport angular momentum, $\Lambda_{\rm i} \gtrsim 1$ (Salmeron et al. 2007; Königl et al. 2010, and references therein).

[20] A magnetic field is considered 'strong' in this context when the ratio of the disc midplane Alfvén speed, $v_{\rm A,0}$, to the isothermal sound speed, $c_{\rm s}$, is not much smaller than unity. A 'weak' field is where $v_{\rm A,0} \ll c_{\rm s}$ (Königl et al. 2010).

[21] The angular momentum condition is relaxed in the ambipolar diffusion regime (Kunz & Balbus 2004).

[22] Formally, the equations of motion for a differentially rotating, magnetized accretion disc are identical to those for two bodies bound together with a spring of frequency kv_A whilst in orbit around a third, central body, where $v_A = B/\sqrt{4\pi\rho}$ is the Alfvén speed in the disc (Balbus 2011).

[23] The requirements for magnetically-launched outflows are discussed in §1.2.2.

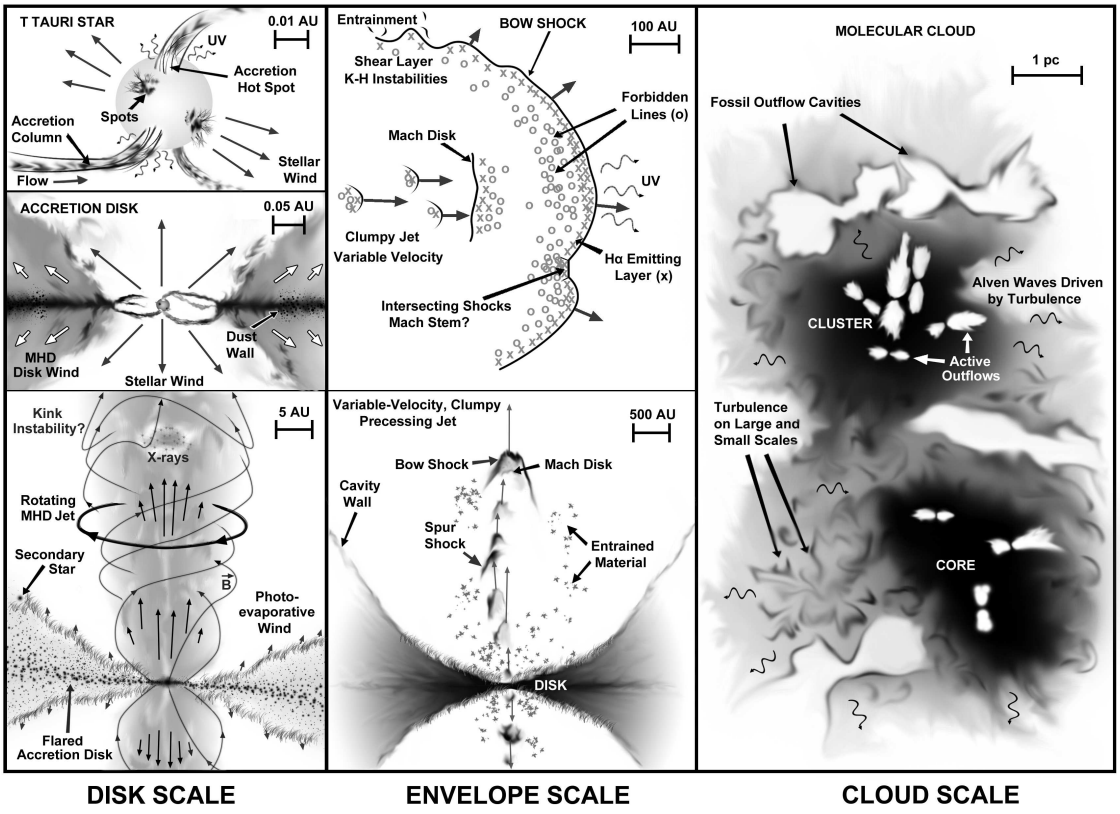

Figure 1.5 Outflows from young stellar objects at multiple length scales (Frank et al. 2014). Shown left-to-right are the outflow processes occurring on disc (§1.2.1.3), envelope (§1.2.1.2) and molecular cloud (§1.2.1.1) scales.
Disk scale: Magnetized accretion columns funnel material onto the protostellar surface, producing strong optical/UV excess emission which veils the stellar lines (§1.1.2.2). The strong magnetic activity also produces sunspot activity (Walter et al. 1988; Bouvier et al. 1993; *top panel*). The stellar magnetic field also truncates the inner radius of the circumstellar disk (Bouvier et al. 2007; *middle panel*). The outflows appear on observable scales as a rotating MHD jet (§1.2.1.3; *bottom panel*).
Envelope scale: The jets propagate to distances of hundreds, if not thousands, of AU from the central protostar (§1.2.1; *bottom panel*). They are dominated by bow-shock shaped structures, probably generated by velocity variations in the outflow (e.g. Raga et al. 1990; *top panel*). The jet may entrain additional material (§1.2.1.3, §3) along the jet walls, or in the bow shock wings, from the cavity walls, the ambient cloud (not shown) or the wider-angle/molecular outflows that often encase the jet (Fig. 1.7; not shown here).
Cloud scale: Multiple stars form within a molecular cloud (§1.1.1.2). The outflows create observable shocks in the cloud structure, and may contribute to the turbulence that seeds further star formation (e.g. Federrath et al. 2014).
Sourced from http://arxiv.org/abs/1402.3553. *Reproduced with the permission of A. Frank.*

driving mechanisms, is illustrated in Fig. 1.5.

Most modern theories of outflow launching rely on some form of magnetohydrodynamic, typically magnetocentrifugal, acceleration process, although exactly which process(es) are viable remains unclear (§1.2.2). Significant computational effort has been made to investigate the processes of outflow launching and propagation (see Pudritz et al. 2007 for a review of recent progress; for specific examples, see, e.g., Zanni et al. 2007; Romanova et al. 2009; Staff et al. 2010; Zanni & Ferreira 2013), but to date observational data has not reached a quality where the predictions of these works can be accurately tested (§1.2.1). Determining the nature of protostellar outflows and their launching is important for several

reasons. First, by linking the observed outflow properties to those on the disc surface, the outflows are one of the few probes available of the physical conditions on the disc surface $\lesssim$ a few AU from the star, which is unresolved with current NIR/optical telescope technology. This region is of particular interest, as it encompasses the range of disc radii where Earth-like planets may form (e.g. Combet & Ferreira 2008). Secondly, determination of the launch mechanism will reveal if the outflows are playing a significant role in the extraction of angular momentum from the system (§1.1.3). Outflows launched very close to the central star (e.g. X-winds; §1.2.2.2) will only remove angular momentum from the very inner disc radii, and will not contribute to solving the wider angular momentum problem.

1.2.1. Observations of Protostellar Outflows

The first observation of the outflow from a young stellar object was made in the T Tauri system, fifty years before it was recognised that that object was a forming star (Burnham 1890). It was another ninety years until such nebulosity (§1.2.1.2) was inferred to be from a protostellar outflow (Dopita 1978). Since then, there has been an extensive and concerted effort to observe and analyse protostellar outflows, and determine their role in the star formation process. In this section, we detail the key aspects of the three broad regimes of protostellar outflows — the large-scale molecular outflows (§1.2.1.1), the large-scale optical outflows (§1.2.1.2), and the 'microjet'-scale outflows (§1.2.1.3). This is by no means a complete account of such outflows; the interested reader is directed to the recent review of Frank et al. (2014), and references therein, for details.

As shown in Fig. 1.5, the predominant method for detecting outflows in the NIR/optical/UV is through the observation of shocked structures related to the jets/winds. Ignoring for a moment the issue of variable velocity jets (§1.2.1.3), there should be two shocks at the head of a jet caused by the impact of the jet on the ambient medium; a reverse shock ('Mach disc'), and a preceding shock ('bow shock') that propagates into the medium (Fig. 1.5, envelope scale, top panel; Smith 2012).[24] Our ability to detect these shocks is then limited by the fact that they must have a particular combination of shock velocity and density (typically, at least a few tens of km s^{-1}, and 10^3–10^5 cm^{-3}, respectively), which produce shock temperatures $\gtrsim 10^4$ K, in order to be detectable (McKee & Ostriker 2007).

1.2.1.1. Molecular Outflows

Millimetre-wavelength observations have shown that Class 0 and Class I protostars drive large-scale (or 'giant') molecular outflows, seen in CO rotational transitions (Stahler

[24] The relative brightness between the two shocks depends on the jet density with respect to the ambient medium. 'Heavy' jets, which are significantly denser than the ambient medium, will show bow shock-dominated emission, as they easily sweep up material in their path; 'light' jets will show enhanced Mach disc emission, due to their inability to penetrate the ambient medium (Hartigan 1989; Smith 2012).

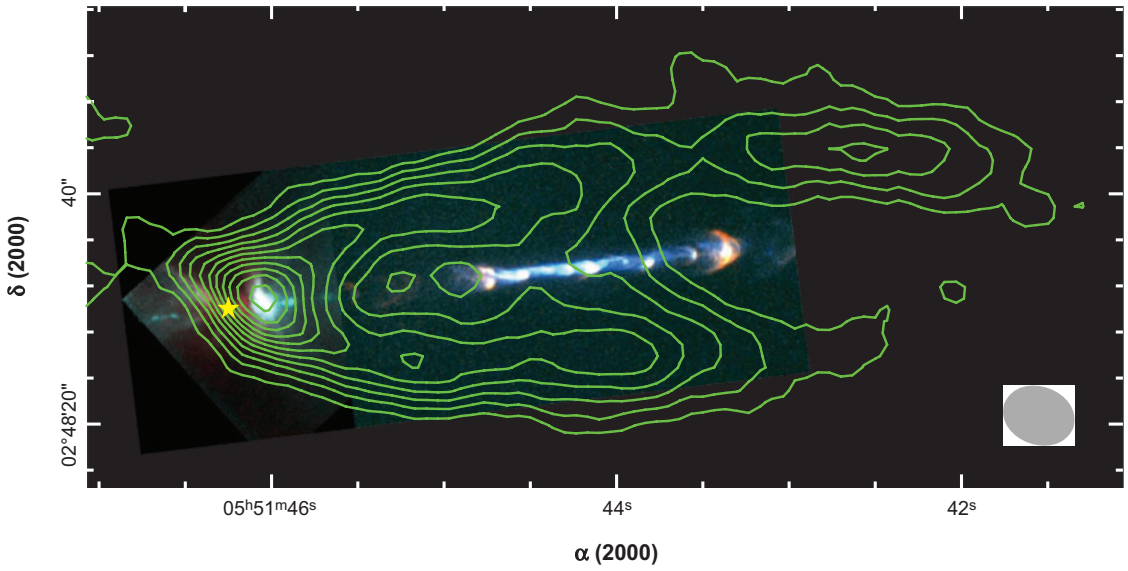

Figure 1.6 Outflows in the HH 111 system (McKee & Ostriker 2007). The color scale shows a composite *HST* image of the inner regions of the jet (optical data from Wide Field and Planetary Camera 2, WFPC2) and of the stellar source region (IR data from Near Infrared Camera and Multi-Object Spectrometer, NICMOS) from Reipurth et al. (1999). Overlaid in green are contours showing the $v = 6$ km s^{-1} channel map of CO $J = 1–$ emission by Lee et al. (2000). The yellow star marks the driving source position, the grey oval represents the beam size of the BIMA CO observations. The length of the outflow lobe is ~ 0.2 pc. The chain of nebulous objects centred at $\sim 44^s$ are Herbig-Haro objects. *Reproduced with the permission of Annual Reviews.*

1994a,b). First detected around the protostar L1551 IRS 5 (Snell et al. 1980), CO outflow lobes were soon realized to be a ubiquitous component of early star formation (Reipurth & Bachiller 1997), and their long cooling time provides a history of the object's outflow activity (Ray 2000). In contrast to many smaller-scale outflows (§1.2.1.3), bipolar molecular outflows are the norm, although some monopolar flows have been detected (Bachiller 1996). Given that the mass of many CO outflows exceeds that of their related protostar, it is presumed that they form through nascent protostellar outflows entraining ambient molecular gas, predominantly through prompt entrainment by a jet bow shock (Masson & Chernin 1992; Raga & Cabrit 1993; Cabrit et al. 1997; Micono et al. 2000; Ray 2000; Frank et al. 2014). Observational evidence has linked observed CO outflows to embedded jets, which act as the momentum source for the molecular outflow (e.g. Fig. 1.6; Mitchell et al. 1994; Davis et al. 1997; Rossi et al. 1997; Arce & Goodman 2002; Stojimirović et al. 2006; Teixeira et al. 2008; Santiago-García et al. 2009). Recent surveys (e.g. Narayanan et al. 2012) have shown that molecular outflows often extend $\gtrsim 1$ pc from the driving source. Well-collimated molecular 'jets', consistent with having been formed by entrainment, have been observed in some objects (e.g. Santiago-García et al. 2009). These jets also show cross-outflow velocity asymmetries, which are interpreted to be direct evidence of the outflows extracting angular momentum from the protostellar system (e.g. Pech et al. 2012).

1.2.1.2. Herbig-Haro Objects & Outflows

The nebulosity detected by Burnham (1890) close to T Tauri was, in fact, a Herbig-Haro (HH) object. Named for their discoverers (Herbig 1950, 1951; Haro 1950, 1952, 1953), the nature of HH objects was a mystery until Dopita (1978) suggested they could be formed as a result of protostellar mass loss. The spectral definition of a Herbig-Haro object is provided by Dopita (1978), taken from Herbig (1969):

> The H emission lines are strong and [O I] and [S II] are unusually intense. The [N II] lines are also strong, and in those Objects that are not too heavily reddened, [O II] [occurs] as well... A number of weaker emission lines [are seen] that are not ordinarily found in appreciable strength in gaseous nebulæ: H and K of Ca II, the infrared [Ca II] lines, Mg I 4571 Å, and lines of [Fe II] and [Fe III].[25]

The realization that some HH objects appear in highly-collimated chains, of 'jets' (e.g. Fig. 1.6; Dopita et al. 1982; Mundt & Fried 1983), led to the development of the present concept of HH objects as internal working surfaces in collimated protostellar outflows (Reipurth & Bally 2001).[26] These surfaces arise as the result of velocity variations in the underlying jet (Raga et al. 1991, 2002b, 2005, 2007, 2009; Raga & Noriega-Crespo 1992; Kofman & Raga 1992); as the jet velocity varies from slow to fast in a periodic fashion, fast jet material collides with slower-moving material upstream, creating characteristic bow-shock features that strongly mimic the morphology of HH objects (Eislöffel & Mundt 1998; Hartigan et al. 1999; Reipurth & Bally 2001; Beck et al. 2004). Both monopolar and bipolar HH complexes have been observed; in bipolar HH outflows, there is usually a clear correspondence between the HH objects in each lobe (e.g. HH212, Zinnecker et al. 1998; Frank et al. 2014). In the case of monopolar HH complexes, assuming the driving outflow is not intrinsically asymmetric, the asymmetry may be caused by obscuration of the opposing HH complex by the circumstellar disc of the driving source (§1.2.1.3), or because the opposing HH complex has receded into the dense molecular cloud behind the protostar (McGroarty et al. 2007).

1.2.1.3. Microjet-Scale Outflows

The presence of enhanced blueshifted forbidden emission lines (FELs) is a typical characteristic of T Tauri stars (§1.1.2.1). The 'FEL regions' close to the stars were found by Kepner et al. (1993) to be the signature of 'microjet'-scale outflows, based on *HST* imaging. Since then, YSO microjets have been extensively studied in the optical/NIR regime through

[25] A more detailed discussion of the spectral properties of HH objects may be found in Böhm (1983).

[26] Not all Herbig-Haro objects are internal working surfaces; for example, part of the HH 110 outflow complex is thought to be the result of a collision between the HH 270 outflow and an ambient molecular cloud (Reipurth et al. 1996; Raga et al. 2002a; Kajdič et al. 2012).

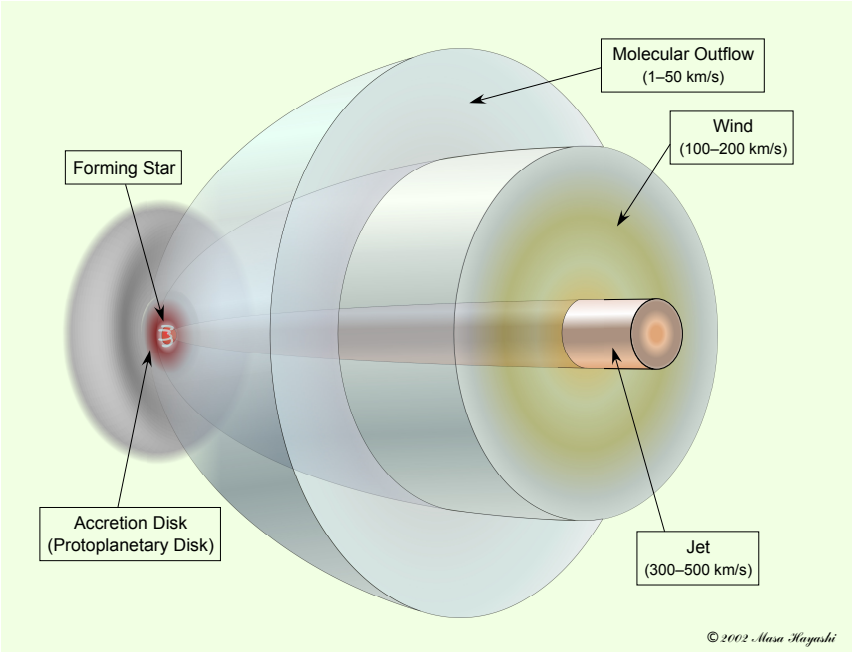

Figure 1.7 The nested velocity structure of microjet-scale outflows from YSOs (Pyo et al. 2003a). As seen in forbidden line emission, YSO microjets typically show a central, well-collimated, high-velocity 'jet', surrounded by a slower, wider-angle 'wind'. Some objects also show evidence for an even wider-angle, very slow molecular outflow. The outer shells of material may assist in preventing jet instabilities, such as the 'kink' instability, from developing (footnote 32, p. 24). *High-resolution figure courtesy of M. Hayashi, and reproduced with his permission.*

imaging, spectroscopy and spectroimaging, as well as in other bands through a myriad of techniques. Microjet studies are especially critical to the determination of the launch mechanism of protostellar outflows, as it is expected that the microjet will not interact significantly with ambient material in the first few hundred AU of propagation (Raga et al. 1995).

Although YSO microjets show a great deal of variety and complexity in their morphologies, a general picture of their structure has been developed (Fig. 1.7). Typically, the outflow consists of a central, high-velocity, well-collimated 'jet', with a velocity $\gtrsim$ 200–300 km s^{-1}. It is unclear if these jets are launched by the disc wind (§1.2.2.1) or X-wind (§1.2.2.2) mechanisms. The jet is surrounded by a wider-angle, lower-velocity ($\sim$ 100–200 km s^{-1}) outflow component, commonly referred to as a 'wind'. This component is usually interpreted to be a disc wind encasing the high-velocity jet, although some studies suggest that this component indicates the formation of an entrainment layer along the jet boundaries (e.g. Pyo et al. 2003b). The latter model is often discounted due to the expectation that the jet apex bow shock will clear any ambient material near the star as the jet is launched (Raga et al. 1995), although some studies do attempt to resurrect the concept by imposing special conditions (e.g. a cross-jet ambient wind; López-Cámara & Raga 2010). Finally, some objects show evidence for a microjet-scale molecular outflow component, which typically takes the form of a very wide angle (opening angle $\sim 90°$), low-velocity molecular wind (e.g. Takami et al. 2004; Beck et al. 2008; Agra-Amboage et al. 2014). However, in some objects, H_2 emission appears to be coming from the central jet (e.g. V4046 Sgr; Donati et al. 2011b).

Much like the accretion mechanism that is thought to drive the outflows (§1.1.3), protostellar microjets are time-variable phenomena. One of the most striking manifestations of this is the presence of shock-excited 'knots' that move down the jet channel. First detected in DG Tau by Kepner et al. (1993), and shown to be moving in HH 30 by Dutrey et al. (1996), these knots can be thought of as the small-scale analogue of Herbig-Haro objects; indeed, the knots in the small-scale jet driving HH 34 show a bow-shock morphology at high resolution (Hartigan et al. 2011). Recent numerical simulations by Raga et al. (2012) have shown that these microjet knots may merge downstream to form the large-scale Herbig-Haro complex (§1.2.1.2). However, the cause of the velocity variability that is suggested as the cause of these knots remains uncertain.

Of the three scales of protostellar outflows discussed here, the microjet-scale outflows are the most likely to exhibit monopolarity. This is typically due to the obscuration of the receding outflow by the circumstellar disc, leading to the protostar exhibiting only blueshifted FELs. However, protostars with bipolar microjet-scale outflows commonly display velocity and/or structural asymmetry between the outflows. Of the sample of young stars with bipolar FEL regions studied by Hirth et al. (1994b), over half of the targets exhibited a significant (factor ~ 2) velocity asymmetry between the two outflow lobes. Further observations, including of DG Tau (§1.3.2.1), have shown that structural bipolar asymmetries are also present. The cause of these asymmetries is a topic of significant debate. Recent simulations of protostellar collapse by Nordlund et al. (2014) suggest that bipolar asymmetric outflows are the norm amongst young stars, but the physical cause of the asymmetries has yet to be revealed. Several specific models for the production of bipolar outflow asymmetry have been proposed (see discussion in §4.7.1), some of which have been tested numerically (Fendt & Sheikhnezami 2013), but a definitive answer has yet to be found.

Due to the assumption that microjets have not interacted significantly with ambient material, they have been considered a prime target for outflow rotation studies. Indeed, computer simulations have determined that rotation should persist in protostellar jets out to $\lesssim 100$ AU from the central star (Staff et al. 2010). Direct observation of outflow rotation would prove that the outflows extract angular momentum from the system, as well as provide a means for calculating their launch points (Anderson et al. 2003; Ferreira et al. 2006). Spectroscopic studies using *HST* and 8 m-class telescopes with adaptive optics have inferred cross-jet Doppler line velocity shifts in the microjets of several YSOs (e.g. Coffey et al. 2004, 2007, 2011; Woitas et al. 2005), including DG Tau (§1.3.2.1; Bacciotti et al. 2002; Coffey et al. 2007), suggesting the presence of rotation. However, more recent observations have cast doubt on these claims. In particular, Coffey et al. (2012) found that the implied rotational velocity in the microjet from RW Aurigae varied, and even changed rotational sense, on periods of ~ 6 months. This casts doubt on rotation being the cause of the observed Doppler shifts, and indeed, alternative models have been suggested

(e.g. interaction between the microjet and a warped disc, Soker 2005).

The most recent addition to the study of YSO microjets has been the inclusion of high-energy X-ray data, primarily from the *Chandra* satellite. It is now known that many objects, including DG Tau (§1.3.2.1), emit soft X-ray emission from regions in the first few arcseconds of their outflows (e.g. Skinner et al. 2011; Schneider et al. 2011). There are two candidate explanations for this emission. The first is that it arises from a core, hot, fast outflow component in the jet interior, that has yet to be observed at other wavelengths, and is possibly launched from close to the stellar surface (§1.2.2.3; Günther et al. 2009). Alternatively, Bonito et al. (2011) successfully modelled the X-ray emission from the L1551 IRS 5 jet as the result of a stationary recollimation shock in the jet channel (Gómez de Castro & Pudritz 1993).

1.2.2. Launch Models

Early protostellar outflow studies quickly recognized that the momentum carried by protostellar outflows was more than what could be supplied by radiation pressure (Lada 1985).[27] Thermal pressure is also considered insufficient to drive these outflows, as the high temperatures that would be required are not observed near the base of the outflow (although thermal pressure does affect the mass loading of MHD winds; Königl & Salmeron 2011). Although the precise driving mechanism of protostellar outflows remains fiercely debated, the consensus view is that the ejection process involves some form of interaction between the accreting matter and the stellar and/or disc magnetic fields (McKee & Ostriker 2007; Frank et al. 2014). There are two main theories that aim to explain the origin of collimated protostellar outflows — the magnetocentrifugal disc wind (§1.2.2.1) and the X-wind (§1.2.2.2).[28] Such models are favoured because they provide both sufficient momentum to the outflows to match observations, and they also possess a natural collimation mechanism (§1.2.2.1, particularly footnote 33, p. 24). Some additional, specialised launch mechanisms have been suggested to explain specific observations of single YSOs, and such models relevant to this thesis are detailed in §1.2.2.3.

1.2.2.1. Disc Winds

The theory of MHD winds driven from the surfaces of accretion discs was addressed by the seminal paper of Blandford & Payne (1982), and was first suggested as a candidate launch mechanism for YSO outflows by Pudritz & Norman (1983). The full analytical

[27] The typical momentum carried by bipolar molecular outflows from YSOs is 10^2–10^3 times greater than what could conceivably be provided by radiation pressure from low-/intermediate-mass protostars (Königl & Salmeron 2011).

[28] Although there is frequently extensive debate about which of these launch mechanisms operates in a particular YSO, the theoretical models are not mutually exclusive; indeed, it is completely reasonable that both mechanisms may operate in concert, at different disc radii (Larson 2003; McKee & Ostriker 2007).

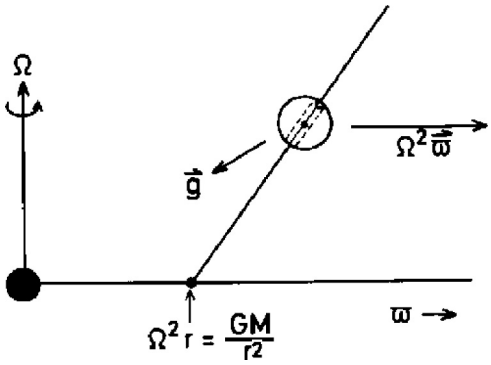

Figure 1.8 Rigid-wire analogy for magnetocentrifugal disc winds (Spruit 1996). Assuming that the magnetic field (inclined line), is strong enough to act as a rigid wire to a fluid parcel (circle), consider the forces acting upon it. At the disc surface, the gravitational force, GM/r^2, equals the centrifugal force, $\Omega^2 r$, assuming Keplerian disc rotation. However, for a disc in near-Keplerian rotation, or at some height above the disc, the centrifugal force, $\Omega^2\boldsymbol{\omega}$, exceeds the gravitational force, $\boldsymbol{g}$, and the fluid parcel moves out along the magnetic field line. *Modified from* http://arxiv.org/abs/astro-ph/9602022*; reproduced with the permission of H. Spruit.*

theory behind this model is extensively described in the literature (e.g. Spruit 1996; Königl & Salmeron 2011), and is not covered here. However, Turner et al. (2014) provides an illuminating qualitative description of the process, which we expand on below.

Consider a thin (disc height-to-radius ratio $\lesssim 0.1$) circumstellar accretion disc threaded by an 'open' magnetic field. Such a field arises through the advection of the interstellar magnetic field threading the nascent protostellar core during the collapse phase (§1.1.1.2; Königl & Salmeron 2011).[29] This results in the hourglass-shape field morphology inferred from far-infrared and sub-millimetre polarisation measurements on sub-parsec scales in several molecular clouds (e.g. Schleuning 1998; Girart et al. 2006; Kirby 2009). Now, consider a frame co-rotating with a fluid parcel at some distance from the central star; a fluid packet initially at rest in the disc will experience an effective potential that is the sum of the gravitational and centrifugal potentials. If the poloidal magnetic field threading the disc is strong (see footnote 20, p. 15), it acts like a rigid wire. If the field line is inclined at less that 30° to the disc surface[30], the effective potential decreases with distance from the central star, leading to the magnetocentrifugal acceleration of the fluid packet along the field line (Fig. 1.8). It is also a requirement that the accreting material in the disc can 'slip' across magnetic field lines, to prevent a large magnetic flux accumulating near the disc centre and halting further accretion (Turner et al. 2014).

For an axisymmetric MHD disc wind, there are several quantities that may be shown to be flux-surface constants (Königl & Salmeron 2011, §4.3 therein). One such quantity is the total (matter plus electromagnetic) specific angular momentum,

$$l = \underbrace{rv_\phi}_{\text{matter}} - \underbrace{\frac{rB_\phi}{4\pi k}}_{\text{EM}}, \tag{1.2}$$

where $k = \rho v_\mathrm{p}/B_\mathrm{p}$ is the wind mass-load function (also a flux-surface constant), r is the radial distance from the central star, ρ is the density, and v_ϕ (v_p) and B_ϕ (B_p) are the toroidal (poloidal) velocity and magnetic field respectively. Close to the disc surface, the magnetic component dominates, but at large distances the opposite is true. This transfer

[29] The magnetic field may also be generated by dynamo action in the disc (Königl & Salmeron 2011).
[30] See §2.3 of Königl & Salmeron (2011) for an analytical derivation of this requirement.

of angular momentum from the magnetic field threading the disc to the outflowing material is the essence of centrifugal acceleration, and is accomplished by the exertion of a 'back torque' on the disc by the magnetic field (Königl & Salmeron 2011).

The behaviour of MHD disc winds is determined by the location of the critical points of the outflow. Critical points are defined as the location where the component of flow velocity perpendicular to both the directions of axisymmetry and self-similarity equals the MHD wave speed in that direction. Arguably, the Alfvén point, where the poloidal speed of the outflow equals the local Alfvén speed, is the most important of these points for two reasons. First, magnetocentrifugal acceleration occurs until (approximately) this point; beyond it, the flow winds the magnetic field into toroidal coils[31], which provide collimation through magnetic hoop stress[32,33] (Königl & Salmeron 2011; Turner et al. 2014).

Secondly, the magnetic field enforces approximately constant angular velocity out to the Alfvén point, so the torque applied to the disc may be expressed as $l = \Omega_0 r_{\rm A}^2$, where $r_{\rm A}$ is the Alfvén lever arm[34], and Ω_0 is the disc angular velocity at the flow line footpoint. By defining the mass outflow rate in the wind as $\dot{M}_{\rm w}$, and the mass accretion rate as $\dot{M}_{\rm a}$, we may express the angular momentum transport by the outflowing and accreting material as $\sim \dot{M}_{\rm w}\Omega_0 r_0^2$ and $\sim \dot{M}_{\rm a}\Omega_0 r_0^2$ respectively, where r_0 denotes the radius of the flow line footpoint. Therefore, MHD disc winds enable accretion at a rate

$$\dot{M}_{\rm a} = (r_{\rm A}/r_0)^2 \dot{M}_{\rm w}. \tag{1.3}$$

The magnetic level arm parameter, $\lambda \equiv (r_{\rm A}/r_0)^2 \sim 3^2$ for reasonable parameters (Königl & Salmeron 2011), which is in broad agreement with observed mass outflow to mass accretion ratio observed in late-stage protostars (Cabrit 2007a, and references therein). This parameter also plays an important role in estimating the launch radius of outflows from observational data (e.g. §2.4.1.3; Anderson et al. 2003; Ferreira et al. 2006).

Whilst the origin of atomic jets and winds in microjet-scale outflows remains an open question (§1.2.1.3; Fig. 1.7), the wide-angle molecular winds observed in K-band H_2 emission are almost certainly the product of a disc wind, due to the low likelihood of molecular material surviving within $\lesssim 0.1$ AU of the protostar, as required for the X-wind

[31] This is beautifully illustrated by the simulations of Zanni et al. (2007).

[32] One should note that an isolated jet with strong toroidal magnetic fields is highly susceptible to the 'kink' instability, to an extent not seen in extended protostellar jets (Shang et al. 2007; Pudritz et al. 2007). Although it is not yet entirely clear how protostellar jets avoid being destroyed by this instability, candidate mechanisms include forms of self-regulatory stability (Ouyed et al. 2003), or the 'nesting' of the jet within wider-angle MHD wind components (Fig. 1.7; Shang et al. 2007).

[33] The hoop stress mechanism (referred to as the z-pinch in the plasma physics literature; Königl & Pudritz 2000), which is ubiquitous to all MHD winds launched along open rotating magnetic field lines (Cabrit 2007b), may be summarised thus. After crossing the Alfvén surface, the magnetic surfaces within the outflow open up. As this happens, the outflow material drags along the magnetic field lines, producing a large toroidal field (Ferreira 2002). As the toroidal field becomes stronger, the cross-product force generated by it and the downstream current density (i.e. $\boldsymbol{B}_\phi \times \boldsymbol{j}_z$) will overcome the centrifugal force, hence providing collimation (Königl & Pudritz 2000).

[34] This is also referred to as the Alfvén radius.

mechanism (see below; Takami et al. 2004). The uncertainty then lies in what stimulates the molecular material into emission. The cooling timescale of $\sim$ 2000 K molecular gas is less than a year (Hollenbach & Natta 1995), whereas the dynamical timescale of observed molecular winds is $\gtrsim$ 10 yr, indicating a heating mechanism must be acting (Takami et al. 2004). There are four main candidate mechanisms (Takami et al. 2004; Beck et al. 2008): shock heating, similar to the atomic jet components (e.g. Gredel 1994; Chrysostomou et al. 2000; Eislöffel et al. 2000), UV fluorescence from Ly α pumping (e.g. Ardila et al. 2002; Herczeg et al. 2006), X-ray stimulation (often cited as a possible cause of H_2 emission from circumstellar disks, e.g. Bary et al. 2002, 2003; Greene et al. 2010), and ambipolar diffusion (e.g. Safier 1993). Most recent studies conclude that observations are best matched by the shock or ambipolar diffusion scenarios (Takami et al. 2004; Beck et al. 2008; Agra-Amboage et al. 2014).

1.2.2.2. X-Wind

The X-wind model invokes the interaction between the stellar magnetosphere and disc magnetic field to provide a mechanism for extracting angular momentum from material in a narrow region at the inner disc radius. The model, first proposed by Shu et al. (1994), was designed to allow the central protostar to accrete material without suffering from excessive spin-up. The recent review of Bouvier et al. (2014) provides an excellent overview of the X-wind mechanism, which we summarize below.

The picture of the steady-state X-wind mechanism (Fig. 1.9) is as follows. The stellar magnetic flux that would nominally thread the accretion disc is instead trapped in the so-called 'X-region'. This region straddles the co-rotation radius, R_X, where the Keplerian angular velocity of the disc equals the stellar angular velocity.[35] The overwhelming magnetic pressure in this region forces it to rotate as a solid body. This has two effects. First, material just inside R_X becomes sub-Keplerian, and may efficiently climb field lines that lead onto the stellar surface and accrete; second, material just outside R_X is super-Keplerian, allowing it to efficiently climb field lines that lead outward and escape as a wind.

Angular momentum is transferred from the infalling material via the torques exerted on the X-region by the magnetized accretion funnels, which tends to push the X-region outwards. Simultaneously, the outflowing material extracts angular momentum from the X-region via magnetic back torques (see §1.2.2.1), which tends to push the X-region inwards. This balance between the two forces attempting to move the X-region traps the magnetic flux in that region[36], and represents a net transfer of angular momentum from the infalling material to the outflowing wind. This allows the central protostar to accrete material without experiencing significant spin-up.

[35] This phenomenon is referred to as disc-locking (Ghosh & Lamb 1979; Bouvier et al. 2014).

[36] Incidentally, this balance is also what truncates the disc at this position in the first place (Bouvier et al. 2014).

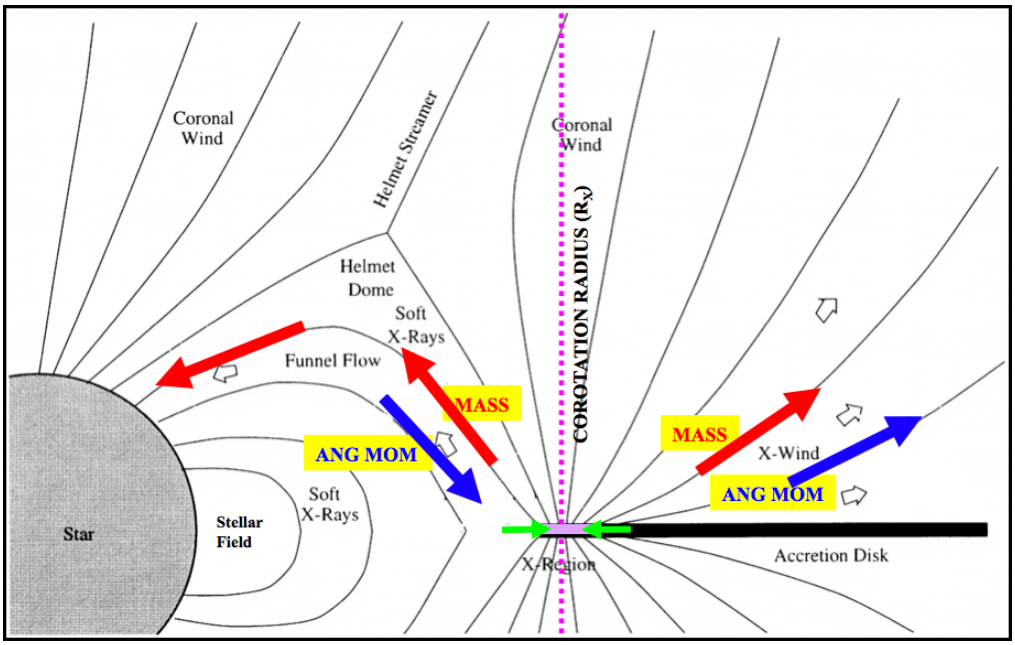

Figure 1.9 Schematic of the steady-state X-wind mechanism (Bouvier et al. 2014, after Gallet & Bouvier 2013). Material within the X-region rotates as a solid body due to magnetic pressure. Magnetic torques then transfer angular momentum from the infalling material to the X-region, and through to the outflowing wind. *Reproduced with the permission of J. Bouvier.*
Legend: Black thick line: circumstellar disc. Black solid curves: magnetic field. Purple dotted line: co-rotation radius. Purple thick horizontal line: X-region. Red arrows: mass flux. Blue arrows: angular momentum flux.

The original X-wind model assumes a bipolar stellar magnetic field (Ostriker & Shu 1995), but spectropolarimetry has shown that the surface magnetic fields of T Tauri stars are significantly more complex (e.g. Donati et al. 2008, 2011a,b, 2013). The model has been successfully generalized to the case of arbitrary multipole stellar fields by Mohanty & Shu (2008), who showed that their model requirements for the stellar magnetic field matched the observations of, e.g. Donati et al. (2008). However, there are still limitations to this model. Simulations have shown that particular conditions[37] are required in order to permit the necessary flux-trapping (Romanova et al. 2007). Furthermore, non-ideal MHD effects will cause time-varying accretion/outflow phenomena. Whilst such phenomena are observed (§1.2.1), the X-wind *model*, as a steady-state formulation, can only represent a time-averaged description of the process, and MHD simulations are necessary to investigate these time-varying effects in detail (Bouvier et al. 2014).

1.2.2.3. Other Theories

The presence of hot, low-mass-flux X-ray emitters in the microjets of some TTS (§1.2.1.3) has led to the resurrection of stellar and magnetospheric wind ejection mechanisms as a potential contributor to YSO outflows (Frank et al. 2014). Specifically, the discrepancy

[37] Specifically, the X-wind requires that magnetic field diffusion out of the X-region is offset by fluid advection of the field into the region (Romanova et al. 2007; Bouvier et al. 2014).

between the mass flux of X-ray emitting material and the wider outflows leads some authors to suggest that the X-rays emanate from the very core of the nested outflow structure, which could be driven by stellar or magnetospheric processes (e.g. §1.3.2.1; Günther et al. 2009). This outflow component would need to be sufficiently hot (∼ few MK) and/or fast (several hundred km s^{-1}) in order to cause the observed X-ray emission. Coronally driven stellar winds in T Tauri stars would be incapable of providing sufficient mass flux to match observations (Matt & Pudritz 2007); however, stellar winds driven by Alfvén waves created by impacting accreting material may be viable (Cranmer 2009). Other possible mechanisms are the ejection of hot 'plasmoids', akin to a coronal mass ejection from the Sun (Skinner et al. 2011), or 'magnetospheric ejections' of material created by reconnection events between the stellar and disc magnetic fields (the 'reconnection X-wind'; Ferreira et al. 2000; Zanni & Ferreira 2013). However, without direct evidence of such a high-velocity, low-mass-flux core to YSO outflows, these models largely remain the domain of theoretical work.

1.3. The Young Stellar Object DG Tauri

One of the most extensively studied protostars is DG Tauri. Basic information on the DG Tau system is detailed in Table 1.3, and stellar and spectral parameters are listed in Table 1.4. It is a transitional Class I/Class II classical T Tauri star (flat-SED, footnote 13, p. 11; Fig. 1.10; Adams et al. 1990; Pyo et al. 2003b; White & Hillenbrand 2004) located in the Taurus-Auriga star formation complex at a distance of 140 pc (Elias 1978). DG Tau has a companion Class I object, DG Tau B, at a distance of approximately 53″ (∼ 7500 AU) to the south-east. DG Tau B has similar proper motion to DG Tau (Rodríguez et al. 2012a), but it is unclear if the two objects are bound (e.g. Najita et al. 2007). Searches for a close companion to DG Tau have yielded no candidate objects (Leinert et al. 1991; White &

Table 1.3 Basic parameters of the DG Tau system. Adapted & updated from Farage (2007).

Parameter	Value	Reference
IRAS source ID[a]	04240+2559	Helou & Walker 1988
2MASS source ID[a]	J040270469+2606163	Cutri et al. 2003 (2MASS)
Right ascension[b]	4h 27m 4.71s	
Declination[b]	+26° 6′ 16.″8	
Distance from Sun (pc)	140	Elias 1978
Age (Myr)	0.55	Hartigan et al. 1995
	1.3–2.2	Güdel et al. 2007
	$0.28^{+0.12}_{-0.08}$	Guilloteau et al. 2011

[a] Further identifiers are available on the SIMBAD database (http://simbad.u-strasbg.fr/simbad/).
[b] J2000 epoch.

Table 1.4 Stellar and spectral parameters of the DG Tau system. Where multiple values are available in the literature, values are sorted by publication date. Adapted & updated from Farage (2007).

Parameter		Value	Reference
Spectral class		K7 – M0	Kenyon & Hartmann 1995
		K6 ± 2	White & Ghez 2001
		K3 ± 2	White & Hillenbrand 2004
		G1–K2	Connelley & Greene 2010
Spectral index, 2 – 25 μm		0.1	Greene & Lada 1996
		0.18	White & Hillenbrand 2004
		-1.2	Robitaille et al. 2007
Magnitude (mag)	U	13.57	Audard et al. 2007
	V	12.43 ± 0.06	Kenyon & Hartmann 1995
		10.50	Ducati 2002
	R	12.28	Zacharias et al. 2003
	J	8.691	Cutri et al. 2003 (2MASS)
	H	7.72	
	K	6.992	
Variability (mag)	K	0.8	Skrutskie et al. 1996
V-band extinction (mag)		1.6	Beckwith et al. 1990
		3.2	Hartigan et al. 1995
		2.2	Muzerolle et al. 1998
		1.6	Gullbring et al. 2000
		3.32	White & Hillenbrand 2004
K-band veiling		2.0 ± 0.10	Doppmann et al. 2005
		2.67 ± 0.41	Johns-Krull 2007
		$0.00^{+1.68}_{-0.00}$	Connelley & Greene 2010
Mass ($M_\odot$)		0.56	Beckwith et al. 1990
		0.67	Hartigan et al. 1995
		0.88	White & Ghez 2001
		0.9 – 1.8	Güdel et al. 2007
		1.19	Rigliaco et al. 2013
Radius ($R_\odot$)		2.5	Güdel et al. 2007
		3.03	Rigliaco et al. 2013
Rotational velocity ($v \sin i$, km s^{-1})		20	Basri & Batalha 1990
		28.6 ± 5.1	White & Hillenbrand 2004
		24 ± 2.0	Doppmann et al. 2005
		24.7 ± 0.7	Nguyen et al. 2012
Mean surface magnetic field strength (kG)		2.55	Johns-Krull 2007

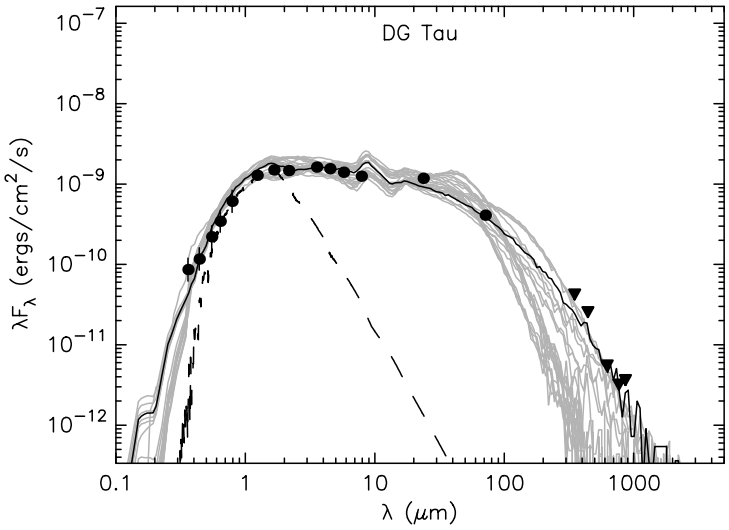

Figure 1.10 Spectral energy distribution (SED) of DG Tau, from ultraviolet to millimetre wavelengths (Robitaille et al. 2007, data sources detailed therein). Triangles denote upper limits; error bars are only shown if they exceed the size of the plotted symbol. The black line shows the best-fit model[a] to the SED, and grey lines show other models that were considered adequate fits. The SED of the stellar photosphere in the best-fit model is shown by the dashed line; there is a significant IR, and moderate UV, excess. *© AAS. Reproduced with permission.*

[a]Envelope accretion rate, 5.48×10^{-9} $M_\odot$; central star temperature, 4549 K; SED spectral index, -1.2; disc accretion rate, 8.5×10^{-7} $M_\odot$. Best-fit values for stellar mass & luminosity, and accretion disc inner radius, outer radius and height are not provided.

Table 1.4 Stellar and spectral parameters of the DG Tau system (continued).

Parameter	Value	Reference
Photospheric temperature (K)	3890	Beckwith et al. 1990
	4395	Hartigan et al. 1994
	4205	Briceño et al. 2002
	4775	White & Hillenbrand 2004
	4549	Robitaille et al. 2007
Photospheric luminosity ($L_\odot$)	1.7	Beckwith et al. 1990
	1.74	Hartigan et al. 1995
	3.62	White & Hillenbrand 2004
Bolometric luminosity ($L_\odot$)	> 8	Cohen & Kuhi 1979
	6.36	Kenyon & Hartmann 1995
	3.5	Connelley & Greene 2010

Ghez 2001; Connelley et al. 2008, 2009; Kraus et al. 2011), nor has another candidate wide-binary companion been detected (e.g. Kraus & Hillenbrand 2009).

1.3.1. Circumstellar Disc and Accretion

The circumstellar disc of DG Tau has been investigated by multiple authors. A disc mass of 0.04 $M_\odot$ was determined from model fitting to the 1.3 mm continuum disc luminosity (Beckwith et al. 1990). Subsequent estimates of the disc mass utilizing different measurement techniques do not deviate significantly from this value (Kitamura et al. 1996b; Andrews & Williams 2005; Robitaille et al. 2007; Podio et al. 2013, although note that the range of input parameters to the models of Podio et al. 2013 allows disc masses of up to 0.1 $M_\odot$). The dust grains in the disc have a characteristic temperature $\sim$ 40 K (Beckwith et al. 1990), although Podio et al. (2013) claim that the strong UV field of the central star irradiates the disc upper layer 10–90 AU from the central star to $\sim$ 600 K, stimulating the observed bright water lines at 557 and 1113 GHz. The motions of the inner regions of the disc, as observed in ^{13}CO(2–1) emission, are consistent with a disc orbiting a 0.67 $M_\odot$ central star (Table 1.4), with the same rotational sense as was inferred for the approaching DG Tau microjet through optical observations (§1.3.2.1; Testi et al. 2002). Attempts to probe the magnetic field geometry threading the disc via millimetre-wavelength polarisation measurements have proved fruitless (Hughes et al. 2013), although it is hoped high-angular resolution instruments such as ALMA will be able to reveal complex, small-scale magnetic structure.

The accretion rate on to the DG Tau central protostar has been monitored using a variety of methods for $\sim$ 20 yr (Table 1.5). As may be expected for a variable star, the accretion rate changes with time[38], and peaked at $\sim 10^{-6}$ $M_\odot$ yr^{-1} in the late 1980s (Hartigan et al. 1995, although White & Hillenbrand 2004 cautions this may be an overestimation). However, the mean accretion rate appears to be $\sim$ a few $\times 10^{-7}$ $M_\odot$ yr^{-1}, which is 0.5–2 dex greater than the field population of classical T Tauri stars (e.g. White & Hillenbrand 2004). Given that DG Tau still has a remnant protostellar envelope feeding material onto the circumstellar disc (§1.3.3), it is not surprising that more material is accreting onto the central star than

[38] It is important to acknowledge the complexities inherent in attempting to calculate protostellar mass accretion rates. The mass accretion rate is typically estimated from the accretion shock emission, which is believed to be represented by the blue/UV excess emission in protostellar SEDs (§1.1.2.2; Table 1.5, p. 31). The estimates of this excess emission are sensitive to the assumed extinction towards the central protostar, which is in turn sensitive to the presumed stellar colours of the object. In objects such as DG Tau, which tend to show 'veiled' stellar spectra (Greene & Lada 1996; Hessman & Guenther 1997) due to the strong continuum emission from accretion (e.g. Gullbring et al. 2000), the objects may appear bluer than the true stellar photosphere, leading to an overestimate of the extinction and a discrepancy in the calculated mass accretion rate (see Gullbring et al. 1998 and Hartmann 1998 for discussions). The extinction correction for the observed excess emission may also be geometry dependent if the optical light is mostly scattered, as is suggested in DG Tau, based on optical polarization measurements (Pereyra et al. 2009, and references therein). Therefore, whilst the CO variability of DG Tau is a strong indicator of accretion variability (Table 1.6, p. 33), some of the accretion 'variability' seen in Table 1.5 may be due to differing assumptions made in the accretion rate calculations.

Table 1.5 Estimated disc accretion rates in DG Tau. Estimates are ordered by publication date. Brief notes are provided on the method employed in each reference.

Observing epoch	Mass accretion rate (10^{-7} $M_\odot$ yr^{-1})	Reference	Notes
1988 Jan – 1990 Jan	19.95	Hartigan et al. 1995	Reddening at 5700 Å converted to an accretion boundary layer luminosity, assuming the stellar photosphere blocks half of the boundary layer emission. The accretion rate on to the central star is computed assuming that the material does not fall ballistically onto the star from a large distance.
1979–1990	5	Gullbring et al. 2000	Shock modelling, as per Calvet & Gullbring (1998), used to estimate the energy flux in the accretion column. Energy flux then converted to an accretion rate based on energy arguments. Assumes a stellar mass of 0.5 $M_\odot$, and a stellar radius of 2$R_\odot$. Data taken from the *International Ultraviolet Explorer* (*IUE*) archive.
1962 – 1984, Sep 1991	0.48	White & Ghez 2001	Accretion luminosity estimated from *U*-band excess. Luminosity converted to mass accretion rate by the method of Gullbring et al. (1998), which estimates luminosity released by impact of the accretion flow from the energy equation. Data from Herbst et al. (1994, 1962–1984 epoch) and Hessman & Guenther (1997, 1991 Sep epoch).
1999 Dec, 2002 Dec, 2003 Feb	7.4	White & Hillenbrand 2004	Computed the excess emission in the 6000–6500 Å passband, made a bolometric correction, and converted to a mass accretion rate by assuming luminosity equals gravitational energy of accreting material free-falling from 3 $R_\odot$.
Late 1980s–[a]	8.5	Robitaille et al. 2007	Comparison of observed SED with a grid of 200,000 models. The models are of pre-main-sequence stars with a wide range of physical parameters, as well as various combinations of circumstellar discs, infalling flattened envelopes, and outflow cavities.
2005 Oct 25	0.96	Beck et al. 2010	Assumes that all Br γ flux emanates from the accretion process. This is converted to a total accretion luminosity as per Muzerolle et al. (1998). Then assumes that luminosity is from a shock at the base of a free-fall accretion column.
2005 Oct 15	1	Agra-Amboage et al. 2011	As for Beck et al. (2010), but assuming a lower *V*-band extinction and stellar mass.

[a] SED formed from multiple sources of literature data.

would be the norm for a CTTS.

A common feature of the K-band spectra of young stellar objects with circumstellar discs is CO first overtone bands. These bands appear in emission or absorption in many YSOs, including DG Tau, where the bands have been observed to oscillate between the two states (Table 1.6). When observed in emission, protostellar CO bandheads typically take on a shape that indicates they arise in a temperature-inverted Keplerian disc very close (a few stellar radii) from the central star (Carr et al. 1993; Chandler et al. 1993; Carr 1995). Although this behaviour has never been modelled in DG Tau, the presence of CO bandhead emission appears to correlate with strong veiling of the photospheric spectrum in this object (e.g. Greene & Lada 1996; Doppmann et al. 2005). Given that both the photospheric veiling continuum and CO bandheads appearing in emission have been taken as signs of enhanced accretion activity[39], this suggests that DG Tau experiences transient or periodic accretion bursts, which may be related to the structures observed in its small-scale outflows (§1.3.2.1).

1.3.2. Outflows

As one of the first protostars to be connected to a collimated outflow (Mundt & Fried 1983), the outflows driven by DG Tau have been extensively studied over the last thirty years. Below, we summarize the current understanding of the these outflows.

1.3.2.1. Small-Scale Outflows

Since the microjet of DG Tau was first imaged by Kepner et al. (1993), numerous studies at multiple wavelengths have characterised the nature of these small-scale outflows. As seen in optical/NIR forbidden lines, the approaching (blueshifted) outflow takes on the archetypal microjet morphology of a high-velocity jet, typically termed the high-velocity component (HVC), nested within a lower-velocity emission component, termed the medium- or intermediate-velocity component (MVC/IVC; Fig. 1.7; Lavalley et al. 1997; Bacciotti et al. 2000; Bacciotti 2002; Pyo et al. 2003b; Agra-Amboage et al. 2011; Maurri et al. 2014). The HVC has a centroid velocity of $\sim$ 200–400 km s^{-1} depending on the observing epoch, whereas the velocity of the wider-angle component is typically $\sim$ 100 km s^{-1} (e.g. Pyo et al. 2003b; Agra-Amboage et al. 2011). The HVC is dominated by moving, shock-excited knots that are ejected periodically into the jet channel (Kepner et al. 1993; Lavalley-Fouquet et al. 2000; Pyo et al. 2003b; Agra-Amboage et al. 2011). The period of this ejection is presently an open question, with estimates ranging from 2.5 yr (Agra-Amboage et al. 2011) to 5 yr (Pyo et al. 2003b; Rodríguez et al. 2012b). The IVC is usually interpreted to be a steady, wide-angle disc wind (e.g. Agra-Amboage et al. 2011), although Pyo et al. (2003b) suggests

[39]The temperature inversion stimulating the CO emission may be caused by heating from the magnetospheric accretion shock (Najita et al. 2000).

Table 1.6 *K*-band CO bandhead emission/absorption in the spectrum of DG Tau. Measurements of the magnitude of CO emission are provided where available. Measurements are ordered by observing epoch.

Obs. epoch	E/A[a]	CO flux[b] (10^{-13} erg cm^{-2} s^{-1})	CO EW[c] (Å)	L_{CO}[d] (10^{-2} $L_\odot$)	$F_{CO}/S_{2.3}$[e] (10^{10} Hz)	Reference
1983 Nov	E	9.2 ± 1.3	12 ± 1.7	—	—	Hamann et al. 1988
1986 May – 1987 Jan	E	8.7 ± 0.3	—	—	6.69	Carr 1989[f]
1992 Sep	E	—	—	3.1	—	Chandler et al. 1993
1994 Sep	A?	—	—	—	—	Greene & Lada 1996
1995 Jan	E?	—	—	—	1.11	Biscaya et al. 1997
1995 Nov	E	—	—	—	—	Greene & Lada 1996; Biscaya et al. 1997[g]
1996 Sep	E	—	—	—	16.53	Biscaya et al. 1997
1996 Dec 21	E	—	—	—	18.91	"
1996 Dec 22	E	—	—	—	15.95	"
1996 Dec 23	E	—	—	—	11.14	"
1996 Dec 24	E	—	—	—	13.2	"
1996 Dec 26	E	—	—	—	20.69	"
1996 Dec 29	E	—	—	—	14.29	"
1996 Dec 31	E	—	—	—	14.63	"
1997 Jan 27	E&A[h]	—	—	—	—	Najita et al. 2003
2001 Nov 06	A?	—	—	—	—	Doppmann et al. 2005
2005 Oct 26	A	—	—	—	—	Beck et al. 2008[i]

[a] Bandheads appear in emission (E) or absorption (A).
[b] Flux in the $v = 2$–0 bandhead. Integrated from 2.293 to 2.317 μm for Carr (1989).
[c] Equivalent width of the $v = 2$–0 CO bandhead.
[d] Total luminosity of observed CO first overtone bands.
[e] F_{CO} is the $v = 2$–0 bandhead flux above the linear continuum level, integrated from 2.293 to 2.317 μm. $S_{2.3}$ is the continuum flux at 2.3 μm, which was linearly extrapolated from the continuum fitted shortward of 2.29 μm.
[f] $F_{CO}/S_{2.3}$ for these data reported by Biscaya et al. (1997).
[g] Reported by Tokunaga (private comm.) in these references.
[h] The observed spectrum of the $v = 1$–0 R(3) was consistent with broad CO emission, but there was a central (possibly interstellar) absorption feature.
[i] The *K*-band spectrum from these data is shown in Fig. 2.1, p. 52.

that the increase in width of this component with distance from the central star indicates that there may be a contribution from jet entrainment. A wide-angle approaching molecular wind is detected in H_2 1-0 S(1) 2.1218 μm emission within 0.″4 of the central star, with line velocities $\lesssim$ 10–15 km s^{-1} (Takami et al. 2004; Beck et al. 2008; Agra-Amboage et al. 2014). Spectroimaging of the outflows has revealed that the receding (redshifted) outflow is a factor of 1.4 slower than the approaching outflow (Lavalley et al. 1997), and takes on a bubble-like morphology (Agra-Amboage et al. 2011); this feature has been interpreted to be a Herbig-Haro-like bow-shock in the process of being launched (Agra-Amboage et al. 2011, 2014), possibly through the so-called 'magnetic tower' mechanism (Ciardi et al. 2009).

Spectroscopy and spectroimaging have allowed the physical parameters of the DG Tau approaching outflow to be determined, either through the Bacciotti & Eislöffel (1999), hereafter BE99, optical line ratio diagnostic technique[40], or through the relationship between the ratio of the H-band [Fe II] lines at 1.533 and 1.644 μm and electron density (Pesenti et al. 2003). Based on these techniques, typical measured jet electron densities are of order 10^4 cm^{-3}, temperatures are of order 10^4 K, and ionization fractions are from 0.1 to 0.5 (Bacciotti et al. 2000; Bacciotti 2002; Agra-Amboage et al. 2011; Maurri et al. 2014). All of these parameters tend to be higher in the HVC, but within the same order of magnitude. Most recently, Maurri et al. (2014) determined that the HVC hydrogen number density may reach $\sim 10^6$ cm^{-3} close to the central star. Determination of these physical parameters allows for the calculation of the mass-loss rate in the approaching outflow (Table 1.7, optical/near-infrared/ultraviolet section). The typical mass-loss rate from these data, $\sim 10^{-8}$ M$_\odot$ yr^{-1}, leads to a mass outflow to mass accretion ratio, $\dot{M}_\mathrm{w}/\dot{M}_\mathrm{a} \sim 0.1$ (Agra-Amboage et al. 2011), which is in broad agreement with the predictions of MHD wind launch theory (§1.2.2.1).

The DG Tau approaching outflow has also been probed at radio wavelengths, utilizing the Very Large Array (Lynch et al. 2013) and the e-MERLIN aperture synthesis telescope (Ainsworth et al. 2013). Those authors report a mass flux similar to the optical observations, but higher than the near-infrared data (Table 1.7, radio section). This is almost certainly due to different observing regimes tracing different streamlines, densities and temperatures within the outflow (Lynch et al. 2013). Also, the data of Ainsworth et al. (2013) show that the DG Tau outflow has an opening angle $\sim 90°$ very close to the central star, implying that collimation of the outflows must occur $\lesssim$ 50 AU above the circumstellar disc surface.

DG Tau was the first protostar for which the detection of microjet-scale outflow rotation was claimed. Bacciotti et al. (2002) aligned the slit of the Space Telescope Imaging Spectrograph (STIS) aboard *HST* to the axis of the DG Tau outflows at seven different offsets from the axis. By carefully separating the components of the forbidden emission lines through multiple Gaussian fits, they were able to demonstrate an apparent consistent

[40]The lines used are the [S II] doublet at 6716/6731 Å, the [O I] lines at 6300 and 6363 Å, and the [N II] lines at 6548 and 6583 Å (Bacciotti & Eislöffel 1999).

Table 1.7 Estimates of the mass-loss rate in the DG Tau approaching outflow. Estimates are ordered by observation epoch. References assuming a spherical outflow geometry have been excluded. Brief notes are provided on the method employed in each reference. Adapted & updated from Farage (2007).

Observing epoch	Mass loss rate ($M_\odot$ yr^{-1})	Reference	Notes
		Optical/near-infrared/ultraviolet	
1985 Feb, 1986 Feb	6×10^{-7}	Cohen et al. 1988	Relationship between [O I] 63 μm luminosity for the single shock model of Hollenbach (1985).
1988 Jan – 1990 Jan	3×10^{-7}	Hartigan et al. 1995	*(1)* High-velocity component [O I] 6300 Å emission compared to shock models to determine outflowing mass, converted to mass outflow rate by multiplying by flow velocity divided by outflow aperture (scale length). Assumes distributed heating of the emitting material.
	3×10^{-5}	Hartigan et al. 1995; Lavalley et al. 1997	*(2)* Correlation between high-velocity component [O I] 6300 Å flux and mass flux, assuming the [O I] emission is generated by a single shock front.
1994 Nov 03	$(0.1–1.9) \times 10^{-7}$	Lavalley et al. 1997	As for Hartigan et al. (1995) *(1)*, allowing for the electron density to be close to the critical density of the [O I] line.
	6.5×10^{-6}	Lavalley et al. 1997	As for Hartigan et al. (1995) *(2)*.
1998 Jan 23–26	1.4×10^{-8}	Lavalley-Fouquet et al. 2000	Methods from Hartigan et al. (1994, 1995) for [O I] line luminosities. Value quoted is agreement between the three methods at 1.″2 from the central star; the mass outflow rate closer to the central star may be 10–100 times higher, depending on the method used.
1999 Jan 14	2.4×10^{-7}	Bacciotti et al. 2002	Bacciotti & Eislöffel (1999) (BE99) optical forbidden line ratio diagnostic method, within 1.″5 of the central star (Bacciotti et al. 2000)
	6.7×10^{-8}	Coffey et al. 2008	Calculated from the total hydrogen density, jet radius and jet velocity assuming an axisymmetric jet (cf. §2.4.1.4). Quoted value is sum of HVC and IVC mass fluxes.
	$(8 \pm 4) \times 10^{-7}$	Maurri et al. 2014	Uses a refined version of the BE99 method to determine density. Mass flux calculated from velocity, density and radius, assuming flow is along nested magnetic surfaces.

Table 1.7 Estimates of the mass-loss rate in the DG Tau approaching outflow (continued).

Observing epoch	Mass loss rate ($M_\odot$ yr^{-1})	Reference	Notes
		Optical/near-infrared/ultraviolet	
1999 Dec, 2002 Dec, 2003 Feb	6.5×10^{-7}	White & Hillenbrand 2004	As for Hartigan et al. (1995) *(1)*, using high-velocity [S II] 6731 Å line luminosity; assumes electron density is in the high-density limit for [O I] emission.
2002 Nov 25	$\gtrsim 2.2 \times 10^{-9}$	Takami et al. 2004	Calculated from H_2 1-0 S(1) 2.1218 μm emission, assuming a conical emitting volume geometry, a filling factor of 1, and a gas temperature of 2000 K.
2005 Oct 15	3.3×10^{-8}	Agra-Amboage et al. 2011	Three methods using [Fe II] line luminosities (electron density & jet cross-sectional area, volume emission from uniform jet slab, and emission from shock fronts). Quoted value is sum of high- and medium-velocity emission component mass fluxes.
	$\sim 1 \times 10^{-9}$	Agra-Amboage et al. 2014	As for Takami et al. (2004), but taking a more extended emitting region.
	$\geq 6.7 \times 10^{-8}$	Agra-Amboage et al. 2014	Computed from the assumption that H_2 emission arises in a reverse shock formed by a wide-angle molecular wind impacting the walls of an outflow cavity.
2005 Oct 25	$> 1.8 \times 10^{-8}$	Beck et al. 2010	Calculated from spatially extended Br γ flux, assuming this emission is thermally excited and optically thin.
2011 Feb	$(1\text{–}2) \times 10^{-9}$	Schneider et al. 2013a	Two methods from C IV doublet emission in the ultraviolet (cooling cylindrical outflow, and localised outflow heating).
		Radio	
2011 June	$\gtrsim 5 \times 10^{-8}$	Lynch et al. 2013	Comparison of radio- and optically-derived (Maurri et al. 2014) electron density profiles to form analytical axial density and velocity profiles, which are integrated to give mass flux for all ionized outflow components.
2011 Aug 01–04	1.5×10^{-8}	Ainsworth et al. 2013	As for Lynch et al. (2013).
		X-ray	
2004 Jan, 2005 Dec, 2006 Apr	1.3×10^{-11}	Schneider & Schmitt 2008	Correlation between the inferred soft X-ray volume emission measure and density, and assuming a cylindrical radiating volume, with a length equal to the cooling length of the emitting material.
	2.7×10^{-11}	Günther et al. 2009	As for Schneider & Schmitt (2008).

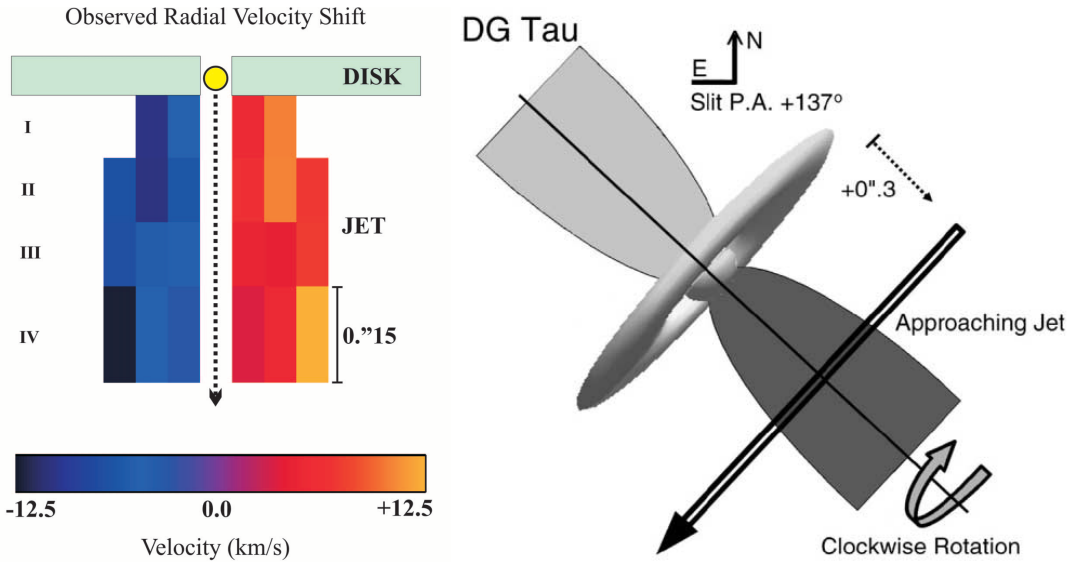

Figure 1.11 Investigations of rotation in the approaching outflows from DG Tau. *Left:* Doppler shifts observed in the DG Tau approaching optical forbidden line IVC (Bacciotti et al. 2002). Velocities are determined from seven *HST* STIS slits placed along the jet axis, and are shown relative to the velocity in the central slit. *Right:* Inferred rotation in the DG Tau jet (Coffey et al. 2007). The double-line arrow shows the position and orientation of the *HST* STIS slit used to infer rotation in the DG Tau approaching optical forbidden line HVC. The inferred sense of rotation agrees with both the rotation inferred by Bacciotti et al. (2002), and the circumstellar disc rotation inferred by Testi et al. (2002). © *AAS. Reproduced with permission.*

Doppler shift in the IVC across the jet axis (Fig. 1.11, left-hand panel), indicative of rotation of 6–15 km s^{-1} up to 100 AU above the disc midplane. Subsequently, Coffey et al. (2007) placed the STIS slit across the jet 0.″3 from the central star, and inferred a rotational velocity in the HVC of 6–15 km s^{-1} (Fig. 1.11, right-hand panel). Whilst the claim of rotation in the DG Tau outflows was the catalyst for many further studies (e.g. Coffey et al. 2004, 2007), it needs to be verified in the wake of the findings of Coffey et al. (2012, see §1.2.1.3), who found that the apparent rotation signature in the jet from RW Aur changes with time.

DG Tau is also one of the prototype objects for the study of soft X-rays from protostellar outflows. Güdel et al. (2005, 2008, 2011) report soft X-ray emission in the DG Tau jet detected by *Chandra*, up to $\sim 5''$ from the central star. Intriguingly, there is a peak of X-ray emission $\sim$ 0.″1–0.″2 from the central star that has remained stationary over a period of 8 yr (Güdel et al. 2011). This X-ray feature has also been investigated by Schneider & Schmitt (2008) and Günther et al. (2009), who report a mass-flux through the emitting region $\sim$ 2 dex less than what is inferred from optical/NIR data (Table 1.7, X-ray section). This discrepancy led those authors to propose there must be a central, hot, high-velocity component to the DG Tau outflows nested inside the optical/NIR HVC responsible for this emission. This may be supported by the $\sim$ 500 km s^{-1} blueshifted He I 1.083 μm absorption feature reported by Takami et al. (2002), which they propose is due to an accelerating wind very close to the star.

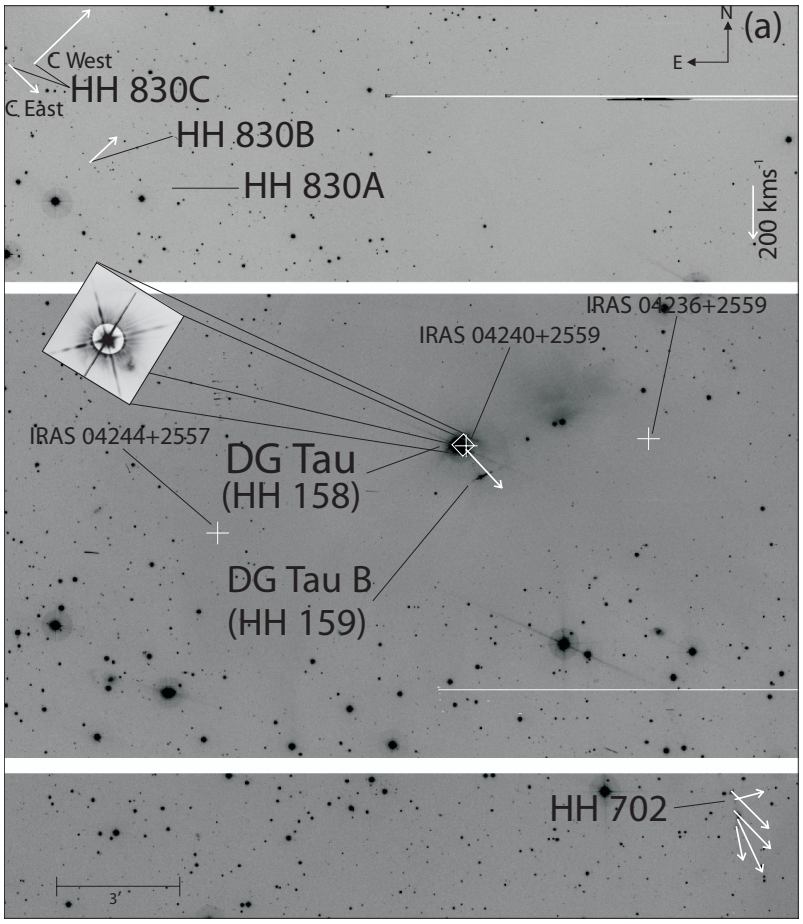

Figure 1.12 Herbig-Haro objects in the vicinity of DG Tau, as seen in [S II] (McGroarty et al. 2007).[a] HH 158 is the nebulosity visible to the south-west of DG Tau in the inset; an enlarged view of this complex is available in Eislöffel & Mundt (1998). White arrows show the inferred proper motions of the Herbig-Haro objects; the arrow length is an indication of the magnitude of proper motion, as per the scale in the top-right of the figure. It can be inferred that the HH 830 complex is inconsistent with being driven by DG Tau. *Source: McGroarty, F., Ray, T. P., Froebrich, D.* A&A*, 467, 1197–1207, 2007, reproduced with permission © ESO.*

[a]Observed using a narrow-band filter of central wavelength 672.5 nm, and a wavelength range of 8 nm.

1.3.2.2. Large-Scale Outflows

DG Tau is known to drive two Herbig-Haro complexes. HH 158 was first detected by Mundt & Fried (1983), and was investigated in detail by Eislöffel & Mundt (1998). It is a chain of four Herbig-Haro objects, extending out to 16″ from the central star as of 2007 (McGroarty et al. 2007). Analysis of the proper motion and radial velocity of the leading HH object, HH 158 C, yields a jet inclination to the line of sight of $37.7° \pm 2°$, which is assumed to be the inclination of the approaching microjet to the line of sight.

Sun et al. (2003) and McGroarty & Ray (2004) independently located another Herbig-Haro complex, HH 702, $\sim 11' \approx 0.5$ pc from the DG Tau central star. McGroarty & Ray (2004) suggested that HH 702 was likely driven by the DG Tau system; this was later confirmed by analysis of the proper motions within the complex (McGroarty et al. 2007). Another HH complex, HH 830, was observed in the vicinity, diammetrically opposed to HH 702 with respect to DG Tau (McGroarty & Ray 2004). However, proper motion analysis showed that this complex is unrelated to the DG Tau outflows (McGroarty et al. 2007). Therefore, the bipolar asymmetry in the DG Tau outflows (§1.3.2.1) extends out to ~ 0.5 pc from the central star.

There is no known CO outflow associated with DG Tau. However, the decrease in

^{13}CO $J = 1$–0 column density within ~ 4000 AU of the central star (Kitamura et al. 1996a) indicates that the molecular material has been somewhat cleared out, suggesting a CO outflow was once present, but has likely cooled to the point where it no longer emits at a detectable level. This is consistent with DG Tau being an object currently transitioning from Class I to Class II on the protostellar evolutionary sequence (§1.1.2.2).

1.3.3. Circumstellar Environment

Although much of the molecular material surrounding DG Tau has been cleared (see above), a remnant protostellar envelope remains close to the central star, as seen in ^{13}CO $J = 1$–0 emission (Kitamura et al. 1996a). The envelope has a radius of 2800 AU, a mass[41] of 0.03 $M_\odot$, and is 'clumpy' in nature; it is presumed to be flattened, but no information is available on the envelope extent above the circumstellar disc midplane. The velocity of the ^{13}CO emission tentatively suggests that the envelope is expanding at a few km s^{-1}, although this is open to interpretation. The presence of this envelope has yet to be taken into account in the study and interpretation of the DG Tau outflows.

1.4. Near-infrared Integral Field Spectrograph (NIFS)

Integral-field spectroscopy is a powerful technique for astronomical observations. The simultaneous acquisition of spatial (structural) and spectral (kinematic) information is applicable to a wide range of scientific objectives, from analysing the kinematics of active galactic nuclei and stars close to supermassive black holes, to investigating nearby stellar populations (e.g. McGregor et al. 2001). An integral-field spectrograph (IFS) is an instrument that forms a spectrum for every spatial pixel ('spaxel') in the telescope focal plane. This can be achieved using an integral-field unit (IFU) in one of three ways (Fig. 1.13).[42] Lenslets may be used to segment the focal plane image of the target, with each segment then dispersed into a discrete spectrum. Such instruments are affected by issues of overlap between spectra, and are hence suited for applications that only require a short spectrum[43]. Optical fibres may be used to re-arrange the lenslet outputs into a single vertical pseudo-slit, increasing coverage on the camera detector, but such instruments are difficult to manufacture. Finally, a series of image-slicing mirrors may be used to re-arrange the light from vertical 'slitlets' on the focal plane into a single slit for dispersion. This system is ideal for cryogenically-cooled (e.g. infrared-sensitive) instruments, although

[41] The mass of the envelope is calculated as per equation 1 of Kitamura et al. (1996a), assuming a ^{13}CO fractional abundance of 1×10^{-6} (Frerking et al. 1982), a line excitation temperature of 10 K, and optically-thin ^{13}CO emission.

[42] We adopt the following nomenclature for these instruments. An integral-field spectrograph (IFS) describes the entire instrument (IFU plus spectrograph); the integral-field unit (IFU) is the suite of optics that segments/slices the telescope focal plane.

[43] One may obtain either a low-resolution spectrum over a large wavelength range, or a high-resolution spectrum over a short wavelength range (Allington-Smith & Content 1998).

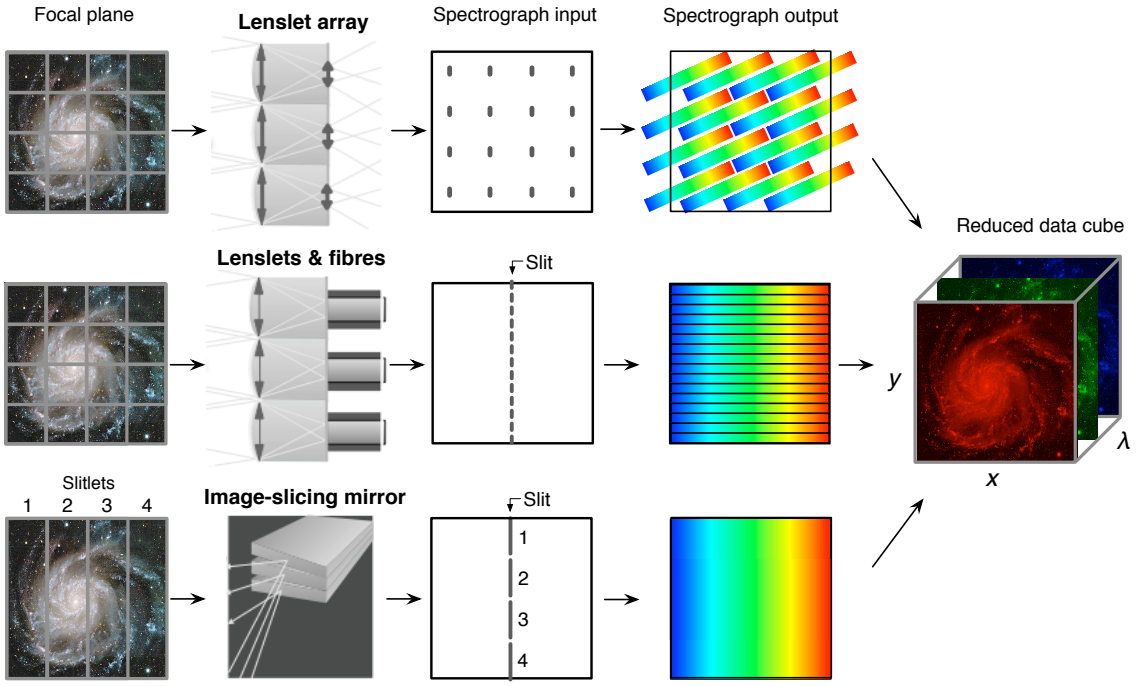

Figure 1.13 Basic schematics of different integral-field unit designs (Farage 2007, based on figures from Allington-Smith & Content 1998). *Top-to-bottom*: lenslet array, fibre-fed and image-slicing integral-field units; NIFS uses an image-slicing IFU. All three methods split the focal plane of the telescope into separate regions, which are then passed to a spectrograph and dispersed. Reduction of these data yields a three-dimensional data cube, with two spatial dimensions (x and y) and one spectral dimension (λ). *Reproduced with the permission of C. Farage.*

Table 1.8 Available gratings, and related performance data, for the NIFS instrument (McGregor et al. 2003).

Band	Central wavelength (μm)	Spectral range (μm)	Resolving power	Velocity resolution (km s^{-1})
Z	1.05	0.94 – 1.15	4990	60.1
J	1.25	1.15 – 1.35	6050	49.6
H	1.65	1.49 – 1.80	5290	56.8
K	2.20	1.99 – 2.40	5290	56.7

the optics are not suited to blue wavelengths. For a full discussion of the methods of integral-field spectroscopy, see Allington-Smith & Content (1998).

The data presented in this thesis were obtained using the Near-infrared Integral Field Spectrograph (NIFS).[44] The instrument was commissioned on the Gemini North telescope, Mauna Kea Observatory, Hawaii in 2005.[45] NIFS consists of an image-slicing-type IFU (Hart et al. 2003) with a moderate-resolution, near-infrared spectrograph, and utilizes the output from the ALTAIR adaptive optics system, which provides an AO-corrected spatial

[44] Full information on the observing constraints and procedures for NIFS may be found on the NIFS website at http://www.gemini.edu/sciops/instruments/nifs/.

[45] Indeed, the 2005 epoch data included in this thesis are from the NIFS commissioning run.

resolution $\sim 0\farcs1$ (Herriot et al. 1998). NIFS splits a $3'' \times 3''$ field-of-view into 29 slitlets of width $\sim 0\farcs1$, and provides $0\farcs04$ spatial sampling in the dispersion direction. The output is formatted for the 2048×2048 pixel Rockwell HAWAII-2RG HgCdTe detector such that each near-infrared photometric band can be observed at a single grating setting. The detector housing is cryogenically cooled to a temperature of 60 K. NIFS performance in each band is given in Table 1.8; for a full description of the instrument construction, see McGregor et al. (2003).

NIFS has two features that are particularly useful for the study of protostellar outflows. The first is a suite of occulting discs, of diameter $0\farcs2$ and $0\farcs5$, that may be used to obscure the central star, thereby increasing sensitivity to extended outflow structure. This removes a major restriction that was placed on previous IFU studies of protostellar outflows (e.g. Agra-Amboage et al. 2011). Secondly, protostars such as DG Tau are sufficiently bright in the K-band (Table 1.4) to act as the ALTAIR guide star during the observations, removing the need to find a separate guide object within $25''$ of the target. This opens up the outflows of relatively isolated protostars to adaptive-optics studies.

1.5. Thesis Motivation

Protostellar outflows have been extensively studied over the past thirty years. However, several key questions in the field remain unanswered. This Section outlines the questions that will be addressed in this thesis; §1.6 summarizes how these issues will be investigated.

Until the mid-1990s, protostellar outflow studies were primarily limited by the resolution that could be achieved using ground-based telescopes without AO-correction. Such observations, taken with natural seeing of ~ 1–$2''$, were restricted to studying the large-scale Herbig-Haro-type outflows (e.g. Mundt & Fried 1983; Eislöffel & Mundt 1998). Studies of the microjet-scale outflows were limited to spectroscopically examining the unresolved FEL regions adjacent to the star, which are weak compared to the stellar continuum and hence difficult to investigate (e.g. Hirth et al. 1994a,b; see also the review of Appenzeller & Mundt 1989). These studies were unable to spatially resolve the innermost regions of the outflows, which are believed to be the best indicator of the intrinsic properties of the outflows prior to any interactions.

The advent of *HST* and ground-based adaptive-optics systems opened the microjet-scale outflows to spatially-resolved observation (§1.2.1.3). However, observations to date have been somewhat limited by the instruments and techniques used. *HST* is capable of achieving spatial resolutions $\sim 0\farcs1$, and is useful for imaging studies of microjet knots, and outflow structure in general (e.g. Kepner et al. 1993; Burrows et al. 1996; Krist et al. 1997, 1999; Padgett et al. 1999; Schneider et al. 2013b). However, such imaging cannot provide kinematic or line-excitation information on the outflowing gas. STIS has been widely used

for this purpose (e.g. Bacciotti et al. 2000, 2002; Coffey et al. 2004, 2007, 2012; Melnikov et al. 2009; Ardila et al. 2013; Schneider et al. 2013a), but single-slit spectroscopy only provides structural information along a single axis.[46] Integral-field spectroscopy (§1.4) acquires both structural (spatial) and kinematic (spectral) information simultaneously, and is an advantageous technique for microjet-scale outflow studies. Initial spectroimaging studies of protostellar outflows with adaptive optics achieved spatial resolutions $\sim 0\farcs5$–$1\farcs0$ (Lavalley et al. 1997; Lavalley-Fouquet et al. 2000); more recent studies have achieved resolutions closer to that of *HST* (e.g. the $0\farcs15$ resolution achieved by Agra-Amboage et al. 2011, 2014), but suffer from short individual and total integration times, leading to poor signal-to-noise ratios. Improved observations of protostellar outflows can be obtained by taking multiple long-exposure frames (which requires an occulting disc to prevent saturation by the central star) using instruments capable of AO-corrected seeing of $\sim 0\farcs1$, such as NIFS (§1.4).

DG Tau (§1.3) is a promising target for such a study for several reasons. As a nearby protostar (140 pc away; Elias 1978), an angular resolution of $0\farcs1$ corresponds to a spatial resolution $\sim$ 14 AU, providing the tantalizing possibility of resolving the width of the central high-velocity outflow component. Such resolution would allow for the accurate determination of jet parameters such as density, velocity, and possible rotation signatures (see below). DG Tau is one of the most active CTTS known in terms of mass accretion and ejection rates, making it an ideal candidate for studying these processes. Finally, the fact that DG Tau is at an earlier evolutionary phase (transition Class I/Class II) than the field population of CTTS means that it may provide clues to the accretion-outflow processes occurring in earlier-phase, embedded protostars.

The goal of this thesis is to investigate YSO outflow structure and propagation as applicable to DG Tau, by using innovative techniques to analyse our state-of-the-art NIFS data, coupled with novel, physically-based modelling. The resolution (both spectral and spatial) and signal-to-noise ratio of previous observations have led to a relatively simple view of multicomponent microjet-scale YSO outflows as independent, self-similar flows, launched from a range of disc radii (e.g. Fig. 1.7). In particular, it has led to the presumption that outflow parameters determined several hundred AU from the central star are directly representative of the launch conditions of the outflow (e.g. Anderson et al. 2003; Ferreira et al. 2006). The high-resolution, high signal-to-noise ratio data provided by NIFS allow for this assumption to be tested by careful examination of all outflow components close to the driving source. In particular, it is of great interest to determine if the outflow components are truly self-similar, if they interact with each other, and if they interact with ambient material (e.g. the circumstellar disc or envelope) in a way that significantly alters their

[46] We note that Bacciotti et al. (2002) created a pseudo-IFU by aligning multiple STIS slits to the jet axis, and spacing them across the jet (e.g. Fig. 1.11); however, such techniques are poorly suited for detecting cross-outflow structure (e.g. §2.4.1.6).

morphology and kinematics. For example, the recent work of Coffey et al. (2012) showed that apparent rotation signatures in the RW Aur jet are time-variable, suggesting there may be some physical process generating a spurious rotation signature, or masking a real one. Melnikov et al. (2009) suggested that the bipolar asymmetry of the outflows from this object are also being caused close to the outflow source; we aim to determine if a similar scenario is occurring in DG Tau (cf. the large-scale bipolar asymmetry found by McGroarty et al. 2007). Answering these questions in relation to DG Tau will provide avenues of exploration for the wider field of protostellar outflows.

1.6. Thesis Outline

Our investigation of the microjet-scale outflows from DG Tauri is arranged as follows.

In Chapter 2, we present our unique, multi-epoch spectroimaging data of the DG Tau system. These data represent the deepest optical/NIR investigation of a protostellar outflow to date, with a spatial resolution equal or superior to previous work. The unparalleled depth of our observations, made possible by the use of an occulting disc over the central star, allows us to rigorously separate the emission from the two approaching outflow components at all spatial positions for the first time. We then proceed to analyse the structure and kinematics of each component. In the approaching high-velocity component (jet), we infer the presence of a stationary recollimation shock for the first time in this object. This has important implications for the study of rotation in YSO jets, and attempts to infer the launch radii of the outflows from downstream flow parameters. Indeed, taking the presence of this shock into account, we derive a smaller launch radius for the jet than previously thought, and also find no evidence for rotation in either outflow component. We also measure the knot periodicity and physical parameters of the jet, with a view to constraining the time-variability of the outflows in the future.

In Chapter 2, we propose that the approaching IVC represents a turbulent lateral entrainment layer, as opposed to a disc wind put forward by previous studies. The entrainment layer forms at the interface between the jet and the wide-angle molecular wind, which is seen in H_2 emission. The toroidal magnetic field surrounding the jet (§1.2.2.1) renders the jet-wind boundary susceptible to the Kelvin-Helmholtz instability, facilitating entrainment. In Chapter 3, we present a two-dimensional analytical model of such an entrainment layer. This model is a major improvement over previous work in that it only depends upon directly observable (or inferable) quantities, such as jet density, velocity, and the growth rate of the mixing layer. The model is based on a Riemann decomposition of these quantities into average and time-variable components, and analysis of the resulting equations of the system. In particular, the model estimates the luminosity and mass entrainment rate of the mixing layer from directly observable outflow parameters. We apply this model to the

approaching outflows of DG Tau, and show that the luminosity and mass entrainment rate are well-estimated by the model. Therefore, we conclude that the approaching IVC in DG Tau is emitted by a turbulent mixing layer.

We investigate the nature of the receding microjet-scale outflow from DG Tau in Chapter 4. The morphology of this outflow is markedly different from the approaching outflow, taking on a bubble-like structure. We disagree with previous interpretations of this structure as a bow shock, particularly after analysis of our multi-epoch data set. Instead, we conclude that the bubble forms because the receding counterjet is being obstructed by the clumpy protostellar envelope above the circumstellar disc surface (§1.3.3). We reach this conclusion by constructing models of the gas velocity field inside a turbulent, quasi-static bubble, and comparing to observations. We then phenomenologically compare our observations to simulations of radio galaxy jet-blown bubbles, and determine that an analogous process may be occurring. Analytical estimates of the bubble structure indicate that our model is consistent with observations.

We summarize our results in Chapter 5. We also discuss the implications of our work in the field of protostellar outflows. We conclude by briefly proposing some interesting lines of investigation for future work, in order to expand our work and further advance the field.

CHAPTER 2

DG Tau in the 2005 Observing Epoch

This chapter has been published as **White, M. C., McGregor, P. J., Bicknell, G. V., Salmeron, R., Beck, T. L.** ***MNRAS*****, *441*, 1681–1707, 2014c**, *referenced as White et al. (2014c). This chapter is not modified from the published version, except in the following respects:*

- *Section, figure, footnote and table numbering, and general formatting, have been modified for consistency with the remainder of the thesis;*
- *References to White et al. (2014b) and White et al. (2014a) have been changed to point to Chapters 3 and 4 of this thesis respectively;*
- *An additional footnote (footnote 47, p. 53) has been added, referencing material in Chapter 1;*
- *Appendices A, B and C to this paper have been moved to Appendices A, B and C of this thesis.*

The original paper is available at `http://mnras.oxfordjournals.org/content/441/2/1681` *.*

The initial reduction of the NIFS data used in this chapter was performed by Professor Peter McGregor prior to the start of the candidature. Subsequent re-reductions were conducted jointly by the candidate and Professor McGregor, but did not constitute major changes to the reduction procedure, and used pre-existing reduction scripts written by Professor McGregor. The data reduction section of this chapter (§2.2) was written by the candidate, based on notes provided by Professor McGregor.

Abstract

Investigating the outflows emanating from young stellar objects (YSOs) on sub-arcsecond scales provides important clues to the nature of the underlying accretion-ejection process occurring near the central protostar. We have investigated the structures and kinematics of the outflows driven by the YSO DG Tauri, using the Near-infrared Integral Field Spectrograph (NIFS) on Gemini North. The blueshifted outflow shows two distinct components in [Fe II] 1.644 μm emission, which are separated using multi-component line fitting. Jet parameters are calculated for the high-velocity component. A stationary recollimation shock is observed, in agreement with previous X-ray and FUV observations. The presence of this shock indicates that the innermost streamlines of the high-velocity component are launched at a very small radius, 0.01–0.15 AU, from the central star. The jet accelerates and expands downstream of the recollimation shock; the 'acceleration' is likely a sign of velocity variations in the jet. No evidence of rotation is found, and we compare this non-detection to previous counter-claims. Moving jet knots, likely the result of the jet velocity variations, are observed. One of these knots moves more slowly than previously observed knots, and the knot ejection interval appears to be non-periodic. An intermediate-velocity component surrounds this central jet, and is interpreted as the result of a turbulent mixing layer along the jet boundaries generated by lateral entrainment of material by the high-velocity jet. Lateral entrainment requires the presence of a magnetic field of strength a few mG or less at hundreds of AU above the disc surface, which is argued to be a reasonable proposition. In H_2 1-0 S(1) 2.1218 μm emission, a wide-angle, intermediate-velocity blueshifted outflow is observed. Both outflows are consistent with being launched by a magnetocentrifugal disc wind, although an X-wind origin for the high-velocity jet cannot be ruled out. The redshifted outflow of DG Tau takes on a bubble-shaped morphology, which will be discussed in a future paper.

2.1. Introduction

It is likely that the outflows driven by accreting young stellar objects (YSOs) play a critical role in solving the angular momentum problem of star formation by removing angular momentum from circumstellar disc material. The nature of this coupled accretion-ejection mechanism remains poorly understood. Magnetic fields are almost certainly integral to this process (McKee & Ostriker 2007), but the ejection mechanism is still a matter of debate. Outflows could be launched from the stellar surface (e.g. Sauty & Tsinganos 1994; Matt & Pudritz 2005), from points near the truncation radius of the disc, as in the X-wind model (Shu et al. 1994), or from a range of disc radii via magnetocentrifugal acceleration (Blandford & Payne 1982; Pudritz & Norman 1983). Indeed, multiple launch mechanisms may act in concert (Larson 2003; Ferreira et al. 2006; Shang et al. 2007).

Determining the nature of the outflow mechanism is critical in order to understand the underlying accretion process (Edwards 2009). Magnetic fields are believed to drive these outflows, and they may also be responsible for inducing disc turbulence via the magnetorotational instability (MRI; Balbus & Hawley 1991; Balbus 2011). Both of these processes extract angular momentum from the disc, enabling mass accretion onto the central protostar (McKee & Ostriker 2007). It is therefore important to determine the physical processes that lead to jet launching, and link these with the properties of the resulting outflow.

Direct observation of the jet launching region is not possible with current optical/near-infrared telescope technology. However, constraints on the jet launching mechanism can be inferred from observations of the outflows close to the central star. For low-mass stars, this takes the form of observing the 'microjets' of optically-visible classical T Tauri stars (CTTS). These microjets, which make up the first $\sim$ 200–300 AU (1$''$.4–2$''$.1 at 140 pc) of the outflow, are thought to be largely unaffected by ambient gas, as the jet is expected to clear a channel much wider than the jet via a wide bow shock as it emerges (Raga et al. 1995). Most models predict that jet collimation and acceleration occur within $\lesssim$ 50 AU of the star (Cabrit 2007b). Significant effort has been expended over the previous two decades observing these YSO microjets at high angular resolution, first with the space-based *Hubble Space Telescope* (*HST*), and later with ground-based adaptive-optics (AO) systems (see, e.g. Ray et al. 2007, and references therein).

One of the most intensely studied T Tauri stars is DG Tauri, which drives the HH 158 and HH 702 outflows (Mundt & Fried 1983; McGroarty et al. 2007). The accretion and outflow rates determined for this object are amongst the highest of any CTTS (Bacciotti et al. 2002), with accretion rates approaching 10^{-6} $M_\odot$ yr^{-1} at some epochs (White & Ghez 2001; White & Hillenbrand 2004). A multi-velocity structure is observed in the first $\sim$ 300 AU of the approaching outflow, consisting of a well-collimated high-velocity flow near the axis of the system, confined within slower, more spatially extended material. The absolute line-of-sight velocities of the high-velocity component (HVC) are in the range 200–400 km s^{-1}, with the highest-velocity material positioned closest to the central jet axis and showing bright, shock-excited regions (e.g. Lavalley et al. 1997; Bacciotti et al. 2000; Pyo et al. 2003b). The intermediate-velocity component (IVC) typically shows much broader line widths than the HVC, and is centered around a line-of-sight velocity of $\sim$ 100 km s^{-1} (Pyo et al. 2003b).

It is important to understand whether the presence of multiple velocity components in the outflow is the result of multiple launch mechanisms and/or locations, or if it can be described through a single outflow model. For example, Pyo et al. (2003b) suggested a dual-origin model for the DG Tau outflow, combining a magnetospheric jet with a disc wind. However, it was suggested in the same paper that at least part of the DG Tau IVC could be due to entrainment of this disc wind by the HVC. It would also be possible

for a single-component jet to exhibit a double-peaked line profile if, for example, the ionization of the outflow material varied greatly between inner and outer streamlines, as demonstrated by Pesenti et al. (2004) with analytical models of magnetohydrodynamic disc winds. Therefore, higher-quality data on both velocity components, especially regarding spatial positions, accurate radial velocities, and relative intensities between the components, are required in order to constrain these scenarios.

Improved line velocity determination, coupled with spatial information, will also provide improved constraints on jet rotation. Not only would the unambiguous detection of rotation provide direct evidence that the outflows are extracting angular momentum from the circumstellar disc, but it may also be used to place constraints on the launch radius of the outflow, assuming an MHD disc wind scenario (McKee & Ostriker 2007). Since the first claims of jet rotation in the DG Tau outflow from *HST* Space Telescope Imaging Spectrograph (STIS) data (Bacciotti et al. 2002), many CTTS outflows have been investigated for this signature (e.g. Coffey et al. 2004), including a repeat investigation of DG Tau (Coffey et al. 2007). Radial velocity differences observed across the DG Tau jet have been interpreted as rotation (Bacciotti et al. 2002; Coffey et al. 2007) having the same sense as the rotation inferred for the DG Tau circumstellar disc (Testi et al. 2002). The claimed rotation in the IVC is consistent with an MHD disc wind launched from a radius of ~ 3 AU (Bacciotti et al. 2002; Pesenti et al. 2004), whilst the velocity differences across the HVC match a disc wind launched from ~ 0.2–0.5 AU under the assumption that the entire outflow is an MHD disc wind (Coffey et al. 2007). However, if the IVC results at least partially from entrainment, the line-of-sight velocities could be skewed at any one position by the turbulent motions of shocked gas. In a recent observation of the extreme T Tauri star RW Aurigae, Coffey et al. (2012) found that the apparent rotation signatures in the outflows from that object change direction over time, and occasionally disappear, indicating that other effects overwhelm any rotation signal present. It is therefore important to understand how the velocities of each component are expected to evolve due to the natural progression of the outflow, and compare this with the observational evidence.

We have obtained three epochs of integral-field spectrograph data of the DG Tau system in the H band over a four-year period (2005–2009). Each epoch provides images of the outflows in [Fe II], in particular the 1.644 μm line, over an approximately $3'' \times 3''$ field of view. [Fe II] is one of the strongest forbidden lines present in the near-infrared spectrum, and is less affected by extinction than optical lines (Pyo et al. 2003b). In this paper, we present the data from the initial observing epoch (2005), and a small amount of data from the 2006 and 2009 observing epochs. In a future paper, we will introduce the full data from the 2006 and 2009 observing epochs, and discuss the time-evolution of the DG Tau outflows in more detail.

The outflows of DG Tau were most recently investigated in [Fe II] emission by Agra-Amboage et al. (2011), using the SINFONI instrument on the Very Large Telescope. Their

data, obtained in 2005 Oct, one month prior to our observations, demonstrate the potential of high-angular resolution spectroimaging for explaining the origin of various outflow components. Here we use our significantly longer ($\sim 20\times$) on-source exposure time, our increased sensitivity to extended structure due to our use of a stellar occulting disc, and our resulting higher signal-to-noise ratio, to rigorously separate the emission from different jet components (Appendix A), and examine the physical parameters of each one in detail.

This paper is organised as follows. The observations and data reduction methods are described in §2.2. The results of the data reduction are detailed in §2.3. We analyse and then remove the stellar spectrum from the data cube, revealing the extended emission structure of the DG Tau outflows. We use multi-component Gaussian line fitting to separate the blueshifted emission into high- and intermediate-velocity components. We analyse each of these components in detail in §2.4. The blueshifted high-velocity component denotes the high-velocity jet driven by DG Tau. The knot ejection period of DG Tau cannot be conclusively determined from our data; we suggest that knot ejections in this object are less periodic than previously thought (§2.4.1.1). A stationary recollimation shock is detected at the base of the outflow (§2.4.1.2), which implies that the innermost streamlines of the jet are initially launched at a high velocity, $\sim$ 400–700 km s^{-1}, from a small launch radius, $\sim$ 0.01–0.15 AU (§2.4.1.3). Following this rapid deceleration, the jet velocity increases beyond the point where magnetocentrifugal acceleration ceases (§2.4.1.4), probably as a result of intrinsic velocity variations (§2.4.1.5). There is no indication of rotation in the jet (§2.4.1.6). The intermediate-velocity blueshifted component emanates from a turbulent entrainment layer which forms between the jet and either the ambient medium, or the wider-angle molecular wind observed in H_2 emission (§2.4.2.1). A magnetic field of strength a few hundreds of μG to a few mG is expected at these heights above the circumstellar disc, and would facilitate this entrainment (§2.4.2.2). We summarize these results in §2.5.

2.2. Observations and Data Reduction

Initial observations of the DG Tau system in the H-band (1.49–1.80 μm) were obtained using the Near-infrared Integral Field Spectrograph (NIFS) on the Gemini North telescope, Mauna Kea, Hawaii, as part of the NIFS commissioning process on 2005 Nov 12 UT. Data were recorded with the ALTAIR adaptive-optics system in natural guide star mode, using DG Tau itself as the adaptive-optics reference star. NIFS is an image-slicing type integral-field spectrograph that achieves a spectral resolving power $R \sim 5400$ in the H band. The NIFS field has a spatial extent of $3'' \times 3''$, which is split into 29 slitlets that each pass to the spectrograph. This results in individual spaxels of $0\farcs103 \times 0\farcs045$, with a two-pixel velocity resolution of $\sim$ 60 km s^{-1} in the H-band (McGregor et al. 2003). A spatial resolution of $0\farcs11$ was achieved during our observations, based on the observed full width at half-maximum (FWHM) of a standard star observed immediately after the

DG Tau observations. This corresponds to a distance of 15.4 AU at the assumed distance to DG Tau of 140 pc (Elias 1978). This distance is intermediate between the radius of Saturn's orbit (9.5 AU) and that of Uranus (19.1 AU). The instrument was set to a position angle of PA = 316°, so that the horizontal image axis, corresponding to the coarser spaxel dimension, runs along the known direction of the large-scale HH 158 outflow (PA = 226°, Mundt & Fried 1983). This places the finer sampling perpendicular to the outflow axis.

A partially transmissive 0.″2 diameter occulting disc was used to obscure the central star during the observations, allowing for longer exposures with greater sensitivity to extended structure. Eleven 600 s exposures were taken, with DG Tau being recentred behind the occulting disc every two to five exposures. Two 600 s sky frames were also obtained, with an offset of 30″ in both RA and Dec. The A0 standard star HIP25736 was observed immediately afterwards, to allow for telluric correction and flux calibration. Flux calibration was based on the 2MASS magnitude ($H = 7.795$) for HIP25736, and a shape derived from a blackbody function with a temperature of 7000 K that was fit to the 2MASS $J - K$ colour. Flat field, arc, and spatial calibration exposures were obtained on the same night. Standard star observations and flat fields were taken with the occulting disc in place as for observations of DG Tau in order to remove fringing effects generated by the 0.5 mm thick silica occulting disc substrate. These flat-field exposures also allowed for approximate correction of the attenuation of the central star caused by the partially transmissive occulting disc.

Data reduction was performed using the Gemini NIFS IRAF package. An average dark frame was subtracted from each object frame and averaged sky frame. The dark-subtracted average sky frame was then subtracted from the dark-subtracted object frame. A flat-field correction was applied to each slitlet by dividing by a normalized flat-field frame. Bad pixels identified from the flat-field and dark frames were then corrected via 2D linear interpolation.

The individual 2D spectra for each slitlet were transformed to a rectilinear coordinate grid using the arc and spatial calibration frames, and the transformed spectra for each slitlet were stacked in the second spatial direction to form a 3D data cube. All spectra were transformed to a common wavelength scale during this step, so that only spatial registration was required in subsequent data reduction steps. The data cubes derived from each object exposure were then corrected for telluric absorption by division with a normalized 1D spectrum extracted from the observations of the telluric standard star. Hydrogen absorption lines intrinsic to the H-band spectrum of the A0 standard star were removed using Gaussian fits to the lines. Flux calibration was achieved using a large-aperture 1D spectrum of the same standard star, which was also corrected for telluric absorption. These final object frames were then spatially registered using the position of DG Tau, and median-combined to produce a final data cube.

Table 2.1 NIFS observations of DG Tau, 2005–2009.

Date	Epoch	No. of on-source exposures[a]	Telluric standard star
2005 Nov 11	2005.87	11	HIP25736
2006 Dec 24	2006.98	9	HIP25736
2009 Nov 08	2009.88	6	HIP26225[b]

[a] All on-source exposures were 600 s.
[b] 2MASS H-band magnitude: 7.348. Blackbody function temperature: 9400 K.

The location of the central star in the final data cube was required in order to accurately fix a reference point for the outflow. This location was determined by fitting a two-dimensional Gaussian function to an image produced by collapsing the data cube in the wavelength direction, over wavelength ranges chosen to avoid strong emission lines. The fit was made only over those spaxels within $\sim 0\farcs25$ of the brightest spaxel in the image, and located the position of the star to within $0\farcs02$ in the outflow direction ($0\farcs10$ spaxels), and $0\farcs01$ in the cross-outflow direction ($0\farcs04$ spaxels). The FWHM of the continuum image of the DG Tau star is $0\farcs14$.

We include a portion of our multi-epoch data in order to further our arguments regarding the knots in the approaching outflow (§2.4.1.1). These data were acquired on 2006 Dec 24 and 2009 Nov 08. The data from each epoch were reduced in the fashion described above, with the main difference being the choice of telluric standard star and the number of on-source 600 s exposures taken. These details are provided in Table 2.1. We reserve a complete analysis of these multi-epoch data for a future paper. Unless explicitly stated otherwise, all data used within this paper are from the 2005 observing epoch.

Similar NIFS observations of the DG Tau system in the K band (1.99–2.40 μm), but without the occulting disc, were obtained as a part of the same commissioning process on 2005 Oct 26 UT, and have been presented by Beck et al. (2008). We make use of these data in this paper.

2.3. Results

2.3.1. Stellar Spectrum

Scattered stellar light is apparent across the entire data field. The H- and K-band stellar spectra of DG Tau were extracted using a $0\farcs8$ diameter circular aperture, centred on the spatial location of the star in each data cube. It has not been possible to obtain an accurate flux calibration for the K-band spectrum as these data were recorded as a flexure test of the NIFS instrument over an extended period in non-photometric conditions. The

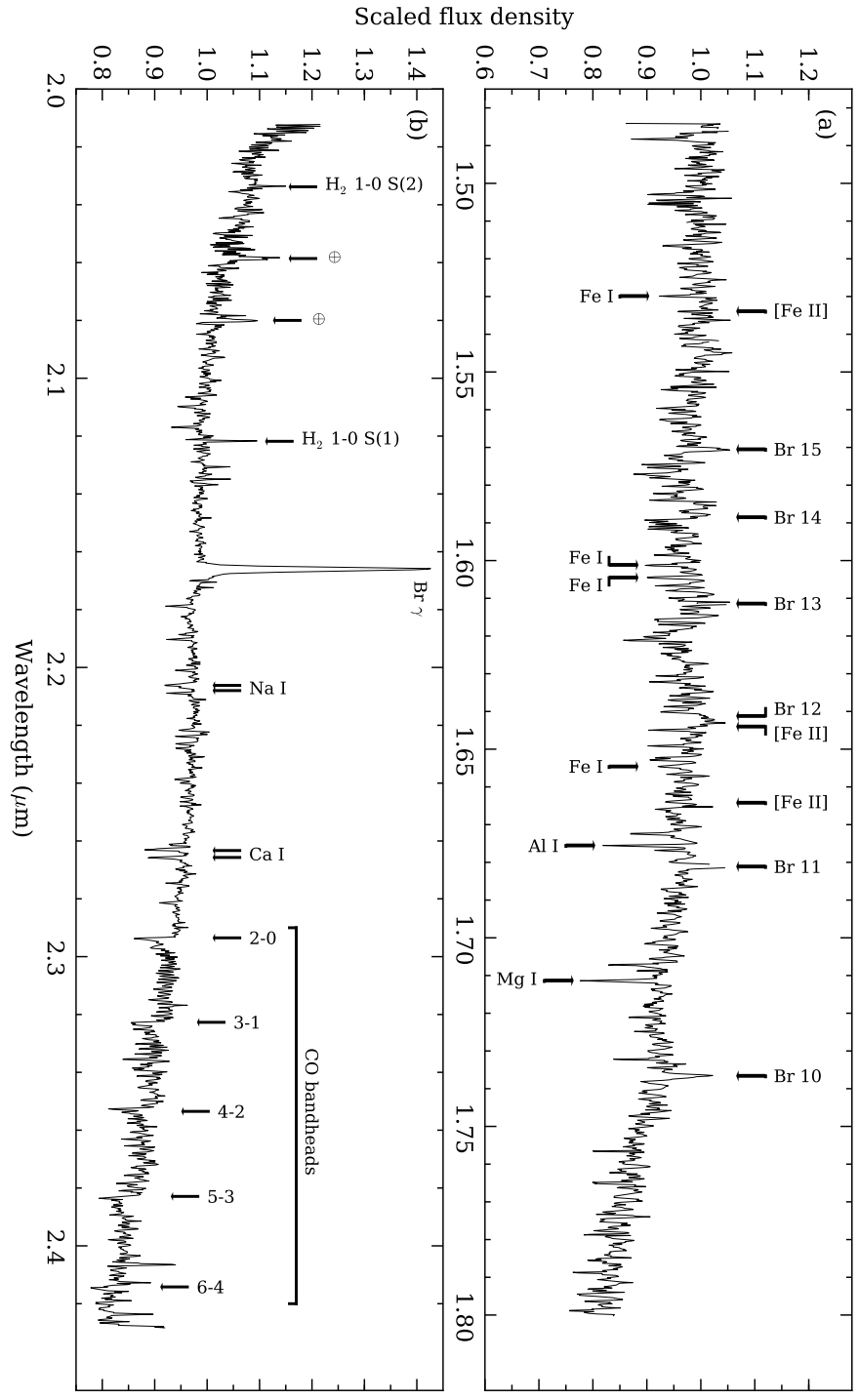

Figure 2.1 The stellar spectrum of DG Tau. The spectrum is extracted from a 0.″8 diameter circular aperture centered on the star. Panel (a) shows the *H*-band (1.49–1.80 μm) spectrum, and panel (b) shows the *K*-band (1.99–2.40 μm) spectrum. The flux density has been normalized to unity at 1.60 μm in the *H*-band and 2.2 μm in the *K*-band. Prominent emission features are labelled, as are absorption features, which are used to determine the accuracy of the wavelength calibration (§2.3.4). The CO bandheads visible in the *K*-band spectrum are also marked. The *K*-band data have been presented previously by Beck et al. (2008).

normalized stellar spectra are presented in Fig. 2.1.

The H-band stellar spectrum shows photospheric absorption features, with clearly identifiable K I, Fe I, Al I, and Mg I lines (Fig. 2.1a). The K-band spectrum shows stellar absorption lines of Na I and Ca I (Fig. 2.1b). Previous near-infrared observations of DG Tau on 1994 Dec 14 showed significantly veiled H- and K-band spectra with few discernible stellar absorption features (Greene & Lada 1996). A similarly veiled spectrum was also seen on 2001 Nov 06 UT (Doppmann et al. 2005). Furthermore, previous optical observations of DG Tau, where the photospheric spectrum peaks, have shown a highly veiled stellar spectrum, with very few discernible absorption features (Hessman & Guenther 1997). The source of this veiling continuum is thought to be the accretion shocks occurring close to the stellar surface (Gullbring et al. 2000). Hence, the lack of a veiling continuum indicates DG Tau was in a phase of low accretion activity during the period of our observations.

CO $\Delta v = 2$ bandheads are visible in absorption in the K-band spectrum (Fig. 2.1b), and arise in the stellar photosphere. On the other hand, these bandheads appear in emission in many actively accreting YSOs (Carr 1989, 1995). When this occurs, the bandheads typically exhibit a double-peaked structure characteristic of emission from a Keplerian disc, which indicates that the emission arises from the inner radii of the circumstellar disc (Carr 1995). The CO $\Delta v = 2$ bandheads in the DG Tau spectrum have been observed to oscillate between appearing in emission (Hamann et al. 1988; Carr 1989; Chandler et al. 1993; Biscaya et al. 1997) and absorption or being absent (Greene & Lada 1996; Doppmann et al. 2005). They also vary significantly in flux, by up to 50%, on time-scales of days (Biscaya et al. 1997).[47] The presence of CO bandheads in emission is often associated with an increase in accretion activity, and conversely, the absence, or presence in absorption, of the bandheads is usually associated with a decrease in accretion activity, e.g. the V1647 Orionis outburst of 2003 (Reipurth & Aspin 2004; Aspin et al. 2008, 2009). Our observation of the DG Tau CO bandheads in absorption provides further evidence that DG Tau was in a low accretion activity phase during the 2005 epoch.

The dominant emission line in the K-band spectrum is H I Br γ 2.166 μm. The nature of this line in DG Tau was investigated by Beck et al. (2010). They determined that the majority of the Br γ emission emanates from accretion in the circumstellar disc, but approximately 2% of the emission is extended, and coincident with the DG Tau microjet.

2.3.2. Stellar Spectrum Removal

It is necessary to subtract the stellar spectrum and associated spatially unresolved line emission to adequately study the extended emission-line structure of the DG Tau outflows. The H-band stellar spectrum shows significant structure in the region of the [Fe II] 1.644 μm emission line. This consists of a dominant unresolved continuum component, as well as

[47] See Table 1.6, p. 33 for details.

spatially unresolved H I Br 12 emission (Fig. 2.1a). H-band stellar spectrum subtraction was performed using a custom PYTHON routine. Our procedure for subtracting the stellar light takes advantage of the orientation of the large-scale DG Tau outflows in the NIFS data cube, and the lack of [Fe II] line emission from the circumstellar disc. Two sample spectra of scattered starlight were formed over a pair of 0.″25 diameter circular apertures, centered at opposing positions 0.″5 from the star perpendicular to the outflow direction, and then averaged. For each spaxel, this stellar spectrum was scaled to match the flux observed adjacent to the spectral region of interest for the line being investigated. In the case of the [Fe II] 1.644 μm line, the region of interest covers a velocity range of -380 to 340 km s^{-1}. This scaled stellar spectrum was then subtracted from the spectrum of the spaxel.

Accurate stellar spectrum subtraction is less important in the K band, due to the less-structured nature of the stellar spectrum in the vicinity of the H_2 1-0 S(1) 2.1218 μm line. K-band stellar spectrum subtraction was performed by forming a pair of continuum images adjacent to the spectral region of interest around the H_2 1-0 S(1) line, averaging them, and subtracting this averaged continuum image from each wavelength plane of the data cube.

2.3.3. Circumstellar Environment

Fig. 2.2 shows channel maps of the circumstellar environment of DG Tau, as seen in [Fe II] 1.644 μm line emission, with the stellar and unresolved line emission components removed. The top-left and bottom-right frames show the velocity ranges used for continuum scaling. Here, and in all subsequent figures, the outflow axis is labelled as x, and the axis across the outflow as y. The data have been binned into 40 km s^{-1}-wide slices in order to discern sub-spectral-resolution structure. There are three major outflow components:

1. A well-collimated, high-velocity blueshifted jet, concentrated in knots of emission. This blueshifted outflow is present in channel maps up to an absolute line-of-sight velocity of ~ 300 km s^{-1}, with the highest-velocity material appearing at the largest observed distance from the central star. This jet has an observed width of 0.″20–0.″25 $\sim$ 28–35 AU (approximately the radius of the orbit of Neptune) at the distance of DG Tau;

2. An intermediate-velocity, less-collimated, edge-brightened, 'V'-shaped structure in the blueshifted outflow. Within approximately 1″ of the central star, the outer edges of this structure are linear, and are aligned radially with respect to the central star. The opening half-angle of this feature is $15° \pm 1°$. Agra-Amboage et al. (2011) obtained an opening half-angle of 14° for the same structure from SINFONI data of DG Tau obtained on 2005 Oct 15. This structure is 'pinched' $\sim$ 1″ from the

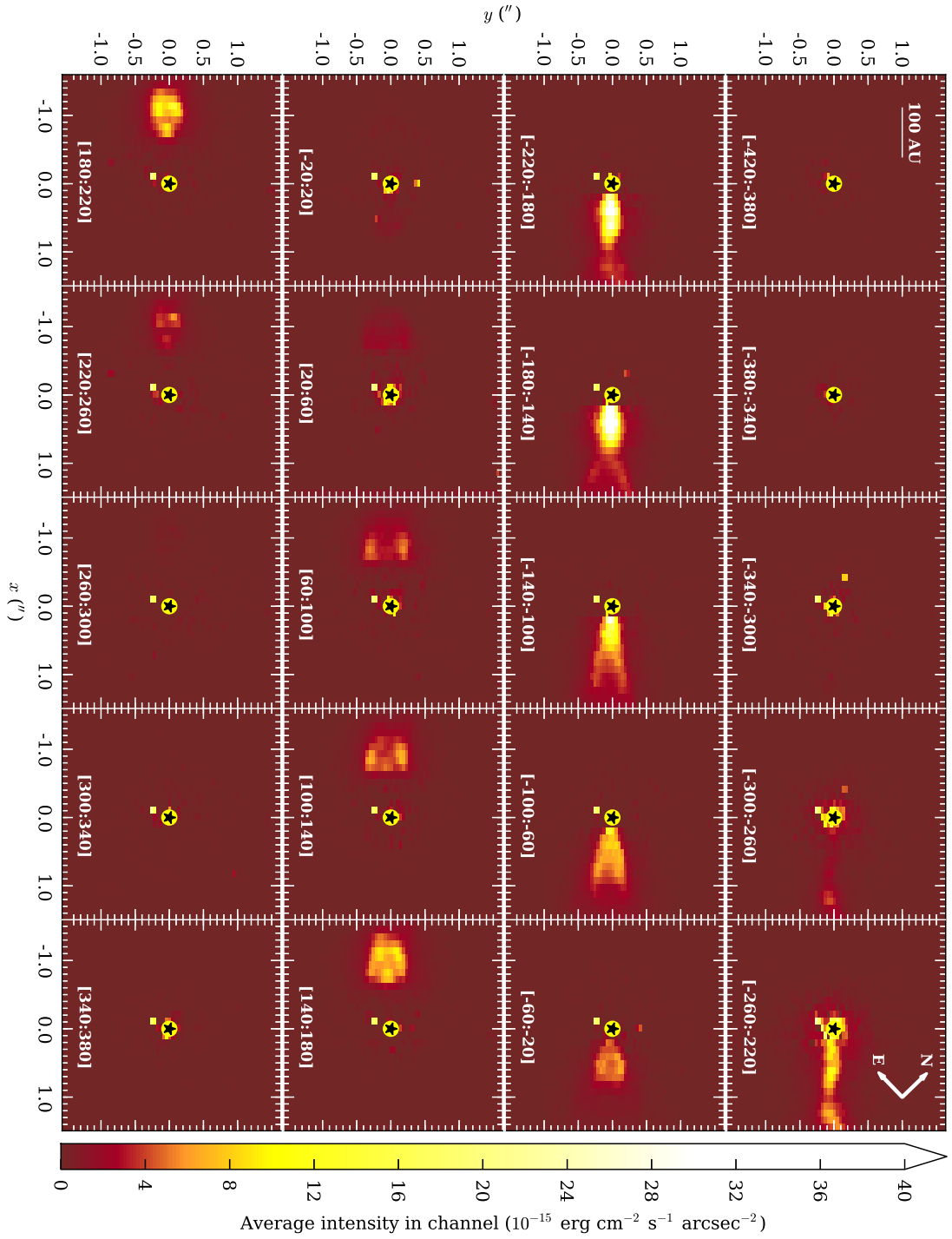

Figure 2.2 Channel maps of the DG Tau outflow. Panels show images of the extended [Fe II] 1.644 μm line emission around DG Tau, binned into 40 km s^{-1}-wide slices. The velocity range of each slice is shown at the bottom of each slice. The velocity ranges used for continuum scaling are also included (top-left and bottom-right panels). The intensity values quoted are the average intensity in each channel over the 40 km s^{-1} velocity range. The black star corresponds to the position of the central star, DG Tau, and the yellow circle indicates the position and size of the 0.″2 diameter occulting disc.

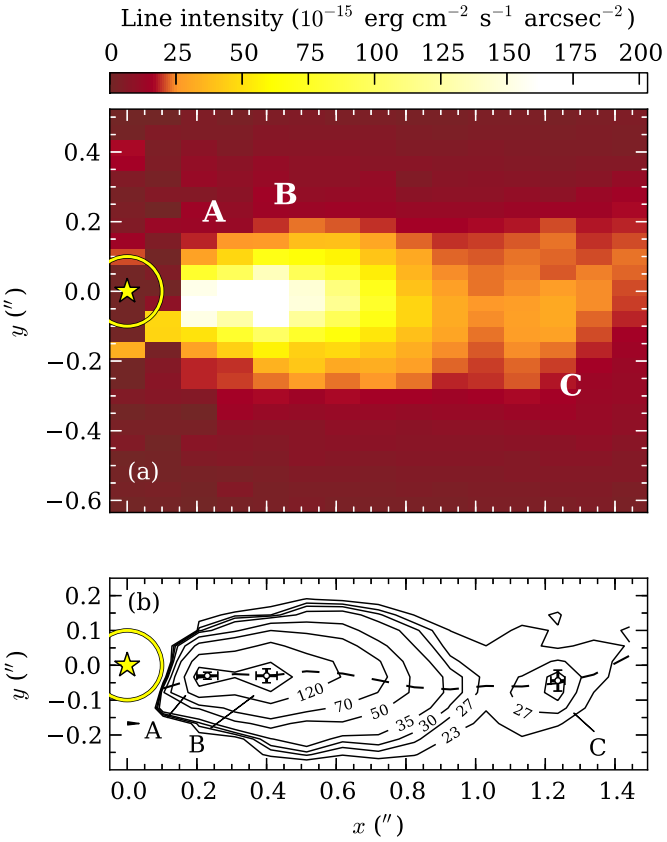

Figure 2.3 The DG Tau approaching outflow. (a) Integrated [Fe II] 1.644 μm line flux of the approaching outflow from DG Tau. The line flux is computed over the velocity range -300 to 0 km s^{-1}. Knots A, B and C are labelled. (b) Contour plot of the same integrated [Fe II] line flux. Contours are labelled in units of 10^{-15} erg cm^{-2} s^{-1} arcsec^{-2}. The unlabelled contour corresponds to 170×10^{-15} erg cm^{-2} s^{-1} arcsec^{-2}. Knots A, B and C are labelled, and the knot centroid positions and associated uncertainties are indicated. The jet ridgeline is shown as a dashed line. The position of the central star and the position and size of the occulting disc used during the observations are shown in both panels by a yellow star and circle, respectively.

star, and then re-expands with increasing distance from DG Tau (Fig. 2.2, panel $[-180 : -140]$ km s^{-1});

3. A redshifted outflow, which becomes visible approximately 0.″7 from the central star. The inner region of this structure is obscured by the circumstellar disc around DG Tau. We estimate the radial extent of the obscuration, and hence of the DG Tau circumstellar disc, to be ~ 160 AU, after correction for the inclination of the jet-disc system to the line of sight (38°; Eislöffel & Mundt 1998). This is in agreement with the measurement by Agra-Amboage et al. (2011), who used this obscuration to place limits on the disc models of Isella et al. (2010). The redshifted outflow takes the form of a bubble-like structure. The material with the greatest receding line-of-sight velocity is concentrated on the outflow axis, and at the apex of the bubble. The material along the edges of the structure emits at progressively lower line-of-sight velocities with decreasing distance from the central star.

2.3.3.1. Approaching Jet Trajectory

The high-velocity blueshifted jet does not travel a linear path, but bends along its length (Fig. 2.2, rightmost-top panel). We define the ridgeline of the jet as the location of the jet brightness centre at each position along the outflow axis. Single-component Gaussian

Table 2.2 Knot positions in the approaching DG Tau jet, 2005 epoch.

Knot	Position along outflow axis[a] (″)	Position across outflow axis[a] (″)	Velocity range used for fitting (km s^{-1})	Centroid [Fe II] line velocity[b] (km s^{-1})
A	0.23±0.03	-0.03±0.01	-260 to -100	—
B	0.40±0.03	-0.03±0.02	-300 to -100	∼ 180
C	1.24±0.02	-0.04±0.03	-300 to -180	∼ 250

[a] Quoted uncertainties to the knot positions are the quadrature sum of the fitting errors to the star and knot positions. The fitting uncertainties for knot A are visual estimates.
[b] Centroid line velocities are for the high-velocity outflow component (Fig. 2.6).

fits were performed across the jet, at every recorded position along the outflow axis, on an image of integrated [Fe II] 1.644 μm emission-line flux formed over the velocity range −300 to −180 km s^{-1}. This velocity range was chosen so that the ridgeline was computed for the highest-velocity gas, corresponding to the high-velocity jet (see below, also, Pyo et al. 2003b). The ridgeline computed from these fits is shown in Fig. 2.3(b). The uncertainties in the lateral position of the fitted ridgeline are of order ±0.″01.

The jet ridgeline was fit in spatial coordinates with a simple sinusoidal function in order to characterise the nature of the jet trajectory. The amplitude of the fitted sinusoid is $0.''027 \pm 0.''001 \approx 3.8$ AU, and the wavelength is $1.''035 \pm 0.''006$. Deprojecting this distance to account for the jet inclination to the line of sight yields a physical wavelength of 235 AU. If the sinusoidal jet trajectory is due to jet precession, the amplitude corresponds to a precession angle of $\sim 4°$.

2.3.3.2. Approaching Jet Knots

Figs 2.2 and 2.3 show that the [Fe II] 1.644 μm line emission from the blueshifted DG Tau jet is concentrated in a series of three emission knots. We label these features as knots A, B, and C, in order of increasing distance from the central star.[48] Such emission knots are a common feature of YSO outflows, and have previously been observed in the blueshifted DG Tau outflow on large scales (several arcseconds from the central star; Eislöffel & Mundt 1998), as well as on the scale of the microjet (less than 2″ from the central star; Kepner et al. 1993; Solf & Böhm 1993; Lavalley et al. 1997; Dougados et al. 2000; Bacciotti et al. 2000; Lavalley-Fouquet et al. 2000; Takami et al. 2002; Pyo et al. 2003a; Agra-Amboage et al. 2011). With some exceptions (see below, also, Lavalley-Fouquet et al. 2000), these knots move along the outflow channel at an approximately constant speed.

Accurate positions of knots A, B and C relative to the star were determined in order to track their proper motions over time. Two-dimensional spatial Gaussian fits to each knot

[48] We choose not to continue the nomenclature of Pyo et al. (2003b) and Agra-Amboage et al. (2011) due to multiple plausible interpretations of the knot ejection history of DG Tau — see §2.4.1.1.

in integrated [Fe II] 1.644 μm emission-line flux images were utilized to determine the positions of the knot centroids. The velocity ranges used to form the images for each knot were determined by visual inspection of Fig. 2.2. The results of this fitting are presented in Table 2.2 and shown in Fig. 2.3. The characteristics of each knot are discussed below.

Knot A is situated $0\farcs23 \pm 0\farcs03$ along the outflow axis from the central star. The NIFS data Nyquist sample the point spread function across the jet, but undersample the spatial profile in the coarsely-sampled spaxel direction along the outflow. This makes fitting knot A with a two-dimensional Gaussian profile difficult. Visual inspection of these data indicate that the FWHM of the knot is $\sim 0\farcs1$ in both axes, making it significantly more compact than knots B and C. The difficulty in accurately fitting a Gaussian profile also results in a larger uncertainty in the knot centroid position.

Similar knots at the location of knot A have been observed previously in [S II] 6716 Å/6731 Å (Solf & Böhm 1993), [O I] 6300 Å (Solf & Böhm 1993; Lavalley et al. 1997) and He I 10830 Å (Takami et al. 2002). Furthermore, Lavalley et al. (1997) report that the emission feature they observe at $\sim 0\farcs15 \approx 34$ AU deprojected distance from the central star[49] exhibits very little proper motion, suggesting that the knot represents a steady region in the flow where emission is enhanced. A feature similar to knot A appears to be present in the data of Agra-Amboage et al. (2011, fig. 3 therein); however, those authors did not mention it. We interpret knot A as a stationary shock in the jet, resulting from the recollimation of the flow. We expand further on this interpretation in §2.4.1.2.

Knot B is well-described by a Gaussian profile, which is extended in the outflow direction with an axial ratio of ~ 2.3. This knot was most recently detected by Agra-Amboage et al. (2011), who reported a position of $0\farcs37 \pm 0\farcs03$ along the outflow axis from the central star on 2005 Oct 15. Our positions agree to 1σ. Knot C is significantly fainter than knots A and B, at $\sim 15\%$ of their peak intensity (Figs 2.2 and 2.3). As with knot B, knot C is elongated in the outflow direction, but with an axial ratio of ~ 1.7. This knot was also detected by Agra-Amboage et al. (2011), with a reported position of $1\farcs2 \pm 0\farcs05$ along the outflow axis from the central star on 2005 Oct 15. This agrees with our measurement to 2σ, although our fitted knot position is within their uncertainties. We conduct an analysis of the recent knot ejection history of DG Tau in §2.4.1.1.

2.3.3.3. Receding Outflow Morphology

The morphological appearance of the DG Tau redshifted outflow, shown in Fig. 2.4, is different from that of the blueshifted outflow (Fig. 2.3). First, there is no clearly discernible fast outflow, nor ridgeline. Secondly, the emission from this outflow comes predominantly from a bubble-like structure (Figs 2.2 and 2.4). This structure was observed by Agra-

[49] Lavalley et al. (1997) report the knot position as $0\farcs17 \pm 0\farcs05$ from the star in the raw image, and $0\farcs13$ after deconvolution.

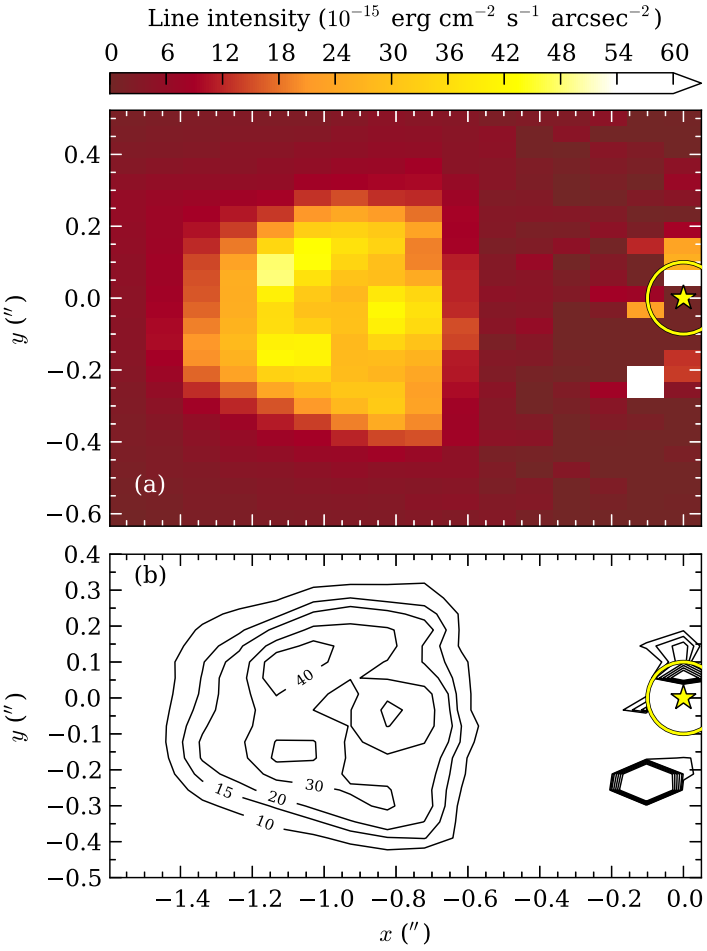

Figure 2.4 DG Tau receding outflow. (a) Integrated [Fe II] 1.644 μm line flux of the receding outflow from DG Tau. The line flux is computed over the velocity range 0 to 300 km s^{-1}. (b) Contour plot of the same integrated [Fe II] line flux. Contours are labelled in units of 10^{-15} erg cm^{-2} s^{-1} arcsec^{-2}. The position of the central star and the position and size of the occulting disc used during the observations are shown in both panels by a yellow star and circle, respectively.

Amboage et al. (2011), and was interpreted as being the redshifted equivalent of a faint 'bubble' they claimed in the approaching outflow at similar distances from the central star. We do not observe such a structure in the blueshifted outflow (§2.3.4), and we will discuss and model the cause of this bipolar outflow asymmetry in a forthcoming paper (§4).

2.3.4. Fitted Line Components

Visual inspection of our spectra clearly indicates the presence of at least two [Fe II] 1.644 μm line components at every spatial position with significant signal-to-noise ratio. In many spatial locations, these two components are significantly blended. A multicomponent Gaussian fit was performed to separate these spectral components. Both one- and two-component fits were made, and an F-test (Appendix A) was utilized to determine the statistically appropriate number of components to retain in the final fit (Westmoquette et al. 2007). Stricty speaking, the use of a likelihood ratio test such as the F-test in this situation is statistically incorrect (see Appendix A.1; Protassov et al. 2002). However, given the absence of a statistically correct alternative that could be sensibly applied to the number of spectra presented here, and the obvious presence of two line components at most positions, we opt to continue with this approach (e.g. Westmoquette et al. 2012, also see Appendix

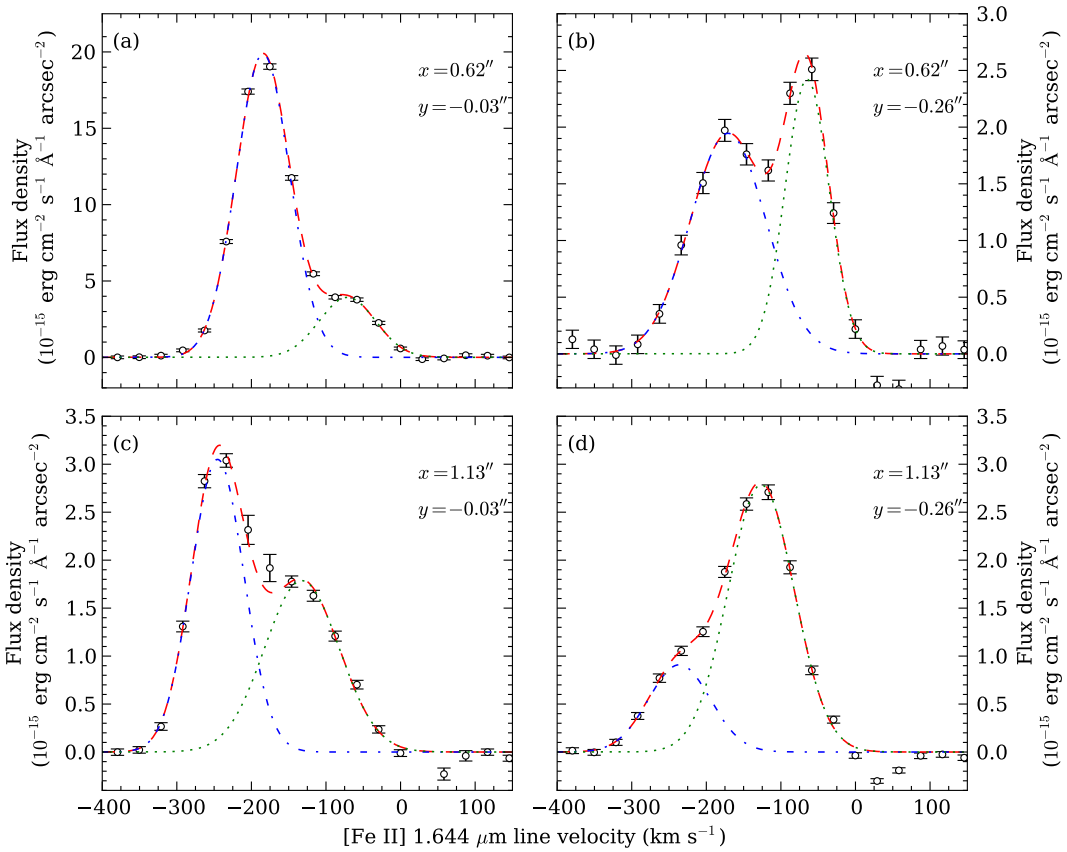

Figure 2.5 Two-component Gaussian fits to the spectra of four spaxels in the approaching DG Tau outflow. The spaxels are located at a distance of (a, b) $x = 0\farcs62$ and (c, d) $1\farcs13$ along the outflow axis. The spaxels shown in panels (a, c) are on the jet ridgeline at $y = -0\farcs03$, and the spaxels in panels (b, d) are offset from the ridgeline at $y = -0\farcs26$. Actual data and uncertainties are indicated by black circles and error bars, fitted line components are shown as blue dot-dashed and green dotted lines, and the total fit is shown as red dashed lines.

A.1). Spaxels were excluded from fitting if the signal-to-noise ratio of the brightest spectral pixel in the vicinity of the emission line was less than 10, or if the relative error on the fitted line amplitude and/or width exceeded unity. Spaxels that could not be fit with two components were also excluded. Applying these criteria, it was found that acceptable fits were produced over a region comparable to the detected emission in Figs 2.2, 2.3 and 2.4. Example spectra, and the fits obtained to those spectra using the above procedure, are shown in Fig. 2.5.

To determine line velocities relative to the systemic velocity, it was necessary to determine the velocity of the central star in our data. To accomplish this, Gaussian profiles were fit to several stellar absorption features in the H-band stellar spectrum (Fig. 2.1a). The velocity correction obtained was then applied to all line velocities.

The velocity resolution of our H-band data was measured to be 55 km s^{-1}, based on Gaussian line fits to observed sky lines. The intrinsic line widths of each fitted profile were determined by quadrature subtraction of this instrumental velocity resolution from the

fitted line width, via the formula $\mathrm{FWHM}^2_{\mathrm{intrinsic}} = \mathrm{FWHM}^2_{\mathrm{fitted}} - \mathrm{FWHM}^2_{\mathrm{instrumental}}$. We discuss the properties of each fitted component below.

2.3.4.1. Approaching High-Velocity Component

The [Fe II] 1.644 μm emission-line intensity image of the blueshifted HVC in Fig. 2.6(a) shows the classic morphology of a well-collimated, high-velocity jet. Knots B and C are reproduced. Knot A is not visible, as that region of the outflow is not fit due to its low signal-to-noise ratio, which results from the proximity of the central star. The 'pinching' of the outflow $\sim 1''$ along the outflow axis from the central star is also reproduced. We interpret this to be due to a lack of emitting gas between the two jet knots, rather than an actual narrowing of the jet.

The peak line velocity at each position along the outflow occurs on the jet ridgeline (Fig. 2.6b). The line-of-sight line velocity is constant at ~ 170 km s^{-1} in the region of knot B, $0\farcs40 \approx 91$ AU deprojected distance from the central star. The peak absolute line velocity increases with distance from the central star between knots B and C. This is in agreement with previous observations of the DG Tau microjet that generally show increasing absolute line velocity with distance from the central star (Bacciotti et al. 2000; Pyo et al. 2003b), although Pyo et al. (2003b) shows some evidence for sinusoidal velocity variations (§2.4.1.1). The fitted line width is lowest along the jet ridgeline (Fig. 2.6a), and the region of lowest line width corresponds to the region of highest line component intensity at each position along the outflow axis. This indicates the presence of a narrow jet with a relatively undisturbed core.

2.3.4.2. Approaching Intermediate-Velocity Component

The integrated line intensity image of the IVC shown in Fig. 2.6(d) differs significantly from that of the HVC (Fig. 2.6a). The emission is spread further from the outflow axis than the HVC. Interestingly, the edge-brightened 'V'-shaped structure is not reproduced. This is because the channel maps (Fig. 2.2) show intensity over a narrow range of velocities, whilst Fig. 2.6(d) displays the total intensity. This indicates that it is the velocity structure that is stratified (Fig. 2.6e). None of the observed emission knots is reproduced in the IVC. There is a small increase in the IVC line intensity and absolute line velocity at the position of knot B. The small spatial extent of this increase (a few spaxels), and the dominance of the HVC at this position, leads us to conclude that these increases are fitting artefacts.

The IVC velocity structure (Fig. 2.6e) is similar to the HVC velocity structure but at lower absolute velocities. The IVC line width profile (Fig. 2.6f) shows a different structure to the HVC, with the regions of highest line width being found on the outflow axis, and the fitted line width decreasing with lateral distance from the outflow axis.

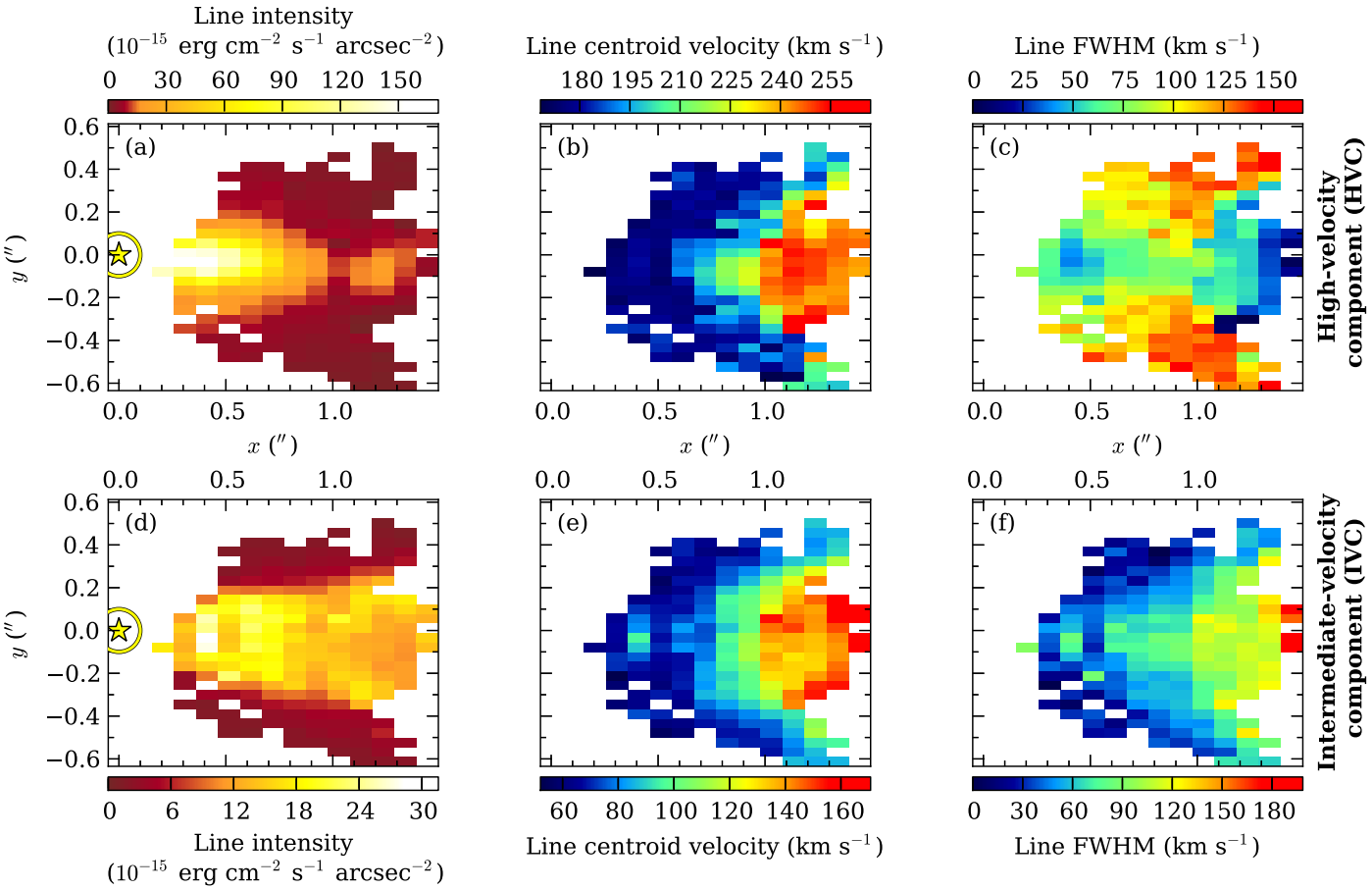

Figure 2.6 [Fe II] 1.644 μm emission characteristics from the high- and intermediate-velocity components fit to the DG Tau approaching outflow. Panels (a) to (c) show fitted parameters for the high-velocity component. Panels (d) to (f) show fitted parameters for the intermediate-velocity component. Panels (a) and (d) show the fitted line intensity. Panels (b) and (e) show the absolute fitted line velocities, which have been corrected to the systemic velocity of the central star. Panels (c) and (f) show the line FWHM, which has been approximately deconvolved from the instrumental velocity resolution through quadrature subtraction. The yellow star and circle in (a) and (d) represent the position of the star, and the position and size of the occulting disc, respectively.

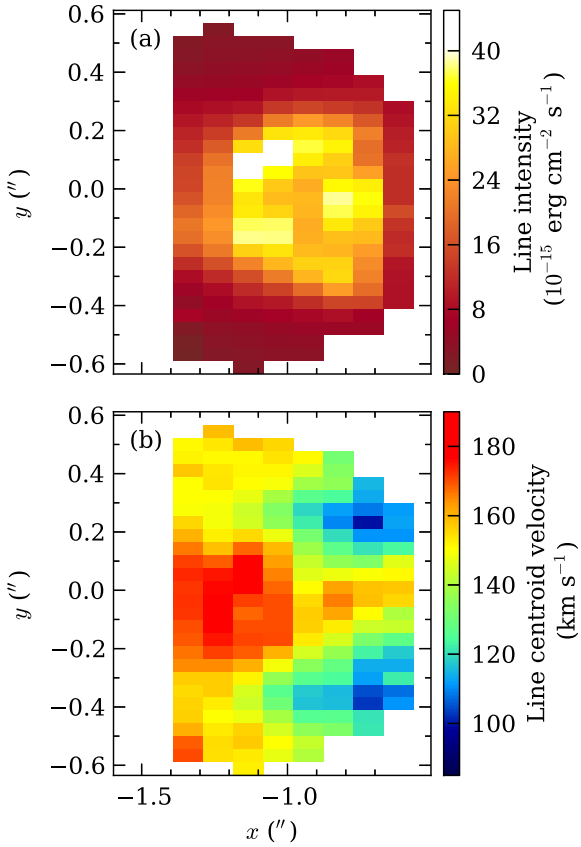

Figure 2.7 [Fe II] 1.644 μm emission characteristics from the single component fit to the DG Tau receding outflow. Panel (a) shows the fitted line intensity and panel (b) displays the fitted line velocity of the redshifted outflow based on a single-component Gaussian fit. The fitted line velocity has been corrected for the systemic velocity of the central star.

2.3.4.3. Receding Outflow

The redshifted [Fe II] 1.644 μm line emission from the receding outflow was fit using the procedure described above. Fits were restricted to a single component, as this is all that is warranted by the data. The resulting fitted [Fe II] 1.644 μm line component for the receding DG Tau outflow is shown in Fig. 2.7.

There are several distinctive features in the receding outflow velocity profile shown in Fig. 2.7(b). The highest line velocities of $\sim$ 180 km s^{-1} are found at the 'apex' of the bubble-like structure, 1.″3 from the central star. The line velocities of the emission from the structure decrease with decreasing distance from the central star, reaching $\sim$ 100 km s^{-1} at the edge of the observable emission closest to the star. A ridge of emission with velocity $\sim$ 160 km s^{-1} runs along the outflow axis for the length of the structure. This suggests that there is an underlying stream of material driving the evolution of this structure. As noted above, we will discuss this further in a future paper (§4).

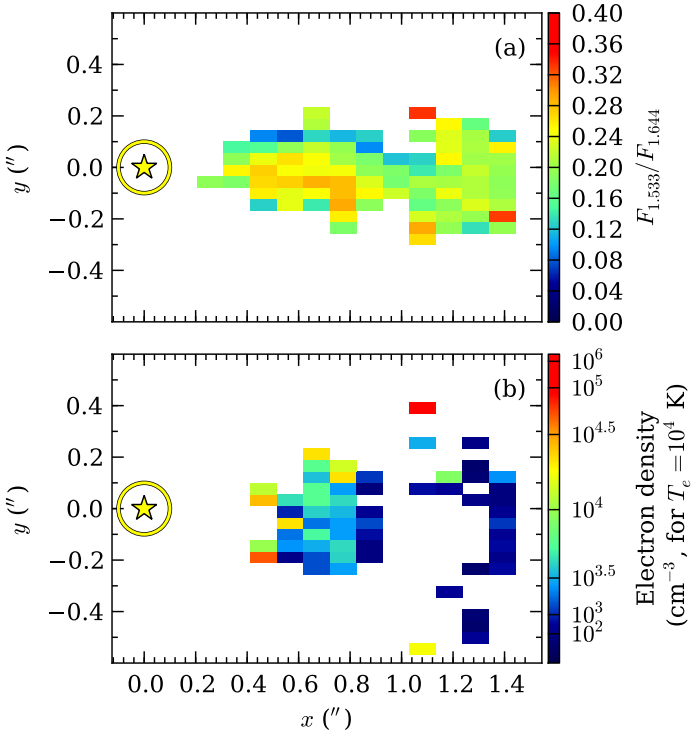

Figure 2.8 Ratio of integrated flux between [Fe II] 1.533 μm and [Fe II] 1.644 μm line emission for approaching outflow components. Shown is the computed line ratio for (a) the HVC and (b) the IVC. Line fluxes were determined by integration of the raw, stellar-subtracted spaxel spectra over the velocity ranges −380 to 0 km s^{-1}, and then splitting the integrated fluxes about the velocity where the two fitted [Fe II] 1.644 μm line components have equal flux density. Spaxels have been masked where either a threshold signal-to-noise ratio of 5 in the high-velocity component, or two in the intermediate-velocity component has not been reached, or where the ratio value is in the saturation limit for determining electron density ($F_{1.533}/F_{1.644} \gtrsim 0.40$; Pesenti et al. 2003). Electron density has been calculated for an electron temperature of $T_e = 10^4$ K over the range of ratios $0.035 < F_{1.533}/F_{1.644} < 0.395$ (second colour bar). The yellow star and circle represent the position of DG Tau, and the position and size of the occulting disc, respectively.

2.3.5. Approaching Outflow Electron Density

The near-infrared lines of [Fe II] arise from low-lying energy levels, and are useful tracers of electron density, n_e. In particular, the intensity ratio between the [Fe II] lines at 1.533 μm and 1.644 μm provides a diagnostic of electron density in the range $n_e \sim 10^2$–10^6 cm^{-3} (Pradhan & Zhang 1993). The derived electron density is only weakly dependent upon the electron temperature, T_e, in the range $T_e \sim (0.3\text{–}2.0) \times 10^4$ K. We assume an electron temperature of $T_e = 10^4$ K for the DG Tau outflow (Bacciotti 2002). Pesenti et al. (2003) have computed the relation between this line ratio and electron density for a 16-level Fe$^+$ model.

The [Fe II] 1.533 μm/1.644 μm flux-ratio map of the approaching outflow components derived from our data is shown in Fig. 2.8. Integrated line fluxes were determined via integration of the stellar-subtracted spectra in each spaxel over the velocity range −380 to 0 km s^{-1}. The integrated line fluxes were then split about the velocity at which the two fitted [Fe II] 1.644 μm line components have the same flux density to form individual flux-ratio measurements for the high- and intermediate-velocity components. Spaxels were excluded where the relative uncertainty in the computed line ratio exceeded 20% for the high-velocity component, and 50% for the intermediate-velocity component. Therefore, line ratios for each component could only be obtained where the 1.533 μm [Fe II] emission

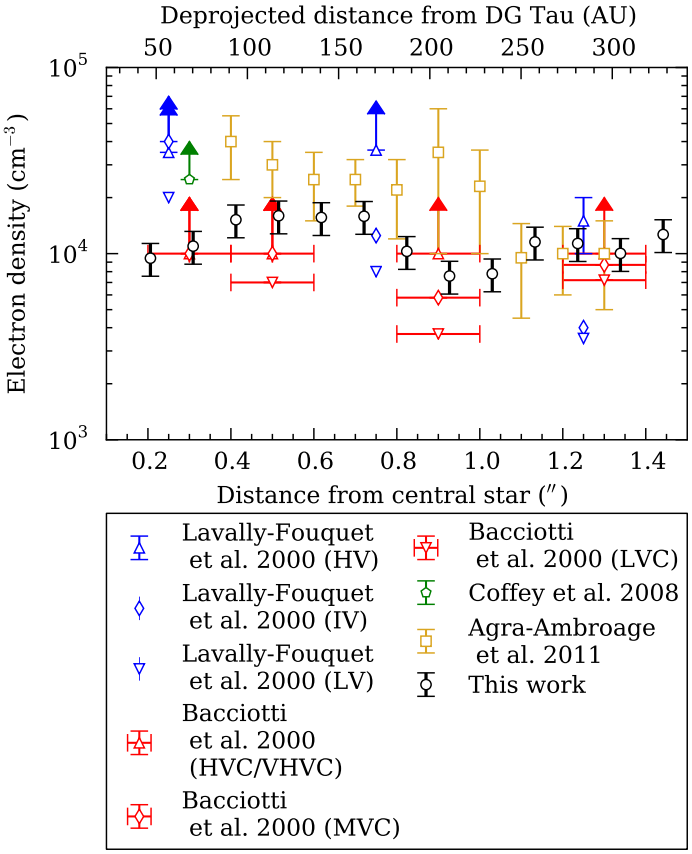

Figure 2.9 Electron density measurements of the DG Tau approaching jet. Black circles show the electron density derived in this work for the DG Tau jet from the [Fe II] 1.533 μm/1.644 μm line ratio at each position along the outflow axis, averaged over all spaxels within $\pm 0\farcs5$ of that axis in the perpendicular direction. All determinations of electron density from the literature are made using the optical line ratio technique developed by Bacciotti & Eislöffel (1999), except for those by Agra-Amboage et al. (2011), which use the [Fe II] line ratio technique. Where provided, electron densities are quoted for high-velocity (HV), intermediate/medium-velocity (IV/MV) and low-velocity (LV) components. Uncertainties are as quoted in the relevant reference, except for where they have been estimated from 2D maps of electron density (Bacciotti et al. 2000; Coffey et al. 2008).

line was detected with sufficient signal-to-noise ratio to satisfy this criterion. A flux-ratio map for the receding outflow will be presented in a future paper (§4, Fig. 4.3).

The electron number density of the approaching outflow high-velocity component is greatest $0\farcs3$ to $0\farcs5$ from the central star, with an average value of $\lesssim 4 \times 10^4$ cm^{-3}. The electron density decreases to $\sim 10^{-4}$ cm^{-3} within $0\farcs8$ of the central star, and remains approximately constant to the edge of the observed field. There are no identifiable density enhancements at the positions of knots B and C. The electron number density of the intermediate-velocity component is more variable, between $\sim 10^{-3}$ cm^{-3} to $\sim 10^{-4}$ cm^{-3} within $0\farcs9$ of the central star. Beyond that point, the signal-to-noise ratio of the [Fe II] 1.533 μm emission line is insufficient to form line ratios.

Our determination of the electron density of the approaching DG Tau jet (HVC) is compared with determinations from the literature in Fig. 2.9. We calculate an uncertainty-weighted average electron density at each position along the outflow axis from all spaxels within $\pm 0\farcs5$ of the axis. Our results are in agreement with the previous determination of electron density from the [Fe II] line ratio by Agra-Amboage et al. (2011), with slight discrepancies due to our different method of measuring the electron density of the jet component. Our results are also in reasonable agreement with electron density measurements of the outflow based on the [S II] 6716Å/6731Å line ratio using the BE99 technique (Bacciotti & Eislöffel 1999; Lavalley-Fouquet et al. 2000; Bacciotti et al. 2000; Coffey et al. 2008). Slight differences

between electron densities derived from different spectral features are to be expected because the [S II] and [Fe II] lines arise in different regions of the cooling post-shock gas.

2.4. Discussion

In §2.2 and §2.3, we discussed our observations of the outflows from DG Tau at sub-arcsecond resolution, and with sufficient sensitivity to reveal their detailed structures. We have identified the approaching jet (high-velocity component), the blueshifted intermediate-velocity component, and the receding outflow. In this section, we discuss the origins and physical parameters for the blueshifted outflow components that can be inferred from these data. A detailed analysis of the nature of the receding outflow will be presented in a future paper (§4).

2.4.1. The Approaching Jet

We interpret the blueshifted [Fe II] 1.644 μm HVC emission to be from an approaching, high-velocity, well-collimated jet launched from the DG Tau star-disc system. We investigate the propagation of knots in the jet (§2.4.1.1), which leads us to identify a stationary recollimation shock in the jet channel (§2.4.1.2). We use the properties of this shock to form estimates for the launch radii of the innermost streamlines of the jet (§2.4.1.3). We then proceed to calculate parameters of the jet downstream of this shock (§2.4.1.4), and investigate the cause of the changes in jet velocity along the outflow axis (§2.4.1.5). Finally, we analyse our data for any indication of rotation in the DG Tau jet (§2.4.1.6).

2.4.1.1. Knots

Three knots were observed in the DG Tau microjet (§2.3.3.2). Our unique multi-epoch data allow us to track the position of these knots over time, without the need to link disparate observations to form a knot evolution. The position of the knots as a function of time is given in Table 2.3, and shown in Fig. 2.10. The most remarkable finding is that knot A remains stationary over a period of ~ 4 years. We discuss the nature of this stationary feature in §2.4.1.2.

We were able to track the progression of knot B over this interval. The knot moves at a constant speed of $0\farcs17 \pm 0\farcs01$ yr^{-1} along the jet channel, which implies a knot launch date of 2003.5 ± 0.2 by linear extrapolation[50] (Fig. 2.11). This speed is slower than that of knots previously observed in the DG Tau jet (e.g. $0\farcs29$ yr^{-1}, Dougados et al. 2000), and slower than the knot proper motions of $0\farcs27$–$0\farcs34$ yr^{-1} suggested by Agra-Amboage et al. (2011).

[50]This extrapolation includes the position of knot B/A5 quoted by Agra-Amboage et al. (2011).

Table 2.3 Knot positions in the approaching DG Tau jet, 2005–2009.

Knot	Positions[a]			Average proper motion[b]		Centroid line velocity[c]	Deprojected velocties[d]		Alternate designations
	2005.87	2006.98	2009.88				Proper	Radial	
	(″)	(″)	(″)	(″ yr^{-1})	(km s^{-1})	(2005.87, km s^{-1})	(km s^{-1})		
A	0.23±0.03	0.20±0.04	0.23±0.02	0	0	—	0	—	—
B	0.40±0.03	0.60±0.02	1.07±0.02	0.17±0.01	113±7	~ 180	183 ± 11	~ 230	A5[e]
C	1.24±0.01	—	—	—	—	~ 250	—	~ 320	A3[e] (?), A4[e] (?)

[a] Quoted uncertainties to the knot positions are the quadrature sum of the fitting errors to the star and knot positions. The fitting uncertainties for knot A are visual estimates.
[b] Fig. 2.10.
[c] Fig. 2.6(b).
[d] Velocities are deprojected assuming an inclination of the jet axis to the line of sight of 38° (Eislöffel & Mundt 1998).
[e] Agra-Amboage et al. (2011).

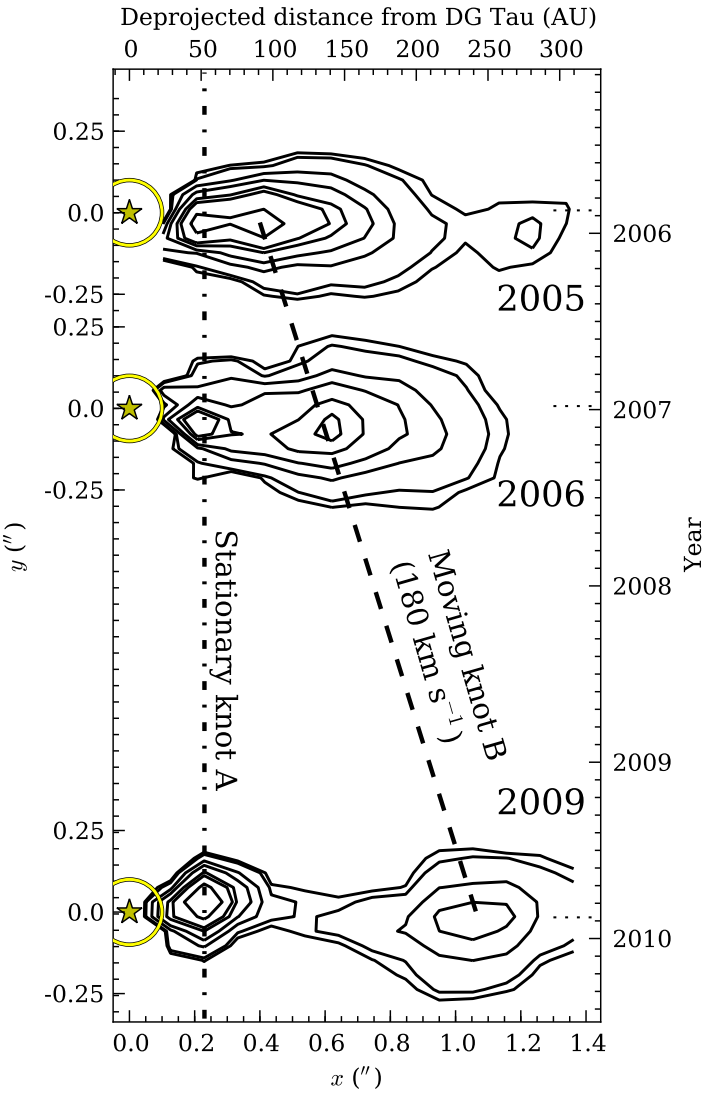

Figure 2.10 Progression of knots in the approaching DG Tau outflow, 2005–2009. Shown is a contour plot of [Fe II] 1.644 μm line emission from the approaching DG Tau outflow at 2005.87, 2006.98 and 2009.88. Images are formed by integrating over the velocity range -380 to 0 km s^{-1}. Contours have levels of $[25, 30, 50, 70, 100, 120, 170] \times 10^{-15}$ erg cm^{-2} s^{-1} arcsec^{-2}. Short dotted lines represent the observation date of each epoch.

The presently-favoured model for the formation of moving jet knots is intrinsic variability in the jet velocity (e.g. Raga et al. 1990). In this scenario, as the jet velocity oscillates, faster regions of the jet catch up to slower-moving regions, forming shocked internal working surfaces which appear as jet knots. Our data show evidence of such velocity variations in the jet (§2.4.1.5), in agreement with previous studies (e.g. Pyo et al. 2003b). A basic prediction of this theory is that the proper motion and radial velocity of the shocked material in the knots should be two projections of the same knot velocity (Raga et al. 1990). This does not appear to be the case for knot B (Table 2.3) if we assume a constant jet inclination and therefore adopt a jet inclination of 38° as determined on scales of $\sim 10''$ (Eislöffel & Mundt 1998). However, the jet ridgeline is not a straight line, and the jet inclination may therefore vary locally by $\sim$ 3–4° (§2.3.3.1). Taking a local jet inclination of 34.5° at the location of knot B reconciles the proper motion and radial velocity when deprojected. Therefore, we conclude that knot B could have been formed by intrinsic velocity variations in the jet.

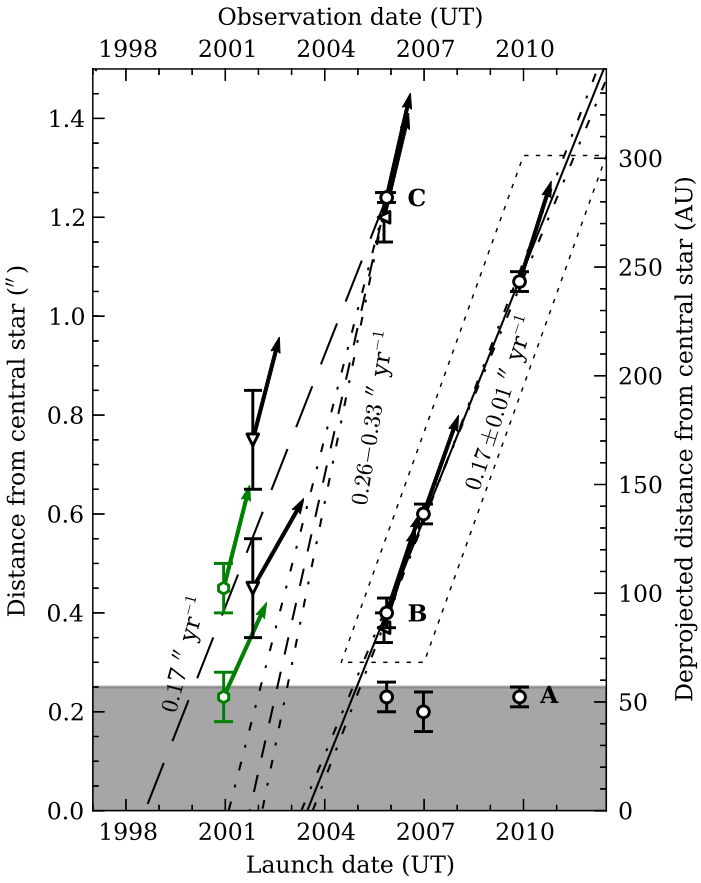

Figure 2.11 Knot positions in the DG Tau approaching microjet at less than 1.″5 from the central star, plotted over the period 1997–2010, taken from multiple sources. The uncertainties in the knot positions have been visually estimated if uncertainties are not quoted in the relevant reference. Markers denote the source of the observations; colours denote the emission line(s) with which the observation was made. Where known, arrows denote the radial line velocity of the observed knot projected onto the plane of the sky. The solid line shows the linear fit made to the trajectory of knot B. The short-dashed line shows the trajectory of knot C assuming a proper motion of 0.″30 yr^{-1} for that knot, corresponding to the radial velocity of that knot projected onto the sky using a jet inclination of 38°. Dot-dashed lines show the uncertainties in these trajectories: for knot B, this is the fitting uncertainty; for knot C, this results from a ±3.5° variation in the jet inclination (§2.3.3.1). The long-dashed line shows the trajectory of knot C assuming a proper motion of 0.″17 for that knot, as for knot B. The grey area denotes the region ≤ 0.″25 from the central star, where knot observations are excluded from fitting. Knot observations used for fitting the trajectory of knot B are grouped by the dotted parallelogram.
References. *Hexagons:* Takami et al. (2002). *Down-pointing triangles:* Pyo et al. (2003b). *Left-pointing triangles:* Agra-Amboage et al. (2011). *Circles:* This work.
Green: He I 1.0830 μm. *Black:* [Fe II] 1.644 μm.

The knot periodicity of DG Tau has been studied by previous authors, but has remained unclear. Pyo et al. (2003b) determined a knot ejection period of $\sim$ 5 yr, which was revised downwards to 2.5 yr by Agra-Amboage et al. (2011). However, Rodríguez et al. (2012b) used a different interpretation of knot motions to claim a 5 yr ejection period. Our observations support the notion that the knot ejection interval in DG Tau varies. We offer the following arguments in favour of this interpretation. First, we note the absence of a new moving knot in our 2009 data (Figs 2.10, 2.11). We would expect to observe a new knot somewhere between knots A and B at this epoch if there were a knot ejection every 2.5 yr, hence we exclude the proposition that a new knot was launched 2.5 yr after knot B.

Secondly, we consider the other moving knot in our data, knot C. This knot only appears in our 2005 data, having moved out of the NIFS field by 2006.98 (Fig. 2.10). We do not attempt to link this knot directly to previous observations, due to the inherent uncertainty in doing so (see below). We instead assign knot C two possible proper motions, and examine the implications of each scenario. First, we presume that the radial velocity of knot C ($\sim$ 250 km s^{-1}, Table 2.3) represents a projection of the true knot velocity. Allowing for a variation of $\pm3.5°$ in the canonical jet inclination of 38° (§2.3.3.1; Eislöffel & Mundt 1998), this gives a proper motion for knot C of 0.″26–0.″33 yr^{-1}. This is consistent with the interpretation of Agra-Amboage et al. (2011), and yields a knot launch date of $2001.7^{+0.2}_{-0.6}$, consistent with a 2.5 yr ejection period. Secondly, we assign knot C a proper motion of 0.″17 yr^{-1}, which is consistent with the proper motion of knot B. This is significantly slower than the knot velocity implied by the radial velocity of knot C; however, we note that the knots in Herbig-Haro objects often show discrepancies between their proper motion and radial velocity (Eislöffel & Mundt 1992, 1994). This knot trajectory passes through the cluster of knot observations reported by Takami et al. (2002) and Pyo et al. (2003b) (Fig. 2.11). This proper motion gives a launch date of 1998.6 for knot C, which would imply a knot launch period of $\sim$ 5 yr.

In light of the above complications, we leave the knot ejection interval in DG Tau, and the true knot velocity of knot C, as open questions. We have not attempted to directly link our knot observations with those from the literature. This is because, with the exception of the fast knot detected by Dougados et al. (2000) mentioned above, most DG Tau jet knots reported in the literature are single observations made in different emission lines, and using different instruments. This means that disparate observations need to be linked to form an interpretation of the knot ejection history. We prefer to await further, consistent multi-epoch data of the DG Tau jet in order to attempt to draw a final conclusion on the knot ejection interval of this object. Indeed, in light of the large difference between the knot proper motions observed by us and Dougados et al. (2000), we suggest there is significant variability in the ejection interval, and in the knot ejection velocity. We are intrigued to see if there will be a repeat of the fast knot reported by Dougados et al. (2000) at a later date. However, if the knot ejection interval and velocity are reasonably constant with a

a 5 yr ejection period, we predict that a new jet knot should have been launched from the position of the central star in mid-2008, and would have become visible beyond the stationary recollimation shock in approximately mid-2010. There is currently no available data with which to test this hypothesis.

2.4.1.2. The Recollimation Shock

We interpret knot A in the approaching jet as a stationary recollimation shock. Stationary [O I] 6300 Å emission in the region of this feature has been detected previously by Lavalley et al. (1997), $\sim 0\farcs15 \approx 24$ AU from the central star. Stationary soft X-ray emission has been observed in the DG Tau jet, centred $\sim 0\farcs14$–$0\farcs21 \approx 32$–48 AU from the central star (Güdel et al. 2005, 2008, 2011; Schneider & Schmitt 2008; Günther et al. 2009). Stationary far-ultraviolet C IV emission is observed slightly further along the jet, centred $0\farcs2 \approx 46$ AU from the central star (Schneider et al. 2013a). The temperature of the X-ray emitting material is estimated to be $\gtrsim 3 \times 10^6$ K (Güdel et al. 2008; Günther et al. 2009), whilst the emissivity of C IV strongly peaks at temperatures of 10^5 K (Schneider et al. 2013a). We interpret this as being indicative of an extended post-shock cooling region, where a recollimation shock occurs ~ 25 AU from the central star, and material then cools as it progress downstream on the scale of a cooling length (e.g. Frank et al. 2014).

In classical hydrodynamic jet theory, recollimation shocks appear when a jet emerging from a nozzle is under- or over-expanded, and undergoes lateral expansion and/or contraction to attain pressure equilibrium with the ambient medium. In the context of magnetocentrifugally driven jets and winds, recollimation of outflows into stationary shocks above the disc is due to the magnetic field acting like a nozzle. Recollimation shocks occur naturally in magnetocentrifugal outflows with terminal poloidal velocities $\gtrsim 2$ times the fast magnetosonic speed in the outflowing material (Gómez de Castro & Pudritz 1993). In this scenario, once the flow expands to a critical radius, the magnetic tension acting inwards towards the outflow axis exceeds the centrifugal force acting outwards, and the jet begins to recollimate into a stationary shock (Blandford & Payne 1982; Contopoulos & Lovelace 1994). Such recollimation shocks have been explored in the theoretical literature, and are predicted to occur tens of AU above the circumstellar disc for reasonable YSO accretion rates and disc parameters (Pelletier & Pudritz 1992; Gómez de Castro & Pudritz 1993; Ouyed & Pudritz 1993; Gómez de Castro & Verdugo 2001; Ferreira & Casse 2004), in agreement with observations of the stationary feature in the approaching DG Tau jet. Finally, Ainsworth et al. (2013) utilized e-MERLIN data to measure the opening angle of the DG Tau jet to be 86°, implying that collimation must occur somewhere $\backsimeq 50$ AU along the jet channel. This is in excellent agreement with the observed position of the stationary feature in the DG Tau jet.

Previous analyses of the stationary soft X-ray emission in the DG Tau jet have concluded

that the mass flux through the X-ray emitting region is $\sim$ a few $\times\ 10^{-11}$ $M_\odot$ (Schneider & Schmitt 2008; Günther et al. 2009), which is two orders of magnitude less than the mass flux seen in the NIR/optical (§2.4.1.5). However, the geometry used by Schneider & Schmitt (2008) and Günther et al. (2009) to compute the X-ray mass flux may result in an underestimation. Those authors used a cylindrical geometry of height $d_{\rm cool}$ (i.e., the adiabatic cooling length) and radius R to describe the X-ray emitting region. However, Bonito et al. (2011) generated a numerical simulation of a YSO jet recollimation shock[51] to investigate the stationary X-ray emission in the outflow from L1551 IRS 5[52], which shows that such shocks take on an inverted-cone structure. Repeating the calculation of Schneider & Schmitt (2008) using an inverted cone of height $d_{\rm cool}$ and radius R has two effects on the result. First, the volume of the emitting region is decreased by a factor of three. Secondly, the area through which mass enters the X-ray emitting region is increased by a factor of $\sqrt{1+(d_{\rm cool}/R)^2}$, where $d_{\rm cool}/R \sim 4$ from the simulation of Bonito et al. This results in a mass flux ~ 12 times higher than that reported by Schneider & Schmitt (2008) and Günther et al. (2009), which for DG Tau increases the X-ray mass flux to $\sim$ few $\times\ 10^{-10}$ $M_\odot$.

There remains a discrepancy of at least an order of magnitude between the X-ray and optical/NIR-derived mass fluxes. This has led several authors to suggest that there must be an inner, very fast component of the DG Tau approaching outflow, not visible at other wavelengths and perhaps of stellar or magnetospheric origin, nested within the optical/NIR high-velocity outflow component (e.g. Günther et al. 2009; Frank et al. 2014). The mass-flux discrepancy may be explained by considering the geometry and emission characteristics of a diamond recollimation shock. The results of the simulation of Bonito et al. (2011) show that, whilst the *entire* jet is shocked to a temperature of $\gtrsim 10^6$ K around the recollimation shock, only the small central core of the diamond structure significantly emits in X-rays (Bonito et al. 2011, fig. 4 therein, right-hand panels). The balance of the jet material is focused around the central emission peak by the diamond shock structure, and does not achieve the pressure necessary to strongly emit in X-rays. This neatly explains the discrepancy between the mass flow rates of the soft X-ray source and optical/NIR flow in DG Tau. Hydrodynamic simulation of the recollimation shock in DG Tau is required in order to quantify the expected mass flux through the X-ray emitting region.

There are alternate explanations for the presence of this stationary feature. It has been suggested that stationary knots in the outflows from massive protostars may be the result of the stellar wind bouncing off the walls of a cleared jet channel and recollimating above the stellar surface (Parkin et al. 2009). As mentioned above, there may also be another, unresolved central outflow component, possibly launched from the magnetosphere of the

[51] This simulation involves the launching of a jet with a uniform cross-jet velocity profile, which is forced to recollimate after passing through a nozzle.

[52] The large-scale outflow this object drives is HH 154. The soft X-ray knot in the outflow is located 0.″5–1.″0 from the outflow source (Bonito et al. 2011).

star, that may be the cause of this hot X-ray emission (e.g. Ferreira et al. 2006). Our interpretation has the advantage that it does not require invoking an as-yet undetected outflow component. Regardless of its origin, the presence of such a bright, strong, hot shock directly in the jet channel must affect the jet material that passes through/by it.

The implications of the presence of stationary recollimation shocks on the study of YSO jets are profound. The shock will modify the flow parameters downstream of its position. Therefore, extreme care and caution is required when attempting to link parameters in the outflow beyond the stationary shock, such as terminal velocities, to a specific launch radius (§2.4.1.3). Passage through such a strong shock will create turbulence in the jet, and may remove any jet rotational signature (§2.4.1.6). We now proceed to investigate each of these in detail.

2.4.1.3. Innermost Jet Streamlines: Terminal Velocity and Launch Radius

Determining the radii at which protostellar outflows are launched is one of the major goals of studies such as ours. Determination of launch radius is crucial information for determining the outflow launch mechanism. A constraint on the launch radius of protostellar outflows can be arrived at from measurements of the poloidal and toroidal jet velocities at some distance from the central star under a steady, magnetocentrifugal acceleration model (Anderson et al. 2003). Ferreira et al. (2006) provide a diagnostic diagram to this end, for various forms of MHD wind acceleration. However, this method must be applied with caution to DG Tau. We must account for the presence of the strong recollimation shock in the outflow channel (§2.4.1.2). Furthermore, we find no evidence for rotation in the DG Tau jet (§2.4.1.6). Therefore, we proceed to make an estimate of the launch radius of the innermost streamlines of the DG Tau jet including the observed properties of the recollimation shock, assuming that these streamlines are launched by an MHD disc wind. We consider pressure-driven stellar winds at the end of this section.

We estimate the launch radius of the innermost radii of the DG Tau jet as follows. For magnetocentrifugal, axisymmetric winds, the specific energy of the flow, which is constant along field lines, can be expressed as

$$E = \frac{1}{2}\left(v_p^2 + v_\phi^2\right) + \phi + h + \Omega_0\left(\Omega_0 r_{\rm A}^2 - \Omega r^2\right) \tag{2.1}$$

(e.g. Königl & Pudritz 2000; Königl & Salmeron 2011), where ϕ is the gravitational potential, h is the specific enthalpy, $r_{\rm A}$ is the Alfvén radius, i.e. the radius at which the outflow velocity equals the Alfvén speed, r is the radial distance from the central star, $v_{\rm p}$ and v_ϕ are the flow poloidal and azimuthal velocity components, respectively, and Ω is the angular velocity; subscript zero denotes values at the flow footpoint. For dynamically cold flows of gas, the enthalpy term can be neglected, and the gravitational potential is usually

considered unimportant far from the disc. Further assuming that $E \approx v_{p,\infty}^2/2$ as $r \to \infty$, where $v_{p,\infty}$ is the flow poloidal velocity at large distances, and that $(r_{\rm A}/r_0)^2 \gg 1$, the terminal flow poloidal velocity may be written as

$$v_{\rm p,\infty} \simeq \sqrt{2}\,\Omega_{\rm K} r_{\rm A}. \tag{2.2}$$

This equation can be obtained from equation 8 of Ferreira et al. (2006) by neglecting their β term, which encompasses all pressure effects, and assuming that their parameter $\lambda_\phi = r v_\phi/\Omega_0 r_0^2 \gg 3/2$. The Keplerian angular velocity, $\Omega_{\rm K}$, at the disc launch radius of the wind, r_0, is given by

$$\Omega_{\rm K} = \frac{v_{\rm K}}{r_0} = \frac{1}{r_0}\left(\frac{GM_\star}{r_0}\right)^{1/2}, \tag{2.3}$$

so equation (2.2) becomes

$$v_{\rm p,\infty} \simeq \sqrt{2}\,v_{\rm K}\frac{r_{\rm A}}{r_0} = \sqrt{2}\left(\frac{GM_\star}{r_0}\right)^{1/2}\left(\frac{r_{\rm A}}{r_0}\right). \tag{2.4}$$

A stellar mass for DG Tau of $M_\star = 0.67$ M$_\odot$ is adopted (Hartigan et al. 1995). Then, for convenience, equation (2.4) can be expressed as

$$v_{\rm p,\infty} \simeq 109 \text{ km s}^{-1}\left(\frac{r_0}{0.1 \text{ AU}}\right)^{-1/2}\left(\frac{r_{\rm A}}{r_0}\right). \tag{2.5}$$

A wide range of values are both observationally justified and theoretically possible for the magnetic lever arm parameter, $\lambda = (r_{\rm A}/r_0)^2$. Casse & Ferreira (2000) calculated steady MHD wind solutions for λ exceeding $\sim 2 \Rightarrow (r_{\rm A}/r_0) \gtrsim 1.4$. In the analysis of the launch radii of various protostellar outflows by Ferreira et al. (2006), the observationally-inferred magnetic lever arm λ_ϕ for high-velocity outflows is in the range 4–16. Given that the observational estimate λ_ϕ may underestimate the true λ due to the sampling of multiple magnetic surfaces in the jet (Ferreira et al. 2006), we adopt a range of $4 \leq \lambda \leq 20$, which leads to $2 \leq r_{\rm A}/r_0 \lesssim 4.5$, as an illustrative parameter range for YSO jets. We also note the typical observation that the ratio of mass outflow rate to mass accretion rate, $\dot{M}_{\rm out}/\dot{M}_{\rm acc} \sim 0.1$, implies $\lambda \sim$ a few to 10 assuming that the rate at which angular momentum is lost by the accreting matter ($\dot{M}_{\rm acc} r_0^2/\Omega_0$) equals the rate of angular momentum transport by the wind ($\dot{M}_{\rm out} r_A^2/\Omega_0$; see Cabrit 2007a).

The presence of the stationary recollimation shock (§2.4.1.2) must be taken into account when determining the terminal poloidal velocity, $v_{\rm p,\infty}$, of the jet. Under standard theories of magnetocentrifugal acceleration, terminal velocity is reached beyond the fast magnetosonic point in the outflow, which is predicted to be a few tens of AU above the circumstellar disc surface at most (e.g. Gómez de Castro & Pudritz 1993; Cabrit 2007b). Most authors assume acceleration largely ceases beyond this point, and the jet then flows ballistically.

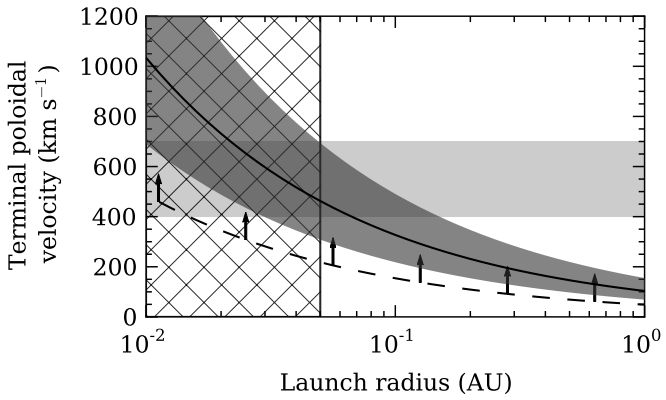

Figure 2.12 Estimated DG Tau asymptotic poloidal jet velocities as a function of launch radius, assuming an MHD disc wind. The solid line denotes the solution for a stellar mass of $M_\star = 0.67$ M$_\odot$ (Hartigan et al. 1995) and $r_A/r_0 = 3$ (e.g. Königl & Salmeron 2011). The dark grey region shows the range of solutions for $2 \leq r_A/r_0 \leq 4.5$ (Ferreira et al. 2006); the dashed line shows the limit of solutions for $1.4 \leq r_A/r_0$ (Casse & Ferreira 2000). The light grey horizontal bar represent the range of possible terminal velocities for the DG Tau jet, based on analysis of the stationary recollimation shock (§2.4.1.2). The dark grey hatching denotes a launch radius of less than 0.05 AU, where the jet could be launched via the X-wind mechanism.

However, a stationary recollimation shock will slow the jet material, so that the jet velocity observed immediately beyond knot A will not be indicative of the magnetocentrifugal terminal velocity. X-ray observations of the stationary knot suggest a shock velocity of 400–600 km s^{-1}, based on an inferred shock temperature of 3–4 MK (Güdel et al. 2008; Schneider & Schmitt 2008; Günther et al. 2009). Further observations have indicated that this shock velocity may be as high as 700 km s^{-1} (Güdel, private communication). For a stationary shock, the shock velocity is equal to the pre-shock gas velocity. Therefore, the innermost streamlines of the DG Tau jet must be accelerated to a terminal poloidal velocity of $v_{p,\infty} \sim$ 400–700 km s^{-1} in order to form the observed shock. This is a significantly higher poloidal velocity than used by previous authors to determine the launch radius of the DG Tau jet (Coffey et al. 2007). Such pre-shock velocities for the jet core were proposed for DG Tau by Günther et al. (2009). However, the implied launch radius of such a jet was not considered therein.

The terminal poloidal velocity of the innermost streamlines of DG Tau jet, equation (2.5), is plotted as a function of launch radius for DG Tau in Fig. 2.12, for a range of magnetic level arm values. For a terminal jet velocity of $v_{p,\infty} \approx$ 400–700 km s^{-1}, we determine a jet launch radius of 0.01–0.15 AU for the innermost jet streamlines, using $2 \leq r_A/r_0 \lesssim 4.5$ (e.g. Ferreira et al. 2006, table 1 therein). Using the canonical value $r_A/r_0 = 3$ gives a launch radius range of 0.02–0.07 AU. The constraint $r_A/r_0 \gtrsim 1.4$ yields a minimum launch radius of 0.005 AU. We note that outer jet streamlines that do not radiate in X-rays may be launched from larger radii. Previous estimates of the launch radius of the jet have been in the range $\lesssim$ 0.1 AU (Anderson et al. 2003) to 0.3–0.5 AU (Coffey et al. 2007). The smaller launch radius calculated here is a direct result of using a significantly higher jet

terminal poloidal velocity. For comparison, had we inferred a terminal poloidal velocity of ~ 215 km s^{-1} from the approaching jet velocity after the stationary shock, we would have calculated a launch radius of 0.23 AU for $r_A/r_0 = 3$. A jet launched from such a radius would unequivocally be interpreted as originating from a disc wind.

We are unable to exclude the possibility that the innermost streamlines in the DG Tau jet originate from a magnetospheric wind such as the X-wind (Shu et al. 2000). The stellar radius of DG Tau has been determined previously to be $2.5R_\odot \approx 0.01$ AU (Güdel et al. 2007), so that launch points within a few stellar radii of the central star, characteristic of an X-wind, are possible. However, the circumstellar disc may also approach this close to the central star (e.g. Pelletier & Pudritz 1992; Gómez de Castro & Pudritz 1993), so that disc wind contribution to this fast outflow is feasible. Indeed, an MHD disc wind launched from a radius of five stellar radii, approximately 0.05 AU for DG Tau, would most readily explain the high ejection-accretion efficiencies generally observed in YSOs (Cabrit 2007a). Finally, we note that a pressure-driven stellar wind with a ratio of thermal to magnetic pressure, β, between 5.2 and 11.8 could also produce a 400–700 km s^{-1} wind in DG Tau (assuming a magnetic level arm parameter $\lambda < 200$; Ferreira et al. 2006).

2.4.1.4. Jet Parameters

The parameters of the approaching jet have been computed based on the HVC line fits (Fig. 2.6a,b) and density estimates (Fig. 2.8). Jet parameters are essential in order to compare these observational results with numerical simulations of the DG Tau outflows. Determining the jet mass flux is also useful as an input for modelling the receding outflow (§4).

The derived parameters of the approaching DG Tau jet are shown in Fig. 2.13. From top to bottom, the panels correspond to integrated [Fe II] 1.644 μm emission-line intensity, velocity, density, diameter, kinetic energy flux density, and kinetic power. Each measurement is derived from the spaxel that is closest to the jet ridgeline at each position along the outflow axis. Axial distances and velocities are deprojected using a jet inclination to the line of sight of 38°. This inclination was determined by comparing the radial and proper motions of the bow shock at the head of the HH 158 outflow (Eislöffel & Mundt 1998). The 1.533 μm/1.644 μm line ratio is converted to electron density using the formula presented by Agra-Amboage et al. (2011, based on Pesenti et al. 2003), which they claim has an intrinsic accuracy of 20 per cent. This calculation is performed for an electron temperature of 10^4 K, as estimated for the DG Tau jet by Bacciotti (2002) through ratios of optical lines (Bacciotti & Eislöffel 1999). The jet diameter $D_{\rm jet}$ is estimated by forming Gaussian fits to the HVC integrated intensity image (Fig. 2.13a) transverse to the jet direction, and then approximately deconvolving this width from the PSF via the formula $D^2_{\rm jet} = {\rm FWHM}^2_{\rm obs} - {\rm FWHM}^2_{\rm PSF}$.

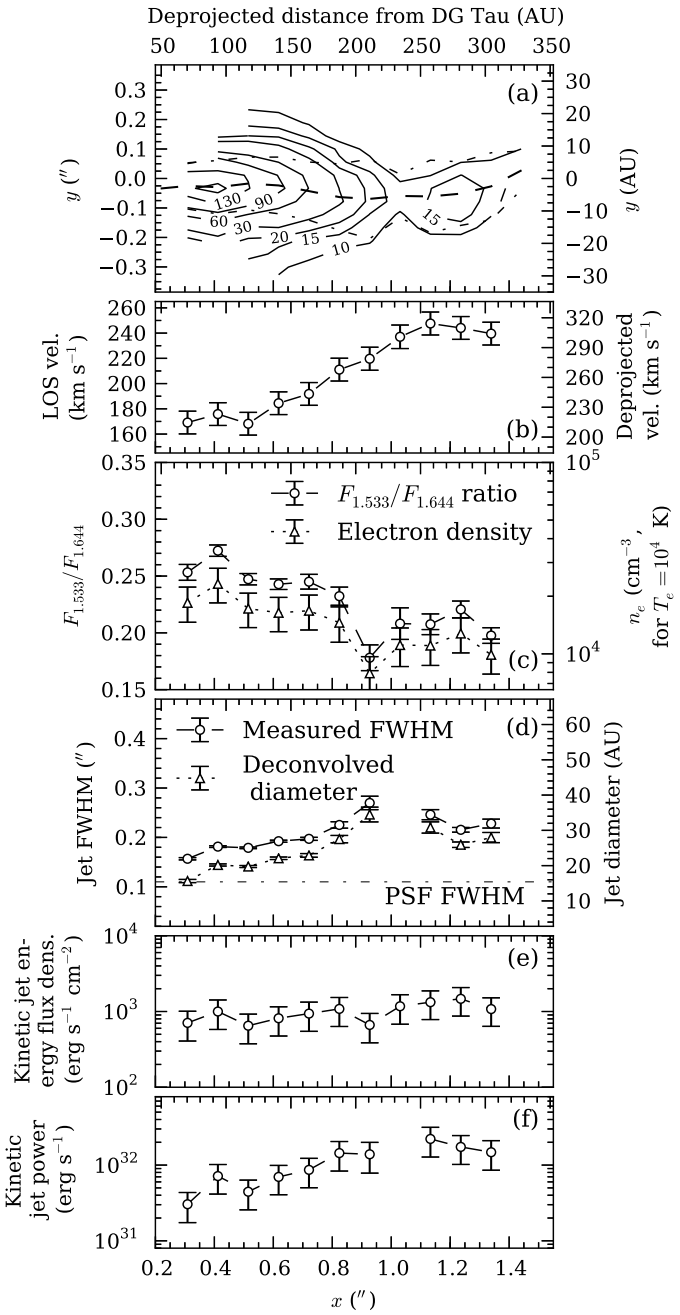

Figure 2.13 Derived parameters for the approaching DG Tau jet. (a) Contours of [Fe II] 1.644 μm blueshifted HVC emission, in units of 10^{-15} erg cm^{-2} s^{-1} arcsec^{-2}. The unlabelled contour is at 160 $\times$ 10^{-15} erg cm^{-2} s^{-1} arcsec^{-2}. (b) Line-of-sight and deprojected [Fe II] 1.644 μm HVC line velocity along the jet ridgeline. The errorbars are the quadrature sum of the fitting and stellar velocity uncertainties. (c) [Fe II] 1.533 μm/1.644 μm ratio and electron density along the jet ridgeline. The electron density is calculated for an electron temperature of 10^4 K. (d) Observed and deconvolved jet FWHM of the blueshifted HVC. The PSF FWHM is shown by the dot-dashed line. (e) Computed jet kinetic energy flux density along the jet ridgeline. (f) Computed jet kinetic power, $L_{\rm jet}$, along the jet ridgeline.

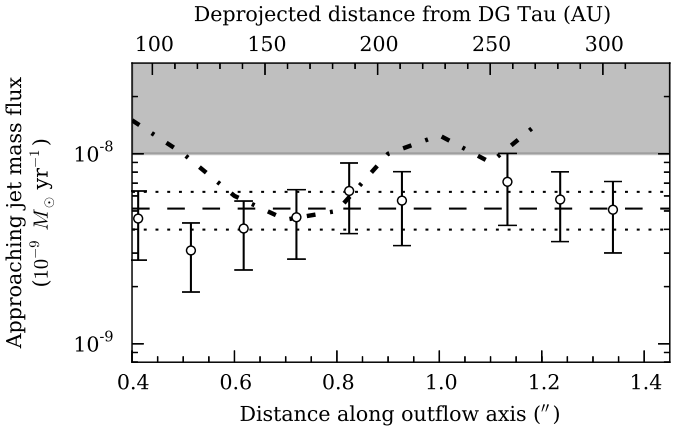

Figure 2.14 Jet mass flux in the approaching jet of DG Tau. The circles and error bars show the mass flux computed from the measured physical parameters of the jet, and the associated uncertainties. The dashed line represents the average value of all data points, and the dotted lines show the standard deviation of the measurements. The jet mass flux determined by Agra-Amboage et al. (2011) via a similar method is shown as a thick dot-dashed line. The jet mass flux determined by Lynch et al. (2013) from VLA data is represented by the grey shaded region.

In order to calculate the kinetic jet energy flux, it is necessary to determine the jet density, $\rho_{\rm jet}$. To accomplish this, the electron density, n_e, determined from the [Fe II] line ratio was converted to jet density using the formula $\rho_{\rm jet} = n_{\rm H} m_{\rm H} \mu$, where $\mu = 1.4$ for a typical gas composition of 90 per cent hydrogen and 10 per cent helium. The hydrogen number density, $n_{\rm H}$, is given by the ratio of the electron density and the ionization fraction, χ_e, which is taken to be $\chi_e = 0.3 \pm 0.1$, as determined for the high-velocity components of the DG Tau jet by Bacciotti (2002), and later refined by Maurri et al. (2014), from ratios of optical lines (Bacciotti & Eislöffel 1999). The jet kinetic energy flux density is then calculated via the formula $F_{\rm E} = (1/2)\rho_{\rm jet} v_{\rm jet}^3$. Finally, multiplying the jet kinetic energy flux density by the jet cross-sectional area, estimated as $A_{\rm jet} = \pi (D_{\rm jet}/2)^2$, gives the jet kinetic power.

The approaching jet from DG Tau is observed to accelerate from a deprojected velocity ~ 215 km s^{-1} to ~ 315 km s^{-1} over the region $0\farcs5$–$1\farcs15 \approx 115$–260 AU from the central star (Fig. 2.13b). This corresponds to a region of steadily increasing jet diameter, from ~ 19 AU to ~ 28 AU (Fig. 2.13d). The jet kinetic power increases over this region, from $(4.4 \pm 1.9) \times 10^{31}$ erg s^{-1} to $(2.2 \pm 0.9) \times 10^{32}$ erg s^{-1}. The jet acceleration and related increase in jet kinetic power are discussed further is §2.4.1.5.

The approaching jet mass flux, determined by the formula $\dot{M} = \rho_{\rm jet} v_{\rm jet} A_{\rm jet}$, is shown in Fig. 2.14. The jet mass flux is constant within measurement errors, with an average value of $(5.1 \pm 1.2) \times 10^{-9}$ M$_\odot$ yr^{-1}. Our measurements typically agree to within 1σ with the measurements made by Agra-Amboage et al. (2011) using a similar technique, with discrepancies most likely due to our differing methods of determining the electron density of the jet. Our jet mass flux is also consistent with that determined by Maurri et al. (2014), $(8 \pm 4) \times 10^{-9}$ M$_\odot$ yr^{-1}. Both our mass flux determination and that of Agra-Amboage

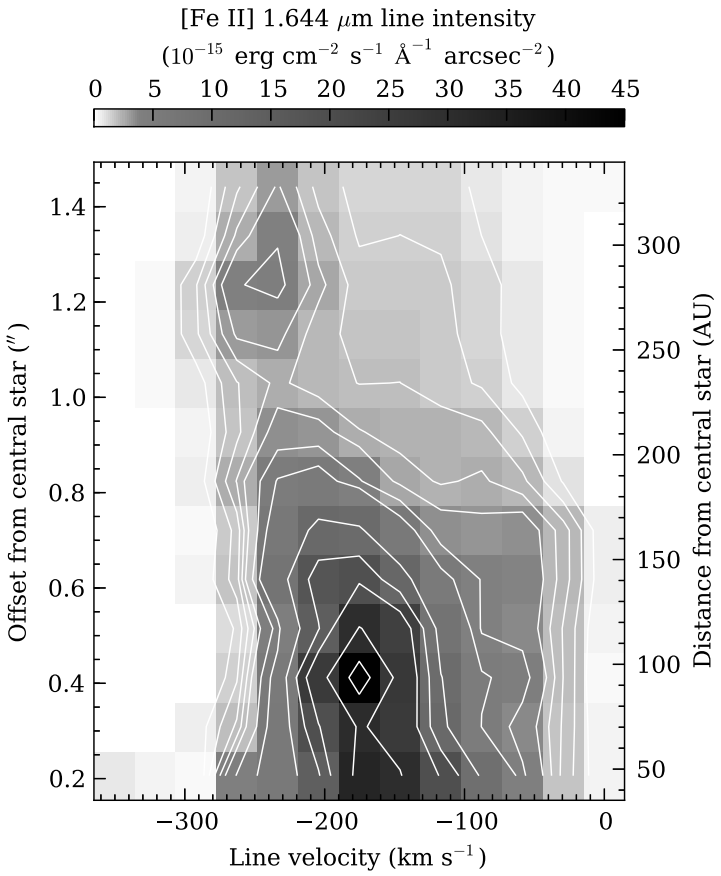

Figure 2.15 Position-velocity diagram of the blueshifted outflow from DG Tau. At each downstream position, the spaxel containing the jet ridgeline is dispersed. Contours are plotted at levels of [1, 1.5, ..., 3, 4, 5, 10, 15, 20, 30, 40] × 10^{-15} erg cm^{-2} s^{-1} Å^{-1} arcsec^{-2}.

et al. (2011) are lower than previous estimates from VLA data of $\dot{M} \sim 1$–5×10^{8} M$_{\odot}$ yr^{-1} (Lynch et al. 2013). However, as noted by those authors, the uncertainties in estimating this quantity makes detailed comparison difficult. We conclude that the DG Tau jet has a constant mass flux within $\sim$ 350 AU of the central star within our measurement uncertainties.

2.4.1.5. Jet Velocity Variability

Hydromagnetic winds are initially accelerated via magnetocentrifugal processes, which are efficient up to approximately the Alfvén critical surface (e.g. Blandford & Payne 1982). This surface is expected to be located within at most a few tens of AU of the central star (e.g. Gómez de Castro & Pudritz 1993; Cabrit 2007a). However, our data show a clear increase in velocity in the approaching jet over the region $\sim$ 115–260 AU from the central star, well beyond the predicted location of the Alfvén surface. This trend can also be seen in a position-velocity diagram of the approaching outflow, formed along the jet axis (Fig. 2.15). The increase in velocity is smooth, with no sudden velocity changes. This acceleration has been observed in previous studies of the approaching jet from DG Tau (Bacciotti et al. 2000; Takami et al. 2004; Agra-Amboage et al. 2011), but has not been definitively explained. It is possible that this "acceleration" is a stroboscopic effect when observing a jet with intrinsic velocity variations, as suggested by the observations of Pyo

et al. (2003b). We discuss other possible causes of this apparent acceleration below.

Purely hydrodynamic pressure-driven acceleration is not possible in the DG Tau jet for the following reasons. Acceleration in a jet may be driven by thermal pressure coupled with expansion. In the adiabatic case, this process is governed by the Bernoulli equation,

$$\frac{1}{2}v^2 + h = \text{const.}, \tag{2.6}$$

(Landau & Lifshitz 1987), where v is the flow velocity, and h is the enthalpy. The gravitational potential has been neglected, as it is expected to be unimportant at distances of hundreds of AU from the central star. The coupling of acceleration and expansion arises from energy stored as enthalpy being transferred to kinetic energy. However, enthalpy is unimportant in these regions of protostellar outflows (e.g. Zanni et al. 2007). There may be some exceptions to this assumption, such as in the post-shock cooling region of the recollimation shock where the temperature $\gtrsim 1$ MK (§2.4.1.2), but the enthalpy in the region of the flow that is observed to be expanding and accelerating is unimportant. For an isothermal jet, it can be shown via dynamical calculation that the inferred pressure gradient in the DG Tau jet is incapable of accelerating the flow (Appendix B). Therefore, a purely hydrodynamic acceleration cannot occur in the DG Tau jet. One possible alternative would be the presence of a core, hot flow nested within the jet, formed from or indicated by the presence of the hot stationary X-ray shock in the jet. This material could then accelerate the jet via thermal pressure. The theoretical plausibility of this model is difficult to ascertain, due to the strong dependence of the X-ray material cooling length on both density and shock velocity (Günther et al. 2009). However, the close proximity of the stationary X-ray and [Fe II] features (18–30 AU separation) suggests the hot shocked material cools over this distance, and would therefore be incapable of driving acceleration at hundreds of AU from the central star.

Magnetic fields sufficiently modify the flow dynamics in a way that could, in principle, provide a mechanism for acceleration to occur (Appendix C). A tangled magnetic field within the jet may accelerate the jet by the conversion of Poynting flux to kinetic energy. The DG Tau jet is observed to accelerate from $v_0 \approx 215$ km s^{-1} to $v \approx 315$ km s^{-1} over the region $\sim$ 115–260 AU from the central star, and expands from a diameter of $2R_0 \approx 20$ AU to $2R \approx 30$ AU (Fig. 2.13). For an initial electron number density of $n_{\mathrm{e},0} = 2 \times 10^4$ cm^{-3}, equation (C.9) gives a required initial magnetic field strength $B_0 = 49$ mG at a distance of $\sim$ 115 AU from the central star in order to facilitate the coupled acceleration-expansion of the jet. The scaling relationship between density and magnetic field, equation (C.7), then yields a magnetic field strength of 31 mG at the end of the acceleration region, where the electron density has decreased to $\sim 1 \times 10^4$ cm^{-3}.

A field strength of several tens of mG is plausible, but unlikely, in this region of the outflow. Modelling of the shocks in DG Tau (Lavalley-Fouquet et al. 2000) suggests that the shock

velocities in DG Tau are $\lesssim 100$ km s^{-1}. However, the field strengths calculated above imply an Alfvén velocity in the jet of ~ 315–350 km s^{-1}, which is inconsistent with the inferred shock velocities. Even if the tangled field were perfectly isotropic, with an effective Alfvén speed of ~ 105–115 km s^{-1} in any direction, this speed would still be too high to easily allow for shocks of the velocity determined by Lavalley-Fouquet et al. (2000). Therefore, we conclude that magnetic acceleration beyond the recollimation shock is unlikely in the DG Tau jet.

In the absence of a source of extra kinetic energy for the jet, we conclude that velocity variations are the most likely cause of the observed "acceleration" of the DG Tau jet. We have argued above (§2.4.1.1) that these velocity variations are the cause of the moving knots in the DG Tau jet. However, the irregularity in knot ejection intervals and knot proper motions suggests that the underlying jet velocity variation is also irregular. Further time monitoring of DG Tau is necessary to determine the parameters of this variation.

2.4.1.6. Rotation

The search for jet rotation has been an important component of YSO outflow studies in recent times. The unambiguous determination of rotation in a YSO jet would provide direct evidence that the outflow extracts angular momentum from the circumstellar disc, and offer an answer to the angular momentum problem in star formation (e.g. Balbus 2011). An accurate measurement of the jet rotation would also allow an alternate estimate of the extent of the wind-launching region in the disc (§2.4.1.3; Bacciotti et al. 2002; Anderson et al. 2003).

Our data have been investigated for a rotation signature using a method based on that of Bacciotti et al. (2002). If the jet is rotating, the gas on either side of the jet axis will emit lines with slightly different Doppler shifts. At every point along the outflow axis, the fitted HVC line velocities of the third spaxel above and below the jet ridgeline were differenced, covering $0\farcs11$–$0\farcs16 \approx 15$–22 AU on either side of the jet. The upper limit of this range was chosen to correspond to the greatest observed jet diameter of $\lesssim 40$ AU (Fig. 2.13d). The lower limit of the range was chosen to minimize the beam-smearing of rotational measurements identified in the simulations of Pesenti et al. (2004), by only including spaxels with central offsets similar to or greater than the PSF ($0\farcs11$). This procedure measures any velocity asymmetry about the jet ridgeline. The resulting velocity differences are shown in Fig. 2.16.

There is no clear indication of rotation in our data of the approaching DG Tau jet. At almost all positions along the jet, the velocity differences are $\lesssim 2\sigma$ from 0 km s^{-1}. Furthermore, the velocity differences across the ridgeline change sign along the jet, which is not consistent with bulk jet rotation. The average velocity difference across the jet ridgeline for all measured locations is 0.0 ± 6.8 km s^{-1}, corresponding to a rotational

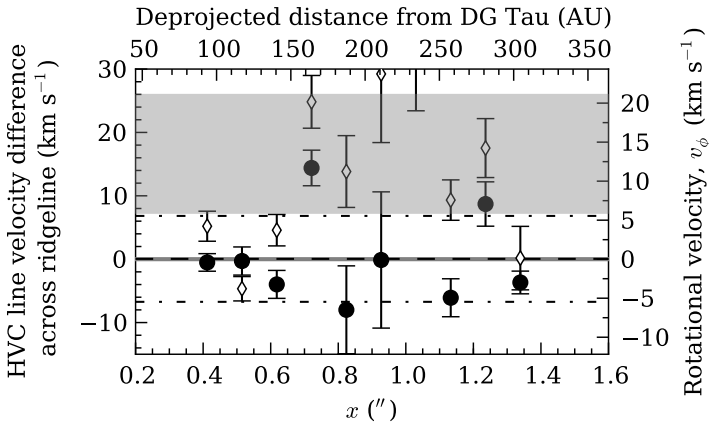

Figure 2.16 Velocity differences across the approaching jet ridgeline. Velocities are taken from the third spaxel above and below the jet ridgeline at each position along the outflow axis, and then subtracted. These differenced velocities are shown as large, filled circles. The average of these differences is shown by the dashed line; the estimated 1σ uncertainty in this average is denoted by the dot-dashed lines. A velocity difference of 0 km s^{-1} is shown by the thick grey line. Open diamonds show the velocity differences found by the same procedure, but forming differences about the large-scale outflow axis. The grey shading represents the rotational velocities reported by Coffey et al. (2007). The rotational velocity is calculated from the velocity difference via the formula $v_\phi = \Delta v/(2\sin i)$, where i is the jet inclination to the line-of-sight (Coffey et al. 2007).

velocity of $v_\phi = 0.0 \pm 5.5$ km s^{-1} after correction for the jet inclination, i, by the formula $v_\phi = \Delta v/(2\sin i)$ (Coffey et al. 2007). This result refutes the lowest rotational velocity claimed by Coffey et al. (2007) to 0.88σ, and implies an upper limit on observable rotation in the DG Tau jet of 6 km s^{-1}. The large uncertainties $\sim 1''$ from the central star are due to the low signal-to-noise ratio and some spurious line component fits in that region.

An alternative method for detecting rotation in protostellar outflows is the analysis of position-velocity (PV) diagrams. A rotating jet will show a 'tilted' PV diagram-profile when a spectrograph slit is placed along the cross-jet direction (e.g. Pesenti et al. 2004; Coffey et al. 2004, 2007). We have formed cross-outflow PV diagrams of the approaching DG Tau outflow (Fig. 2.17) by extracting vertical 'slices' of IFU data at positions intermediate between the moving jet knots, $0\farcs45$, $0\farcs80$ and $1\farcs00$ along the jet. We observe that there is no clear, consistent 'tilt' in any of these profiles, particularly in the high-velocity component. The intermediate-velocity component may show some small 'tilt' at both $0\farcs8$ and $1\farcs0$ from the central star, but the direction of this tilt, which corresponds to the inferred direction of rotation, is not the same. Therefore, we conclude that our data do not support the detection of rotation in the approaching DG Tau outflow. We suggest that the any rotation signature originally present in the jet may be degraded by passage through the strong recollimation shock in the jet channel (§2.4.1.2).

We now briefly discuss two possible systematic uncertainties in our data. The first is uneven slit illumination, as described by Bacciotti (2002) and Marconi et al. (2003). The effect of uneven slit illumination is to create a spurious velocity offset between two positions along the slit due to the convolution of the velocity profile with the pixel width and slit width.

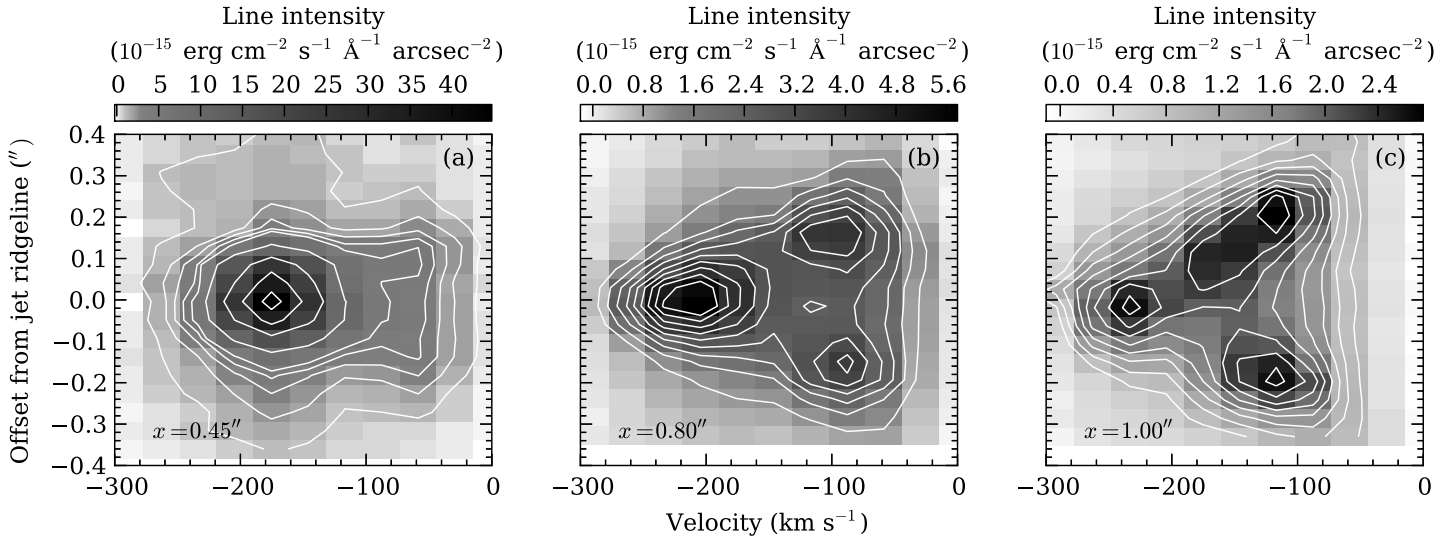

Figure 2.17 Cross-jet position-velocity diagrams of the blueshifted DG Tau outflow at (a) 0.″45, (b) 0.″80 and (c) 1.″00 along the jet. The position offset shown is measured from the position of the jet ridgeline at that distance from the central star. Indicative contours are plotted with the following levels:
(a) $[1, 2, \ldots, 5, 10, 20, 30, 40] \times 10^{-15}$ erg cm^{-2} s^{-1} Å^{-1} arcsec^{-2};
(b) $[1.0, 1.5, \ldots, 5.0] \times 10^{-15}$ erg cm^{-2} s^{-1} Å^{-1} arcsec^{-2};
(c) $[0.75, 1.0, \ldots, 2.5] \times 10^{-15}$ erg cm^{-2} s^{-1} Å^{-1} arcsec^{-2}.

However, this is only an issue if the slit width is greater than the PSF width. In our case, our effective slit width for cross-outflow slits ($0\farcs103$) is comparable to our measured PSF ($0\farcs11$), so we predict that the impact of this effect on our results will be small. This has recently been confirmed for similar observations of DG Tau in the K band obtained using SINFONI, a similar instrument to NIFS, where it was determined the effect of uneven slit illumination was less than 2 km s^{-1} (Agra-Amboage et al. 2014). Secondly, we must consider the possible effect of residual velocity calibration effects along individual slitlets. This was analysed by Beck et al. (2008), and the effect was found to have a magnitude of $\pm \sim 3$ km s^{-1}. This is less than the 1σ uncertainty on our determination of the rotation velocity of the DG Tau jet; hence, we determine that this effect is likely negligible on the measured velocity differences.

We proceed to investigate previous claims of rotation in the DG Tau approaching jet. The spectral resolution of STIS, the instrument used to make the previous measurements of claimed rotation, is ~ 25 km s^{-1} pix^{-1}, with Gaussian fitting typically achieving an effective spectral resolution of one-fifth of the velocity sampling when determining line velocities (Coffey et al. 2007). The measured velocity differences across the jet in previous rotation studies of DG Tau are factors of a few greater than this uncertainty of ~ 5 km s^{-1} (Coffey et al. 2007), which implies that a real velocity asymmetry was detected in previous studies. We shall now investigate possible systematic uncertainties affecting these results.

Our IFU data have an advantage over previous studies in that the location of the jet ridgeline at each downstream position, and the velocity differences at all downstream positions, can be tracked simultaneously. By comparison, the long-slit spectroscopy methods used by Bacciotti et al. (2002) and Coffey et al. (2007) can only do one of these, depending on the technique employed. Using multiple slit positions aligned parallel to the large-scale HH 158 outflow axis makes it difficult to locate the centroid of the jet at each downstream position. This requires that the large-scale outflow axis be used as the centre of the jet for forming velocity differences (Bacciotti et al. 2002). However, it is shown above (§2.3.3.1) that the jet does not follow a linear path along the outflow axis. Repeating our analysis, but forming velocity differences about the large-scale outflow axis, yields an average velocity difference along the jet of $\sim$ 6–17 km s^{-1}, allowing for a $\pm 0\farcs05$ uncertainty in the outflow axis position. We show in Fig. 2.16 individual velocity differences formed using the large-scale outflow axis as the jet centre (open diamonds in that Figure). These velocity differences are clearly greater than those formed about the jet ridgeline at most downstream positions, especially $0\farcs7$–$1\farcs2$ from the central star.

We note that Bacciotti et al. formed velocity differences using the *intermediate*-velocity component of the approaching outflow. We investigate this measurement to demonstrate the importance of our IFU-based method for measuring rotation. First, repeating the analysis described here on the intermediate-velocity component yields the same result as for the jet, with no rotation if the jet ridgeline is taken as the outflow centre, and a rotation

velocity of $\sim$ 5–20 km s^{-1} if the large-scale outflow axis is taken to be the component centre. Secondly, Bacciotti et al. interpreted the IVC as being an intermediate-velocity wind, whereas we have leveraged the capabilities of integral-field spectroscopy to interpret the IVC as a turbulent entrainment layer (§2.4.2). Any rotation signature in such a layer is likely to be masked by the turbulent motion of the entrained gas. We conclude that not centring the velocity difference measurements on the local ridgeline position introduces a possible systematic error in the Bacciotti et al. (2002) IVC rotation claim.

Conversely, placing the slit across the jet at one downstream position allows for the jet centroid position to be accurately determined (Coffey et al. 2004, 2007). However, this measurement provides a velocity difference at only one position along the outflow axis. It can be seen in Fig. 2.16 that the velocity difference across the jet at any one position may not be an accurate representation of the velocity difference profile of the jet as a whole. Indeed, when the procedure was repeated over multiple epochs for the YSO RW Aurigae, it was found that the cross-jet velocity difference at the sampled position was time-varying on scales of six months (Coffey et al. 2012), and hence any one measurement of cross-jet velocity difference at one downstream position cannot be reliably used to ascertain the presence of rotation.

The measurement of rotation in YSO jets and outflows is a key piece of evidence supporting MHD disc winds as the driving mechanism, and an important diagnostic in attempting to measure their launch radii (Bacciotti et al. 2002; Anderson et al. 2003; Coffey et al. 2004, 2007; Ferreira et al. 2006). The non-detection of rotation may be interpreted as weakening the evidence for MHD disc-driven winds. However, we emphasize that other effects may obscure the detection of rotation. Specifically, both the passage of the jet through the recollimation shock (§2.4.1.2), and the presence of a turbulent entrainment layer (§2.4.2) kinematically process the jet and/or induce turbulence, masking or destroying any rotation that is originally present. In order to definitively confirm or refute jet rotation, it is necessary to either attempt to measure jet rotation upstream of the recollimation shock, investigate rotation in jets without recollimation shocks if they exist, or await higher-resolution integral-field spectrographs (e.g. GMTIFS; McGregor et al. 2012) that will allow for the undisturbed jet core to be resolved.

2.4.2. Entrainment Region

The presence of an intermediate-velocity component (IVC) in the DG Tau blueshifted outflow has been noted by many authors. This component is typically interpreted to be emitted by a less-collimated MHD wind accelerated from the disc around DG Tau, from a radius of a few AU from the central star (Bacciotti et al. 2000; Dougados et al. 2000; Pyo et al. 2003b; Anderson et al. 2003). Pyo et al. (2003b) suggested that at least some part of the DG Tau IVC emission is due to entrainment of such a disc wind by the high-velocity

jet, based on the expansion of the IVC as it progresses downstream.

[Fe II] emission is generated by shock interactions (Nisini et al. 2002). This raises the question as to how a steady, poorly-collimated disc wind radiates in [Fe II]. The HVC radiates predominantly due to the presence of shock-excited knots in the jet (§2.3.3.2), but no such structures appear in the IVC (Fig. 2.6d). Sideways ejection of material from the jet knots is also ruled out as the source of shock excitation of the IVC, given the lack of discernible IVC emission enhancements at the knot positions. The formation of a turbulent, shocked entrainment layer between the high-velocity jet and either a wide-angle disc wind, or the ambient medium into which the outflow is emerging, would provide the excitation necessary to dissociate molecules in the wind/ambient medium, and produce [Fe II] emission. We therefore investigate the possibility that the IVC represents a turbulent, shocking entrainment layer.

Entrainment, which is also referred to as turbulent mixing, can occur at two distinct locations within a jet. *Lateral* entrainment occurs along the jet walls, as the fast-moving jet material flowing along the interface pulls the slower-moving/stationary ambient material into a turbulent mixing layer (e.g. Cantó & Raga 1991; Raga et al. 1995). *Head*, or *prompt*, entrainment is the term used to describe the pushing and mixing that occurs at the head of the jet in a bow shock (Raga & Cantó 1997). The head of the approaching DG Tau outflow is at least several arcseconds from the central star (Eislöffel & Mundt 1998; McGroarty & Ray 2004; McGroarty et al. 2007), so we consider lateral entrainment only. However, full jet flow simulations show that the leading jet bow shock will push aside the ambient medium when the jet is first launched, forming a bubble that keeps the ambient material away from the jet walls (Taylor & Raga 1995; Lim et al. 1999). Therefore, recent models of lateral entrainment apply special conditions to the ambient medium, e.g. an ambient flow perpendicular to the jet (López-Cámara & Raga 2010), to bring the jet and the surrounding medium into contact. There is no evidence for such flows existing in the DG Tau system.

It is often suggested that the high-velocity jets driven by YSOs are nested within a lower-velocity wind (e.g. Pyo et al. 2003a). Such a wind would come into contact with the jet, and provide a constant supply of molecular material with which to form a mixing layer. This would remove the requirement to apply special conditions to the ambient medium to facilitate entrainment. This scenario was proposed by Pyo et al. (2003b) as the partial origin of the blueshifted IVC they observed in the DG Tau outflow. Below, we provide evidence that a poorly-collimated molecular disc wind does exist, and argue that the blueshifted IVC is predominantly emitted by a turbulent mixing layer.

2.4.2.1. Origin of the Near-Side H_2 Region

The extended H_2 1-0 S(1) 2.1218 μm line emission from the near side of the DG Tau circumstellar disc takes on a bowl-shaped morphology, as shown in Fig. 2.18 (also, Beck

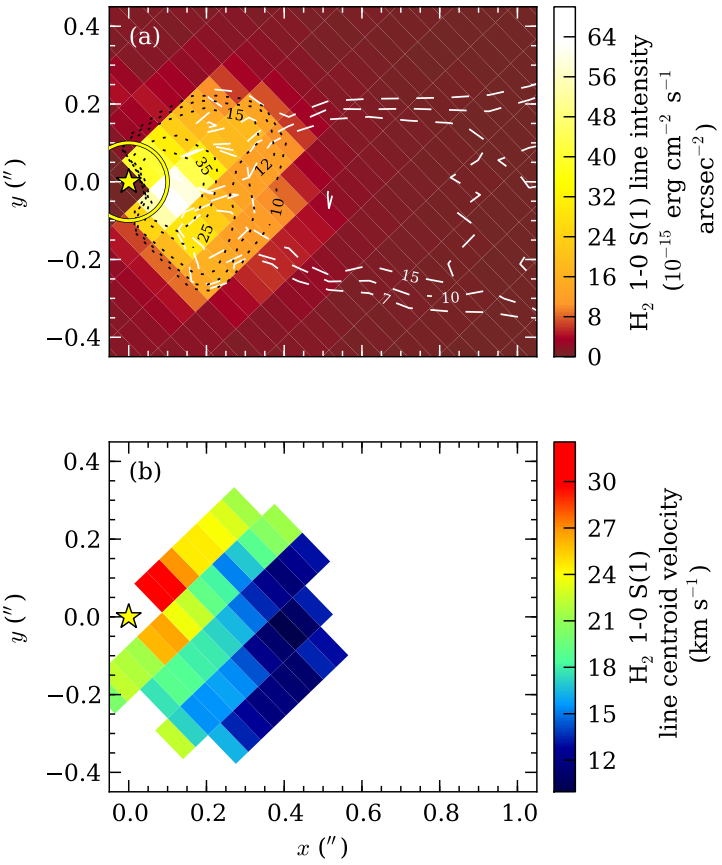

Figure 2.18 H_2 1-0 S(1) 2.1218 μm emission in the approaching DG Tau outflow. (a) H_2 1-0 S(1) 2.1218 μm integrated emission flux, formed over the velocity range −100 to 60 km s^{-1}. Dotted lines (black) show contours of this emission. Overlaid as dashed lines (white) are three contours of fitted [Fe II] 1.644 μm IVC line intensity (Fig. 2.6d). Contours are labelled in units of 10^{-15} erg cm^{-2} s^{-1} arcsec^{-2}. (b) Line velocity centroid of H_2 1-0 S(1) 2.1218 μm emission in each spaxel, as determined by single-component Gaussian fitting. The velocities quoted are blueshifted velocities, and are adjusted for the stellar velocity, as determined from photospheric absorption line fitting. In both panels, the position of the central star and the position of the occulting disc (panel a only) are shown by a yellow star and circle, respectively.

et al. 2008). This H_2 emission was interpreted by Takami et al. (2004) as being from a warm, wide-angle molecular wind encasing the inner regions of the HH 158 outflow. Data on the approaching H_2 emission obtained in the ultraviolet by Ardila et al. (2002) and Herczeg et al. (2006) are consistent with this explanation, and Beck et al. (2008) and Agra-Amboage et al. (2014) also concluded that their data support this assertion. We provide further evidence below that this emission comes from a wider-angle molecular wind.

To investigate the velocity structure of the H_2 emission, spectral Gaussian fits were made to the H_2 1-0 S(1) 2.1218 μm line at every position in the K-band data cube, using the same method applied to the [Fe II] 1.644 μm line in the H-band data cube (§2.3.4). Fits were restricted to a single line component. Furthermore, a lower signal-to-noise ratio threshold of 2.5 was applied to fits in the K-band data cube. The line velocities were adjusted to account for the systemic stellar velocity, based on absorption line fits to the Na I and Ca I doublets visible in the K-band stellar spectrum (Fig. 2.1b). The resulting line centroid velocity profile is shown in Fig. 2.18(b).

The near-side H_2 emission is all blueshifted with respect to the systemic velocity (Fig. 2.18b). This eliminates the circumstellar disc surface as the origin of the emission, through either emission or scattering by the disc surface. If the emission was produced or scattered by the disc surface, it would be expected to have zero line velocity with respect to the systemic

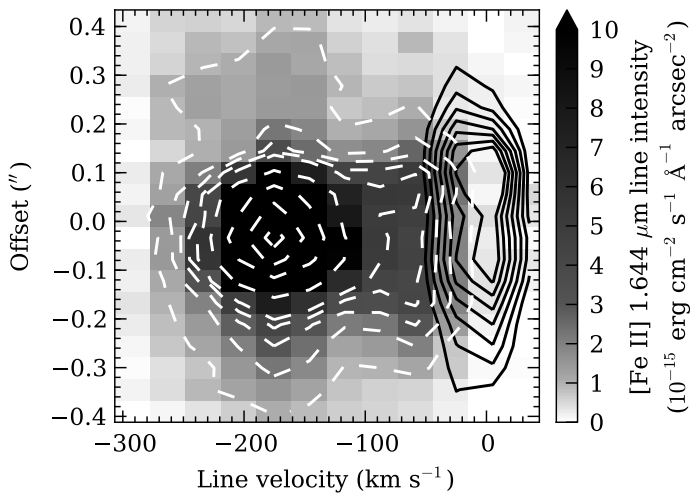

Figure 2.19 Cross-outflow position-velocity diagram of H_2 1-0 S(1) 2.1218μm and [Fe II] 1.644 μm emission in the approaching DG Tau outflow, formed 0.″425 from the central star. The [Fe II] 1.644 μm emission is shown in greyscale. [Fe II] 1.644 μm emission contours (white, dashed) are placed at levels of $[1, 2, \ldots, 5, 10, 20, 30, 40] \times 10^{-15}$ erg cm^{-2} s^{-1} Å^{-1} arcsec^{-2}. H_2 contours (black, solid) are placed at levels of $[0.4, 0.6, \ldots, 1.6] \times 10^{-15}$ erg cm^{-2} s^{-1} Å^{-1} arcsec^{-2}. The K-band data have been re-gridded onto the H-band pixel grid by linear interpolation.

velocity, with a small asymmetry of $\sim$ a few km s^{-1} about the outflow axis, caused by the rotation of the disc. Such an asymmetry is present $\sim$ 0.″2 along the outflow axis, but it is too large, $\sim$ 9 km s^{-1}, to represent disc rotation. It also shows the opposite rotational sense to the known rotation direction of the DG Tau circumstellar disc (Testi et al. 2002). We determine line centroid velocities between -10 and -30 km s^{-1} for the H_2 emission, which are larger than the -2.4 ± 18 km s^{-1} reported by (Beck et al. 2008). This discrepancy results from Beck et al. reporting the line centroid velocity of all the emission, which includes the $\sim$ 0 km s^{-1} H_2 emission on the far side of the disc. Indeed, our approaching centroid line velocity determinations are mostly within the uncertainties given by Beck et al. (2008). Our measurements may also suffer from the effects of uneven slit illumination, as described by Agra-Amboage et al. (2014). Indeed, those authors report lower blueshifted velocities ($\sim$ 5 km s^{-1}) for the majority of the H_2 emission.

The H_2 1-0 S(1) line velocity map provides clues as to the nature of this outflow. The line velocity peaks near the central star, and decreases with distance along the outflow axis. This effect was also observed by Agra-Amboage et al. (2014). We interpret this to be the profile of a poorly-collimated wind. The higher approaching line velocities near the base of the wind correspond to where the wind has just been launched, and has yet to be collimated into the outflow direction. The gas on the near side of the wind is therefore flowing towards the observer, increasing the line-of-sight velocity component. As the flow becomes collimated, the gas flows in the outflow direction, and hence the line-of-sight velocity component becomes smaller.

We search for a kinematic link between the H_2-emitting material and the IVC of the [Fe II] emission. Fig. 2.19 shows a position-velocity diagram of both the [Fe II] and H_2 emission at the observable edge of the latter. This diagram tentatively suggests that the 'wings' of the [Fe II] IVC form a 'bridge' between the H_2 emission, and the higher-velocity [Fe II] emission, which may be indicative of shearing and entrainment. We also note that the

[O I] LVC reported by Coffey et al. (2007) may further spatially and kinematically link the H_2 and [Fe II] HVC emitting material (Agra-Amboage et al. 2014). This suggests that all three components are kinematically linked, supporting our interpretation of the [Fe II] IVC as an entrainment layer between the molecular wind and the high-velocity jet.

2.4.2.2. Requirements for Lateral Entrainment

Lateral entrainment occurs via instabilities that form along the walls of the jet and cause turbulent mixing of jet and ambient material. The relevant instability in the formation of mixing layers is the Kelvin-Helmholtz (KH) instability (Chandrasekhar 1961). Velocity shears are well-known to be stabilized against the KH instability for a Mach number difference, M_Δ, between the flows of $M_\Delta \gg 1$ (Trussoni 2008). Hydrodynamic simulations have shown that entrainment is unimportant in jet flows with a Mach number difference of $M_\Delta > 6$ (Chernin et al. 1994). It has been shown analytically that hydrodynamic shear layers are stabilized against the KH instability if $M_\Delta \geq \sqrt{8} \approx 2.8$ for disturbances propagating in the jet flow direction (Trussoni 2008). More generally, taking into account instability modes which propagate at an angle ϕ to the outflow, the criterion for stability is $M \cos\phi < \sqrt{8}$ (Fejer & Miles 1963). This means that some KH instability modes may be unstable for $M_\Delta > \sqrt{8}$, permitting more modest entrainment at higher Mach number differences. However, given that the DG Tau jet is highly supersonic, with $M_\Delta \approx M_{\rm jet} \sim 18$–$27$ for a monatomic jet at temperature $T = 10^4$ K, lateral entrainment is unimportant if the DG Tau jet is purely hydrodynamic.[53]

Magnetic fields can permit lateral entrainment to occur in highly supersonic jets. The effects of magnetic fields on the KH instability in shear layers are complex, and are sensitive to both the initial physical conditions of the flow, and the orientation of the magnetic field lines with respect to the flow and shear directions (Chandrasekhar 1961; Trussoni 2008). Consider a slab shear layer between magnetized compressible gases in the y, z-plane, with the velocity shear occurring in the y-direction, and the fast-moving gas on one side of the shear layer flowing in the z-direction. The shear layer then extends infinitely in the x-direction. There are three basic magnetic field orientations that illustrate the complexities at hand. First, if the magnetic field is parallel to both the shear interface and the flow direction, that is, $\boldsymbol{B} = B\hat{\boldsymbol{z}}$, then the shear layer is stabilized against the KH instability if $v_{\rm A} \geq c_{\rm s}$ (Chandrasekhar 1961; Ray & Ershkovich 1983). This condition is satisfied for the magnetic field strengths inferred for protostellar jets (Lavalley-Fouquet et al. 2000; Hartigan et al. 2007). Secondly, a magnetic field perpendicular to both the interface and flow direction, that is, $\boldsymbol{B} = B\hat{\boldsymbol{y}}$, has no effect on the suppression of the KH instability (Chandrasekhar 1961).

[53] $M_\Delta = M_{\rm jet}$ if the ambient material is at rest with respect to the star-disc system. If the ambient material is the less-collimated molecular wind, it is significantly slower than the jet, such that $M_\Delta \approx M_{\rm jet}$.

Consider an astrophysical jet described in cylindrical coordinates (r, ϕ, z), flowing in the z-direction. In this case, the shear layer between the jet and the ambient medium (or an encasing wind) will be in the (ϕ, z)-plane. Beyond the Alfvén surface a few to tens of AU above the circumstellar disc, the magnetic field in the outflow will be predominantly toroidal (Hartigan et al. 2007; Zanni et al. 2007). Then, the most physically accurate two-dimensional shear layer approximation for a protostellar jet is that with a magnetic field parallel to the shear interface, but perpendicular to the flow direction, such that $\boldsymbol{B} = B\hat{\boldsymbol{x}}$. For this field configuration, the KH instability criterion is as for a purely hydrodynamic jet, but with the Mach number difference across the shear layer determined with respect to the quadrature sum of the sound and Alfvén speeds, $\sqrt{c_{\rm s}^2 + v_{\rm A}^2} \approx v_{\rm A}$ for $v_{\rm A} \gg c_{\rm s}$ (Miura & Pritchett 1982; Ray & Ershkovich 1983). The Alfvénic speed becomes the effective sound speed.

To destabilize the interface between the jet and ambient wind in DG Tau, the magnetic field encompassing the jet would need to result in an Alfvén jet velocity of 75–115 km s^{-1}. Such an Alfvén velocity is low enough to allow for the formation of shocks with the velocities inferred by Lavalley-Fouquet et al. (2000). The upper limit on the required magnetic field strength is 7.5–11 mG, based on our determination of the density of the DG Tau jet (§2.4.1.4). This field strength is an order of magnitude greater than that inferred by Lavalley-Fouquet et al. (2000) for DG Tau from shock modelling, but is an order of magnitude less than the magnetic field strength in protostellar jets considered reasonable by Hartigan et al. (2007).[54] As stated above, shear layer disturbances propagating at an angle to the flow direction will not be stabilized until higher Mach number differences are reached (Fejer & Miles 1963). A weaker field could facilitate a lower entrainment rate in the DG Tau jet. Indeed, the DG Tau jet does not become fully turbulent over the region where entrainment is occurring (§2.3.4.1), suggesting that only moderate turbulent mixing is occurring. Therefore, we consider the magnetic field strength necessary to enable turbulent entrainment to be physically reasonable, and conclude that the magnetic field providing collimation to the DG Tau jet also allows the jet to entrain material from the ambient wind.

2.4.2.3. Relationship to Large-Scale Molecular Outflows

One of the most striking features of Class 0 and Class I protostars are large-scale bipolar molecular outflows detected in millimetre rotational transitions of CO (Stahler 1994a). Such outflows were first detected around the protostar L1551 IRS 5 (Snell et al. 1980), and were quickly identified as being common in star-forming regions (Reipurth & Bachiller 1997). The masses of these outflows are greater than the mass of the driving protostar, implying that the outflow must be composed of swept-up material (Masson & Chernin

[54] Incidentally, this magnetic field is also significantly weaker than the field strength necessary to cause extended acceleration in the jet (§2.4.1.5).

1992). Typically these outflows have ages $\sim 5 \times 10^{3-4}$ yr (Masson & Chernin 1993), and the long cooling time of the CO molecule provides a history of the outflow (Ray 2000). These swept-up shells are generally interpreted as being driven by prompt entrainment from an outflow bow shock (Cabrit et al. 1997; Davis et al. 1997; Reipurth & Bachiller 1997; Arce & Goodman 2002; Stojimirović et al. 2006).

We argued above for the presence of lateral entrainment in the DG Tau microjet. Such entrainment provides another candidate source for the momentum in the large-scale swept-up molecular outflows. Previous studies argued against lateral entrainment as a driving mechanism for CO outflows (e.g. Raga & Cabrit 1993; Davis et al. 1997; Reipurth & Bachiller 1997). These studies relied on the argument that the KH instability would not develop in protostellar jets; however, we argued above that in fact, this is possible when magnetic effects are taken into account (§2.4.2.2). Lateral entrainment would be particularly useful in objects such as HH 286, where the molecular outflow ends closer to the protostar than the location of the first optical Herbig-Haro object, indicating the jet has pushed past the head of the CO outflow. Hence the jet can no longer drive the CO outflow in a snowplow fashion (Stojimirović et al. 2006), and lateral entrainment becomes a possible CO outflow driving mechanism. However, it should be noted that in many recent high-angular resolution observations of molecular outflows, the structure and kinematics of the outflow has favoured the bow-shock driving model (Gueth & Guilloteau 1999; Lee et al. 2002), and the driving in such an object may be from a wide-angle wind instead of a well-collimated jet (Arce et al. 2007, and references therein). However, lateral entrainment may still provide some contribution, albeit small, to the driving of CO outflows.

There is no detected CO outflow associated with DG Tau. However, DG Tau is currently transitioning between evolutionary Class I and Class II (Pyo et al. 2003b; White & Hillenbrand 2004), and any CO outflow that was previously present must have cooled to the point where it is no longer emitting. A decrease in ^{13}CO column density ~ 4000 AU from the central star indicates that a major part of the disc-shaped envelope around DG Tau has already been blown away, and the molecular outflow responsible for the dispersion is no longer visible (Kitamura et al. 1996a). Attempting to locate lateral entrainment in the microjets of younger YSOs that drive CO outflows would be difficult, due to the significant extinction towards these highly embedded objects. Therefore, numerical simulations will be useful to test the viability of lateral entrainment as a mechanism for driving CO outflows. Such models would need to account for the magnetic fields in and around the outflows from the YSO in order to facilitate lateral entrainment.

2.5. Conclusions

We have investigated the YSO DG Tauri, and its associated outflows, in detail using H- and K-band data from the NIFS instrument at Gemini North taken on 2005 Oct and Nov. The H-band stellar spectrum shows significant photospheric absorption features, in contrast to previous studies of DG Tau that showed a veiled continuum spectrum. The K-band stellar spectrum also shows significant photospheric absorption features, as well as CO $\Delta v = 2$ bandheads in absorption. These bandheads appear to oscillate between absence, emission and absorption, depending upon the observing epoch. The lack of a veiling continuum, and the absence of CO bandheads in emission, suggests that DG Tau was in a low accretion rate phase during this observation epoch. This is consistent with our observation epoch being between periodic outflow episodes.

Two regions of extended emission were detected about the central star, on opposing sides of the circumstellar disc. Three distinct emission components were observed in the blueshifted, or approaching, outflow, out to a distance of $1\farcs5$ from the central star:

High-velocity jet. A high-velocity, well-collimated central jet is seen as the high-velocity component (HVC) of [Fe II] 1.644 μm line emission. A stationary emission knot is observed at the base of the outflow, $\sim 0\farcs2$ from the central star. We interpret this feature as a jet recollimation shock, based on comparison with X-ray (Güdel et al. 2005, 2008, 2011; Schneider & Schmitt 2008; Günther et al. 2009) and FUV (Schneider et al. 2013a) observations. The entire jet shocks to a temperature of $\sim 10^6$ K, but only a small region of this shock emits strongly in X-rays (Bonito et al. 2011). The jet material then cools as it flows downstream. Using the pre-shock flow velocity inferred from X-ray observations of $\sim$ 400–700 km s^{-1}, we calculate that the innermost streamlines of the jet are launched from a radius of 0.01–0.15 AU from the central star, assuming an MHD disc wind. This range of launch radii could correspond to either a disc wind or an X-wind. The post-recollimation-shock jet is seen as the HVC of [Fe II] emission, having been decelerated to $\lesssim 215$ km s^{-1}. The jet follows a non-linear path in the NIFS field, and changes in both velocity and diameter along its length. After accounting for the wandering jet trajectory, we find no evidence of rotation in the jet, which is consistent with the effects of passage through a strong recollimation shock.

Two moving jet knots are detected, and labelled knots B and C. Knot B is seen to move at $0\farcs17 \pm 0\farcs01$ yr^{-1}, much slower than previously observed knots in the DG Tau jet. Knot C is only observed in our 2005 epoch data, and hence we are unable to reliably constrain the proper motion and launch date of that feature. Our data suggest that the interval between knot ejections is non-periodic, and the velocity of the ejected knot varies between ejection events. The jet velocity increases from

215 km s^{-1} to 315 km s^{-1} deprojected between the moving knots, which after the elimination of alternative explanations we interpret to be the result of intrinsic jet velocity variations. These velocity variations are likely the cause of the formation of the moving knots.

Entrainment region. A second outflow component in [Fe II] 1.644 μm emission was separated from the jet emission, using a multicomponent Gaussian line fitting routine based on the statistical F-test. This intermediate-velocity component (IVC) takes the appearance of a wider-angle flow. Comparison to the molecular wind detected in the K-band (see below), as well as consideration of the excitation method of the forbidden [Fe II] lines, suggests that this component represents a shocking, turbulent entrainment layer between the central jet and the wide-angle molecular wind. A magnetic field of with a strength of $\lesssim$ a few mG allows for entrainment to occur by destabilizing the jet-wind interface, although careful analysis of the effects of field orientation is required. The presence of lateral entrainment in a YSO outflow provides an interesting alternative driving mechanism for large-scale CO outflows in younger-type YSOs. An analytical model of this entrainment will be presented in a future paper (§3).

Molecular outflow. Wide-angle H_2 1-0 S(1) 2.1218 μm emission was observed on the near side of the DG Tau circumstellar disc, as reported by Beck et al. (2008). Line velocity mapping of this emission indicates that it is most likely due to a wide-angle molecular wind, which agrees with the conclusions of Beck et al. and Agra-Amboage et al. (2014).

A receding outflow was detected on the far side of the DG Tau circumstellar disc. This disc obscures our view of this outflow out to $\sim 0\farcs7$ from the central star, corresponding to an outer disc radius of $\sim$ 160 AU. The redshifted outflow takes the form of a bubble-like structure in [Fe II] 1.644 μm line emission. There is tentative evidence for the presence of an underlying jet, although this cannot be confirmed without further data from later epochs. We will discuss the nature of this structure in a future paper (§4).

Many of the above conclusions depend on time-varying mechanisms. Further multi-epoch data are therefore required in order to validate these findings. In particular, confirmation of the knot launch period and proper motions requires multi-epoch data taken in the same fashion. It is also of interest to see how the velocity differences across the jet evolve with time, and if any trend attributable to rotation can be identified. Multi-epoch data will also help to settle the question of whether the mass flux and kinetic power of the approaching jet are constant or time-varying. In the future, the advent of 30 m-class telescopes such as GMT will allow for a finer cross-jet sampling, which is necessary to detect complex velocity structures within the jet.

Acknowledgements

Based on observations obtained at the Gemini Observatory, which is operated by the Association of Universities for Research in Astronomy, Inc., under a cooperative agreement with the NSF on behalf of the Gemini partnership: the National Science Foundation (United States), the National Research Council (Canada), CONICYT (Chile), the Australian Research Council (Australia), Ministério da Ciência, Tecnologia e Inovação (Brazil) and Ministerio de Ciencia, Tecnología e Innovación Productiva (Argentina).

We are extremely grateful for the support of the NIFS teams at the Australian National University, Auspace, and Gemini Observatory for their tireless efforts during the instrument integration, commissioning and system verification: Jan Van Harmleen, Peter Young, Mark Jarnyk (deceased), Nick Porecki, Richard Gronke, Robert Boss, Brian Walls, Gelys Trancho, Inseok Song, Chris Carter, Peter Groskowski, Tatiana Paz, John White, and James Patao.

We thank the anonymous referee for their detailed comments. MW acknowledges the generous travel support from Academia Sinica to attend the conference Star Formation Through Spectroimaging at High Angular Resolution in July 2011, which provided useful information for this study. This work was supported by the Australian Research Council through Discovery Project Grant DP120101792 (R. Salmeron).

CHAPTER 3

Turbulent Mixing Layers in Supersonic Protostellar Outflows

This chapter has been submitted to The Monthly Notices of the Royal Astronomical Society as **White, M. C., Bicknell, G. V., Salmeron, R., McGregor, P. J. *MNRAS*, *in review*, 2014b**, *referenced as White et al. (2014b), and is currently under review. This chapter is not modified from the submitted version, except in the following respects:*

- *Section, figure, footnote and table numbering, and general formatting, have been modified for consistency with the remainder of the thesis;*
- *References to White et al. (2014c) and White et al. (2014a) have been changed to point to Chapters 2 and 4 of this thesis respectively.*

The MAPPINGS IV shock models used in this chapter were computed by Dr Ralph Sutherland of The Research School of Astronomy and Astrophysics, The Australian National University. The text detailing the models (§3.3.1) was written by the candidate, based on notes provided by Dr Sutherland. The application of the results of these models to the mixing layer calculation in §3.3 was performed by the candidate.

Abstract

Turbulent entrainment processes may play an important role in the outflows from young stellar objects at all stages of their evolution. In particular, lateral entrainment of ambient material by high-velocity, well-collimated protostellar jets may be the cause of the multiple emission-line velocity components observed in the microjet-scale outflows driven by classical T Tauri stars. Intermediate-velocity outflow components may be emitted by a turbulent, shock-excited mixing layer along the boundaries of the jet. We present a formalism for describing such a mixing layer based on Reynolds decomposition of quantities measuring fundamental properties of the gas. In this model, the molecular wind from large disc radii provides a continual supply of material for entrainment. We calculate the total stress profile in the mixing layer, which allows us to estimate the dissipation of turbulent energy, and hence the luminosity of the layer. We utilize MAPPINGS IV shock models to determine the fraction of total emission that occurs in [Fe II] 1.644 μm line emission in order to facilitate comparison to previous observations of the young stellar object DG Tauri. Our model accurately estimates the luminosity and changes in mass outflow rate of the intermediate-velocity component of the DG Tau approaching outflow. Therefore, we propose that this component represents a turbulent mixing layer surrounding the well-collimated jet in this object. Finally, we compare and contrast our model to previous work in the field.

3.1. Introduction

Outflows are a near-universal component of young stellar objects (YSOs) throughout their evolution. They play a major role in star formation, and drive both the CO outflows seen in early-stage forming stars (e.g. Bachiller 1996; Reipurth & Bachiller 1997) and the Herbig-Haro flows emanating from more mature protostars (e.g. Reipurth & Bally 2001). These outflows are thought to be launched either from the protostellar surface (e.g. Ferreira et al. 2006), magnetocentrifugally from magnetic reconnection points near the circumstellar disc truncation radius (the X-wind and related models; Shu et al. 1994; Romanova et al. 2009) or from the disc surface at larger radii (disc winds; Blandford & Payne 1982; Pudritz & Norman 1983). In fact, more than one launch mechanism may be in operation (e.g. Larson 2003).

The advent of the *Hubble Space Telescope* and adaptive optics on ground-based telescopes has allowed the few hundred AU of protostellar outflows closest to the protostar to be studied. The outflows associated with optically-revealed T Tauri stars take the form of well-collimated 'microjets'. The study of these microjets is important because it is thought that they should not have interacted with the wider interstellar medium so close to the star (although interactions may occur if there is a remnant protostellar envelope, e.g. §4). If so,

such observations may provide information on the outflow before it significantly interacts with the ambient medium.

The small-scale outflows from YSOs typically show an onion-like kinematic structure in optical and near-infrared (NIR) forbidden lines, with a well-collimated, high-velocity jet surrounded by a less-collimated, intermediate-velocity component (e.g. §2; Hirth et al. 1997; Woitas et al. 2002; Pyo et al. 2003b; Coffey et al. 2008; Rodríguez-González et al. 2012; Caratti o Garatti et al. 2013). The nature of the high-velocity jets in many sources have been studied extensively, including searches for signs of jet rotation (§2.4.1.6; Bacciotti et al. 2000; Coffey et al. 2004, 2007), recollimation shocks (§2.4.1.2; Güdel et al. 2005, 2008; Günther et al. 2009; Bonito et al. 2011; Schneider et al. 2013a) and studies of the propagation of shock-excited moving knots (§2.4.1.1; Burrows et al. 1996; Reipurth et al. 2002; Pyo et al. 2003b; Agra-Amboage et al. 2011). The nature of the intermediate-velocity emitting material is still debated. Many authors attribute this emission to the presence of an intermediate-velocity disc-wind outflow component (e.g. Podio et al. 2011), which bridges the gap in launch radii between low-velocity ($\lesssim 50$ km s^{-1}) molecular winds (e.g. Takami et al. 2004; Beck et al. 2008; Agra-Amboage et al. 2014) and high-velocity (> 200 km s^{-1}) jets. However, such an explanation does not provide a natural mechanism for the generation of forbidden optical- and NIR-line emission, which is attributed to shock excitation (e.g. Nisini et al. 2002). It has yet to be explained how a steady-state intermediate-velocity disc wind would undergo shock excitation with relatively uniform intensity along the observable length of the feature.

It has been proposed that the intermediate-velocity forbidden-line emission components (IVCs) of small-scale protostellar outflows result from the lateral entrainment of ambient material, or a disc wind, by the high-velocity jet (e.g. Pyo et al. 2003b). This suggestion is based on the observation that in some objects, the spatial width of the intermediate-velocity component increases with distance from the central star. Entrainment would cause the formation of a turbulent mixing layer between the supersonic jet and the material surrounding it, which would become shock-excited and emit in forbidden lines (e.g. Binette et al. 1999). Such a layer naturally grows in thickness with distance along the jet, reproducing the observations of low- to intermediate-velocity forbidden-line emission components in protostellar outflows (e.g. Cantó & Raga 1991; Raga et al. 1995).

The entrainment explanation has fallen out of favour recently for two reasons. First, jet simulations show that the jet pushes the ambient medium aside as it is launched (López-Cámara & Raga 2010), preventing ambient material from interacting with the sides of the jet. However, as suggested by Pyo et al. (2003b) and White et al. (2014c), the presence of a wide-angle molecular wind surrounding the central jet could supply a constant reservoir of material for entrainment by the jet. Secondly, hypersonic jets, such as protostellar microjets, should not form lateral entrainment layers if they are regarded as high Mach number, purely hydrodynamic flows. The formation of turbulent mixing layers is driven by

the action of the Kelvin-Helmholtz (KH) instability at the jet-ambient material interface, and the growth rate of the KH instability decreases as the Mach number difference between the flows increases (Chernin et al. 1994; Trussoni 2008). However, protostellar jets are expected to exhibit strong toroidal magnetic fields (e.g. Zanni et al. 2007). The alignment of these fields with respect to the interface between the jet and the surrounding material, and their perpendicularity to the flow, may destabilise the interface to the KH instability (§2.4.2.2; Miura & Pritchett 1982; Ray & Ershkovich 1983). Therefore, entrainment remains an open possibility in protostellar jets. For a more detailed discussion of this argument, see §2.4.2.2.

Lateral entrainment in protostellar jets has been investigated analytically by Cantó & Raga (1991) and Raga et al. (1995). Their models provide useful predictions of mass entrainment rates and radiative luminosities associated with mixing layers. Their models involve an 'entrainment efficiency' parameter, which determines how effectively ambient material is drawn in to the mixing layer by the KH instability. They constrained this parameter using the results of laboratory jet experiments, which may not be applicable to protostellar jets (see §3.4.1). In this paper, we develop an alternative semi-empirical approach to radiative mixing layers, which relies solely upon directly observable quantities. In this way, we generate estimates for mixing layer bulk properties from our model based on the observed parameters of YSO outflow components, and compare them to observation.

This paper is organized as follows. In §3.2 we describe our model, which parametrizes the physical properties of the mixing layer using the observed layer growth rate. In §3.3, we first compute a grid of shock models to determine the ratio between the observable [Fe II] line emission of protostellar jet mixing layers, and the mixing layer bolometric luminosity estimated by our model. We then directly compare our model to the [Fe II] IVC of the approaching outflow from the YSO DG Tauri, and find that it is in excellent agreement with observations. §3.4 compares our model to the previous work of Cantó & Raga (1991) and Raga et al. (1995), and includes an estimation of the laminar jet length in DG Tau. We summarize our work in §3.5.

3.2. Model

We construct an analytical, semi-empirical model of a two-dimensional turbulent entrainment layer in oder to interpret the [Fe II] 1.644 μm IVC line emission observed in DG Tau. The model describes the turbulent mixing layer that forms between a high-velocity jet and a low-velocity wider-angle wind, and depends only upon directly observable quantities, removing the requirement to specify an 'entrainment efficiency' parameter (e.g. Cantó & Raga 1991; Raga et al. 1995). We use the observed spreading rate of the layer to calculate the dissipation of turbulent energy in the entrainment layer, and its resulting luminosity.

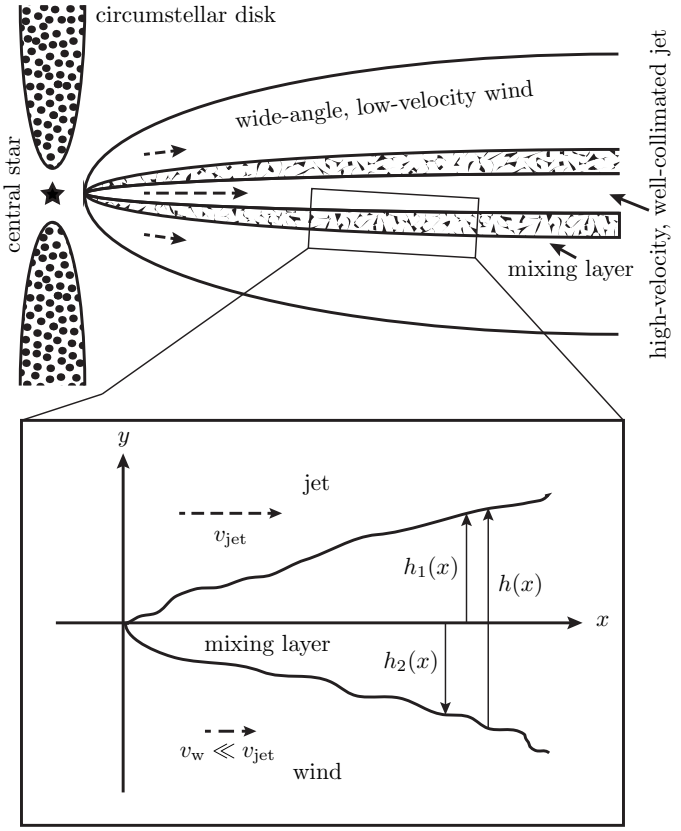

Figure 3.1 A representation of the model setup used throughout this paper. A high-velocity, well-collimated jet is launched from a protostar-circumstellar disc system. This jet is surrounded by a wider-angle disc wind (top panel). The interface between the jet and the wind is approximated by a two-dimensional turbulent shear layer (bottom panel). The x-axis of the model is placed where the jet-wind interface would lie in the absence of the mixing layer, and is parallel to the direction of the jet. Dashed arrows show the flow direction of the components. Model components are not to scale.

The first step in this process is the calculation of total turbulent stress, t_{xy}, in the mixing layer.

The model setup is shown in Fig. 3.1. A high-velocity jet with density $\rho_{\rm jet}$ propagates at velocity $v_{\rm jet}$ away from the star-disc system. The jet is surrounded by a wider-angle molecular wind, with density $\rho_{\rm w}$ and velocity $v_{\rm w} \ll v_{\rm jet}$. We henceforth refer to this wind as the 'ambient wind'. A turbulent mixing layer forms at the interface between the two flows, as a result of the KH instability. We approximate this interface with a two-dimensional model. In this model, the x-axis is defined as the unperturbed jet-wind boundary. This is the streamwise direction; the transverse coordinate is y. The mixing layer width, $h(x)$, increases monotonically with distance from the central star. We define the depth the mixing layer expands in to the jet as $h_1(x)$, and the depth it penetrates the ambient wind as $h_2(x)$, where $h_2(x) < 0$. Hence, $h(x) = h_1(x) - h_2(x)$.

An averaging prescription is used to describe the mean flow. We adopt the mass-weighted statistical averaging prescription of Favre (1969), which was introduced to the study of astrophysical flows by Bicknell (1984); see also Kuncic & Bicknell (2004). All time-varying quantities are decomposed in to an average component and a fluctuating component. Quantities such as pressure, p, density, ρ, and magnetic field, B, are expressed in terms of mean (bar) and fluctuating (primed) components, such that the time-average of the

fluctuating component (angle brackets) is zero:

$$p = \bar{p} + p' \quad \text{where } \langle p' \rangle = 0; \tag{3.1}$$

$$\rho = \bar{\rho} + \rho' \quad \text{where } \langle \rho' \rangle = 0; \text{ and} \tag{3.2}$$

$$B_i = \bar{B}_i + B'_i \text{ where } \langle B'_i \rangle = 0, \tag{3.3}$$

where subscript i and j represent generalized coordinates. As prescribed by Favre (1969), the velocity, v_i, is mass-weighted, and is expressed as

$$v_i = \tilde{v}_i + v'_i, \text{ where } \langle \rho v'_i \rangle = 0. \tag{3.4}$$

This approach has two advantages. First, mass is conserved in the mean flow (Favre 1969). Secondly, it prevents the generation of an excessive number of terms when the dynamical equations are statistically averaged; e.g. the mean value of the momentum flux is simply expressed as

$$\langle \rho v_i v_j \rangle = \bar{\rho} \tilde{v}_i \tilde{v}_j + \langle \rho v'_i v'_j \rangle. \tag{3.5}$$

This approach is common in fluid dynamics, and has been used in the theory of compressible turbulent jets and accretion discs (see Bicknell 1984; Kuncic & Bicknell 2004).

3.2.1. Characteristic Equations

Consider a magnetized fluid with density ρ, velocity v, pressure p, magnetic field $\boldsymbol{B}$, in a gravitational potential field $\phi_{\rm G}$. Averaging the mass continuity and momentum conservation equations of magnetohydrodynamics (§D.1) yields, for a quasi-steady state system,

$$\frac{\partial(\bar{\rho}\tilde{v}_x)}{\partial x} + \frac{\partial(\bar{\rho}\tilde{v}_y)}{\partial y} = 0, \text{ and} \tag{3.6}$$

$$\frac{\partial(\bar{\rho}\tilde{v}_i)}{\partial t} + \frac{\partial(\bar{\rho}\tilde{v}_i\tilde{v}_j)}{\partial x_j} = -\bar{\rho}\frac{\partial \phi_{\rm G}}{\partial x_i} - \frac{\partial \bar{p}}{\partial x_i} + \frac{\partial(t^R_{ij} + t^B_{ij})}{\partial x_j}. \tag{3.7}$$

The magnetic stress tensor is defined as

$$t^B_{ij} = \frac{\langle B'_i B'_j \rangle}{4\pi} - \delta_{ij}\frac{\langle B'^2 \rangle}{8\pi}, \tag{3.8}$$

assuming that the magnetic field is dominated by its turbulent component, so that $\bar{B}_i = 0$. We define the Reynolds stress tensor as

$$t^{\rm R}_{ij} = -\langle \rho v'_i v'_j \rangle \tag{3.9}$$

(Kuncic & Bicknell 2004). The total turbulent stress is

$$t_{ij} = t^{\rm R}_{ij} + t^B_{ij}. \tag{3.10}$$

The aim of our calculation is to estimate the mass entrainment rate and bolometric luminosity of the mixing layer, based on directly observed parameters. We consider the $i = x$ momentum equation, that is, the equation governing the streamwise evolution of momentum resulting from the lateral transfer of momentum within the mixing layer. We neglect the streamwise pressure, magnetic and gravitational gradients, so that

$$\frac{\partial(\bar{\rho}\tilde{v}_x^2)}{\partial x} + \frac{\partial(\bar{\rho}\tilde{v}_x\tilde{v}_y)}{\partial y} \equiv \bar{\rho}\tilde{v}_x\frac{\partial\tilde{v}_x}{\partial x} + \bar{\rho}\tilde{v}_y\frac{\partial\tilde{v}_x}{\partial y} = \frac{\partial t_{xy}}{\partial y}, \tag{3.11}$$

where $t_{xy} = t_{xy}^R + t_{xy}^B$ as in equation (3.10).

Finally, we define a pseudo self-similar variable in the transverse direction,

$$\xi(x,y) = \frac{y}{h(x)} \tag{3.12}$$

$$\Rightarrow \xi_1 = \frac{y_1(x)}{h(x)}, \text{ and } \xi_2(x) = \frac{y_2(x)}{h(x)}. \tag{3.13}$$

We note that $\xi_1 - \xi_2 = 1$. This allows us to specify the temperature, T, and streamwise velocity, $\tilde{v}_x$, in the mixing layer as a function of transverse position. As the simplest approximation, we prescribe linear velocity and temperature profiles across the layer:

$$v_x = U(\xi)v_j, \text{ and} \tag{3.14}$$

$$T = S(\xi)(T_\mathrm{j} - T_\mathrm{w}) + T_\mathrm{w}, \text{ where} \tag{3.15}$$

$$U(\xi) = S(\xi) = \xi - \xi_2 = \xi - \xi_1 + 1, \tag{3.16}$$

and T_jet and T_w are the temperatures of the jet and the ambient wind respectively.

3.2.2. Transverse Density, Velocity and Turbulent Stress Profiles

We assume pressure equilibrium across the mixing layer.[55] Let the jet-to-ambient wind density ratio be $\eta = \rho_\mathrm{j}/\rho_\mathrm{w}$. The density is given by

$$\bar{\rho} = \frac{\mu m}{kT}\bar{p}, \tag{3.17}$$

where k is the Boltzmann constant, m is the atomic mass unit, and μ is the molecular weight of the gas. It follows that the mixing layer density profile is given by

$$\bar{\rho}(\eta,\xi) = \frac{\rho_\mathrm{j}}{\eta + (1-\eta)S(\xi)}. \tag{3.18}$$

We now calculate the transverse velocity and turbulent stress profiles within the mixing layer. We transform equations (3.6) and (3.11) in to the (x,ξ) coordinate system. The

[55] In the case of DG Tau, the presence of a stationary recollimation shock in the jet channel (§2.4.1.2) indicates that the jet is in pressure equilibrium with its environs downstream of this shock.

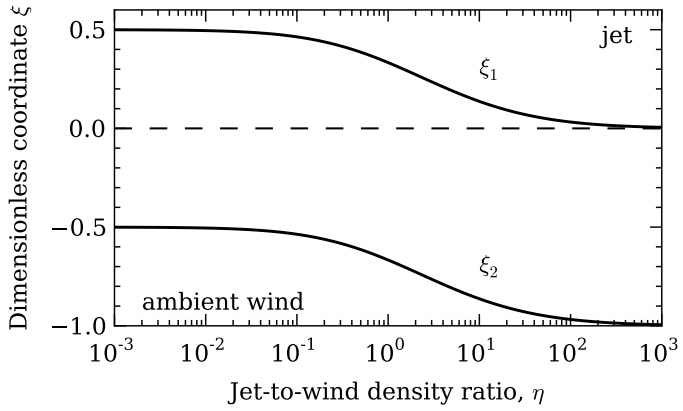

Figure 3.2 Position of the mixing layer boundaries with the jet (ξ_1) and with the ambient wind (ξ_2) as a function of the jet-to-wind density ratio, η. The position of the boundary between the jet and wind in the absence of a mixing layer is shown by the dashed line.

equation of continuity, equation (3.6), becomes

$$\frac{\partial(\bar{\rho}\tilde{v}_y)}{\partial\xi} = h'(x)\xi\frac{\partial\bar{\rho}\tilde{v}_x}{\partial\xi}. \tag{3.19}$$

We can calculate the tranverse velocity profile from this equation, after substituting in the density (equation 3.18) and streamwise velocity (equation 3.14) profiles. This gives:

$$\begin{aligned}\tilde{v}_y(\eta,x,\xi) = v_\mathrm{j}h'(x)\left[\eta+(1-\eta)S(\xi)\right] \\ \times\int_{\xi_1}^{\xi}\xi'\frac{\mathrm{d}}{\mathrm{d}\xi'}\left[\frac{U(\xi')}{\eta+(1-\eta)S(\xi')}\right]\mathrm{d}\xi'.\end{aligned} \tag{3.20}$$

The integral factor in equation (3.20) occurs in many of the subsequent expressions, and we define it as $\mathcal{D}(\eta,\xi)$. This factor has a closed-form solution (§D.2) after imposing the boundary condition $\tilde{v}_y(\xi_1) = 0$, so the transverse velocity varies smoothly from $v_y = 0$ in the jet in to the mixing layer. This is a reasonable boundary condition, because the supersonic jet will approach the mixing layer boundary so quickly that it will not be substantially deflected by turbulence prior to impacting the mixing layer.

Following transformation in to the (x,ξ) coordinate system, the equation of downstream momentum conservation, equation (3.11), can be rearranged to provide an equation for the turbulent stress:

$$\frac{\partial\langle t_{xy}\rangle}{\partial\xi} = \rho_\mathrm{j}v_j^2h'(x)\left(\frac{-(\xi-\xi_1+1)\xi}{\eta+(1-\eta)(\xi-\xi_1+1)}+\mathcal{D}(\eta,\xi)\right). \tag{3.21}$$

Integration of equation (3.21) gives:

$$t_{xy}(\eta,x,\xi) = \rho_\mathrm{j}v_j^2h'(x)\mathcal{F}(\eta,\xi), \tag{3.22}$$

where the function $\mathcal{F}(\eta,\xi)$ is given in §D.2. We set $t_{xy}(\xi_1) = t_{xy}(\xi_2) = 0$ since we expect the turbulence to be confined primarily to the region $\xi_2 < \xi < \xi_1$. The condition $t_{xy}(\xi_1) = 0$ is used to compute the form of $\mathcal{F}(\eta,\xi)$ (§D.2); the condition $t_{xy}(\xi_2) = 0$, and hence

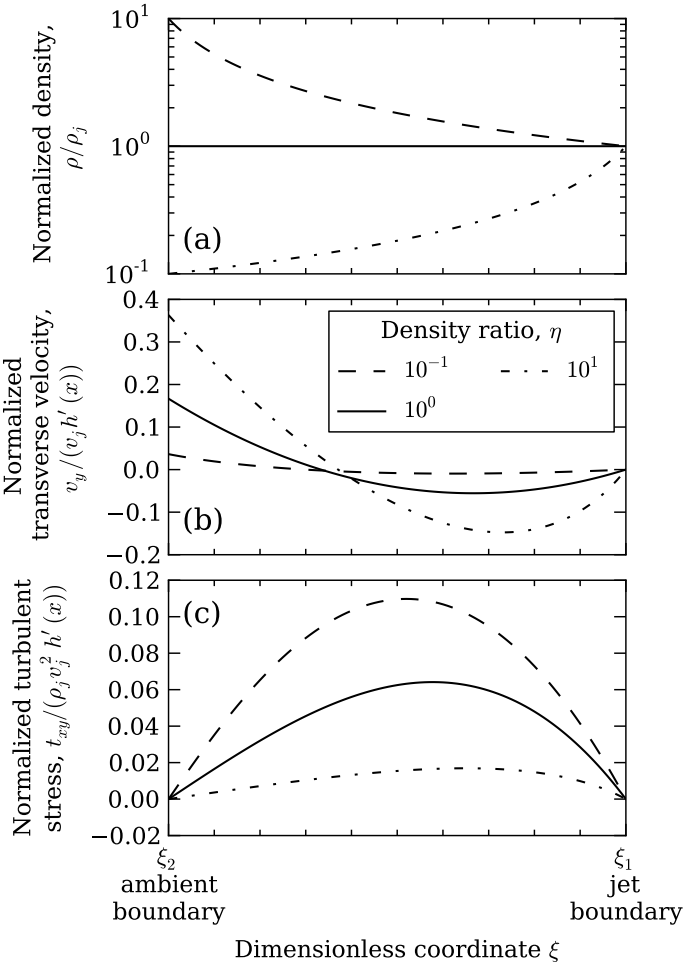

Figure 3.3 Normalized (a) density, (b) transverse velocity and (c) turbulent stress profiles for the mixing layer described by this model. The profiles are plotted between the mixing layer boundaries ξ_2 and ξ_1. The numerical values that these boundaries take are different for different jet-to-wind density ratios η, as per equation (3.23) and Fig. 3.2.

$\mathcal{F}(\xi_2, \eta) = 0$, allows us to calculate the position of the jet-mixing layer boundary, ξ_1, in (x, ξ)-space as a function of only the jet-to-wind density ratio η:

$$\begin{aligned} \xi_1(\eta) &= \frac{2\eta^2 \log(\eta) + (4 - 3\eta)\eta - 1}{2(\eta - 1)^3} \quad \text{for } \eta \neq 1, \text{ and} \\ &= \frac{1}{3} \qquad\qquad\qquad\qquad\quad \text{for } \eta = 1. \end{aligned} \tag{3.23}$$

The position of the mixing layer boundaries as a function of η is shown in Fig. 3.2. In the limit of a significantly underdense jet ($\eta \to 0$), the mixing layer penetrates the jet and wind evenly. In the limit of a significantly overdense jet ($\eta \to \infty$), the mixing layer almost exclusively penetrates the ambient wind.

Knowledge of the position of the mixing layer boundaries allows the forms of the transverse velocity and turbulent stress profiles to be directly calculated as a function of position within the mixing layer, ξ, and the jet-to-wind density ratio, η. The forms of these expressions are algebraically complex, and are given in §D.3. The mixing layer density, transverse velocity and turbulent stress profiles are shown in Fig. 3.3.

As seen in Fig. 3.3(b), ambient wind material is pulled upwards in to the mixing layer at

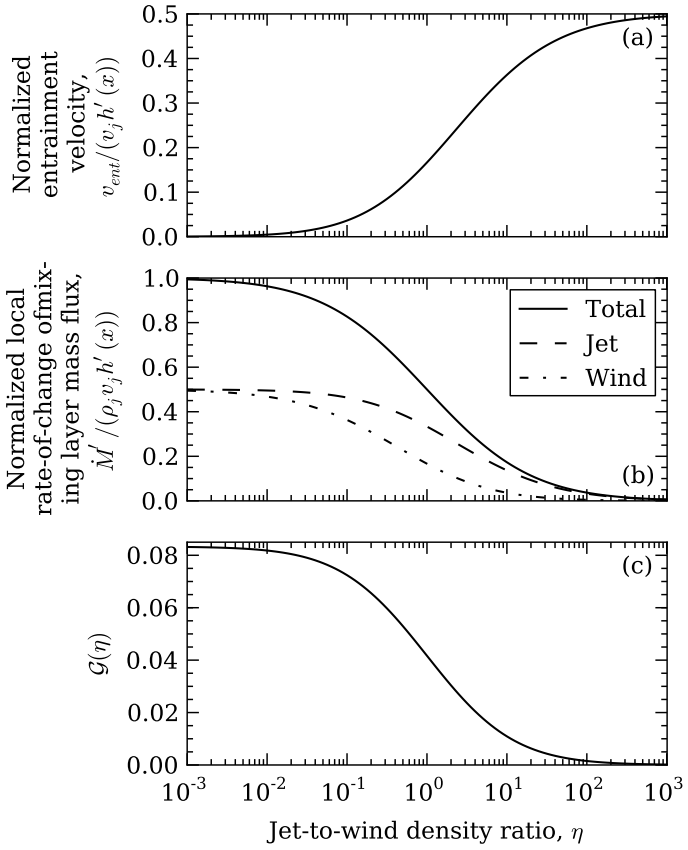

Figure 3.4 Mixing layer parameters which only depend on the jet-to-ambient-wind density ratio, η. (a) Normalized entrainment velocity from the ambient wind, from equation (3.25). (b) Normalized rate-of-change of the mixing layer mass flux, $\dot{M}'$. The contribution to the rate-of-change of the mixing layer mass flux from jet interception and wind entrainment ($\dot{M}'_{\rm ent}$) is shown by the dashed and dot-dashed curves, respectively. (c) Dimensionless function $\mathcal{G}(\eta)$, for the determination of the rate of turbulent energy production per unit area, from equation (3.35).

the wind-mixing layer boundary (ξ_2) with an effective entrainment velocity,

$$v_{\rm ent} = \tilde{v}_y(\eta, x, \xi_2) \tag{3.24}$$

$$= v_{\rm j} h'(x) \frac{\eta(\eta^2 - 2\eta\log(\eta) - 1)}{2(\eta-1)^3} \quad \text{for } \eta \neq 1, \text{ and}$$

$$= \frac{1}{6} \quad \text{for } \eta = 1. \tag{3.25}$$

This is equivalent to the entrainment velocity specified in the models of Cantó & Raga (1991) and Raga et al. (1995). However, it occurs naturally as a result of the boundary conditions of the problem, rather than being specified by an experimentally-determined 'entrainment efficiency' parameter. We compare the entrainment velocity of our model to the earlier work in §§3.3.3.3 and 3.4.1. The normalized entrainment velocity, $v_y/(v_{\rm j}h'(x))$, is plotted as a function of η in Fig. 3.4(a).

3.2.3. Mass Flux and Entrainment Rate

We define the mixing layer mass flux to be

$$\dot{M}(x) \equiv \int_{\xi_2}^{\xi_1} \rho(\xi) v_{\rm j} U(\xi) h(x)\, {\rm d}\xi. \tag{3.26}$$

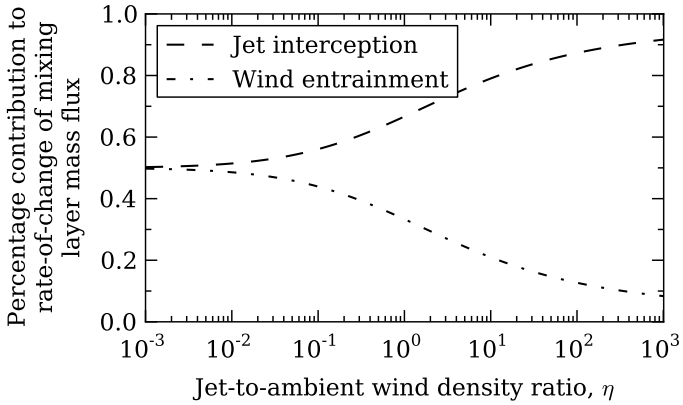

Figure 3.5 Percentage contribution to the rate-of-change of mixing layer mass flux from jet interception (dashed curve) and ambient wind entrainment ($\dot{M}'_{\rm ent}$, dot-dashed curve) as a function of jet-to-ambient-wind density ratio η.

The contribution to the mass flux from intercepted jet material is simply given by

$$\dot{M}_{\rm j}(x) = \rho_{\rm j} v_{\rm j} h(x) \xi_1(\eta). \tag{3.27}$$

(cf. Raga et al. 1995). Therefore, the entrained mass flux is

$$\dot{M}_{\rm ent}(x) \equiv \int_{\xi_2}^{\xi_1} \rho(\xi) v_{\rm j} U(\xi) h(x)\, {\rm d}\xi - \rho_{\rm j} v_{\rm j} h_1(x) \xi_1(\eta). \tag{3.28}$$

The mass entrainment rate from the ambient wind is simply the derivative of equation (3.28) with respect to x. It can be shown (§D.4) that

$$\frac{\partial \dot{M}_{\rm ent}}{\partial x} \equiv \dot{M}'_{\rm ent} = \rho_{\rm w} v_{\rm ent}, \tag{3.29}$$

as expected, since ambient wind material is being drawn in to the mixing layer with velocity $v_{\rm ent}$ (§3.2.2).

The rate-of-change of the mixing layer mass flux, $\partial \dot{M}/\partial x \equiv \dot{M}'$, is shown in Fig. 3.4(b). The contribution of wind entrainment to the mass flux of the mixing layer is greatest for an underdense jet (Fig. 3.5).

3.2.4. Turbulent Energy Production

The ultimate aim of this model is to determine the rate of turbulent energy production and subsequent dissipation and radiation in the mixing layer. The rate of turbulent energy production, $\dot{E}_{\rm turb} = 2 t_{xy} s_{xy}$, where s_{xy} is the shear in the mixing layer (Kuncic & Bicknell 2004). The mean shear may be calculated from

$$s_{xy} = \frac{1}{2}\left(\frac{\partial \tilde{v}_x}{\partial y} + \frac{\partial \tilde{v}_y}{\partial x}\right) \approx \frac{1}{2}\frac{\partial \tilde{v}_x}{\partial y} \tag{3.30}$$

since the average transverse velocity, $\tilde{v}_y$, varies slowly with respect to x.

The rate of turbulent energy production in the mixing layer is directly comparable to the observed luminosity of the mixing layer, assuming that the cooling time of the gas is short, so that the turbulent energy produced is radiated efficiently. This is a reasonable assumption in DG Tau; based on a gas temperature of 10^4 K and using the cooling function of Sutherland & Dopita (1993), we determine a cooling time for the IVC of 2.5 yr, which results in a cooling length ~ 60 AU $\approx 0\farcs26$ projected distance for a flow speed of 110 km s^{-1}. This cooling length is short compared to the length of the mixing layer, which is $\gtrsim 270$ AU (§3.3.3.1).

We now calculate the rate of turbulent energy production at a given point in the mixing layer:

$$\begin{aligned}\dot{E}_{\rm turb}(x,\xi) &= t_{xy}(x,\xi)\frac{\partial \tilde{v}_x}{\partial y} \\ &= t_{xy}(x,\xi)\frac{v_{\rm j}}{h(x)} && (3.31)\\ &= \rho_{\rm j} v_j^3 \frac{h'(x)}{h(x)}\mathcal{F}(\eta,\xi). && (3.32)\end{aligned}$$

We integrate over y to form an expression for the turbulent energy produced per unit area:

$$\begin{aligned}\frac{\dot{E}_{\rm turb}}{A}(x) &= \int_{y_2}^{y_1} \dot{E}_{\rm turb}\,{\rm d}y && (3.33)\\ &= \rho_j v_j^3 h'(x)\mathcal{G}(\eta), \text{ where} && (3.34)\\ \mathcal{G}(\eta) &= \frac{2\eta^3+3\eta^2-6\eta^2\log(\eta)-6\eta+1}{12(\eta-1)^4} \text{ for } \eta\neq 1, \text{ and} \\ &= \frac{1}{24} \qquad\qquad \text{for } \eta = 1. && (3.35)\end{aligned}$$

For the purpose of comparing this model to observations of three-dimensional protostellar jet mixing layers, this is the turbulent energy produced per unit circumference per unit length. Therefore, total turbulent energy production in the layer is calculated multiplying equation (3.34) by $2\pi R_{\rm mix}(x)$, where $R_{\rm mix}(x)$ is the mixing layer radius, and then integrating over the observed mixing layer length, L:

$$\begin{aligned}\dot{E}_{\rm tot} &= \int_0^L 2\pi R_{\rm mix}(x)\rho_{\rm j} v_{\rm j}^3 h'(x)\mathcal{G}(\eta)\,{\rm d}x && (3.36)\\ &= 2\pi R_{\rm mix} L \rho_{\rm j} v_{\rm j}^3 h'(x)\mathcal{G}(\eta), && (3.37)\end{aligned}$$

assuming that $R_{\rm mix}$ and $h'(x)$ are independent of x.

Table 3.1 MAPPINGS IV shock model initial parameters.

Pre-shock condition	Value	
Electron number density	1.09	cm^{-3}
Hydrogen number density	1.0×10^{3}	cm^{-3}
Density	2.27×10^{-21}	g cm^{-3}
Pressure	1.5×10^{-10}	dyne cm^{-2}
Temperature	1.0×10^{3}	K
Magnetic field	61.4	μG
Magnetic pressure	1.5×10^{-10}	dyne cm^{-2}

3.3. Comparison to Observations

3.3.1. [Fe II] 1.644 μm Shock Modelling

Our model provides estimates for the bolometric luminosity of a protostellar outflow mixing layer (§3.3.3.1). However, observations of these outflows are typically made using specific optical and NIR emission lines. Therefore, to compare with observations, we estimate the [Fe II] line luminosities for a given total luminosity. To this end, a grid of shock models capable of heating their post-shock gas to between 2×10^4 and 6×10^4 K were computed using the MAPPINGS IV code (Sutherland & Dopita 1993; Allen et al. 2008; Nicholls et al. 2013), assuming solar abundances (Grevesse et al. 2010). We use this grid as a representative model of partially-ionized gas being heated and subsequently cooling; we are not concerned with the shock structure itself. Therefore, we chose pre-shock gas parameters, detailed in Table 3.1, that yield densities and temperatures in the post-shock region that are comparable to those expected in the mixing layer. These pre-shock parameters are not intended to be representative of protostellar outflows, nor do we imply that the IVC emission is generated in a single flat-planar shock structure, which would not be a good approximation to the shocks occurring in a turbulent mixing layer.

The shocks were driven in to a pre-shock medium that is 99.9 per cent neutral in all atomic species, in equipartition magnetic to thermal pressure. In the first grid of models, the gas phase abundance of iron was taken to be undepleted at solar values, [Fe] = -4.50. In the second grid, the gas phase abundances were depleted by a factor of 100, [Fe] = -6.50, to allow for iron incorporation in to dust grains. Iron gas phase depletion factors between 10-100 have been widely inferred for astrophysical plasmas (Field 1974; Jenkins 2009, and references therein). Here, without a detailed model of how dust is launched with or formed within YSO outflows, we use a range of depletion factors, from no depletion to a factor of 100.

In each MAPPINGS model, the final [Fe II] 1.644 μm line emission from the shock is

expressed as a fraction of the total of all the line emission plus the two-photon emission, which can be a large contributor to total emission in these heated, partially-ionized models. For each initial post-shock temperature, T, and magnetic field, B, a velocity was found, and then used to compute the properties of the post-shock, cooling gas.

The [Fe II] total emission affects the model structure, so that the [Fe II] 1.644 μm luminosity does not simply scale with the gas phase abundance of iron, but nearly so. The cooling fraction in [Fe II] 1.644 μm with undepleted gas is between 5.5×10^{-3} and 8.0×10^{-3}, and between 8×10^{-5} and 1.2×10^{-4} for the depleted models, but mostly a more or less constant 1.1×10^{-4} (Table 3.2). It is therefore reasonable that the [Fe II] 1.644 μm line emission as a fraction of total cooling emission lies between 10^{-2} and 10^{-4} for a range of iron depletion factors. We parametrize the ratio between bolometric luminosity, $\mathcal{L}_{\rm tot}$, and [Fe II] 1.644 μm luminosity, $\mathcal{L}_{1.644}$, as[56]

$$\mathcal{L}_{1.644} = \left(\frac{10^{-2}}{\text{Fe depletion factor}} \right) \times \mathcal{L}_{\rm tot}. \tag{3.38}$$

3.3.2. Parameters of the DG Tau Outflow

We summarize the parameters of the DG Tau jet required as inputs to our model here. The main parameters are the jet density, $\rho_{\rm j}$ (§3.3.2.1); the jet velocity, $v_{\rm j}$ (§3.3.2.2); the mixing layer growth rate, $h'(x)$ (§3.3.2.3); the mixing layer length, L (§3.3.2.3); and the jet-to-ambient-wind density ratio, η (§3.3.2.4). To utilize our MAPPINGS IV models, we also need to know the iron depletion factor in the DG Tau IVC (§3.3.2.5).

3.3.2.1. Jet Density

The electron density may be determined from NIR observations through the ratio of the [Fe II] emission lines at 1.533 μm and 1.644 μm. Pesenti et al. (2003) computed a relationship between this line ratio and electron density for a 16-level model of an Fe^+ atom. The similar BE99 technique makes use of the ratio of the [S II] emission lines at 6731 Å and 6716 Å in the optical regime (Bacciotti & Eislöffel 1999; Maurri et al. 2014). These techniques have been applied to the DG Tau jet (§2.3.5; Bacciotti et al. 2000; Agra-Amboage et al. 2011; Maurri et al. 2014), yielding an typical electron density $n_{\rm e} \sim 10^4$ cm^{-3}. Maurri et al. (2014) reported higher electron densities, up to 10^6 cm^{-3}, close to the central star. However, we do not observe significant IVC emission at this position (§2, Fig. 2.6), so that we use the lower jet density corresponding to the region where we observe a mixing layer.

Our model requires the jet *mass* density as an input. We convert the measured electron density in to physical density as in §2.4.1.4. The hydrogen density is calculated from

[56] Note that zero depletion corresponds to a depletion factor of 1.

Table 3.2 Post-shock conditions and emission from MAPPINGS IV models.

		Solar abundance			Factor 100 iron depletion		
Temperature (K)	Velocity (km s^{-1})	Total line emission[a]	[Fe II] 1.644 μm emission[a]	[Fe II] 1.644 μm fraction	Total line emission[a]	[Fe II] 1.644 μm emission[a]	[Fe II] 1.644 μm fraction
2×10^4	25.9	2653.69	16.62	5.5×10^{-3}	2546.06	0.211	8.3×10^{-5}
3×10^4	32.1	997.74	8.02	8.0×10^{-3}	957.01	0.113	1.2×10^{-4}
4×10^4	37.2	661.93	5.25	7.9×10^{-3}	629.91	0.078	1.2×10^{-4}
5×10^4	41.6	552.70	4.01	7.3×10^{-3}	524.69	0.063	1.2×10^{-4}
6×10^4	45.7	478.77	3.16	6.6×10^{-3}	456.52	0.053	1.2×10^{-4}

[a] Expressed as a multiple of the H β emission produced.

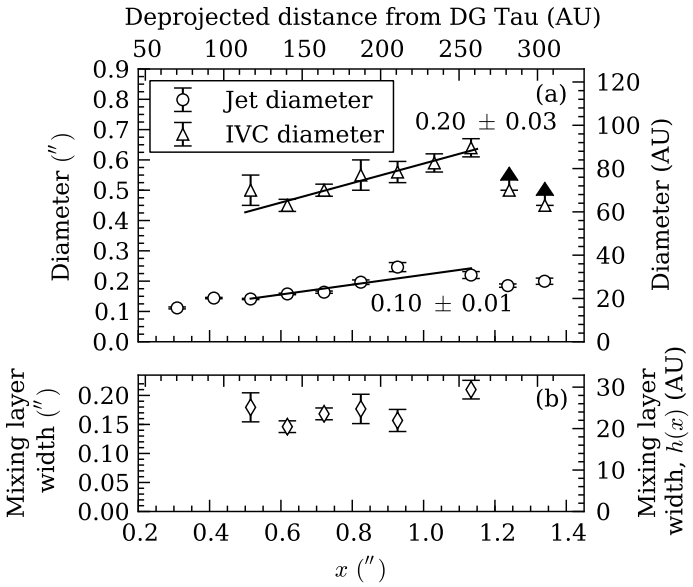

Figure 3.6 Growth rates of the diameter of the approaching DG Tau outflow components. (a) Diameter of the approaching jet (circles) and IVC (triangles) as a function of distance from the central star. Jet diameters were measured using cross-jet Gaussian fits to the high-velocity component intensity of [Fe II] 1.644 μm, and are approximately deconvolved from the PSF (§2.4.1.4). IVC diameters were measured from direct inspection of images and cross-outflow intensity profiles of the [Fe II] 1.644 μm intermediate-velocity component. Linear fits to the growth of both components over the region 0.″5–1.″1 from the central star are shown as solid lines; the labels indicate the slope of the line (i.e. the growth rate of the component diameter). (b) Inferred mixing layer widths over the region 0.″5–1.″1 from the central star, as per equation (3.39).

$n_{\rm H} = n_{\rm e}/\chi_{\rm e}$, where $\chi_{\rm e}$ is the ionization fraction of the gas. Although the ionization fraction of the jet appears to vary with position (Maurri et al. 2014), an average ionization fraction of $\chi_e = 0.3 \pm 0.1$ is a reasonable approximation (Bacciotti et al. 2000). This yields a hydrogen number density $n_{\rm H} = 3.3 \times 10^4$ cm^{-3}. The mass density $\rho = 1.4 m n_{\rm H}$ for a gas consisting of 90 per cent hydrogen and 10 per cent helium, where m is the atomic mass unit. This calculation leads to a jet mass density $\sim 10^{-19}$ g cm^{-3}, which we use as a fiducial value for our model.

3.3.2.2. Jet Velocity

The velocity of the DG Tau jet varies with time (§2.4.1.4; Bacciotti et al. 2002; Pyo et al. 2003b; Agra-Amboage et al. 2011), and this is the likely cause of the observed moving shock-excited knots (e.g. Raga et al. 1990). The jet velocity is typically measured from the high-velocity peak of line emission (Pyo et al. 2003b; Agra-Amboage et al. 2011). More recently, we used multicomponent Gaussian fitting, coupled with a statistical F-test, to rigorously separate the two [Fe II] 1.644 μm line-emission components in the approaching DG Tau outflow (§2.3.4). These fits show that the high-velocity component of the outflow has a range of velocities from 215–315 km s^{-1} in the 2005 observing epoch (§2.4.1.4). Therefore, we adopt an average jet velocity of 265 km s^{-1} for use in our model.

3.3.2.3. Mixing Layer Length and Growth Rate

The deprojected length of the observed mixing layer, 1.″2 $\approx$ 270 AU, can be directly measured from our data (Fig. 2.6). The separation of the line emission from the two

approaching outflow components allows for the calculation of the mixing layer growth rate. The diameter of the HVC (jet), $D_{\rm jet}$, was determined by fitting a Gaussian to the [Fe II] 1.644 μm line emission in the cross-jet direction, and approximately deconvolving the width of this Gaussian from the PSF via the formula $D^2_{\rm jet} = {\rm FWHM}^2_{\rm obs} - {\rm FWHM}^2_{\rm PSF}$ (§2.4.1.4). The diameter of the IVC, $D_{\rm IVC}$, was measured from both an image of that component (Fig. 2.6d) and cross-outflow [Fe II] 1.644 μm IVC profiles at each downstream position. IVC diameters could not be reliably determined beyond $\sim 1''$ from the central star, due to incomplete line fitting coverage in this region, although conservative lower limits could be inferred. The component diameters are shown as a function of downstream position in Fig. 3.6(a). The inferred mixing layer width is simply the difference between the observed *radii*, $r_{\rm jet}$ and $r_{\rm IVC}$, of the jet and IVC,

$$h(x) = r_{\rm IVC} - r_{\rm jet} = \frac{D_{\rm IVC} - D_{\rm jet}}{2}. \tag{3.39}$$

The growth rate of the mixing layer is then

$$h'(x) = (D'_{\rm IVC} - D'_{\rm jet})/2. \tag{3.40}$$

We determine the growth rate of the mixing layer as follows. We construct linear fits to the lateral growth of both the jet and IVC in the approaching DG Tau outflow in the 2005 observing epoch over the region $0\farcs5$–$1\farcs1$ from the central star (Fig. 3.6a).[57] These fits give growth rates of $D'_{\rm IVC} = 0.20 \pm 0.03$, and $D'_{\rm jet} = 0.10 \pm 0.01$. From equation (3.40), the measured growth rates imply a mixing layer growth rate of 0.05 ± 0.02.

The inferred mixing layer width as a function of distance from the central star is shown in Fig. 3.6(b). This is a noisier profile than the individual jet diameters; therefore, it is preferable to determine $h'(x)$ from equation (3.40).

3.3.2.4. Jet-to-Ambient Wind Density Ratio

The density of the jet is well-defined (see §3.3.2.1). In order to estimate the jet-to-ambient-wind ratio, we make approximations to the density of the wider-angle molecular wind in DG Tau, based on the results of Takami et al. (2004). They reported a flow that extended 40 AU along the outflow axis following deprojection, and 80 AU across the outflow direction, resulting in a total wind opening angle of 90°. By considering the K-band extinction towards DG Tau, and the ratio of H_2 1-0 S(1) 2.1218 μm emitting mass to total H_2 mass, they determined a minimum total wind mass in this region of 2.1×10^{-8} $M_\odot$. This corresponds to a minimum average wind H_2 number density of 4×10^4 cm^{-3}, assuming a

[57] The fits were made using the deprojected distance from the central star and the physical diameter of each outflow component, thereby accounting for the projection of the DG Tau outflows to the line-of-sight (38°; Eislöffel & Mundt 1998).

filling factor of 1 and a conical geometry.

We now make approximations about the flow geometry of this wind in order to determine its density in the entrainment region of the outflow. Consider a distance $0\farcs8 \approx 180$ AU from the central star, which is halfway along the observed mixing layer. If the wind undergoes no further collimation beyond what is observed in H_2 emission, and maintains a conical geometry, it will have a total width of 360 AU at this position. Assuming a constant wind mass-loss rate, $\dot{M}$, and wind velocity, v, the wind density, ρ, is inversely proportional to the wind radius, R, squared:

$$\dot{M} = \rho\pi R^2 v = \text{const.} \Rightarrow \frac{\rho_2}{\rho_1} = \frac{R_1^2}{R_2^2}. \tag{3.41}$$

Therefore, an increase in wind radius of a factor 4.5 would mean a decrease in wind density of a factor of ~ 20, resulting in an H_2 number density by $\sim 2 \times 10^3$ cm^{-3} at 360 AU from the central star. Assuming a gas composition of 90 per cent hydrogen and 10 per cent helium by number density, this results in a mass density of 8.2×10^{-21} g cm^{-3}, and a jet-to-ambient-wind density ratio of 12.2.

Takami et al. (2004) notes that their estimates of H_2 mass and density in the wider-angle wind are lower limits, given that cold gas may be present in the outflow, and the filling factor of the wind may be less than unity. Hence, our estimate of the jet-to-ambient wind density ratio represents an upper limit to possible values for this parameter. Therefore, whilst we consider it likely that η lies between 1 and 10, we have investigated a parameter range of $0.1 \leq \eta \leq 10$ for completeness.

3.3.2.5. Iron Depletion

The iron depletion in the approaching outflow components from DG Tau was measured by Agra-Amboage et al. (2011) via comparison of [Fe II] 1.644 μm flux to the [O I] 6300 Å fluxes reported by Lavalley-Fouquet et al. (2000). Through comparison with shock wave models (Hartigan et al. 2004), they determined that the iron depletion factor in the approaching DG Tau outflow is $\sim$ 3–4 in gas faster than -100 km s^{-1} (the jet), and $\sim$ 10–12 for gas at speeds below -100 km s^{-1} (the IVC).

Agra-Amboage et al. (2011) noted that their measurements are tentative, given that they were required to compare [Fe II] and [O I] line fluxes obtained ~ 8 yr apart. Furthermore, it is unlikely that the DG Tau jet would exhibit any iron depletion, as we would expect dust grains to be destroyed by passage through the strong recollimation shock at the base of the approaching outflow (§2.4.1.2). However, it is reasonable that the slower, wider-angle outflow components would exhibit iron depletion, as they are launched from wider disc radii and may be less shock-processed (Agra-Amboage et al. 2011). Indeed, higher depletion at lower flow velocities has been observed in other YSOs (e.g. calcium in the HH 111

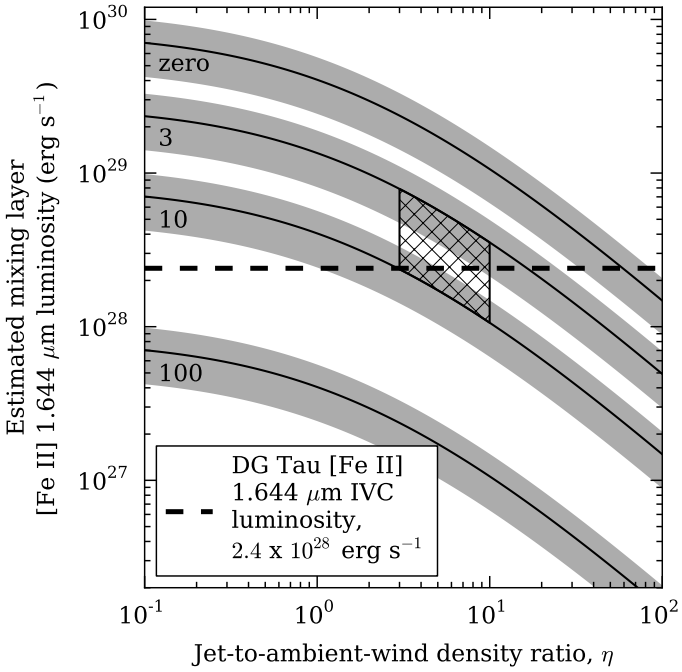

Figure 3.7 Estimates of the DG Tau mixing layer [Fe II] 1.644 μm luminosity, from equations (3.38) and (3.42). Luminosities are calculated for a range of iron depletion factors and jet-to-ambient-wind density ratios, assuming a jet velocity of 265 km s^{-1} and a jet density of 1.0×10^{-19} g cm^{-3}. Solid curves show the estimated luminosity for $h'(x) = 0.05$; the surrounding greyed regions indicate the range of luminosities at a given iron depletion factor for $0.03 \leq h'(x) \leq 0.07$ (§3.3.2.3). Curves are labelled with the corresponding iron depletion factor. The hatched region shows the parameter range applicable to the DG Tau IVC (iron depletion factor $\sim$ 3–10; $3 \lesssim \eta \lesssim 10$). The thick dashed line shows the observed [Fe II] 1.644 μm luminosity of the DG Tau approaching IVC, 2.4×10^{28} erg s^{-1}.

outflow; Podio et al. 2009). The jet iron depletion measurement of Agra-Amboage et al. may be contaminated by IVC emission, given those authors made a simple velocity cut to separate outflow components, rather than using line component fitting (e.g. §2.3.4; Lavalley et al. 1997). Therefore, we take a range of iron depletion factors, 3–10, for the DG Tau approaching IVC.

3.3.3. Model Estimates and Comparison for DG Tau

We now compare the estimates from our model to our previous observations of the approaching DG Tau outflow intermediate-velocity component (§2). These estimates are based on the outflow parameters for DG Tau detailed above (§3.3.2).

3.3.3.1. Mixing Layer Luminosity

The estimated mixing layer luminosity for DG Tau from our model is shown in Fig. 3.7. We compute the total mixing layer bolometric luminosity as per §3.2.4, in particular equation (3.37):

$$\mathcal{L}_{\rm mix,tot} = 2\pi R_{\rm mix} L \rho_{\rm j} v_{\rm j}^3 h'(x) \mathcal{G}(\eta). \tag{3.42}$$

We estimate the mixing layer radius, $R_{\rm mix}$, to be $\sim$ 25 AU (Fig. 3.6). The mixing layer luminosity is estimated using a jet velocity of 265 km s^{-1} (§3.3.2.2) and a jet density of 10^{-19} g cm^{-3} (§3.3.2.1). We take a range of possible mixing layer growth rates, $h'(x) = 0.05 \pm 0.02$ (§3.3.2.3). We consider a range of possible iron depletion factors and jet-to-ambient wind density ratios, as these are the least-constrained parameters (§§3.3.2.4,

3.3.2.5).

We calculate the observed IVC [Fe II] 1.644 μm luminosity from the approaching DG Tau outflow as follows. We consider every spaxel covering the approaching outflow that was successfully fit with two [Fe II] 1.644 μm emission-line components (Fig. 2.6). We then calculate the flux from the fitted IVC component in each spaxel, and sum across the entire outflow to produce a total IVC [Fe II] 1.644 μm luminosity of 2.4×10^{28} erg s^{-1}, assuming a distance to DG Tau of 140 pc (Elias 1978).

Our model estimates for the luminosity of a mixing layer in the approaching DG Tau outflow is in good agreement with our observations of the approaching IVC. For $3 \lesssim \eta \lesssim 10$ (§3.3.2.1), and an iron depletion factor of $\sim$ 3–10, our model estimates a mixing layer luminosity of (1.1–7.9) $\times 10^{28}$ erg s^{-1}. This is a good level of agreement between model and observations, and constitutes a strong indicator that the luminosity of this region of the outflows is driven by turbulent dissipation.

3.3.3.2. Rate-of-Change of Mixing Layer Mass Flux

In our model, mass enters the mixing layer from both the jet via interception, and from the ambient wind via entrainment. From equation (3.26), the rate at which material enters the mixing layer is

$$\frac{\partial \dot{M}}{\partial x} \equiv \dot{M}' = \rho_{\rm j} v_{\rm j} h'(x) \left(\frac{-\eta + \eta \log(\eta) + 1}{(\eta - 1)^2} \right). \tag{3.43}$$

Multiplying by $2\pi R_{\rm mix}$, where $R_{\rm mix} \approx 25$ AU as per §3.3.3.1, gives the entrainment rate per unit length in the outflow direction. Finally, multiplying by the mixing layer length, $L = 270$ AU (§3.3.2.3), gives the total mass being gained by the mixing layer at all observed positions (cf. the calculation of the total turbulent energy production in the mixing layer in §3.2.4).

An important consistency check is that the total mass being gained by the mixing layer at all positions cannot exceed the combined mass-loss rates of the jet and the wind. Otherwise, the mixing layer would cease to exist at some distance downstream, as it exhausts the mass supply from both sources. For an overdense jet ($1 \leq \eta \leq 10$, §3.3.2.4), our model estimates a total mass gain of (3.5–10.0) $\times 10^{-9}$ M$_\odot$ yr^{-1} for the observed mixing layer (Fig. 3.8a). By comparison, the mass-loss rate of the DG Tau jet is $\sim 5 \times 10^{-9}$ M$_\odot$ yr^{-1} (§2.4.1.4; Agra-Amboage et al. 2011) from [Fe II] emission-line ratios; the total mass-loss rate of all ionized outflow components (jet plus IVC) is (1–5) $\times 10^{-8}$ M$_\odot$ yr^{-1} from the VLA data of Lynch et al. (2013). The mass-loss rate of the molecular wind is lower, $\gtrsim 2.2 \times 10^{-9}$ M$_\odot$ yr^{-1} (Takami et al. 2004). However, in the overdense-jet regime, mass interception from the jet is the main contributor to the mass within the mixing layer (Fig. 3.5). Therefore, we conclude that the total mass gain in to the mixing layer estimated

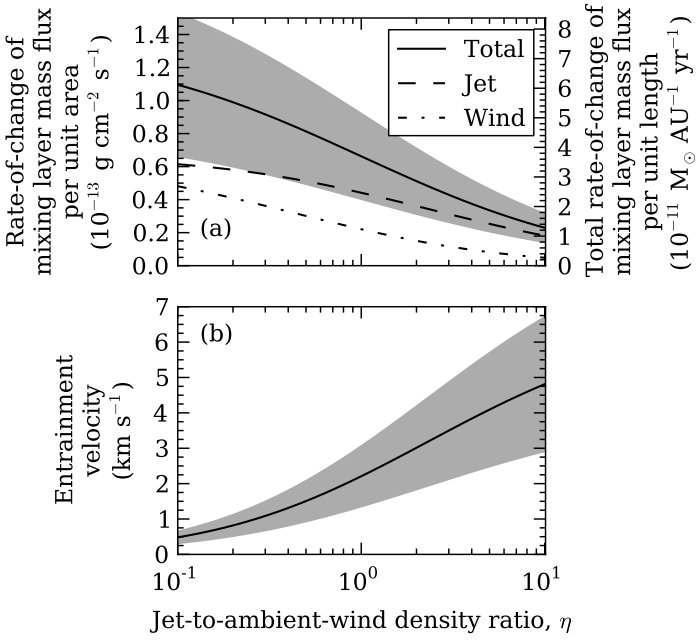

Figure 3.8 Theoretical estimates for the DG Tau mixing layer. (a) Estimated rate-of-change of the mixing layer mass flux (solid line), from equation (3.43); contributions from the jet (dashed curve) and ambient wind (dot-dashed curve) are also shown. Rate-of-change of mixing layer mass flux per unit length (right-hand axis) is calculated assuming a mixing layer radius of 25 AU (§3.3.3.2). (b) Estimated entrainment velocity, from equation (3.25). Estimates are computed using a jet velocity of 265 km s^{-1}, a jet density of 10^{-19} g cm^{-3}, and a mixing layer growth rate of 0.05. Greyed regions in both panels show the estimated parameters for a range of mixing layer growth rates, $0.03 \leq h'(x) \leq 0.07$.

by our model is less than the combined mass-loss rates of the DG Tau jet and molecular wind, as required for consistency.

Recently, Maurri et al. (2014) performed an analysis of the DG Tau approaching outflow using the BE99 technique for determining physical flow parameters from optical line ratios (Bacciotti & Eislöffel 1999). They found that, over the first 0.″7 of the approaching outflow, the mass outflow rate of the jet (identified as the high-velocity interval, or HVI, in their paper) decreased by ~ 0.5 dex. Over the same region, the mass outflow rate of the medium-velocity interval (MVI, which is comparable to our IVC) increased. This is what would be observed if the IVC/MVI represents a turbulent mixing layer which is primarily gaining material from the central jet/HVI.

We compare the observations of Maurri et al. (2014) to our model estimates for the rate-of-change of mixing layer mass flux per unit length, and find them to be consistent. We performed a linear fit to the MVI mass-loss rates of Maurri et al. (2014, fig. 15 therein), and determine an increase in MVI mass-loss rate per unit length of 2×10^{-11} M$_\odot$ AU^{-1} yr^{-1}. For the observed parameters of the DG Tau outflow (§3.3.2), our model estimates a rate-of-change in mixing layer mass flux per unit length along the outflow direction of (1.2–8.6) $\times 10^{-11}$ M$_\odot$ AU^{-1} yr^{-1}, with the lower rate-of-change corresponding to a more overdense jet (Fig. 3.8a).[58] The estimates from our model strongly suggest that the approaching IVC of the DG outflows is consistent with being the signature of a turbulent mixing layer around the central jet.

[58] For $1 \leq \eta \leq 10$, mass entrainment from the ambient wind contributes 20–33 per cent of the rate-of-change of mixing layer mass flux (Fig. 3.5), so the mass entrainment per unit length from the ambient wind is (0.24–2.8) $\times 10^{-11}$ M$_\odot$ AU^{-1} yr^{-1}.

3.3.3.3. Entrainment Velocity and Implied Entrainment Efficiency

In the jet entrainment models of Cantó & Raga (1991) and Raga et al. (1995), material is injected in to the mixing layer from the ambient medium/wind with a prescribed entrainment velocity. This velocity is expressed as a fraction of the sound speed in the ambient wind, $c_{\rm w}$, as it was argued that the ambient wind would be incapable of supplying material at a velocity greater than the sound speed (Cantó & Raga 1991, however, see §3.4.1). This fraction is defined as the entrainment efficiency, $\epsilon \leq 1$, where the entrainment velocity is written as $v_{\rm ent} = \epsilon c_{\rm w}$.

The entrainment velocity of our model is given by equation (3.25), and is shown as a dimensionless function of η in Fig. 3.4(a). For jet-to-ambient-wind density ratios $10^{-1} \leq \eta \leq 10^{1}$, the dimensionless entrainment velocity, $v_{\rm ent}/[v_{\rm j} h'(x)]$ varies between ~ 0.005 and ~ 0.36. For a jet velocity of 265 km s^{-1} and $h'(x) = 0.03$–0.07, we estimate a range of entrainment velocities, $0.3 \leq v_{\rm ent} \leq 6.7$ km s^{-1}. For our inferred values of $\eta \lesssim 10$ and $h'(x) = 0.05$, equation (3.25) estimates an entrainment velocity $\lesssim 5$ km s^{-1} (Fig. 3.8b).

Assuming LTE, the H_2 2.1218 μm emission observed in the approaching DG Tau outflow has a temperature of 2×10^3 K (Beck et al. 2008; Agra-Amboage et al. 2014). As the ambient wind is not directly observable in the region where entrainment is occurring, we may assume that the wind has cooled somewhat. Therefore, we take an indicative temperature of 10^3 K, which leads to a sound speed of 2.2 km s^{-1} in the wind for a molecular gas with mean molecular weight $2.3 m_{\rm H}$.

Direct comparison with the range of entrainment velocities predicted above implies a range of entrainment efficiencies between 0.13 and 3.05 for the full range of possible values for the mixing layer growth rate and jet-to-ambient wind density ratio. Adopting the best-fit value for the mixing layer growth rate, $h'(x) = 0.05$, and assuming that the jet is likely to be overdense by up to a factor of 10 (§3.3.2.4), gives a range of implied entrainment efficiencies from 1.00 to 2.3. We discuss this further is §3.4.1.

3.4. Discussion

3.4.1. Comparison with Earlier Models

Cantó & Raga (1991) and Raga et al. (1995) utilized laboratory experiments (Birch & Eggers 1972) to estimate the entrainment efficiency, ϵ, of protostellar jet mixing layers. Raga et al. propose that $\epsilon \sim 0.03$. Furthermore, both Cantó & Raga (1991) and Raga et al. (1995) claimed that $\epsilon \leq 1$, because the ambient wind should not supply material at greater than the sound speed. However, our model, based only on observable parameters of the protostellar outflows, implies an entrainment efficiency $1 \lesssim \epsilon \lesssim 2.5$, in contradiction

to earlier models. We argue below that our estimated entrainment efficiency is physically viable.

A detailed analysis of the laboratory experiments of Birch & Eggers (1972) is beyond the scope of this paper. However, we make two important points. First, the experiments of Birch & Eggers concern adiabatic mixing layers. However, both observations (e.g. Bacciotti et al. 2002) and analytical estimates of the mixing layer cooling length (§3.2.4) indicate that the DG Tau IVC is radiative. Secondly, the experiments were conducted for jets of Mach number 1–5. The DG Tau jet has a Mach number of 18–25. Whilst magnetic fields within the jet may lower the effective jet Mach number (§2.4.2.2) in to the regime investigated by Birch & Eggers (1972), it is not clear that their experiments are directly relevant to magnetized protostellar mixing layers.

We now address the issue of entrainment velocities greater than the ambient sound speed. Cantó & Raga (1991) argued that the entrainment velocity of the ambient material must be subsonic, otherwise extra shocks would form outside the mixing layer, conflicting with observations. However, a supersonic inflow velocity does not invalidate our model for a number of reasons. First, this velocity is a bulk velocity, not a turbulent velocity and the boundary conditions that we have used imply that the molecular gas adjacent to the mixing layer is not turbulent. Secondly, as the molecular gas is drawn into the mixing layer, the supersonic turbulence within the layer, coupled with its supersonic inflow velocity, ensures that it *is* shocked. This is the reason we have used MAPPINGS IV shock models to determine the [Fe II] emission as a fraction of the bolometric luminosity (§3.3.1).

In reality, the transition from non-turbulent flow outside the mixing layer to fully turbulent flow within would not be as abrupt as we have modelled here. The transition from low-density entraining molecular gas to high-density jet gas is likely to be more gradual. However, even if there are comparable turbulent velocities within the molecular gas being drawn into the layer as in the gas well within the mixing layer, the rate of dissipation per unit volume, $\sim \rho v'^3/l_t$, where ρ is the density, v' is the turbulent velocity, and l_t is the turbulent eddy scale size, is lower in the molecular gas than in the mixing layer, because of the lower density of the former.

3.4.2. The Extent of the Laminar Jet

Jets that undergo lateral entrainment will eventually become completely turbulent, as the inner boundary of the mixing layer expands in to the jet and reaches the symmetry axis (e.g. Bicknell 1984; Dash et al. 1985). This does not appear to occur in the DG Tau jet within $1\farcs5 \sim 340$ AU of the central star, as is evidenced by the low-velocity-dispersion core of the approaching high-velocity [Fe II] 1.644 μm component (Fig. 2.6c). It is therefore relevant to determine if our model predicts the DG Tau jet should remain laminar within the NIFS field. Whilst a fully three-dimensional, axisymmetric model is formally required

to make this calculation (Cantó & Raga 1991), our model provides a useful preliminary exploration.

The jet will become totally turbulent once the jet-mixing layer boundary, y_1, reaches the symmetry axis of the jet. The jet-mixing layer boundary position is given by

$$y_1(x) = h(x)\xi_1(\eta) = h'(x)\xi_1(\eta)x, \tag{3.44}$$

assuming $h(x)$ is linear in x. The downstream distance at which the jet becomes completely turbulent, $x_{\rm turb}$, is then simply

$$x_{\rm turb} = \frac{r_{\rm jet}}{h'(x)\xi_1(\eta)} \rightarrow \frac{x_{\rm turb}}{r_{\rm jet}} = \left(h'(x)\xi_1(\eta)\right)^{-1}. \tag{3.45}$$

For DG Tau, $h'(x) = 0.05$ (§3.3.2.3), $\xi_1(\eta = 10) \sim 0.2$ (§§3.2.2, 3.3.2.4), and the maximum observed jet radius $r_{\rm jet,max} \sim 20$ AU (Fig. 3.6a). The distance from the central star where the DG Tau jet becomes completely turbulent is then ~ 2000 AU $\approx 8\farcs8$ along the outflow axis, accounting for projection effects. This is well beyond the extent of the NIFS field, in agreement with our earlier observations (§2).

3.5. Conclusions

We have constructed a model of the turbulent lateral entrainment of ambient material by a supersonic, collimated jet (§3.2). This model aims to explain the medium-/intermediate-velocity forbidden-line emission that is often seen surrounding YSO jets. The model statistically averages the conservation equations of MHD, and uses only directly observable outflow parameters as inputs. Our model calculates the total production, and subsequent dissipation, of energy in a turbulent mixing layer between the jet and the surrounding molecular wind, via calculation of the total turbulent stress within the layer. This allows theoretical estimates of, e.g. the luminosity and entrainment rate of the mixing layer to be formed.

We computed estimates for the bulk properties of the [Fe II] 1.644 μm IVC observed in the approaching outflow from the YSO DG Tauri (§3.3). We calculated a grid of shock models using the MAPPINGS IV code, to facilitate comparison between the observed [Fe II] luminosity of the component, and the estimated bolometric luminosity from our model. Our model accurately estimates the luminosity and rate-of-change of mass flux of the DG Tau IVC, leading us to conclude that the IVC does indeed represent a turbulent mixing layer between the DG Tau high-velocity jet, and wider-angle disc wind.

We compared our work with previous models of turbulent entrainment by jets, specifically those of Cantó & Raga (1991) and Raga et al. (1995). Unlike the previous models, our model is not dependent upon a free 'entrainment efficiency' parameter, which previous

authors inferred from laboratory experiments. We argued that the requirement for subsonic 'entrainment velocities' from the ambient wind is not necessary in the context of our model. We also estimated the extent of laminar jet flow in DG Tau (§3.4.2), although we note that this is simply an illustrative case due to the limitations of our two-dimensional model (see below).

As observed by Cantó & Raga (1991), three-dimensional axisymmetric models of turbulent entrainment by jets are required for definitive analysis of radiative mixing layers. An obvious next step would be to extend the model presented here to three dimensions, and to remove the restriction on the ambient wind having zero streamwise velocity. MHD simulations of turbulent entrainment would also be helpful for characterising the efficiency of the entrainment process, as well as determining the effects of the jet magnetic field on turbulent entrainment.

Acknowledgements

Based on observations obtained at the Gemini Observatory, which is operated by the Association of Universities for Research in Astronomy, Inc., under a cooperative agreement with the NSF on behalf of the Gemini partnership: the National Science Foundation (United States), the National Research Council (Canada), CONICYT (Chile), the Australian Research Council (Australia), Ministério da Ciência, Tecnologia e Inovação (Brazil) and Ministerio de Ciencia, Tecnología e Innovación Productiva (Argentina).

We are extremely grateful for the support of the NIFS teams at the Australian National University, Auspace, and Gemini Observatory for their tireless efforts during the instrument integration, commissioning and system verification: Jan Van Harmleen, Peter Young, Mark Jarnyk (deceased), Nick Porecki, Richard Gronke, Robert Boss, Brian Walls, Gelys Trancho, Inseok Song, Chris Carter, Peter Groskowski, Tatiana Paz, John White, and James Patao.

MW acknowledges the generous travel support from Academia Sinica to attend the conference Star Formation Through Spectroimaging at High Angular Resolution in July 2011, which provided useful information for this study. This work was supported by the Australian Research Council through Discovery Project Grant DP120101792 (R. Salmeron).

CHAPTER 4

Bipolar Asymmetry in the DG Tau Outflows

This chapter has been published as **White, M. C., Bicknell, G. V., McGregor, P. J., Salmeron, R. *MNRAS*, *442*, 28–42, 2014a**, *referenced as White et al. (2014a). This chapter is not modified from the published version, except in the following respects:*

- *Section, figure, footnote and table numbering, and general formatting, have been modified for consistency with the remainder of the thesis;*
- *An additional footnote (footnote 59, p. 133) has been added;*
- *References to White et al. (2014c) and White et al. (2014b) have been changed to point to Chapters 2 and 3 of this thesis respectively.*

The original paper is available at `http://mnras.oxfordjournals.org/content/442/1/28`.

The initial reduction of the NIFS data used in this chapter was performed by Professor Peter McGregor prior to the start of the candidature. Subsequent re-reductions were conducted jointly by the candidate and Professor McGregor, but did not constitute major changes to the reduction procedure, and used pre-existing reduction scripts written by Professor McGregor. The data reduction section of this chapter (§4.2) was written by the candidate, based on notes provided by Professor McGregor.

The kinetic models presented in §4.4 were constructed by the candidate by adapting a Fortran *script written by Professor McGregor.*

Abstract

The origin of bipolar outflow asymmetry in young stellar objects (YSOs) remains poorly understood. It may be due to an intrinsically asymmetric outflow launch mechanism, or it may be caused by the effects of the ambient medium surrounding the YSO. Answering this question is an important step in understanding outflow launching. We have investigated the bipolar outflows driven by the T Tauri star DG Tauri on scales of hundreds of AU, using the Near-infrared Integral Field Spectrograph (NIFS) on Gemini North. The approaching outflow consists of a well-collimated jet, nested within a lower-velocity disc wind. The receding outflow is composed of a single-component bubble-like structure. We analyse the kinematics of the receding outflow using kinetic models, and determine that it is a quasi-stationary bubble with an expanding internal velocity field. We propose that this bubble forms because the receding counterjet from DG Tau is obstructed by a clumpy ambient medium above the circumstellar disc surface, based on similarities between this structure and those found in the modelling of active galactic nuclei outflows. We find evidence of interaction between the obscured counterjet and clumpy ambient material, which we attribute to the large molecular envelope around the DG Tau system. An analytical model of a momentum-driven bubble is shown to be consistent with our interpretation. We conclude that the bipolar outflow from DG Tau is intrinsically symmetric, and the observed asymmetries are due to environmental effects. This mechanism can potentially be used to explain the observed bipolar asymmetries in other YSO outflows.

4.1. Introduction

Outflows are ubiquitous components of young stellar objects (YSOs). Solar-mass YSOs are capable of driving collimated bipolar outflows of atomic and molecular material to distances of ~ 1 pc (e.g. McGroarty et al. 2007). These outflows extract angular momentum from the star-disc system, allowing material from the circumstellar disc to accrete onto the central protostar. It is generally accepted that the outflows are launched magnetocentrifugally, either from the surface of the circumstellar disc (MHD disc wind; Blandford & Payne 1982; Pudritz & Norman 1983), or from reconnection points in the stellar magnetosphere (the X-wind; Shu et al. 1994). Multiple launch mechanisms may act in concert to produce outflows with multiple velocity components (Anderson et al. 2003; Larson 2003; Ferreira et al. 2006; Shang et al. 2007). The launch region of these outflows is unresolvable with current telescopes. Therefore, detailed observational and theoretical studies of YSO outflows are necessary in order to determine the manner in which they are launched, and the physical conditions at their launching point(s).

Bipolar outflow asymmetry is a common occurrence in large-scale YSO outflows. These outflows, which are characterised by the presence of shock-excited Herbig–Haro (HH)

objects, are often observed to be one-sided, with only a blueshifted, or approaching, outflow visible (e.g. Eislöffel & Mundt 1998; McGroarty & Ray 2004; McGroarty et al. 2007). Such an asymmetry may be caused by the circumstellar disc obscuring the receding component of a symmetric bipolar outflow. Alternatively, the receding outflow may have entered the dense molecular cloud complex behind the YSO, obscuring it from observation (McGroarty et al. 2007). However, radial velocity asymmetry is often seen in objects with observable bipolar HH outflows. For example, Hirth et al. (1994b) found that, of 15 T Tauri stars with observed bipolar HH outflows, 8 showed bipolar velocity asymmetry between the blueshifted and redshifted outflows. The ratio of radial velocities between the opposing outflows in these objects is in the range 1.4–2.6. Further studies have found more asymmetric bipolar HH outflows, such as HH 30, which has a radial velocity ratio ~ 2 between the two outflows (Estalella et al. 2012). One-sided knot ejections have also been detected, such as that from the driving source of the HH 111 outflow (Gómez et al. 2013). Asymmetrical knot ejections and differing mass outflow rates between the two sides of the bipolar outflow from the Herbig Ae star HD 163296 have also been detected (Wassell et al. 2006). This evidence raises the question of whether the asymmetry is caused by environmental effects (Hirth et al. 1994b), or is an intrinsic feature of the outflows, either due to disc conditions (such as warping) affecting the outflow launching (Gómez et al. 2013), or to other effects close to the launch point (Wassell et al. 2006).

With the advent of space-based telescopes such as the *Hubble Space Telescope* (*HST*), and the development of ground-based adaptive-optics systems, the large-scale outflows can be traced back to within a few hundred AU of the central protostar, and are observed as well-collimated 'microjets'. These small-scale outflows provide an excellent laboratory for testing outflow launch models, as the outflow has yet to propagate to a distance where it interacts with the large-scale molecular cloud complex (e.g. McGroarty et al. 2007). Therefore, the search for bipolar outflow asymmetry in these microjets is important in determining if the asymmetry is an intrinsic property of the outflows on all scales.

Velocity asymmetries were observed in the profiles of bipolar forbidden emission line (FEL) regions in several young stars (Hirth et al. 1997). The FELs trace the presence of microjets (e.g. Bacciotti & Eislöffel 1999; Bacciotti et al. 2002; Coffey et al. 2004, 2007). Further long-slit optical and near-IR spectroscopic observations have confirmed kinematic and/or physical bipolar asymmetries occur in the outflows of DG Tauri B (Podio et al. 2011) and FS Tauri B (Liu et al. 2012). There are conflicting views on the cause of these asymmetries. Podio et al. (2011) argue that the asymmetry in DG Tau B is due to an asymmetric ambient medium, based on the observation that only one side of the bipolar outflow is driving the ambient medium into a CO outflow. Liu et al. (2012) argue for a bipolar outflow that is being driven at a different mass-loss rate on either side of the circumstellar disc, with the velocity difference between the two jets keeping a linear momentum balance, so there is no observable recoil. It is important to differentiate between the possible causes of bipolar

outflow asymmetry in order to determine if it is an intrinsic or an environmental effect.

HST and adaptive optics also permits imaging and spectroimaging studies of YSO microjets (e.g. Kepner et al. 1993; Lavalley et al. 1997). Such studies have shown the presence of structural differences in the bipolar small-scale outflows from YSOs. The blueshifted collimated jet from the YSO HL Tauri is spatially coincident with an approximately axisymmetric bubble-like structure (Takami et al. 2007). Bipolar asymmetries in jet collimation are observed in the YSOs RW Aurigae (Melnikov et al. 2009) and DG Tau B (Podio et al. 2011). Such studies have shown that structural bipolar outflow asymmetries are common in YSOs on the microjet scale (Podio et al. 2011).

Another example of bipolar asymmetry in T Tauri star microjets is the transitional Class I/Class II YSO DG Tauri. One of the most actively-accreting T Tauri stars, DG Tau has been used as a laboratory in searches for jet rotation (Bacciotti 2002; Pesenti et al. 2004; Coffey et al. 2007), jet knot generation (Lavalley-Fouquet et al. 2000; Rodríguez et al. 2012b) and links between jet and disc properties (Testi et al. 2002). DG Tau drives the blueshifted HH 158 (Mundt & Fried 1983) and HH 702 (Sun et al. 2003; McGroarty & Ray 2004) outflows, the latter extending to a distance of ~ 0.5 pc from the protostar. There is no known large-scale redshifted HH outflow associated with DG Tau. A bipolar microjet-scale outflow is present, and exhibits velocity asymmetry between the approaching and receding flows (Herbst et al. 1994; Lavalley et al. 1997). This was originally detected through long-slit spectroscopy of optical FELs from the outflows (Hirth et al. 1994b). The receding outflow was first imaged by Lavalley et al. (1997) using spectroimaging of [O I] 6300 Å emission. They determined a radial velocity ratio of 1.4 between the approaching and receding outflows.

More recently, Agra-Amboage et al. (2011) and White et al. (2014c, i.e. §2) detected structural and kinematic differences in the microjet-scale approaching and receding outflows of DG Tau, using spectroimaging data of spatially extended [Fe II] 1.644 μm line emission. The approaching outflow shows the classical YSO microjet morphology of a central, well-collimated, high-velocity jet with deprojected velocity $\sim$ 215–315 km s^{-1}. The jet is dominated by both stationary and moving shock-excited 'knots' of emission. This jet is 'nested' within a region of lower-velocity emission, which may be excited by the formation of a turbulent entrainment layer around the jet (§§2.4.2, 3; Pyo et al. 2003b). A wide-angle approaching molecular wind is observed in H_2 1-0 S(1) 2.128 μm line emission (§2.4.2.1; Beck et al. 2008; Agra-Amboage et al. 2014), providing a supply of material for the jet to entrain. On the other hand, the redshifted outflow shows no evidence of any jet-like components, and instead forms a large bubble-like structure. This was interpreted by Agra-Amboage et al. (2011) as being the counterpart 'magnetic bubble' (Ciardi et al. 2009) to a similar structure they claimed $\sim 1\farcs2$ from the central star in the approaching outflow channel. However, analysis in §2 showed that they appeared to be interpreting the low-velocity entrainment component in that region as part of the central jet. We concluded

that an approaching bubble structure does not exist. Therefore, the nature and cause of the bipolar outflow asymmetry in DG Tau remains an open question.

We investigate the bipolar asymmetry in the microjet-scale DG Tau outflows below, and conclude that environmental effects hamper the propagation of one side of an approximately symmetric bipolar outflow. We proceed as follows. In §4.2, we outline our multi-epoch NIFS observations and our data reduction procedure. §4.3 details our methods of analysing the data. In §4.4, we argue that the structure is a stationary bubble with an internal velocity field describing expansion of gas towards the bubble walls, based on comparisons of the observed velocity structure to kinetic models. §4.5 outlines the results of simulations of bubbles driven by impeded active galactic nuclei (AGN) jets, and links this work to the morphology observed in the DG Tau receding outflow. We propose that the bubble in the DG Tau receding outflow is the result of a receding counterjet being obstructed by clumpy ambient material in the extended envelope around DG Tau (Kitamura et al. 1996a). The receding outflow is currently in the momentum-driven bubble phase, similar to the simulations of radio galaxies by Sutherland & Bicknell (2007) and Wagner & Bicknell (2011). We construct an analytical model of an expanding jet momentum-driven bubble in §4.6, and find that it predicts physical parameters consistent with those observed in the DG Tau bubble and the extended CO envelope around the system. Finally, in §4.7, we discuss the impact of our results on the interpretation of bipolar outflow asymmetry in other YSOs, as well as the implications of episodic variability in YSOs on our model. We summarize our conclusions in §4.8.

4.2. Observations and Data Reduction

A brief outline of the data reduction techniques used is given here. For a more detailed description, the reader is referred to §2.2.

Observations of the DG Tau system were obtained on 2005 Oct 26 UT in the K band (Beck et al. 2008), and on 2005 Nov 12 UT in the H band, with the Near-infrared Integral Field Spectrograph (NIFS) on the Gemini North telescope, Mauna Kea, Hawaii. Further H-band observations were taken on 2006 Dec 24 and 2009 Nov 08. Observing parameters for each epoch of H-band data are detailed in Table 4.1. Data were recorded with the ALTAIR adaptive-optics system in natural guide star mode, utilizing DG Tau itself as the reference star. NIFS is an image-slicing type integral-field spectrograph, splitting a $3'' \times 3''$ field into 29 slitlets, resulting in $0\farcs103 \times 0\farcs045$ spaxels. A spatial resolution of $\sim 0\farcs1$ was achieved in the H-band data, based on the FWHM of a standard star observed immediately after the DG Tau observations. These standard star observations allow for telluric correction and flux calibration. Calibration was based on the 2MASS magnitude of the standard star, and a shape derived from a blackbody function fit to the 2MASS J-K colour of the standard

Table 4.1 Observing parameters of DG Tau H-band observations, 2005–2009.

Date	Epoch	No. of	Telluric standard star			Continuum image FWHM	
		on-source	Star	2MASS H	Blackbody	Telluric	DG Tau
		exposures[a]		(mag)	temp. (K)	standard[b]	
2005 Nov 11	2005.87	11	HIP25736	7.795	7000	0.″11	0.″14
2006 Dec 24	2006.98	9	HIP25736	7.795	7000	0.″11	0.″12
2009 Nov 08	2009.88	6	HIP26225	7.438	9400	0.″09	0.″18

[a] All on-source exposures were 600 s.
[b] Used to estimate the AO seeing achieved.

star. A spatial resolution of $\sim 0\farcs1$ was achieved in the K-band observations (Beck et al. 2008). A $0\farcs2$-diameter partially-transmissive occulting disc was placed over the star during the H-band observations to increase sensitivity to extended emission.

Data reduction was performed using the Gemini IRAF package as follows. An average dark frame was subtracted from each object frame and averaged sky frame. The dark-subtracted average sky frame was then subtracted from the dark-subtracted object frame. A flat-field correction was applied to each slitlet by dividing by a normalized flat-field frame. Bad pixels were identified using the flat-field and dark frames, and were corrected via 2D interpolation. Individual 2D spectra for each slitlet were transformed to a rectilinear coordinate grid using arc and spatial calibration frames, and then stacked in the second spatial direction to form a 3D data cube. All spectra were transformed to a common wavelength scale at this point.

Data cubes from each object exposure were corrected for telluric absorption by division with a normalized 1D spectrum extracted from the observations of a telluric standard star. Hydrogen absorption lines intrinsic to the A0 standard star were removed using Gaussian fits to those lines. Flux calibration was achieved using a large-aperture 1D spectrum of the same standard star, which was also corrected for telluric absoprtion. The finalised object frames were spatially registered using the continuum position of DG Tau, and median-combined to produce the final data cube. The final cube for each epoch was then spatially registered using the position of the central star to allow for comparison of the extended emission structure.

Stellar subtraction was performed using custom PYTHON routines. For H-band data cubes, two $0\farcs25$ diameter apertures were formed, centered at opposing positions $0\farcs5$ from the central star perpendicular to the outflow direction. A stellar spectrum was extracted from each aperture and averaged. For each spaxel in the cube, this stellar spectrum was scaled to match the flux observed adjacent to the spectral region of interest for the line being investigated, and subtracted from the spaxel spectrum. K-band stellar subtraction was performed by forming a pair of continuum images adjacent to the spectral region of interest around the line being investigated. These images were averaged, and then subtracted from each wavelength plane of the data cube. Full details of the data reduction and stellar spectrum subtraction procedures used may be found in Beck et al. (2008) (K band) and §§2.2 and 2.3.1 (H band). We concentrate on the 2005 epoch data in this paper; unless explicitly stated, all data are from that epoch.

The receding outflow from DG Tau is shown in Fig. 4.1, as seen in [Fe II] 1.644 μm line emission (Fig. 4.1a) and H_2 1-0 S(1) 2.1218 μm line emission (Fig. 4.1b). In this Figure, as with all following figures, the large-scale HH 158 outflow axis is labelled as x, and the axis transverse to this as y. The extended H-band emission is dominated by [Fe II] 1.644 μm line emission, and takes the form of a bubble-like structure. The 'apex' of this structure is

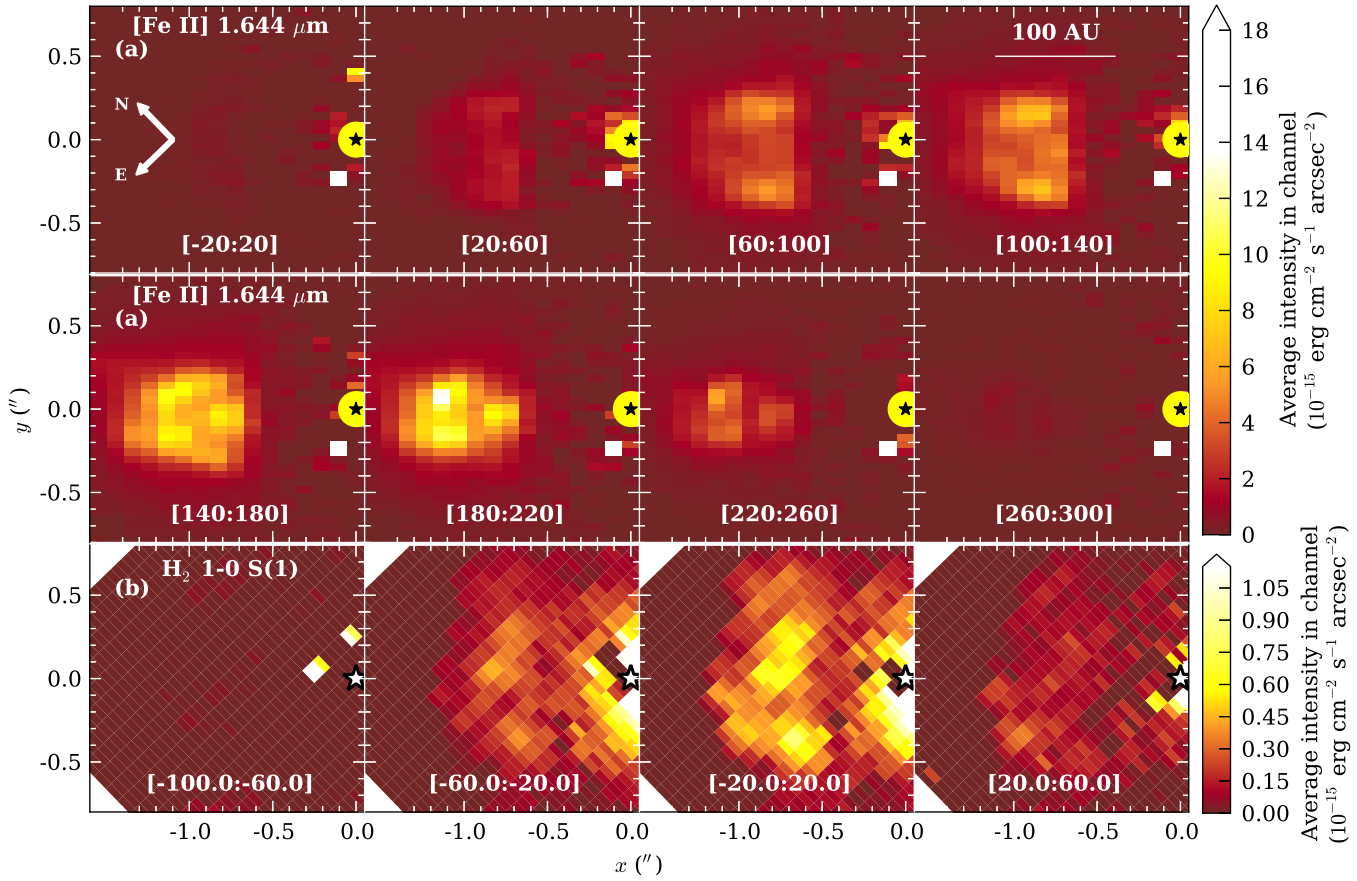

Figure 4.1 Channel maps of emission from the receding DG Tau outflow in the 2005 observing epoch. Panels show images of (a) the extended [Fe II] 1.644 μm line emission, and (b) the extended H_2 1-0 S(1) 2.1218 μm line emission from the receding DG Tau outflow, binned into 40 km s^{-1}-wide slices. The velocity range of each slice is shown in white in km s^{-1}. The intensity values quoted are the average intensity in each channel over the velocity range. The black star corresponds to the position of the central star, DG Tau, and the yellow circle in (a) indicates the position and size of the occulting disc used during the H-band observations. The physical scale is indicated at the top-right. This scale does not account for the inclination of the outflow axis, x, to the line of sight.

$\sim 1\farcs3$ along the outflow axis from the central star. No emission is observed closer than $\sim 0\farcs7$ to the central star, due to obscuration by the circumstellar disc. This obscuration provides a measure of the extent of the disc (Agra-Amboage et al. 2011). The lateral width of the structure at its closest to the central star, which we shall refer to as the 'base' of the structure, is $\sim 0\farcs7 \approx 98$ AU at the distance to DG Tau (140 pc; Elias 1978). The lowest line velocities from the structure occur at this widest point; the highest line velocities occur at both the apex of the structure, and at an emission enhancement $0\farcs84 \pm 0\farcs03$ along the outflow axis from the central star.

The H_2 1-0 S(1) 2.1218 μm line emission from the region of the receding outflow is strongest at positions coincident with the base of the bubble-like structure seen in [Fe II] 1.644 μm line emission (Fig. 4.1b; Beck et al. 2008; Agra-Amboage et al. 2014). This 'patchy' emission has no clear structure. The line emission is concentrated about a velocity of 0 km s^{-1}. Beck et al. (2008) analysed the level populations and line ratios in the observed H_2 emission, and determined that it is likely being excited by collisional J- or C-type shocks. UV and X-ray fluorescence were previously ruled out by Takami et al. (2004), based on the large mass and momentum fluxes resulting from their calculations.

4.3. Data Analysis

4.3.1. Spectral Gaussian Fitting

Upon visual inspection, some regions of the receding outflow appear to exhibit multiple components in [Fe II] 1.644 μm line emission. Multicomponent spectral Gaussian fitting was used to characterise the presence and nature of these components. Both one- and two-component Gaussian fits were made to the [Fe II] 1.644 μm emission line in each spaxel, and an F-test (Appendix A; Bevington & Robinson 1992) was used to determine the statistically appropriate number of components to retain in the final fit (Westmoquette et al. 2007). It has been noted that the F-test is formally not the correct test to use in this situation (A.1; Protassov et al. 2002). However, lacking a statistically correct specific alternative that may be applied to the volume of spectra presented here, we proceed using the F-test (Westmoquette et al. 2012). It was found that a two-component fit could not be consistently applied across the entire receding outflow. This occurs because the two apparent components are too convolved to form a statistically significant fit with our spectral resolution. Alternatively, there may be an underlying 'continuum' of emission velocity components at some spatial positions. This effect is spread evenly across the receding outflow structure. Therefore, Gaussian line fits were restricted to one component at all spatial positions. This is in contrast to the approaching outflow, which shows the clear presence of two [Fe II] 1.644 μm emission-line components at all spatial positions (§2.3.4; Fig. 2.6).

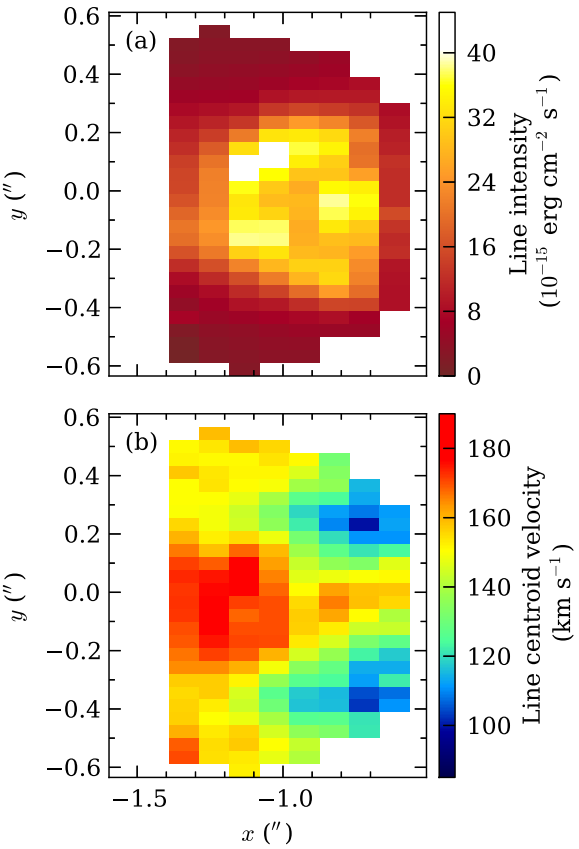

Figure 4.2 Fitted [Fe II] 1.644 μm emission-line component for the DG Tau receding outflow. Panel (a) shows the fitted line intensity and panel (b) displays the fitted line velocity of the receding outflow, based on a single-component Gaussian fit. The fitted line velocity has been corrected for the systemic velocity of the central star, as determined by Gaussian fitting to observed H-band photospheric absorption features. *This Figure is identical to Fig. 2.7.*

The results of the spectral fitting procedure are shown in Fig. 4.2. Line velocities were corrected for the systemic velocity of the central star, as determined by Gaussian fits to multiple photospheric absorption lines observed in the H-band stellar spectrum (Fig. 2.1). Comparison of Fig. 4.2(a) to the channel maps of [Fe II] 1.644 μm line emission (Fig. 4.1a) shows that the fitting procedure accurately replicates the appearance of the receding outflow.

The velocity structure observed in the receding outflow is in agreement with Agra-Amboage et al. (2011). The largest receding line-of-sight velocities of $\sim$ 160–180 km s^{-1} are observed at the apex of the structure (Figs 4.1, 4.2b), as well as along the outflow axis. Line velocities on the edges of the structure decrease with decreasing distance from the central star. The lowest line velocities, $\sim$ 80 km s^{-1}, are located at the base of the observable structure.

4.3.2. Electron Density

The near-infrared lines of [Fe II] arise from low-lying energy levels, and are useful tracers of electron number density, n_e. Pradhan & Zhang (1993) showed that the intensity ratio of the [Fe II] lines at wavelengths 1.533 μm and 1.644 μm are a diagnostic of electron number density in the range $n_e \sim 10^2$–10^6 cm^{-3}, for electron temperatures, T_e, in the

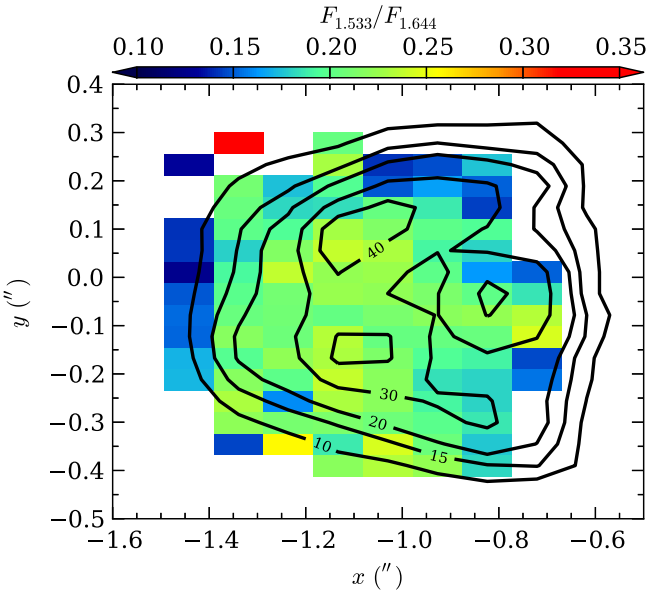

Figure 4.3 Ratio of [Fe II] 1.533 μm to [Fe II] 1.644 μm emission-line intensity from the receding DG Tau outflow. Spaxels have been masked where a threshold signal-to-noise ratio of 10 in the computed ratio has not been met, or where the ratio is in the saturation limit for determining electron density ($F_{1.533}/F_{1.644} \gtrsim 0.45$; Pesenti et al. 2003). Line fluxes are determined by integration of the raw stellar-subtracted spaxel spectra about the line wavelengths, over the velocity range 0 to 340 km s^{-1}. Contours of [Fe II] 1.644 μm line emission, integrated over the same velocity range, are overlaid in black. Contours are labelled in units of 10^{-15} erg cm^{-2} s^{-1} arcsec^{-2}.

range $T_e \sim 3000$–20000 K. Pesenti et al. (2003) have accurately computed the relation between the line ratio, $F_{1.533}/F_{1.644}$, and electron density for a 16-level Fe^+ model.

Fig. 4.3 shows the flux-ratio map derived from our data for the receding DG Tau outflow. Integrated line fluxes were determined by the integration of the stellar-subtracted spectrum of each spaxel over the velocity range 0 to 340 km s^{-1} about the two line wavelengths. Spaxels were excluded from this calculation where a signal-to-noise ratio of 10 in the computed line ratio was not achieved, meaning line ratios could only be determined where the weaker 1.533 μm emission line could be detected with adequate signal-to-noise ratio. This criterion produces density information over a region comparable to the observed redshifted [Fe II] 1.644 μm line emission (Fig. 4.1).

The $F_{1.533}/F_{1.644}$ ratio is approximately constant across the region of observable redshifted emission (Fig. 4.3). The relationship between the line ratio and electron density is only weakly dependent on electron temperature, especially in the range $0.1 \lesssim F_{1.533}/F_{1.644} \lesssim 0.3$ (Pesenti et al. 2003, fig. 2(b) therein), so we can comment on the approximate electron density of the receding outflow without knowledge of the electron temperature. We conclude that the electron density of the receding outflow is of order 10^4 cm^{-3}. It may rise to $\sim 10^{4.5}$ cm^{-3} in the regions of strongest [Fe II] 1.644 μm emission. However, these variations in $F_{1.533}/F_{1.644}$ are barely larger than the uncertainties in their calculation.

4.3.3. Time-Evolution of the Receding Outflow

The time-evolution of the receding outflow over the period 2005–2009 structure is shown in Figs 4.4 and 4.5. The most remarkable feature is the apparent stability of the bubble structure between the 2005 and 2006 observing epochs, 1.11 yr apart. The velocity structure is particularly stable over this period (Fig. 4.4). Furthermore, the faint boundary of low-

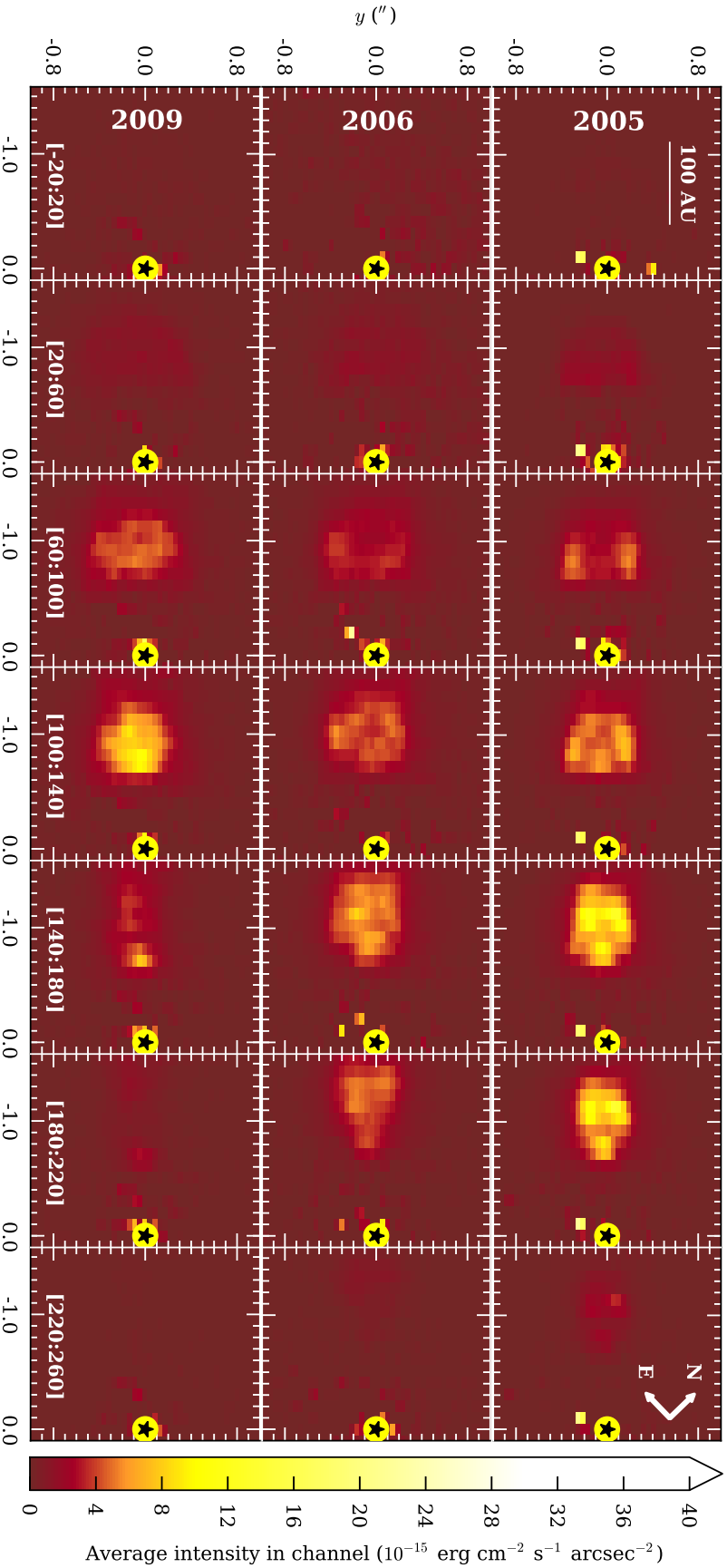

Figure 4.4 Channel maps of the DG Tau outflow for the 2005, 2006 and 2009 observing epochs. Panels show images of the extended [Fe II] 1.644 μm line emission around DG Tau, binned into 40 km s^{-1}-wide slices. The velocity range of each slice is shown at the bottom of each slice in km s^{-1}. The intensity values quoted are the average intensity in each channel over the 40 km s^{-1} velocity range. The black star corresponds to the position of the central star, DG Tau, and the yellow circle indicates the position and size of the 0.″2 diameter occulting disc.

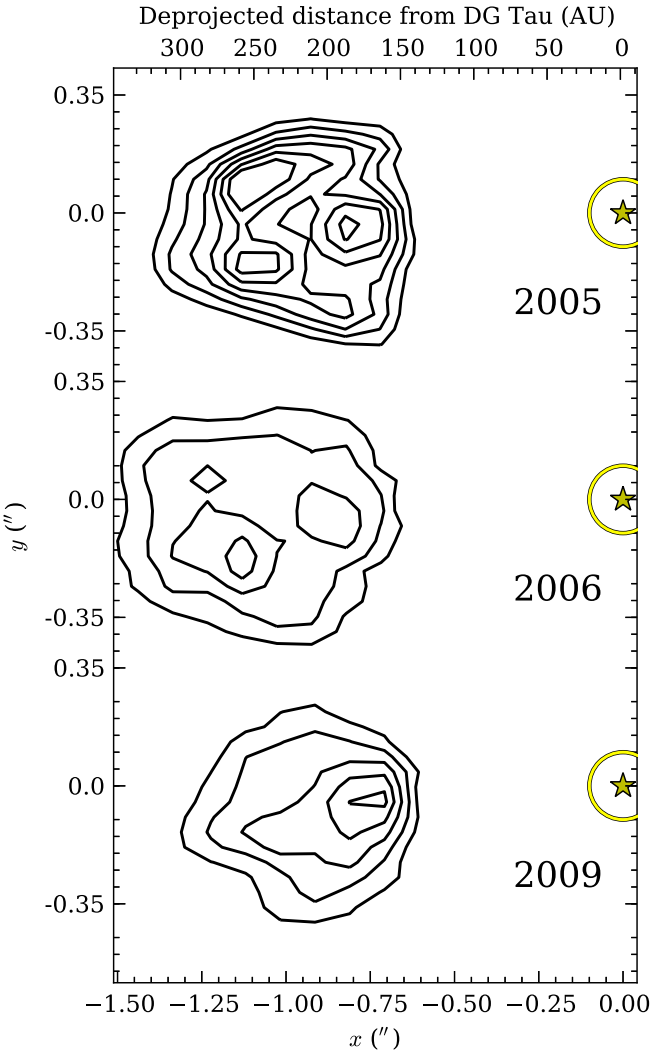

Figure 4.5 [Fe II] 1.644 μm contour image of the receding outflow from DG Tau, formed over the velocity range 0 to 340 km s^{-1}, for observing epochs 2005–2009. Contours are drawn at levels of $[15, 20, \ldots, 40] \times 10^{-15}$ erg cm^{-2} s^{-1} arcsec^{-2}. The location of the central star, and the position and size of the occulting disc used during the observations, are shown as a yellow star and circle, respectively.

velocity emission remains constant across all epochs (Fig. 4.4, [20 : 60] km s^{-1} panel).[59] The greatest change occurs between the 2006 and 2009 observing epochs, when the 'apex' of the structure is no longer visible. The 'apex' is formed of the highest-velocity emission (Fig. 4.4).

We investigate the stability of the receding outflow structure between the 2005 and 2006 observing epochs more carefully. The 'base' of the structure remains in the same position in all observing epochs, $\sim 0\farcs7$ from the central star (Fig. 4.5). Based on the extent of the 15×10^{-15} erg cm^{-2} s^{-1} arcsec^{-2} contour in Fig. 4.5, the 'apex' of the structure appears to have moved $\sim 0\farcs1$ in 1.1 yr, corresponding to a deprojected[60] velocity of ~ 95 km s^{-1}. This apparent motion occurs on the scale of a single NIFS pixel, and the scale of the AO-corrected seeing (Table 4.1). Furthermore, the small discrepancy ($0\farcs03$) between the position of knot A of the approaching outflow in the 2006 observing epoch, and in the 2005 and 2009 epochs (Table 2.3), suggests there may be a larger spatial registration uncertainty

[59] The faint boundary emission can be seen more clearly in Fig. 4.1, [20 : 60] km s^{-1} panel.

[60] We assume an inclination between the outflow axis and the line of sight of 38° (Eislöffel & Mundt 1998).

in the 2006 epoch data. This may reduce the actual bubble 'apex' proper motion to ~ 70 km s^{-1}. The main difference between the receding outflow structure between the 2005 and 2006 epochs is in the highest-velocity emission (Fig. 4.4, panels [140 : 180] and [180 : 220] km s^{-1}). The stationarity of (a) the lower-velocity emission and (b) the 'base' of the structure leads us to conclude that the receding outflow structure is a predominantly stationary feature. We now proceed to consider a possible model for the formation of such a structure.

4.4. Receding Outflow as a Bubble

The nature of the DG Tau receding outflow structure has yet to be adequately determined. Such structures are not unique to DG Tau, having been observed in other YSOs (e.g. HL Tauri; Takami et al. 2007). Agra-Amboage et al. (2011) interpreted the receding outflow structure in DG Tau to be the counterpart of a similar faint bubble they reported at and beyond 1.″2 from the central star in the approaching outflow. We do not observe this approaching bubble (§2). We believe that Agra-Amboage et al. (2011) were interpreting the blueshifted intermediate-velocity component (IVC) at that location as being a separate structure to the rest of the IVC. The IVC accelerates with distance from the central star, so that at distances $\gtrsim 1.''2$ from the central star, the IVC approaches the same velocity that the high-velocity jet exhibits closer to the star. This could lead to the presumption that this material is of the same origin as the jet, particularly if a simple velocity cut is used to differentiate between components, as is the case in Agra-Amboage et al. (2011). We conclude that there is no approaching outflow counterpart to the receding outflow structure (§2).

Ignoring for the moment the question of how DG Tau produces two markedly different structures on two sides of a bipolar outflow (§4.5), one potentially appealing interpretation for the presence of a bubble-like structure in the receding outflow is a bow shock. Bow shocks are the predominant components of the large-scale Herbig-Haro chains observed in many protostellar outflows on larger scales. On smaller scales, moving microjet knots (cf. §2.4.1.1) have been observed to have a mini-bow shock morphology when observed at high angular resolution (e.g. HH 34; Reipurth et al. 2002). However, all of these structures have been observed to possess significant proper motion, of the order of the jet propagation velocity (Reipurth et al. 2002; Hartigan et al. 2005; Raga et al. 2012). This is not observed for the receding outflow structure in DG Tau. Furthermore, if the receding outflow were forming a bow shock, in the absence of significant receding proper motion it would exhibit significantly mixed redshifted *and blueshifted* emission. This would be the result of the backflow of material that is ejected orthogonal to the jet axis at the bow shock head (Lada & Fich 1996). We observe only redshifted emission on one side of the DG Tau system, and only blueshifted emission on the other (Fig. 2.2). Therefore, we exclude the presence of a

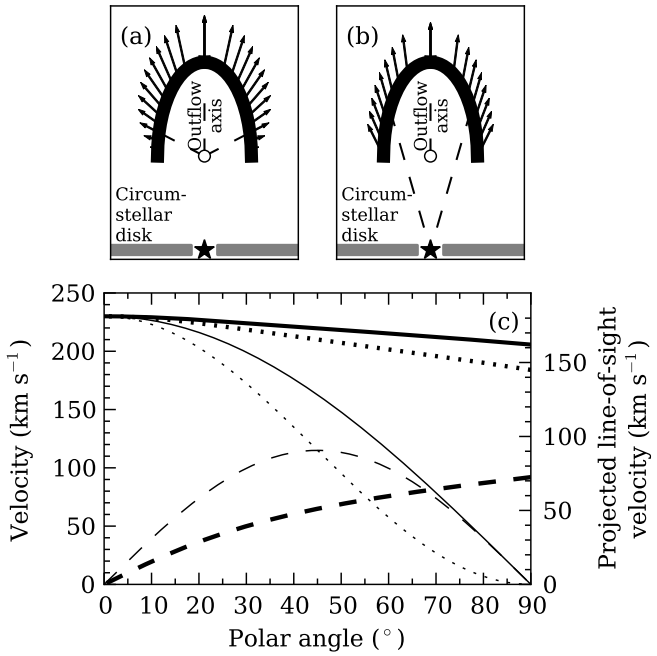

Figure 4.6 Kinetic models of expanding bubbles. The top panels show velocity vectors for snapshots of hemi-ellipsoidal bubbles with velocity fields expanding (a) away from the centre of the bubble, and (b) away from the location of the central star. Note that the vectors represent the velocity field of the dispersed, shocked jet material interior to the bubble walls, which is the source of the emission; the vectors are placed on the outside of the bubble for clarity only. The central star, denoted by the star symbol, is at the same distance from the bubble centre, denoted by the small circle, as the bubble centre is from the bubble apex. The dashed lines show the alignment of the velocity vectors in each model. The bubble major axis is aligned to the outflow axis. The polar angle is defined as the angle from the outflow axis, measured at the bubble centre. Velocities are modulated by the polar angle such that the total gas expansion velocity reduces to zero at the same height above the notional circumstellar disc (grey regions) as the point from which the internal velocity field expands. The star and circumstellar disc are not included in the models. (c) Velocity profiles of the models. Profiles for the internal velocity field expanding away from the bubble centre (panel a) are drawn in thin lines; profiles for the bubble expanding away from the central star (panel b) are drawn in thick lines. The dashed lines show radial velocity profiles, the dotted lines show vertical velocity profiles, and the solid lines show total velocity profiles.

stationary bow shock-type feature in the DG Tau receding outflow.

We investigated the velocity structure of the [Fe II] 1.644 μm line emission from the receding outflow using kinetic models as follows. The models are constructed on a three-dimensional Cartesian grid using the FORTRAN programming language, and represent snapshots of static bubbles, with a distribution of expanding, emitting material interior to the bubble walls. In the first model (Fig. 4.6a), the velocity field expands away from the intersection between the large-scale outflow axis and the base of the structure, which we call the bubble centre. In the second model (Fig. 4.6b), the velocity field expands away from the position of the central star. The central star is assumed to be located on the outflow axis, at the same distance from the bubble centre as the bubble apex. However, the star is not included in the models. Each bubble has a fixed emission region thickness of 15 AU interior to the bubble walls, within which every volume element radiates with the same emissivity. Volume elements interior to these regions do not radiate. The velocity of gas in the emitting

regions is modulated by the angle from the outflow axis, such that the expansion velocity decreases to zero at the same height above the central star as the point from which the bubble expands. This was necessary in order to limit the amount of blueshifted emission predicted by the models. The height (160 AU), elongation (height-to-width ratio ~ 2) and position relative to the central star (160 AU) of the bubble were chosen to approximately match the observed dimensions of the DG Tau bubble (Fig. 4.1). The maximum expansion velocity is set to 230 km s^{-1}, matching the highest deprojected line velocity observed in the bubble-like structure (Fig. 4.2b). The models account for the inclination of the DG Tau jet-disc system to the line-of-sight, and generate a simulated channel map of the emission from the bubble, based on an IFS with $0\farcs05 \times 0\farcs05$ spaxels and 21 km s^{-1} spectral pixels. The simulated channel maps generated from these models are shown in Fig. 4.7.

The redshifted outflow of DG Tau is well-described phenomenologically by a bubble with an internal velocity field describing expansion towards the bubble walls. Our models produce simulated channel maps in reasonable agreement with the observational data. However, the model of the bubble material expanding away from the position of the central star (Figs 4.6b, 4.7b) produces less blueshifted emission than the bubble material expanding away from the bubble centre (Figs 4.6a, 4.7a). Therefore, the model where the bubble material expands away from the central star is in better agreement with observations (Figs 4.1a, 4.7c). This suggests that the location where energy and/or momentum (§4.6.1) is being dispersed to drive the bubble expansion is closer to the central star than the centre of the bubble. We cannot definitively determine the location of this driving centre because of obscuration by the circumstellar disc (although, see §4.5.2). However, it is clear that a simple kinetic bubble model provides a good approximation to the channel maps of the receding outflow structure.

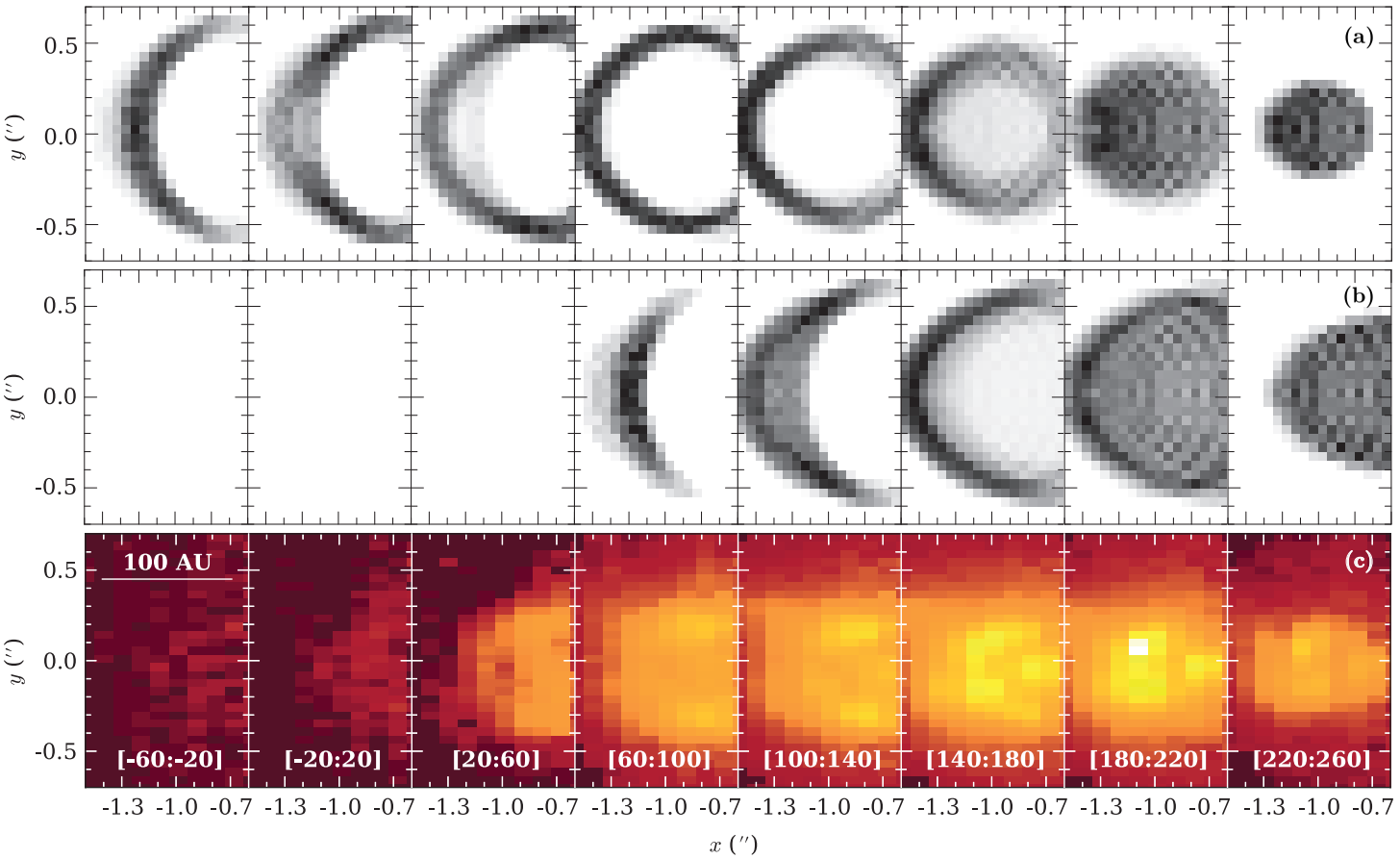

Figure 4.7 Comparison of simulated IFS data of two static, radially symmetric hemi-ellipsoidal bubble models with an internal distribution of emitting material with an expanding velocity field. (a) Bubble model where gas expansion velocity vectors point away from the centre of the bubble. (b) Bubble model where gas expansion velocity vectors point away from the central star. In both cases, the major axis of the bubble is coincident with the outflow axis, and the bubble base is positioned 0.″70 from the central star. The emitting regions of the bubble have a fixed thickness of 15 AU. Maximum gas expansion velocities are set to 230 km s^{-1}. Gas expansion velocities peak at the 'apex' of the bubble stucture, and decrease to 0 km s^{-1} at the same height above the circumstellar disc as the point from which the bubble expands. Simulated data are binned into velocity slices based on a model IFS with 0.″05 × 0.″05 spatial pixels and 21 km s^{-1} spectral pixels. Intensity scaling between each velocity slice is different. (c) Channel maps of the receding bubble in DG Tau, as observed in [Fe II] 1.644 μm line emission. Intensity scaling is the same between individual panels.

4.5. Origins of Asymmetric Outflows from AGN Modelling

We have determined that the redshifted emission from the DG Tau outflow is well-described by a model of a stationary bubble with an internal distribution of expanding, emitting material. This raises the question as to why a bubble has formed on only one side of the DG Tau star-disc system, whereas the opposing outflow has been propagating as a well-collimated large-scale outflow since at least the 1930s (§4.7.2; Eislöffel & Mundt 1998; McGroarty & Ray 2004; McGroarty et al. 2007). Given that protostellar outflows are generally thought to be instrinsically bipolar symmetric, we investigate the possibility that interaction with the ambient medium is obstructing the receding outflow from DG Tau.

Previous studies have considered the interaction of a protostellar outflow with ambient media, which could explain the observed outflow asymmetry. For example, Raga & Cantó (1995), de Gouveia Dal Pino (1999) and Raga et al. (2002a) investigated the effect of a jet impacting a smooth, dense cloud of material, which tended to deflect the jet trajectory. Delamarter et al. (2000) and Wilkin & Stahler (2003) investigated the propagation of spherical winds into a non-spherical protostellar envelope. However, none of these authors replicated the quasi-stationary bubble-like structure we observe in DG Tau.[61] In order to find a study which does replicate this structure, we turn to simulations of quasar-mode feedback.

4.5.1. Bubbles Driven by AGN Jets

In hydrodynamic simulations of outflows on the scales of AGN, Sutherland & Bicknell (2007) identified four distinct phases of a jet penetrating a two-phase interstellar medium, in which the warm phase material is a clumpy distribution of dense, fractal clouds. Immediately after being launched, the jet enters the *flood-and-channel* phase, as it searches for the path of least resistance through the clouds obstructing it. Then, as the jet head nears the edge of the distribution of clouds, it produces an *energy-driven bubble* that grows larger than the region of obstructing material. As the jet enters the *breakout* phase, it clears the remaining ambient material in its path and nears the edge of the bubble. Finally, the jet pushes through the bubble apex, and enters the *classical* phase, forming the traditional bow-shock morphology at the jet head as it propagates into the wider, more evenly distributed ambient medium (cf. the large-scale approaching DG Tau outflow; Eislöffel & Mundt 1998). Wagner & Bicknell (2011) confirmed this evolution for AGN jets driven through a clumpy ambient medium concentrated near a jet source in an approximately spherical distribution, as is believed to occur in gas-rich protogalaxies. Such a distribution of ambient material is

[61] Some of the simulations of de Gouveia Dal Pino (1999) do seem to show a small bubble-like structure being formed by the dispersed jet. This may be indicative of the situation occuring at the head of the obscured jet underlying the DG Tau bubble (§4.5.2).

also likely to result from the collapsing protostellar cloud cores that surround early-class protostars (§1.1.1.2). This evolution is well-illustrated in fig. 2 of Wagner & Bicknell (2011).

Given that the simulations mentioned above deal with AGN jets on scales of kiloparsecs, attempting to apply these results in detail to YSO outflows is inappropriate. However, it is possible to compare the structure of the DG Tau outflows to the evolutionary path described above in a morphological sense. In particular, the morphological similarity that the receding bubble of DG Tau (Figs 4.1a, 4.2a) bears to the simulations of Sutherland & Bicknell (2007, figs 2 and 3 therein), and Wagner & Bicknell (2011, fig. 2 therein), is remarkable. Furthermore, we note that the velocity field of the warm gas inside the bubble in the simulations of Wagner & Bicknell (2011, fig. 4 therein) is also consistent with our observations of DG Tau; the highest-velocity material is near the bubble head, with slower material closer to the driving source of the outflow. We also note the velocity of this gas is greater than the expansion velocity of the bubble, as observed in DG Tau (§§4.3.1, 4.3.3). In the case of DG Tau, the gas within the bubble would be stimulated into [Fe II] 1.644 μm shock-excited line emission by the deceleration of the gas into the bubble walls via shocks, and/or by the turbulence generated by the scattering of the underlying jet.

Before proceeding, we note that the AGN jet-driven bubbles are *energy*-driven, whilst stellar-driven bubbles are typically *momentum*-driven. In both cases, jet material is scattered at the point of obstruction, dissipates to some extent and moves at reduced velocity through the porous medium towards the bubble walls, where it decelerates. In a momentum-driven bubble, the shock-excited material within the bubble walls cools rapidly, so that the bubble expands at a velocity dictated by the conservation of the dispersed jet momentum. However, if the shocked gas does not cool rapidly compared to the dynamical time of the bubble, then the bubble gains a mechanical advantage from the increased thermal pressure and expands more rapidly. This subtle, but important, distinction was first made by Dyson (1984). We propose that the receding outflow of DG Tau is currently in the momentum-driven bubble phase. We present a model consistent with this in §4.6.1.

We can determine the evolutionary state of the DG Tau current outflow episode by studying the features of the approaching outflow. Given that this outflow extends beyond the NIFS field, we cannot draw conclusions concerning its evolutionary state based on our data alone. However, Eislöffel & Mundt (1998) track the blueshifted outflow out to a bow shock-like structure at 8.″7 from the central star in the mid- to late-1980s. This is thought to be the extent of the current outflow episode, with previous ejection episodes having driven outflows out to several arcminutes (§4.7.2; McGroarty & Ray 2004; McGroarty et al. 2007). This indicates that the approaching outflow has been in the classical phase for at least ~ 69 yr at the 2005 epoch, and is driving into the surrounding ISM. There is no evidence of the remnants of a bubble-like structure in the approaching outflow (§4.6.1).

It is generally assumed that collapsing molecular cloud cores are approximately spherically

symmetric (Shu et al. 1987), and outflow generation in YSOs is often assumed to exhibit bipolar symmetry. In this case, the outflows on either side of the circumstellar disc should evolve at similar rates. This is not observed in DG Tau. We appeal to further AGN outflow simulations to explain this discrepancy. Gaibler et al. (2011) simulated a bipolar AGN jet penetrating a clumpy, gaseous disc on each side of the driving galaxy. Each disc had the same mean density, but a different arrangement of dense clouds within the disc. It was found that this variation in distribution of ambient material results in a difference in time-to-breakout between the two jets of nearly a factor of 4, as a result of clouds being present directly in the jet path on one side of the jet source. We propose such an effect is occurring in DG Tau, and causes an impediment to the propagation of the receding counterjet. This makes it unnecessary to invoke an asymmetry in the jet launching mechanism to explain the differences in morphology between the two outflows.

There is observational evidence for the existence of a clumpy ambient medium above the far-side surface of the DG Tau circumstellar disc. The outermost component of the DG Tau system is a disc-shaped envelope, observed in ^{13}CO ($J = 1$–0) aperture synthesis data (Kitamura et al. 1996a). This envelope has a radius of 2800 AU, and a mass of 0.03 $M_{\odot}$, which is calculated from the total ^{13}CO flux of 40 Jy km s^{-1}, and by assuming a fractional abundance $X(^{13}\mathrm{CO}) = 10^{-6}$. It is observed to be 'clumpy' in nature, and the decrease in ^{13}CO column density within $\sim$ 4000 AU of the central star suggests that the outflows from DG Tau have already interacted with the remnant envelope and blown a large portion of it away. We propose that the remnant CO envelope is the clumpy ambient medium impeding the propagation of a receding counterjet. We now search for evidence of the presence of this counterjet.

4.5.2. Evidence for a Jet Driving the DG Tau Bubble

A jet is required to provide the energy to drive the bubble expansion as described above. We search for the presence of such a jet in our data, and determine that the morphology of the [Fe II] 1.644 μm and H_2 1-0 S(1) 2.1218 μm line emission near the base of the receding outflow structure indicates that a jet-ambient medium interaction is taking place at that location.

We investigate the [Fe II] 1.644 μm emission-line morphology and kinematics of the receding outflow to search for the presence of a counterjet. The emission knot $\sim 0\farcs84$ along the outflow axis from the central star does not seem to be a part of the bubble. This knot is located at the same distance to the central star as the tip of the brightest emission region in the approaching jet (Fig. 2.3). Furthermore, the fitted line velocity of this knot (170 km s^{-1}; Fig. 4.2b) is equal to the magnitude of the fitted line velocity of the approaching DG Tau jet at a similar distance from the central star (Fig. 2.6b). Therefore, we interpret this knot to represent a segment of a fast, well-collimated jet emerging from

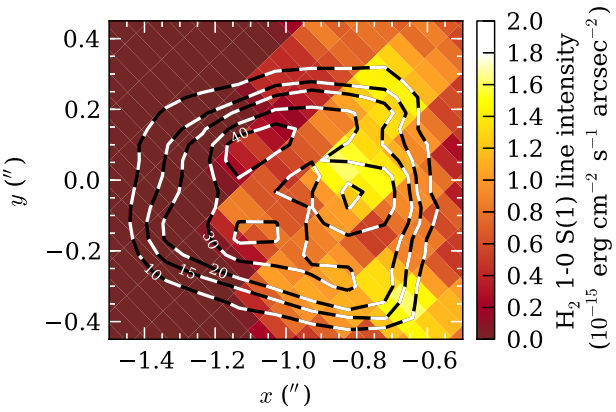

Figure 4.8 H_2 1-0 S(1) 2.1218 μm integrated emission flux of the receding DG Tau outflow, formed over the velocity range −100 to 60 km s^{-1}. Overlaid are contours (black with white dashes) of the redshifted [Fe II] 1.644 μm integrated emission-line flux from the DG Tau outflow (Fig. 4.1a), formed over the velocity range 0 to 340 km s^{-1}. Contours are labelled in units of 10^{-15} erg cm^{-2} s^{-1} arcsec^{-2}.

behind the circumstellar disc. The line-velocity map (Fig. 4.2b) shows the presence of a stream of material moving at a line-of-sight velocity $\sim$ 150–170 km s^{-1} extending from the tip of the fast jet to the apex of the bubble. We interpret this as being indicative of a stream of jet material that is being dispersed by its interaction with the remnant prestellar envelope, and driving the expansion of the bubble.

The time-evolution of the receding outflow from DG Tau (Figs 4.4, 4.5) may also be interpreted as indicating the presence of an underlying jet. Between the 2005 and 2006 observing epochs, the material that appears to have moved is the highest-velocity emitting material. In the 2009 epoch data, the 'apex' of the bubble has disappeared, and a faint trail of high-velocity material can be seen extending from behind the DG Tau disc to the edge of the NIFS field (Fig. 4.4, [180:220] km s^{-1} panel). This may be a signature of the receding DG Tau jet having achieved 'breakout' at some point shortly after the 2006 observing epoch. The small movement of the highest-velocity material at the bubble apex corresponds to the outflow beginning to push clear. The base of the bubble remains visible in [Fe II] at the 2009 epoch as a result of the continued cooling of shock-excited material. Further time-monitoring of the DG Tau outflows is required to confirm this suggestion; in particular, the observation of a typical YSO microjet emerging from the bubble remnant would be conclusive evidence.

To search for signs of the jet interacting with the molecular medium above the circumstellar disc surface, we analyse the H_2 1-0 S(1) 2.1218 μm line emission coincident with the receding outflow (Beck et al. 2008; Agra-Amboage et al. 2014). This emission is shown in Fig. 4.8, overlaid with contours of the receding DG Tau outflow as seen in [Fe II] 1.644 μm line emission (Fig. 4.1a). The H_2 emission is concentrated in three clumps along the base of the bubble. Gaussian line fitting, similar to that performed in §4.3.1, indicates that the H_2 emission is at the systemic velocity. It is unlikely that the material is moving directly across the plane of the sky, so we conclude that this material is stationary with respect to the central star.

That being established, we consider the correlation between the spatial dimensions and

positions of the receding DG Tau outflow as seen in [Fe II] 1.644 μm line emission, and the H_2 2.1218 μm line emission on the same side of the circumstellar disc. The edges of the bubble structure seen in [Fe II] 1.644 μm emission are adjacent to two enhancements in H_2 emission. The third, central H_2 emission enhancement is adjacent to the [Fe II] knot located $0\farcs84$ from the central star. In view of the systemic velocity of the H_2 emission, we propose that it originates from a cloudy ambient molecular medium above the disc surface, which we link to the extended CO envelope around the DG Tau system (§4.5). This also accounts for the 'patchy' nature of the emission compared to the observed blueshifted H_2 emission, which emanates from a wide-angle molecular wind (Beck et al. 2008, Paper I). In this picture, the central H_2 clump is the cloud that impedes the emergence of the receding DG Tau counterjet, causing the generation of an expanding bubble. The adjacent [Fe II] knot suggests that there is a jet-ambient medium interaction occurring at this point. The H_2 clumps at the edge of the bubble correspond to locations where the bubble wall is being driven through the cloud distribution, producing shock-excited emission. Beck et al. (2008) computed H_2 line populations and ratios for the extended emission around DG Tau, and concluded that the emission is stimulated by shock excitation, consistent with our hypothesis. It has previously been suggested that such H_2 emission may be stimulated in the wake of a protostellar bow shock (Hartigan et al. 1996); however, the reader will recall we excluded a bow shock as the cause of the receding outflow structure (§4.4).

Further multi-epoch data are required to confirm this proposed model. If it is correct, then we expect the appearance of a classical YSO microjet from behind the circumstellar disc as the jet continues to push through the inhomogeneous clumpy medium. The intensity of the central H_2 1-0 S(1) 2.1218 μm emission would diminish as the jet propagates further, although some residual interaction associated with entrainment may continue to excite emission. The bubble emission would then disappear over the course of a cooling time, which we estimate to be ~ 26 yr in §4.6.1.

4.6. Analytical Modelling

We have proposed that the asymmetry in the DG Tau bipolar outflow is due to the receding counterjet interacting with an inhomogeneous distribution of material above the circumstellar disc surface. This has the effect of dispersing the jet, causing the jet momentum flux to drive the expansion of a bubble structure (Sutherland & Bicknell 2007; Gaibler et al. 2011; Wagner & Bicknell 2011). The evolution of the bubble does not depend on the width or degree of collimation of the original jet; the dispersed secondary flow streams through the porous cloud distribution in all directions (Wagner et al. 2012). This turbulent, shock-excited dispersed material is the source of the [Fe II] 1.644 μm line emission observed in DG Tau. We now present an analytical model of the bubble to support our suggestion.

4.6.1. Energy-Driven or Momentum-Driven Bubble?

As mentioned above (§4.5), the bubbles driven by stellar outflows are typically momentum-driven. A characteristic of either an energy- or momentum-driven bubble is a shock front/fronts interior to the bubble walls, where dispersed outflowing material is decelerated to the velocity of the bubble wall (Dyson 1984; Bicknell et al. 1997). The ratio between the cooling time of this shocked material, and the dynamical time of the bubble, determines if the bubble is energy- or momentum-driven. If the ratio is small (large), then the bubble is momentum-(energy-)driven.

We show that the bubble in the receding DG Tau outflow is momentum-driven by estimating the cooling time of the shocked material inside the bubble, which is defined by the observable redshifted [Fe II] 1.644 μm line emission. The deprojected velocity observed in the receding outflow ≈ 230 km s^{-1} (§4.3.1). As this velocity is likely to be much greater than the bubble expansion velocity[62], we assume that this is the pre-shock gas velocity[63], $v_1 \approx 230$ km s^{-1}. The post-shock gas temperature, $T_{\rm sh}$, is then given by

$$T_{\rm sh} = \frac{3}{16}\frac{\mu m}{k} v_1^2 \tag{4.1}$$

(Weaver et al. 1977), where k is the Boltzmann constant and m is the atomic mass unit. We take $\mu = 1.4$ for a gas having a helium abundance of 10 per cent of that of hydrogen. The temperature of the post-shock gas, $T_{\rm sh} = 1.7 \times 10^6$ K. We further adopt the solar-abundance cooling function, $\Lambda(T)$, of Sutherland & Dopita (1993), which yields $\Lambda(10^6 \text{ K}) \approx 10^{-22}$ erg cm^3 s^{-1}. The electron density within the bubble is $\sim 10^4$ cm^{-3} (§4.3.2). We assume that the gas is fully ionized in the hot shocked regions. This allows for the hydrogen number density, $n_{\rm H}$, to be computed from estimates of the electron density, and the total number density, $n \approx 2.3 n_{\rm H}$ for total ionization and the above gas composition. For atomic gas, the gas cooling time, $t_{\rm c}$, is then given by

$$t_{\rm c} = \frac{3}{2}\frac{nkT_{\rm sh}}{n_{\rm e} n_{\rm H} \Lambda(T_{\rm sh})}. \tag{4.2}$$

Hence, the cooling time of the shocked gas within the bubble is approximately 26 yr.

There are no direct indicators of the age of the bubble. However, if we assume that the DG Tau outflows are driven symmetrically, we may utilize estimates based on the age of the approaching outflow. Observations of the bow shock at the head of the HH 158 complex imply that the current outflow episode in DG Tau commenced circa 1936 (Eislöffel & Mundt 1998). This defines the minimum age of the bubble of 69 yr at the 2005 epoch.

[62] This *a priori* assumption is justified in §4.6.4.

[63] This model assumes that the outflowing material is stopped in a single strong shock just interior to the bubble walls. It is more likely that this deceleration is gradual, based on the observed velocity profile of the material within the bubble (§§4.3.1, 4.6.4). Turbulence may also play a role in stimulating line emission within the bubble. However, this model remains a useful and illustrative approximation.

If the blueshifted outflow progressed through the stages of evolution described in §4.5 for a significant period of time, then 1936 represents the approximate breakout date of the blueshifted jet, and the age of the redshifted bubble might then be a factor of a few greater, i.e. up to a few hundred years. The lack of any visible bubble remnant in the blueshifted outflow suggests that there may not have been a significant momentum-bubble phase on the near side of the circumstellar disc. However, if there was a prolonged bubble phase in the approaching outflow, the lack of a remnant is not surprising, given the short bubble cooling time determined above. Therefore, we are unable to provide a conclusive upper limit to the age of the DG Tau receding bubble. However, by comparing the cooling length determined above to the minimum age of the bubble, we conclude that the cooling time of the bubble is short compared to the bubble dynamical age, and the bubble is therefore momentum-driven.

4.6.2. Bubble Evolution

Let us now consider a momentum-driven bubble model. Let $\dot{M}_\mathrm{j}$ and v_j be the mass-loss rate and velocity, respectively, of the jet driving the bubble. The radius of a spherical momentum-driven bubble, R_shell, driven by an isotropised outflow into an ambient medium of density ρ_a as a function of bubble age, t, is given by

$$R_\mathrm{shell}(t) = t^{1/2} \left(\frac{\dot{M}_\mathrm{j} v_\mathrm{j}}{\rho_\mathrm{a}} \right)^{1/4} \sqrt{\frac{3}{2\pi}} \tag{4.3}$$

(Dyson 1984). We approximate equation (4.3) to a hemi-ellipsoidal bubble by defining $R_\mathrm{shell}(t)$ to be the radius of a spherical bubble having the same volume as the hemi-ellipsoidal bubble.[64] This makes $R_\mathrm{shell}(t)$ the geometric mean of the bubble height, $x_\mathrm{h}(t)$, and the square of the bubble radius, $r_\mathrm{c}(t)$, multiplied by a geometric factor, such that

$$R_\mathrm{shell}(t) = \frac{[x_\mathrm{h}(t) r_\mathrm{c}^2(t)]^{1/3}}{\sqrt[3]{2}}. \tag{4.4}$$

We introduce a second geometric factor, f, describing the elongation of the bubble, such that

$$x_\mathrm{h}(t) = f r_\mathrm{c}(t). \tag{4.5}$$

This elongation factor may vary with time. However, on short scales compared to the bubble dynamical age, we assume self-similarity so that it is constant. The height of the

[64] Cantó et al. (2006) provide a full analytical treatment of a non-spherically symmetric wind driving into an ambient medium with a power-law density distribution. However, this detailed model is beyond the needs and scope of this comparison.

bubble as a function of time is then

$$x_{\rm h}(t) = t^{1/2} \left(\frac{3 f^{4/3}}{\pi \sqrt[3]{2}} \sqrt{\frac{\dot{M}_{\rm j} v_{\rm j}}{\rho_{\rm a}}} \right)^{1/2} . \tag{4.6}$$

Then, $x_{\rm h} \propto f^{2/3}$ and is not very sensitive to the value of f.

4.6.3. Comparison with Observations

We compare the above model to our observations of the bubble formed by the receding DG Tau outflow. We assume that the outflows driven by DG Tau are symmetric with respect to the circumstellar disc. Therefore, we assign a jet mass-loss rate of $\dot{M} = 5 \times 10^{-9}$ M$_\odot$ yr^{-1}, which is the mass-loss rate of the approaching high-velocity jet (§2.4.1.4), to the receding counterjet. We assign a jet velocity, $v_{\rm j} \approx 230$ km s^{-1}, based on both the velocity of the inner regions of the approaching jet, as well as the gas velocities observed within the bubble (Fig. 4.2).

We determine $f \approx 3.5$ from the observable redshifted emission[65] (Fig. 4.1). The bubble height is measured from the base of the observed structure to the structure apex along the large-scale outflow axis, and is corrected for the inclination of the star-disc system to the line of sight (Eislöffel & Mundt 1998). We assume that the bubble major axis is aligned to the large-scale approaching outflow axis. The observed bubble height of 150 AU is a minimum value for this parameter. If the bubble extends back to the circumstellar disc surface, it would have a height ~ 300 AU. We cannot determine the precise height of the bubble due to obscuration by the circumstellar disc, so we adopt 150–300 AU as an acceptable parameter range. The bubble radius is measured perpendicular to the large-scale outflow axis, along the base of the observable structure.

The predicted bubble height, $x_{\rm h}$, as a function of bubble age, t, is shown in Fig. 4.9. Predicted bubble heights are computed for a range of ambient hydrogen number densities, $n_{\rm H}$, from 10^5 to 10^8 cm^{-3}. Number densities are converted to mass densities assuming an ambient medium where the helium abundance is 10 per cent of the hydrogen abundance. These estimates predict that the medium into which the bubble is being driven has a number density of order $n_{\rm H} \sim 10^6$–10^7 cm^{-3}. This is larger that the average $n_{\rm H} \sim 10^5$ cm^{-3} assumed for molecular cloud cores (Bodenheimer 2011). However, this higher density is reasonable if the initial cloud core surrounding the star-disc system is still in the process of collapsing onto the circumstellar disc, as is the case with transition Class I/Class II YSOs such as DG Tau. This would increase the density in the central regions of the cloud core, as material concentrates and falls onto the circumstellar disc.

[65] Note that $f \approx 3.5$ is a height-to-radius ratio, unlike the height-to-width ratio ~ 2 used in the kinetic models in §4.4.

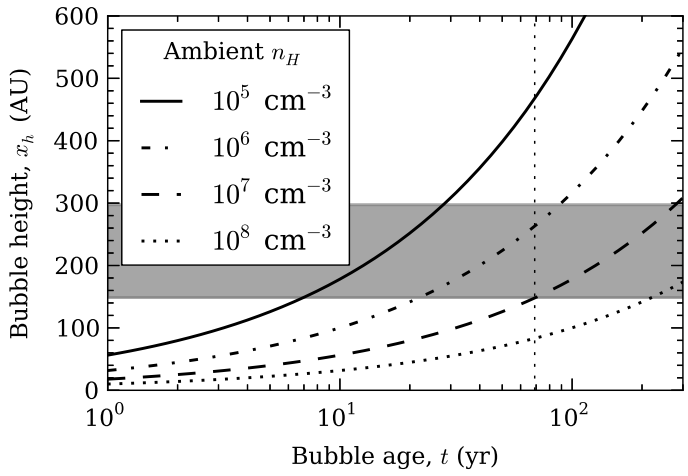

Figure 4.9 Estimated bubble heights, x_h, as a function of time for a driving jet of velocity $v \approx 230$ km s^{-1} and mass flux $\dot{M} \approx 5 \times 10^{-9}$ M$_\odot$ yr^{-1}, and a bubble of elongation factor $f \approx 3.5$, for various ambient hydrogen number densities (equation 4.6). A range of possible measured bubble heights, varying between measurement from the base of the observable receding outflow structure, and measurement from the position of the central star, are shown (grey shaded area). The approximate age of the blueshifted outflow as at 2005 is also shown (thin vertical dotted line, Eislöffel & Mundt 1998).

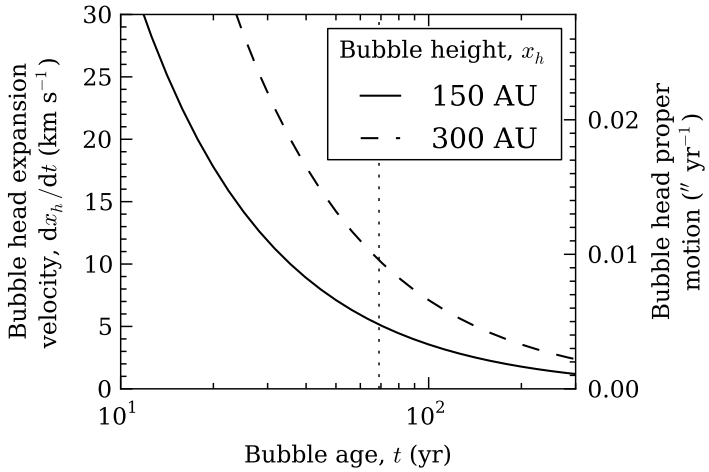

Figure 4.10 Estimated bubble head expansion velocities, d$x_\mathrm{h}(t)$/dt, as a function of bubble age, t, for the two extreme possible bubble heights at the 2005 epoch. The approximate age of the blueshifted outflow at this epoch is denoted by the thin vertical dotted line (Eislöffel & Mundt 1998). Bubble head proper motions are calculated assuming that the bubble major axis is aligned to the large-scale outflow axis.

In DG Tau, the remnant of the cloud core is the CO-emitting envelope surrounding the star-disc system (Kitamura et al. 1996a). We now estimate the density of this envelope. We approximate the envelope shape to be ellipsoidal, with a semi-major axis length of 2800 AU, and a semi-minor axis length of 160 AU, corresponding to the height of the observed molecular H_2 emission above the central star (§4.5.2). Assuming that the envelope is of uniform density, for an envelope mass of 0.03 M$_\odot$ (Kitamura et al. 1996a), we calculate its hydrogen number density $n_\mathrm{H} \sim 10^6$ cm^{-3} for the above composition. This CO-estimated ambient number density is in agreement with that predicted by our bubble model. Therefore, we conclude that our observations of the DG Tau receding outflow are consistent with a momentum-driven bubble, caused by impediment and dispersion of the receding counterjet by clumpy ambient material in the remnant envelope around the YSO.

4.6.4. Bubble Expansion Velocity

The bubble model developed above may be used to predict the expansion rate of the bubble. We note that the rate of expansion of the bubble apex can be written as

$$\frac{\mathrm{d}x_{\mathrm{h}}(t)}{\mathrm{d}t} = \frac{1}{2}\frac{x_{\mathrm{h}}(t)}{t}. \tag{4.7}$$

Estimates of the expansion velocity of the bubble head, $\mathrm{d}x_{\mathrm{h}}(t)/\mathrm{d}t$, are shown in Fig. 4.10. For the range of possible bubble heights and reasonable bubble ages (§4.6.3), the expansion rate of the bubble apex is quite slow, $\lesssim$ 5–10 km s^{-1}. This corresponds to a proper motion on the sky of $\lesssim$ 0.″005–0.″01 yr^{-1}, after accounting for the inclination of the DG Tau disc-jet system to the line of sight (Eislöffel & Mundt 1998), and assuming the bubble major axis is aligned to the large-scale outflow axis. As a result of this low expansion velocity, we predict that multi-epoch data covering at least five to ten years are required to accurately measure the bubble expansion rate, and test the accuracy of this model. However, if the jet has already achieved breakout (§§4.3.3, 4.5.2), this expansion may no longer occur.

4.7. Discussion

4.7.1. Alternative Mechanisms for the Production of Bipolar Outflow Asymmetry

Our interpretation of the observed outflow asymmetry in DG Tau as due to the impediment of the receding jet by ambient material does not necessarily exclude other proposed explanations for bipolar outflow asymmetry (§4.1). Proposed mechanisms include variations in the near-stellar magnetic field morphology (HD 163296; Wassell et al. 2006), a warped circumstellar disc (HH 111, driven by VLA 1; Gómez et al. 2013), an interaction between a bipolar (quadrupolar) stellar magnetic field and a quadrupolar (bipolar) circumstellar disc magnetic field (Matsakos et al. 2012), or some unspecified mechanism that drives bipolar jets with differing mass-loss rates, but a balance of linear momentum between the two sides of the outflow (Liu et al. 2012). We find no evidence through which to exclude any of the proposed mechanisms, predominantly because the obscured counterjet has yet to propagate (and brighten) a sufficient distance from behind the circumstellar disc to measure its physical parameters and kinematics. However, our model of a jet obscured by an asymmetric ambient medium is the only one to explain the *physical* structure of the receding DG Tau outflow. All other models were constructed to explain bipolar *velocity* asymmetry only.

Our model accounts for the velocity asymmetries detected in long-slit spectroscopic data of bipolar YSO outflows (e.g. Hirth et al. 1994b, 1997). Based on our data, a long-slit

spectrographic observation of DG Tau at the 2005 epoch, with the slit aligned along the outflow axis, would have observed a bipolar outflow velocity asymmetry. At the greatest distance from the central star visible in the NIFS field, the line velocity of the receding outflow is $v_{\rm r} \sim 180$ km s^{-1}, whereas the highest-velocity component of the approaching outflow has a line velocity of $v_{\rm a} \sim 240$ km s^{-1} at the same distance from the central star (Fig. 2.6). This would appear in a spectroscopic observation of the DG Tau outflows as a velocity asymmetry between the two outflows of $v_{\rm a}/v_{\rm r} \sim 1.3$. Although at the lower end of the range of detected velocity asymmetries in bipolar YSO outflows (e.g. Hirth et al. 1994b, 1997), it is in agreement with the velocity asymmetry between the DG Tau outflows reported by Lavalley et al. (1997). We suggest spectroimaging follow-up of TTS with bipolar outflow velocity asymmetry would allow structural outflow asymmetry similar to that observed in DG Tau to be detected, and test if the model described above is applicable to other YSOs. We do note that there are some objects, e.g. RW Aur, which show outflow velocity asymmetries ($\Delta v \sim 65$ km s^{-1} between the two outflows lobes) very close to the central star, and no clear sign of jet/cloud interaction (Woitas et al. 2002). An alternative model for bipolar velocity asymmetries in such objects is required.

4.7.2. Implications for Episodic Ejections

The approaching HH 158 outflow driven by DG Tau extends $\sim 12''$ from the central star in 2001–2003 (McGroarty et al. 2007), and terminates in a bow shock that is interpreted to be the head of the current outflow event (Eislöffel & Mundt 1998). More recently, Sun et al. (2003) and McGroarty & Ray (2004) independently identified another Herbig–Haro complex, HH 702, a $\sim 4'$-long shock system centred $\sim 11'$ from DG Tau. This HH complex sits at approximately the same position angle from DG Tau as HH 158, and has been determined to be driven by DG Tau, based on analysis of the proper motions and radial velocities of the knots within the complex (McGroarty et al. 2007). A similar complex, HH 830, was observed at the same distance from DG Tau diametrically opposed to HH 702, but has been determined to not be driven by DG Tau. Hence, the bipolar asymmetry in the DG Tau outflows extends to scales of ~ 0.5 pc from the central star (Fig. 1.12; McGroarty & Ray 2004; McGroarty et al. 2007).

Several other YSOs have also been identified as having associated HH complexes up to ~ 1 pc from the inferred driving source. The location and morphology of these complexes is highly suggestive of periods of relative outflow inactivity, interspersed with mass ejections of various strengths (McGroarty et al. 2007). It has been suggested that this process is linked to the FU Orionis outburst phenomenon, where the optical brightness of a YSO rapidly increases by several orders of magnitude before decreasing back to its original luminosity over a period of 50–100 yr (Hartmann & Kenyon 1996; Reipurth & Aspin 1997). The dynamical time-scales of these parsec-scale YSO outflows were originally thought to

match the mean time estimated between FU Orionis outbursts of 10^4 yr (Herbig 1977; Herbig et al. 2003), although the most recent estimates of these outflow event dynamical time-scales are of order 10^3 yr (McGroarty et al. 2007).

It would appear that previous outflow episodes from DG Tau have failed to clear a path through the ambient medium on the far side of the circumstellar disc, given the lack of associated Herbig–Haro objects at large distances on the receding side of the outflow, and the nature of the current receding outflow close to the circumstellar disc. The shape of the extended CO envelope suggests that a significant amount of ambient material has been driven off by the approaching outflow, but not the receding outflow, which suggests the receding outflow has failed to clear the envelope. However, it is possible that a large-scale redshifted outflow does exist, but is hidden from view as it recedes into the large-scale molecular cloud behind DG Tau (McGroarty et al. 2007). Such an outflow would have cleared a channel through the ambient material immediately above the disc in order to escape. Indeed, the ^{13}CO(2-1) map of Testi et al. (2002) seems to indicate a channel may have been cleared through the material around DG Tau by a receding outflow. If so, this raises the question of why the present receding outflow is not using the same cleared channel, and propagating to the same distance from the central star as the approaching outflow.

We determine that an outflow channel formed through the extended envelope immediately above the circumstellar disc (Kitamura et al. 1996a) could close over between ejection events, based on simple estimates. The dynamical age of the observed large-scale DG Tau outflow is estimated to be $\sim 2.3 \times 10^3$ yr (McGroarty et al. 2007), which leads to a time between high-mass flux ejection events of $\sim 2.2 \times 10^3$ yr, assuming the most recent ejection event began in 1936 (Eislöffel & Mundt 1998). Based on the length of the HH 702 complex of $4'$, and the average proper motion of the HH 702 knots of ~ 175 km s^{-1}, we estimate the dynamical time of the previous high-mass flux outflow event to be ~ 900 yr. This leaves a time period of $\sim 1.3 \times 10^3$ yr during which the outflows from DG Tau would be comparatively weak.

Let us suppose that the receding outflow cleared a path through the extended envelope above the circumstellar disc during a previous ejection event. We assume that the width of this channel is ~ 40 AU, corresponding to the largest jet diameter observed in the approaching DG Tau microjet (Paper I). We estimate the sound speed in the molecular cloud core to be ~ 0.3 km s^{-1}, assuming a typical molecular cloud core temperature of ~ 10 K (Bodenheimer 2011) and a molecular medium with adiabatic index $\gamma = 7/5$. The crossing time over the width of the channel is then ~ 630 yr. The period of inactivity in the outflows is $\gtrsim 2$ times the crossing time of the channel, indicating the channel may become closed over during the period of relative quiescence. Therefore, we conclude that either side of the DG Tau outflow may be required to go through a bubble-driving phase for *any* ejection event. Whether this occurs or not is completely dependent on whether the

motions of the ambient material above the circumstellar disc close the channel created by the previous outflow event. As mentioned above (§4.6.1), the cooling time in these bubbles is short, so there would be little observable remnant of the bubble within a few decades after the jet achieves break-out.

4.8. Conclusions

We have investigated the nature of the receding microjet-scale outflow of the YSO DG Tauri, utilizing high-resolution spectroimaging data taken with the Near-infrared Integral Field Spectrograph (NIFS) on Gemini North. In the H band, the outflow appears as a large bubble-like structure in [Fe II] 1.644 μm line emission. This is in stark contrast to the approaching outflow, which shows a two-component outflow, consisting of a high-velocity jet surrounded by a lower-velocity disc wind, stimulated into emission by turbulent entrainment (§§2.4.2, 3). In the K band, 'clumpy' H_2 1-0 S(1) 2.1218 μm line emission is observed near the edge of the circumstellar disc, coincident with some of the brightest regions of redshifted [Fe II] emission. Line fits of this emission showed that the H_2-emitting gas is at the systemic velocity, indicating that it represents material stationary with respect to the central star instead of an outflow component.

The emission-line velocity structure of the receding outflow is well-described by kinetic models of bubbles with an internal distribution of expanding, radiating gas. These models generate simulated emission line channel maps from input parameters such as bubble height, elongation, distance to the outflow source, and inclination of the outflow axis to the line of sight. Simulated IFU data produced by the models show our observational data are consistent with the presence of a stationary bubble, with an internal distribution of emitting gas expanding towards the bubble walls.

We compared the current appearance of the receding DG Tau bubble with the four-stage evolutionary track for AGN jet-driven bubbles proposed by Sutherland & Bicknell (2007), and further refined by Wagner & Bicknell (2011). We concluded that the DG Tau receding outflow is forming a momentum-driven bubble at the 2005 observing epoch, morphologically similar to the energy-driven bubble phase identified by Sutherland & Bicknell (2007). The receding counterjet is being blocked by a cloud of ambient medium in its path. As the jet begins to push past the clump, it blows a large bubble, which extends further than the distribution of material that is blocking its progress. We interpreted the observed H_2 emission as being indicative of such a clumpy medium above the surface of the circumstellar disc, which is interacting with both the jet and the expanding bubble. This interpretation is supported by the presence of an [Fe II] emission enhancement adjacent to one of the H_2 clumps, which suggests a jet-ambient medium interaction point. The presence of a clumpy, large-scale residual envelope of molecular material around DG Tau has been observed

previously (Kitamura et al. 1996a), lending further weight to this interpretation.

Our multi-epoch data support this interpretation. Between 2005 and 2006, the bubble is effectively stationary, except for a small ($\sim$ 70–90 km s^{-1}) movement of the highest-velocity emitting material at the bubble apex. In 2009, this high-velocity material has disappeared. This may be indicative of the jet driving the bubble achieving breakout at some point after the 2006 observing epoch, leaving just the base of the bubble observable in the 2009 epoch.

We constructed an analytical model of a jet momentum-driven bubble. This model describes the evolution of a bubble driven by a dispersed jet, propagating into a smooth ambient medium. Based on the physical scale of the receding DG Tau bubble, this model predicts that the ambient medium number density above the circumstellar disc surface is of order 10^6 to 10^7 cm^{-3}, which is in agreement with density estimates of the extended CO envelope around DG Tau. The model predicts a bubble expansion of $\lesssim$ 5–10 km s^{-1} at the bubble head, which can be tested with multi-epoch observational data covering a five- to ten-year period. The cooling time of the bubble is estimated to be $\sim$ 26 yr. This is the time-scale on which the bubble disappears due to cooling once the jet head moves beyond the apex of the bubble. This also implies that the bubble is momentum-driven, as this cooling time is short compared to the estimated dynamical age of the bubble.

Our conclusions do not necessarily exclude other proposed models for YSO bipolar outflow asymmetry. However, an asymmetric ambient medium obstructing the evolution of a symmetric bipolar outflow is the only model that explains the morphology of the receding DG Tau outflow. We have demonstrated that a long-slit spectrographic observation of DG Tau would weakly replicate the bipolar outflow velocity asymmetry observed in long-slit spectrographic observations of other YSOs, and is in agreement with the previous spectroscopic measurement for DG Tau (Lavalley et al. 1997). We have also shown that the outflow channel formed by an episode of outflow activity may close over during periods of relative outflow quiescence, based on observations of the large-scale DG Tau approaching outflow $\lesssim$ 0.5 pc from the central star. This implies that both the approaching and receding outflows from DG Tau may be forced to evolve through a bubble phase for any given outflow event.

Multi-epoch data of DG Tau is the best method to test these conclusions. Our analysis has provided robust predictions of the evolutionary path that the bubble will take once the underlying jet breaks free of the ambient medium that obstructs its progress. These predictions may be directly compared to future observations.

Acknowledgements

Based on observations obtained at the Gemini Observatory, which is operated by the Association of Universities for Research in Astronomy, Inc., under a cooperative agreement

with the NSF on behalf of the Gemini partnership: the National Science Foundation (United States), the National Research Council (Canada), CONICYT (Chile), the Australian Research Council (Australia), Ministério da Ciência, Tecnologia e Inovação (Brazil) and Ministerio de Ciencia, Tecnología e Innovación Productiva (Argentina).

We are extremely grateful for the support of the NIFS teams at the Australian National University, Auspace, and Gemini Observatory for their tireless efforts during the instrument integration, commissioning and system verification: Jan Van Harmleen, Peter Young, Mark Jarnyk (deceased), Nick Porecki, Richard Gronke, Robert Boss, Brian Walls, Gelys Trancho, Inseok Song, Chris Carter, Peter Groskowski, Tatiana Paz, John White, and James Patao.

We thank the anonymous referee for his/her comments on the manuscript. We wish to thank A. Y. Wagner for fruitful discussions on the nature of jet-driven bubbles, and for useful comments on a draft version of this paper. MW acknowledges the generous travel support from Academia Sinica to attend the conference Star Formation Through Spectroimaging at High Angular Resolution in July 2011, which provided useful information for this study. This work was supported by the Australian Research Council through Discovery Project Grant DP120101792 (R. Salmeron).

CHAPTER 5

Conclusions

In this thesis, we have conducted a comprehensive analysis of the microjet-scale outflows driven by the protostar DG Tauri. Such protostellar outflows are ubiquitous throughout the accretion phase of the star-formation process, and are thought to play a critical role in extracting angular momentum from young stellar objects (YSOs) as material accretes towards the central object. Although this thesis focuses on a single young stellar object, the conclusions we draw from this work are potentially applicable to a broad range of protostellar outflow studies (see below).

Our data reveal the presence of three main components to the DG Tau small-scale outflows (§2/White et al. 2014c): a high-velocity, well-collimated approaching jet, a wider-angle approaching intermediate-velocity forbidden-line component, and a bubble-shaped receding outflow. We investigated the properties of the approaching outflow components after separating their emission via a rigorous multicomponent Gaussian fitting procedure.

One of the most striking features of the approaching jet is a stationary emission enhancement $\sim 0\farcs2$ from the central star, which we interpret to be a stationary recollimation shock. The properties of this shock indicate that the jet is launched from 0.02–0.07 AU, a much smaller radius than was previously inferred. Also contrary to previous studies, we find no evidence for jet rotation once we account for the variation of the position of the jet ridgeline. There does not appear to be a consistent period between knot ejection events, based on a comparison between knot B (observed by us) and the fast knot reported by Dougados et al. (2000).

Passage through a recollimation shock will significantly alter the downstream properties of the jet. This effect must be taken into account when attempting to calculate outflow properties closer to the source as a function of properties downstream of the shock. Therefore, the detection of recollimation shocks is important to protostellar outflow studies such as this one. Whilst no other protostar is known to possess a recollimation shock

observable in forbidden lines, these shocks can be detected in X-rays (e.g. Güdel et al. 2005, 2008, 2011; Bonito et al. 2011), and we have demonstrated that they may be observed in forbidden lines *if* an occulting disc is used to obscure the central star. We therefore suggest than an effort should be made to detect similar structures in the outflows from other well-studied protostars.

Contrary to previous claims, we find no evidence of rotation in the DG Tau approaching microjet. The previously-claimed signature disappears when the position of the jet ridgeline is taken into account. Previous studies were unable to simultaneously track the jet ridgeline, and the behaviour of the Doppler velocity shifts across the ridgeline, as a function of distance along the outflow. Therefore, we suggest that integral-field spectroscopy is the ideal tool for probing rotation in YSO microjets.[66] However, we also note that the inferred widths of these jets are only marginally greater than the spatial resolution of current adaptive-optics systems. It may be necessary to await 0″.02-resolution optical/NIR instruments, such as the GMTIFS instrument planned for GMT (McGregor et al. 2012), before claiming a definitive answer to the rotation question.

We interpret the approaching intermediate-velocity component as being emitted by an entrainment layer along the jet boundaries (§2.4.2). We argue that the toroidal magnetic field that provides jet collimation can also facilitate the formation of Kelvin-Helmholtz instabilities along the jet boundary, causing turbulent mixing between the jet and the molecular wind. In Chapter 3 (White et al. 2014b), we construct a two-dimensional analytical model of such a mixing layer. The model is based on a Riemann decomposition of the directly observable parameters of protostellar outflows, e.g. density, velocity, pressure and magnetic field, into average and time-varying components. By substituting these components into the conservation equations of MHD, we are able to find expressions for the mixing layer luminosity and mass entrainment rate, which may be directly compared to observations. The estimates provided by our model match our observations to the correct order of magnitude.

Since the mid-1990s, the concept of lateral entrainment in protostellar jets has fallen out of favour, due to (a) the belief that such highly supersonic flows are not susceptible to the KH instability, and (b) the argument that these jets will clear away ambient material as they propagate outwards, leaving no material with which to form a turbulent mixing layer. However, we have shown that lateral entrainment is possible in these jets; the jet toroidal magnetic field may facilitate the formation of KH instabilities, and the presence of the molecular wind provides a reservoir of material for entrainment. The model developed in §3 is an advance to the field, because it does not rely on arbitrary parameters estimated from laboratory experiments. Indeed, the 'entrainment efficiency' obtained from

[66] We note that a spectroscopic technique similar to that of Coffey et al. (2004, 2007, 2012), but utilizing multiple cross-jet slits spaced along the outflow axis, would also allow for simultaneous tracking of the jet centre, and any changes in the inferred rotation along the outflow. However, such observations would be time-consuming compared to equivalent IFS observations.

our modelling is far greater ($\sim$ two orders of magnitude) than what was derived from laboratory experiments used in previous models. Our model provides a consistent framework for testing the suitability of the turbulent mixing layer interpretation in protostellar outflow observations, using only data directly obtained from those observations.

We investigated the nature of the receding outflow in Chapter 4 (White et al. 2014a). Our multi-epoch data reveal that the observed structure is not a classical bow-shock, as has been previously suggested. Instead, we used kinetic models to show that the bubble itself is quasi-stationary, and contains a distribution of emitting gas expanding towards the bubble walls. We compare our observations to the morphology of numerical simulations of the interactions between jets and clumpy ambient media in active galactic nuclei, and propose a similar scenario may be occurring in DG Tau; namely, a receding counterjet is blocked by the clumpy protostellar envelope. The jet is dispersed at this point, producing a bubble-shaped cocoon as it attempts to escape. Comparison to the evolutionary sequence of such structures suggests that the receding DG Tau outflow is currently in the momentum-driven bubble phase. Based on this conclusion, we obtain analytical estimates of the properties of the bubble, and find that they agree with our observations. This work introduces a new paradigm to the possible causes of bipolar asymmetry in YSO outflows.

Our model of the DG Tau microjet-scale outflow system, the most complete such model to date, may be summarized as follows (Fig. 5.1). The DG Tau star-disc system drives intrinsically bipolar-symmetric outflows. The approaching outflow shows the classical YSO microjet morphology of a central, well-collimated, high-velocity jet, surrounded by an intermediate-velocity component, and a wide-angle molecular wind. There is a strong recollimation shock at the base of this jet, $\lesssim 50$ AU from the central star, which significantly reduces the velocity of the jet from the pre-shock velocity, estimated to be 400–700 km s^{-1}, to a velocity of ~ 215 km s^{-1}. The jet then accelerates to ~ 315 km s^{-1}; this is likely due to intrinsic variations in the jet velocity. The jet emission is predominantly from bright, shock-excited moving knots, which are ejected into the jet channel quasi-periodically. The toroidal magnetic field encasing the jet facilitates the growth of the Kelvin-Helmholtz instability at the jet boundaries, which leads to the formation of a turbulent mixing layer between the jet and the molecular wind. This mixing layer is the source of the intermediate-velocity emission. On the far side of the DG Tau circumstellar disc, the clumpy protostellar envelope around DG Tau impedes the progress of the receding counterjet, causing the observed bipolar outflow asymmetry. The receding counterjet drives a slowly-expanding bubble as it attempts to clear a path through the ambient medium.

The work presented in this thesis demonstrates that microjet-scale outflows from YSOs are more complex than previously thought (§1.5; also, compare Fig. 5.1 to Fig. 1.7). Complex interactions between outflow components (e.g. turbulent mixing), and between the outflows and ambient material (e.g. jet-blown bubbles), are important. Furthermore, some outflow components are clearly not self-similar (e.g. the recollimation shock in the approaching jet).

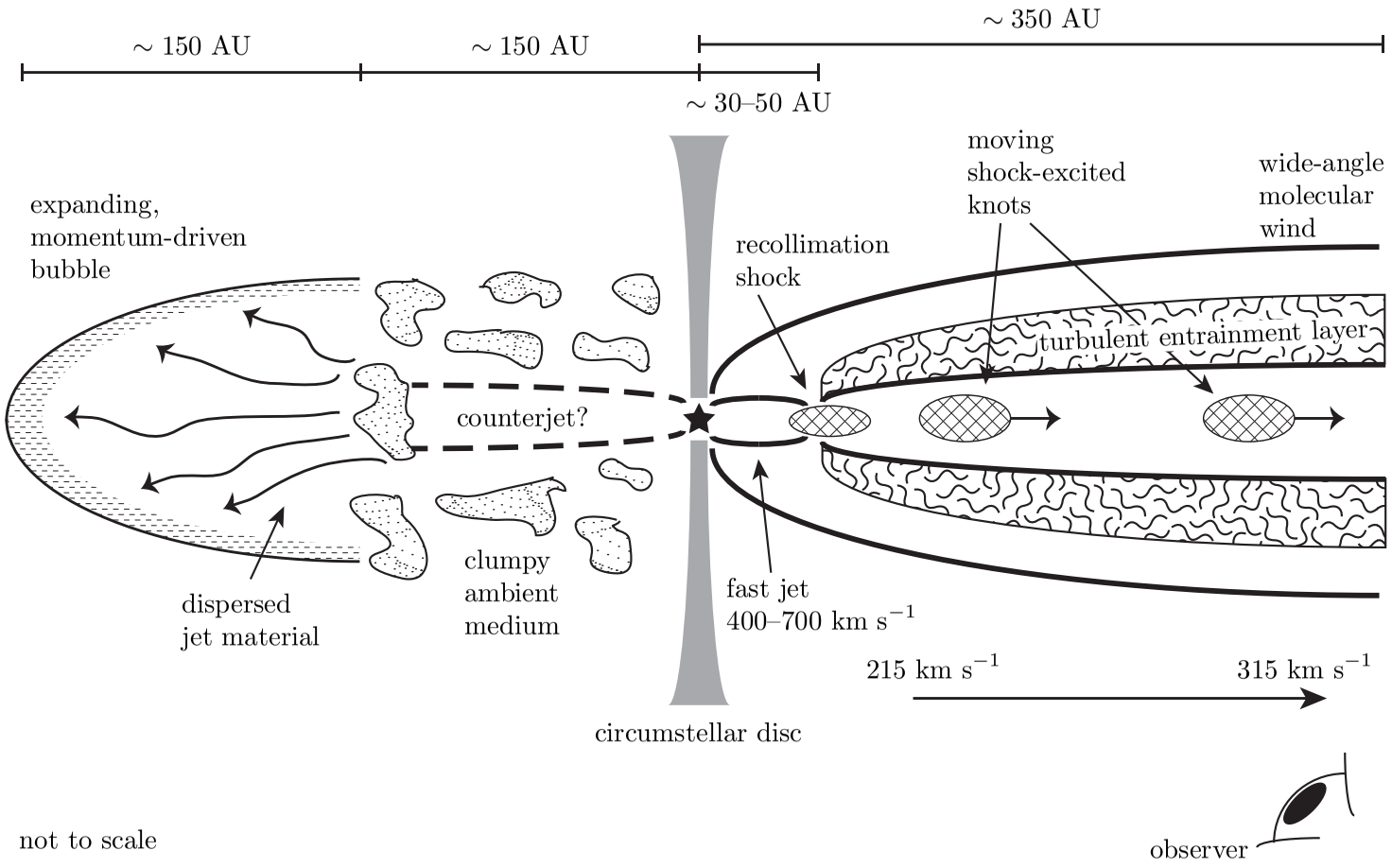

Figure 5.1 Schematic of the DG Tau system, as proposed in this thesis. The outflows are intrinsically bipolar symmetric; the observed asymmetry is the result of the receding counterjet dispersion by the clumpy protostellar envelope above the disc surface. The unimpeded approaching outflow consists of a central, well-collimated, high-velocity jet surrounded by a wide-angle molecular wind. The jet is launched from a disc radius $\lesssim 0.1$ AU, and has a terminal velocity 400–700 km s^{-1}, but is slowed to ~ 215 km s^{-1} by passage through a stationary recollimation shock. Downstream of this shock, the jet is dominated by moving shock-excited knots, which are ejected quasi-periodically into the jet channel. These knots are likely created by the observed velocity variations in the jet. A turbulent mixing layer forms between the jet and the wide-angle molecular wind, giving rise to the observed intermediate-velocity forbidden-line emission component.

Therefore, the parameters of the outflow components observed even as close as 100–200 AU from the central star may not be representative of the intrinsic parameters of the outflow, and thus are not a clear indicator of the outflow launch mechanism.

More generally, this study provides a framework for the study of protostellar outflows in the era of ALMA and GMT. The role of ALMA in examining the chemistry and kinematics of circumstellar discs is well-documented (e.g. van Dishoeck & Jorgensen 2008; Qi et al. 2013). However, ALMA is also suited for the analysis of molecular outflows in deeply embedded Class 0/I protostars (Shepherd 2008); indeed, such work has already begun (e.g. Klaassen et al. 2013; Kristensen et al. 2013). As a transition Class I/Class II protostar, DG Tau provides an example of the complex physics occurring in hundred-AU-scale protostellar outflows in the presence of ambient material. Some of these mechanisms, such as entrainment and differing outflow morphologies, are ALMA science targets (Shepherd 2008). The model proposed here provides a useful guide and comparison to the outflow structures that may be detected when ALMA reaches full spatial and spectral resolution (see below), and complement the ongoing theoretical work to predict the form of these deeply-embedded nascent outflows (e.g. Peters et al. 2014).

5.1. Future Work

As mentioned above, some outstanding questions on the dynamics of YSO microjets, such as rotation, may have to await the advent of GMT to be answered. However, the ongoing commissioning of ALMA provides excellent avenues for further study. As an instrument geared towards observing molecular lines and dust, ALMA is unlikely to be applied directly to atomic microjets; however, significant opportunities for complementary work exist. For example, when ALMA reaches its full design spatial ($\sim 0\farcs01$) and spectral (~ 0.01 km s^{-1}) resolution (Wootten & Thompson 2009), it will be able to map the molecular line emission from the circumstellar disc with exquisite precision. In particular, the potential exists to probe the kinematics of the CO emission from the innermost radii of the disc, and use NIR/optical IFS observations such as those presented here to investigate the correlation between the CO variability and the ejection of 'knots' in to the outflow channel (§2.3.1). ALMA may also be able to detect the wide-angle molecular winds in CTTS, potentially at the point of launching, which would provide unequivocal evidence of their origin.

Below, we briefly detail some possibilities for interesting follow-on work to that presented in this thesis.

Further DG Tau observations. Our multi-epoch data of DG Tau were presented, in part, in §2 and §4. However, a full analysis of the kinematics of the approaching outflow in the 2006 and 2009 observing epochs has yet to be conducted. Channel maps of the approaching outflow for all three epochs (Fig. 5.2) show that the peak

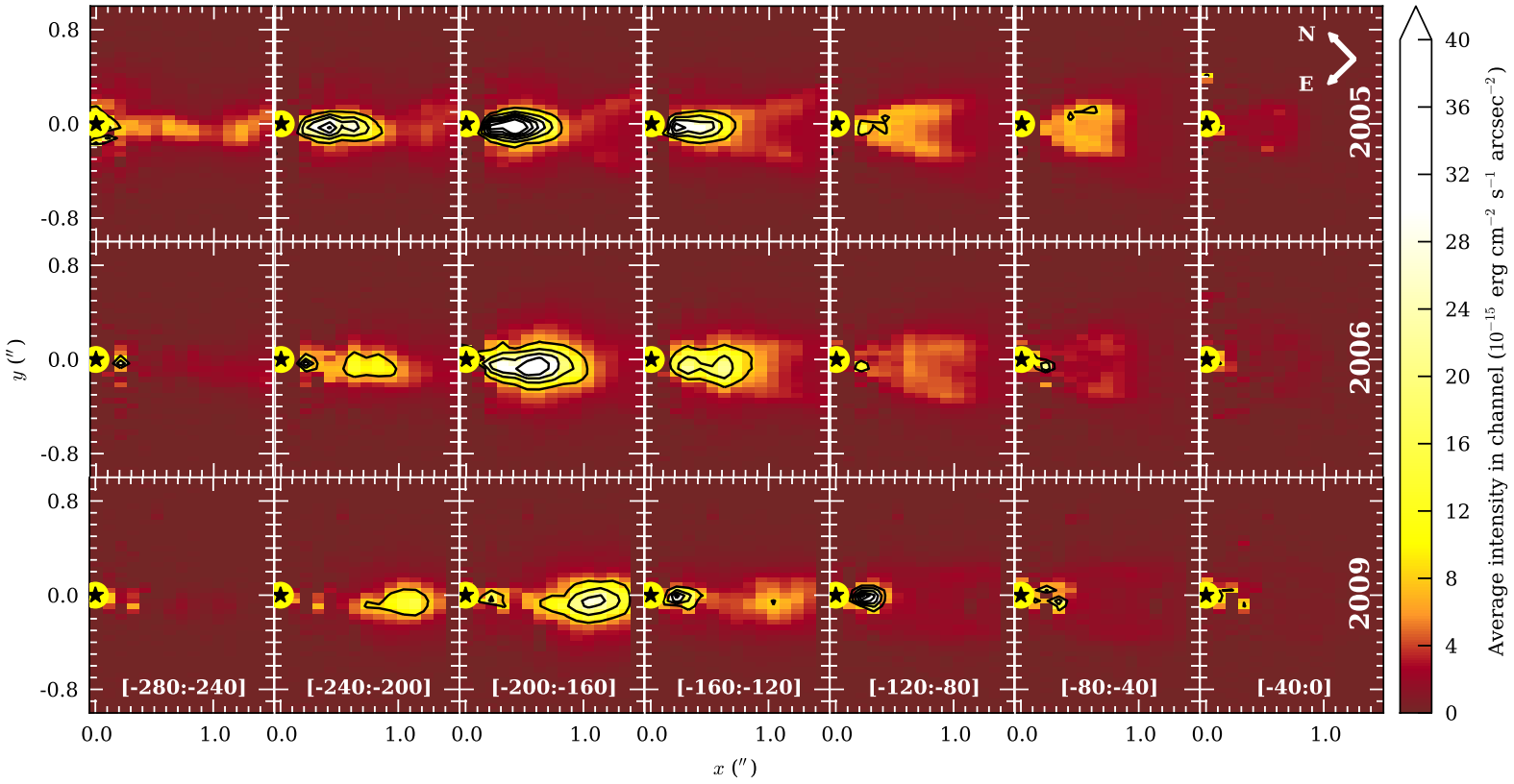

Figure 5.2 Channel maps of the DG Tau approaching outflow, 2005–2009. Panels show images of the extended [Fe II] 1.644 μm line emission around DG Tau, binned into 40 km s^{-1}-wide slices, for (*top-to-bottom*) the 2005, 2006 and 2009 observing epochs. The velocity range of each slice is shown at the bottom of each column. The intensity values quoted are the average intensity in each channel over the 40 km s^{-1} velocity range. Contours are placed at levels of $[8, 16, \ldots, 48] \times 10^{-15}$erg cm^{-2} s^{-1} arcsec^{-2}. The black star corresponds to the position of the central star, DG Tau, and the yellow circle indicates the position and size of the 0.″2 diameter occulting disc.

line velocity of the stationary recollimation shock has decreased from 2005 to 2009. Assuming that the post-recollimation shock velocity of the jet is related monotonically to the pre-shock velocity, this implies jet velocity variability, as invoked to explain the moving knots in the jet channel (§2.4.1.1). Multicomponent line fitting of the 2006 and 2009 epoch data will allow us to quantify this variability, as well as investigate the time-evolution of the turbulent mixing layer as moving knots travel along the jet.

Jet recollimation shocks. The simulation of Bonito et al. (2011) provides convincing evidence that a recollimation shock is the source of the stationary X-ray/FUV/NIR emission observed in the L1551 IRS 5 jet. However, the fraction of jet mass which radiates in X-rays remains unclear. Computing a simulation similar to that of Bonito et al., but tailored to the parameters of the DG Tau outflow, would allow us to investigate the fraction of jet mass flux that emits in X-rays, and could potentially explain the mass-loss rate discrepancy between X-ray and NIR observations (§2.4.1.2). Such simulations could also be used to determine the effect of the recollimation shock on jet rotation signatures (§2.4.1.6), and the effect of jet velocity variability on the shock structure (see above).

Jet-envelope interaction. Our analytical calculations (§4.6) have shown that the jet-driven bubble mechanism of Sutherland & Bicknell (2007) is the likely cause of the receding bubble structure in the DG Tau outflows. To further strengthen this result, calculating simulations akin to Wagner & Bicknell (2011) and Gaibler et al. (2011) will allow us to determine the energetics of this mechanism in the protostellar case, and in particular, quantify the possible times-to-breakout of protostellar outflows from their parent envelopes. This work would also have direct application to the deeply-embedded outflows to be probed by ALMA (see above).

Entrainment. Expansion of our model for turbulent lateral entrainment (§3) to three dimensions will be an illustrative development, and is necessary to correctly calculate the extent of the laminar jet phase (§3.4.2). A numerical parameter-space study of the magnetic field strength and orientation required for lateral entrainment (§2.4.2.2) would also be useful; however, such a program would be highly complex, and computationally expensive.

Bibliography

Adams, F. C., Emerson, J. P., Fuller, G. A. *ApJ*, *357*, 606–620, 1990

Adams, F. C., Lada, C. J., Shu, F. H. *ApJ*, *312*, 788–806, 1987

Agra-Amboage, V., Cabrit, S., Dougados, C., Kristensen, L. E., Ibgui, L., Reunanen, J. *A&A*, *564*, A11, 2014

Agra-Amboage, V., Dougados, C., Cabrit, S., Reunanen, J. *A&A*, *532*, A59, 2011

Ainsworth, R. E., Ray, T. P., Scaife, A. M. M., Greaves, J. S., Beswick, R. J. *MNRAS*, *436*, L64–L68, 2013

Alecian, E., Wade, G. A., Catala, C., Folsom, C., Grunhut, J., Donati, J.-F., Petit, P., Bagnulo, S., Boehm, T., Bouret, J. C., Landstreet, J. D. In J. Bouvier, I. Appenzeller, eds., *Star-Disk Interaction in Young Stars*, vol. 243 of *IAU Symp.*, pp. 43–50. Cambridge: Cambridge University Press, 2007

Allen, L. E., Megeath, S. T., Gutermuth, R., Myers, P. C., Wolk, S. J., Adams, F. C., Muzerolle, J. M., Young, E. T., Pipher, J. L. In B. Reipurth, D. Jewitt, K. Keil, eds., *Protostars and Planets V*, pp. 361–376. Tucson: University of Arizona Press, 2007

Allen, M. G., Groves, B. A., Dopita, M. A., Sutherland, R. S., Kewley, L. J. *ApJS*, *178*, 20–55, 2008

Allington-Smith, J., Content, R. *PASP*, *110*, 1216–1234, 1998

Ambartsumian, V. A. *Stellar Evolution and Astrophysics*. Yerevan: Armenian Academy of Science, 1947

Anderson, J. M., Li, Z.-Y., Krasnopolsky, R., Blandford, R. D. *ApJ*, *590*, L107–L110, 2003

André, P., Ward-Thompson, D., Barsony, M. *ApJ*, *406*, 122–141, 1993

———. In V. Mannings, A. P. Boss, S. Russell, eds., *Protostars and Planets IV*, p. 59. Tucson: University of Arizona Press, 2000

Andrews, S. M., Williams, J. P. *ApJ*, *631*, 1134–1160, 2005

Antonucci, R. *ARAA*, *31*, 473–521, 1993

Appenzeller, I., Mundt, R. *A&AR*, *1*, 291–334, 1989

Arce, H. G., Goodman, A. A. *ApJ*, *575*, 928–949, 2002

Arce, H. G., Sargent, A. I. *ApJ*, *612*, 342–356, 2004

Arce, H. G., Shepherd, D., Gueth, F., Lee, C.-F., Bachiller, R., Rosen, A., Beuther, H. In B. Reipurth, D. Jewitt, K. Keil, eds., *Protostars and Planets V*, pp. 245–260. Tucson: University of Arizona Press, 2007

Ardila, D. R., Basri, G., Walter, F. M., Valenti, J. A., Johns-Krull, C. M. *ApJ*, *566*, 1100–1123, 2002

Ardila, D. R., Herczeg, G. J., Gregory, S. G., Ingleby, L., France, K., Brown, A., Edwards, S., Johns-Krull, C., Linsky, J. L., Yang, H., Valenti, J. A., Abgrall, H., Alexander, R. D., Bergin, E. A., Bethell, T., Brown, J. M., Calvet, N., Espaillat, C., Hillenbrand, L. A., Hussain, G., Roueff, E., Schindhelm, E. R., Walter, F. M. *ApJS*, *207*, 1, 2013

Aspin, C., Beck, T. L., Reipurth, B. *AJ*, *135*, 423–440, 2008

Aspin, C., Reipurth, B., Beck, T. L., Aldering, G., Doering, R. L., Hammel, H. B., Lynch, D. K., Meixner, M., Pecontal, E., Russell, R. W., Sitko, M. L., Thomas, R. C., U, V. *ApJ*, *692*, L67–L71, 2009

Audard, M., Briggs, K. R., Grosso, N., Güdel, M., Scelsi, L., Bouvier, J., Telleschi, A. *A&A*, *468*, 379–390, 2007

Bacciotti, F. *Rev. Mex. A. A. (Ser. de Conf.)*, *13*, 8–15, 2002

Bacciotti, F., Eislöffel, J. *A&A*, *342*, 717–735, 1999

Bacciotti, F., Mundt, R., Ray, T. P., Eislöffel, J., Solf, J., Camezind, M. *ApJ*, *537*, L49–L52, 2000

Bacciotti, F., Ray, T. P., Mundt, R., Eislöffel, J., Solf, J. *ApJ*, *576*, 222–231, 2002

Bachiller, R. *ARAA*, *34*, 111–154, 1996

Balbus, S. A. In P. J. V. Garcia, ed., *Physical Processes in Circumstellar Disks Around Young Stars*, chap. 6, pp. 237–282. Chicago: University of Chicago Press, 2011

Balbus, S. A., Hawley, J. F. *ApJ*, *376*, 214–222, 1991

———. *ApJ*, *400*, 610–621, 1992

Ballesteros-Paredes, J., Klessen, R. S., Mac Low, M.-M., Vázquez-Semadeni, E. In B. Reipurth, J. Jewitt, K. Keil, eds., *Protostars and Planets V*, pp. 63–80. Tucson: University of Arizona Press, 2007

Bary, J. S., Weintraub, D. A., Kastner, J. H. *ApJ*, *576*, L73–L76, 2002

———. *ApJ*, *586*, 1136–1147, 2003

Basri, G., Batalha, C. *ApJ*, *363*, 654–669, 1990

Bastian, U., Finkenzeller, U., Jaschek, C., Jaschek, M. *A&A*, *126*, 438–439, 1983

Beck, T. L., Bary, J. S., McGregor, P. J. *ApJ*, *722*, 1360–1372, 2010

Beck, T. L., McGregor, P. J., Takami, M., Pyo, T.-S. *ApJ*, *676*, 472–489, 2008

Beck, T. L., Riera, A., Raga, A. C., Aspin, C. *AJ*, *127*, 408–419, 2004

Beckwith, S. V. W., Sargent, A. I., Chini, R. S., Güsten, R. *AJ*, *99*, 924–945, 1990

Bertout, C. *Rep. Prog. Phys.*, *47*, 111–174, 1984

———. *ARAA*, *27*, 351–395, 1989

Bevington, P. R., Robinson, D. K. *Data Reduction and Error Analysis for the Physical Sciences*. New York: McGraw-Hill, 2nd edn., 1992

Bicknell, G. V. *ApJ*, *286*, 68–87, 1984

Bicknell, G. V., Dopita, M. A., O'Dea, C. P. *ApJ*, *485*, 112–124, 1997

Binette, L., Cabrit, S., Raga, A. C., Cantó, J. *A&A*, *266*, 260–266, 1999

Birch, S. F., Eggers, J. M. In *Free Turbulent Shear Flows, Vol. I*, vol. SP-321 of *Conf. Proc. NASA*, pp. 11–40. 1972

Biscaya, A. M., Rieke, G. H., Narayanan, G., Luhman, K. L., Young, E. T. *ApJ*, *491*, 359–365, 1997

Blandford, R. D., Payne, D. G. *MNRAS*, *199*, 883–903, 1982

Bodenheimer, P. H. *Principles of Star Formation*. Berlin, Heidelberg: Springer, 2011

Bodenheimer, P. H., Sweigart, A. *ApJ*, *152*, 515–522, 1968

Böhm, K.-H. *Rev. Mex. A. A.*, *7*, 55–70, 1983

Bonito, R., Orlando, S., Miceli, M., Peres, G., Micela, G., Favata, F. *ApJ*, *737*, 54, 2011

Bouvier, J., Alencar, S. H. P., Harries, T. J., Johns-Krull, C. M., Romanova, M. M. In B. Reipurth, D. Jewitt, K. Keil, eds., *Protostars and Planets V*. Tucson: University of Arizona Press, 2007

Bouvier, J., Appenzeller, I. *A&AS*, *92*, 481–516, 1992

Bouvier, J., Cabrit, S., Fernández, M., Martín, E. L., Matthews, J. M. *A&A*, *272*, 176–202, 1993

Bouvier, J., Matt, S. P., Mohanty, S., Scholz, A., Stassun, K. G., Zanni, C. In H. Beuther, R. S. Klessen, C. P. Dullemond, T. Henning, eds., *Protostars and Planets VI*. Tucson: University of Arizona Press, 2014

Braiding, C. R., Wardle, M. *MNRAS*, *427*, 3188–3195, 2012a

———. *MNRAS*, *422*, 261–281, 2012b

Briceño, C., Luhman, K. L., Hartmann, L., Stauffer, J. R., Kirkpatrick, J. D. *ApJ*, *580*, 317–335, 2002

Briceño, C., Preibisch, T., Sherry, W. H., Mamajek, E. E., Mathieu, R. D., Walter, F. M., Zinnecker, H. In B. Reipurth, D. Jewitt, K. Keil, eds., *Protostars and Planets V*, pp. 345–360. Tucson: University of Arizona Press, 2007

Burkert, A., Bodenheimer, P. H. *ApJ*, *543*, 822–830, 2000

Burnham, S. W. *MNRAS*, *51*, 94, 1890

Burrows, C. J., Stapelfeldt, K. R., Watson, A. M., Krist, J. E., Ballester, G. E., Clarke, J. T., Crisp, D., Gallagher III, J. S., Griffiths, R. E., Hester, J. J., Hoessel, J. G., Holtzman, J. A., Mould, J. R., Scowen, P. A., Trauger, J. T., Westphal, J. A. *ApJ*, *473*, 437–451, 1996

Cabrit, S. In J. Ferreira, C. Dougados, E. Whelan, eds., *Jets from Young Stars*, vol. 723 of *Lect. Notes Phys.*, pp. 21–53. Berlin Heidelberg: Springer-Verlag, 2007a

———. In J. Bouvier, I. Appenzeller, eds., *Star-Disk Interaction in Young Stars*, vol. 243 of *IAU Symp.*, pp. 203–214. Cambridge: Cambridge University Press, 2007b

Cabrit, S., Raga, A. C., Gueth, F. In B. Reipurth, C. Bertout, eds., *Herbig-Haro Flows and the Birth of Stars*, vol. 182 of *IAU Symp.*, pp. 163–180. Kluwer Academic Publishers, 1997

Calvet, N., Gullbring, E. *ApJ*, *509*, 802–818, 1998

Cantó, J., Raga, A. C. *ApJ*, *372*, 646–658, 1991

Cantó, J., Raga, A. C., Adame, L. *MNRAS*, *369*, 860–866, 2006

Caratti o Garatti, A., Garcia Lopez, R., Weigelt, G., Tambovtseva, L. V., Grinin, V. P., Wheelwright, H., Ilee, J. D. *A&A*, *554*, A66, 2013

Carr, J. S. *ApJ*, *345*, 522–535, 1989

———. *Ap&SS*, *224*, 25–28, 1995

Carr, J. S., Tokunaga, A. T., Najita, J. R., Shu, F. H., Glassgold, A. E. *ApJ*, *411*, L37–L40, 1993

Casse, F., Ferreira, J. *A&A*, *353*, 1115–1128, 2000

Chandler, C. J., Carlstrom, J. E., Scoville, N. Z., Dent, W. R. F., Geballe, T. R. *ApJ*, *412*, L71–L74, 1993

Chandrasekhar, S. *Hydrodynamic and Hydromagnetic Stability*. Oxford: Clarendon Press, 1961

Chernin, L. M., Masson, C. R., de Gouveia Dal Pino, E. M., Benz, W. *ApJ*, *426*, 204–214, 1994

Chrysostomou, A., Hobson, J., Davis, C. J., Smith, M. D., Berndsen, A. *MNRAS*, *314*, 229–240, 2000

Ciardi, A., Lebedev, S. V., Frank, A., Suzuki-Vidal, F., Hall, G. N., Bland, S. N., Harvey-Thompson, A., Blackman, E. G., Camenzind, M. *ApJ*, *691*, L147–L150, 2009

Cieza, L., Padgett, D. L., Stapelfeldt, K. R., Augereau, J.-C., Harvey, P., Evans, II, N. J., Merín, B., Koerner, D., Sargent, A., van Dishoeck, E. F., Allen, L., Blake, G., Brooke, T., Chapman, N., Huard, T., Lai, S.-P., Mundy, L., Myers, P. C., Spiesman, W., Wahhaj, Z. *ApJ*, *667*, 308–328, 2007

Cleeves, L. I., Adams, F. C., Bergin, E. A. *ApJ*, *772*, 5, 2013

Coffey, D., Bacciotti, F., Chrysostomou, A., Nisini, B., Davis, C. J. *A&A*, *526*, A40, 2011

Coffey, D., Bacciotti, F., Podio, L. *ApJ*, *689*, 1112–1126, 2008

Coffey, D., Bacciotti, F., Ray, T. P., Eislöffel, J., Woitas, J. *ApJ*, *663*, 350–364, 2007

Coffey, D., Bacciotti, F., Woitas, J., Ray, T. P., Eislöffel, J. *ApJ*, *604*, 758–765, 2004

Coffey, D., Rigliaco, E., Bacciotti, F., Ray, T. P., Eislöffel, J. *ApJ*, *749*, 139, 2012

Cohen, M., Hollenbach, D. J., Haas, M. R., Erickson, E. F. *ApJ*, *329*, 963–873, 1988

Cohen, M., Kuhi, L. V. *ApJS*, *41*, 743–843, 1979

Combet, C., Ferreira, J. *A&A*, *479*, 481–491, 2008

Connelley, M. S., Greene, T. P. *AJ*, *140*, 1214–1240, 2010

Connelley, M. S., Reipurth, B., Tokunaga, A. T. *AJ*, *135*, 2496–2525, 2008

———. *AJ*, *138*, 1193–1202, 2009

Contopoulos, J., Lovelace, R. V. E. *ApJ*, *429*, 139–152, 1994

Cranmer, S. R. *ApJ*, *706*, 824–843, 2009

Cutri, R. M., Skrutskie, M. F., van Dyk, S., Beichman, C. A., Carpenter, J. M., Chester, T., Cambresy, L., Evans, T., Fowler, J., Gizis, J., Howard, E., Huchra, J., Jarrett, T., Kopan, E. L., Kirkpatrick, J. D., Light, R. M., Marsh, K. A., McCallon, H., Schneider, S., Stiening, R., Sykes, M., Weinberg, M., Wheaton, W. A., Wheelock, S., Zacarias, N. *The IRSA 2MASS All-Sky Point Source Catalog, NASA/IPAC Infrared Science Archive.* NASA, 2003

Dash, S. M., Wolf, D. E., Seiner, J. M. *AIAAJ*, *23*, 505–514, 1985

Davis, C. J., Eislöffel, J., Ray, T. P., Jenness, T. *A&A*, *324*, 1013–1019, 1997

de Gouveia Dal Pino, E. M. *ApJ*, *526*, 862–873, 1999

Delamarter, G., Frank, A., Hartmann, L. *ApJ*, *530*, 923–938, 2000

Desch, S. J., Connolly, Jr., H. C., Srinivasan, G. *ApJ*, *602*, 528–542, 2004

Donati, J.-F., Gregory, S. G., Alencar, S. H. P., Bouvier, J., Hussain, G., Skelly, M., Dougados, C., Jardine, M. M., Ménard, F., Romanova, M. M., Unruh, Y. C. *MNRAS*, *417*, 472–487, 2011a

Donati, J.-F., Gregory, S. G., Alencar, S. H. P., Hussain, G., Bouvier, J., Jardine, M. M., Dougados, C., Romanova, M. M., Collaboration, T. M. *MNRAS*, *436*, 881–897, 2013

Donati, J.-F., Gregory, S. G., Montmerle, T., Maggio, A., Argiroffi, C., Sacco, G., Hussain, G., Kastner, J., Alencar, S. H. P., Audard, M., Bouvier, J., Damiani, F., Güdel, M., Huenemoerder, D., Wade, G. A. *MNRAS*, *417*, 1747–1759, 2011b

Donati, J.-F., Jardine, M. M., Gregory, S. G., Petit, P., Paletou, F., Bouvier, J., Dougados, C., Ménard, F., Cameron, A. C., Hussain, T. J. H. G. A. J., Unruh, Y., Morin, J., Marsden, S. C., Manset, N., Auriére, M., Catala, C., Alecian, E. *MNRAS*, *386*, 1234–1251, 2008

Dopita, M. A. *ApJS*, *37*, 117–144, 1978

Dopita, M. A., Schwartz, R. D., Evans, I. *ApJ*, *263*, L73–L77, 1982

Doppmann, G. W., Greene, T. P., Covey, K. R., Lada, C. J. *AJ*, *130*, 1145–1170, 2005

Dougados, C., Cabrit, S., Lavalley, C., Menard, F. *A&A*, *357*, L61–L64, 2000

Ducati, J. R. *CDS/ADC Collection of Electronic Catalogues*, *2237*, 2002

Dunham, M. M., Crapsi, A., Evans II, N. J., Bourke, T. L., Huard, T. L., Myers, P. C., Kauffmann, J. *ApJS*, *179*, 249–282, 2008

Dunham, M. M., Stutz, A. M., Allen, L. E., Evans II, N. J., Fischer, W. J., Megeath, S. T., Myers, P. C., Offner, S. S. R., Poteet, C. A., Tobin, J. J., Vorobyov, E. I. In H. Beuther, R. S. Klessen, C. P. Dullemond, T. Henning, eds., *Protostars and Planets VI*. Tucson: University of Arizona Press, 2014

Dutrey, A., Guilloteau, S., Duvert, G., Prato, L., Simon, M., Schuster, K., Ménard, F. *A&A*, *309*, 493–504, 1996

Dyson, J. E. *Ap&SS*, *106*, 181–197, 1984

Edwards, S. In E. Stempels, ed., *Cool Stars, Stellar Systems and the Sun: Proceedings of the 15th Cambridge Workshop on Cool Stars, Stellar Systems and the Sun*, vol. 1094 of *AIP Conf. Ser.*, pp. 29–38. Melville: AIP, 2009

Eislöffel, J., Mundt, R. *A&A*, *263*, 292–300, 1992

———. *A&A*, *284*, 530–544, 1994

———. *AJ*, *115*, 1554–1575, 1998

Eislöffel, J., Smith, M. D., Davis, C. J. *A&A*, *359*, 1147–1161, 2000

Elias, J. H. *ApJ*, *224*, 857–872, 1978

Estalella, R., López, R., Anglada, G., Gómez, G., Riera, A., Carrasco-González, C. *AJ*, *144*, 61, 2012

Farage, C. L. Outflows from T Tauri stars: NIFS observations and hydrodynamic models of the DG Tau microjet. The Australian National University, Honours Thesis, 2007

Favre, A. In L. I. Sedov, ed., *Problems of Hydrodynamics and Continuum Mechanics*, p. 231. Philadelphia: Society for Industrial and Applied Mathematics, 1969

Federrath, C., Schrön, M., Banerjee, R., Klessen, R. S. *ApJ*, *790*, 128, 2014

Feigelson, E. D., Montmerle, T. *ARAA*, *37*, 363–408, 1999

Fejer, J. A., Miles, J. W. *J. Fluid. Mech.*, *15*, 335–336, 1963

Fendt, C., Sheikhnezami, S. *ApJ*, *774*, 12, 2013

Ferreira, J. In J. Bouvier, J.-P. Zahn, eds., *Star Formation and the Physics of Young Stars*, vol. 3 of *EAS Publications Series*, pp. 229–277. Cambridge: Cambridge University Press, 2002

Ferreira, J., Casse, F. *ApJ*, *601*, L139–L142, 2004

Ferreira, J., Dougados, C., Cabrit, S. *A&A*, *453*, 785–796, 2006

Ferreira, J., Pelletier, G., Appl, S. *MNRAS*, *312*, 387–397, 2000

Field, G. B. *ApJ*, *187*, 453–459, 1974

Fischer, W. J., Megeath, S. T., Tobin, J. J., Stutz, A. M., Ali, B., Remming, I., Kounkel, M., Stanke, T., Osorio, M., Henning, T., Manoj, P., Wilson, T. L. *ApJ*, *756*, 99, 2012

Fleming, T., Stone, J. M. *ApJ*, *585*, 908–920, 2003

Frank, A., Ray, T. P., Cabrit, S., Hartigan, P. M., Arce, H. G., Bacciotti, F., Bally, J., Benisty, M., Eislöffel, J., Güdel, M., Lebedev, S. V., Nisini, B., Raga, A. C. In H. Beuther, R. S. Klessen, C. P. Dullemond, T. Henning, eds., *Protostars and Planets VI*. Tucson: University of Arizona Press, 2014

Frerking, M. A., Langer, W. D., Wilson, R. W. *ApJ*, *262*, 590–605, 1982

Gaibler, V., Khochfar, S., Krause, M. *MNRAS*, *411*, 155–161, 2011

Gallet, F., Bouvier, J. *A&A*, *556*, A36, 2013

Ghosh, P., Lamb, F. K. *ApJ*, *234*, 296–316, 1979

Girart, J. M., Rao, R., Marrone, D. P. *Science*, *313*, 812–814, 2006

Gómez, L., Rodríguez, L. F., Loinard, L. *Rev. Mex. A. A.*, *49*, 79–85, 2013

Gómez de Castro, A. I., Pudritz, R. E. *ApJ*, *409*, 748–761, 1993

Gómez de Castro, A. I., Verdugo, E. *ApJ*, *548*, 976–989, 2001

Goodman, A. A., Benson, P. J., Fuller, G. A., Myers, P. C. *ApJ*, *406*, 528–547, 1993

Gredel, R. *A&A*, *292*, 580–592, 1994

Green, J. D., Evans II, N. J., Jorgensen, J. K., Herczeg, G. J., Kristensen, L. E., Lee, J.-E., Dionatos, O., Yildiz, U. A., Salyk, C., Meeus, G., Bouwman, J., Visser, R., Bergin, E. A., van Dishoeck, E. F., Rascati, M. R., Karska, A., van Kempen, T. A., Dunham, M. M., Lindberg, J. E., Fedele, D., Team, D. *ApJ*, *770*, 123, 2013

Greene, T. P., Barsony, M., Weintraub, D. A. *ApJ*, *725*, 1100–1110, 2010

Greene, T. P., Lada, C. J. *AJ*, *112*, 2184–2221, 1996

Greene, T. P., Wilking, B. A., André, P., Young, E. T., Lada, C. J. *ApJ*, *434*, 614–626, 1994

Grevesse, N., Asplund, M., Sauval, A. J., Scott, P. *ApSS*, *328*, 179–183, 2010

Güdel, M., Audard, M., Bacciotti, F., Bary, J. S., Briggs, K. R., Cabrit, S., Carmona, A., Codella, C., Dougados, C., Eislöffel, J., Gueth, F., Günther, H. M., Herczeg, G. J., Kundurthy, P., Matt, S. P., Mutel, R. L., Ray, T. P., Schmitt, J. H. M. M., Schneider, P. C., Skinner, S. L., van Boekel, R. In C. M. Johns-Krull, ed., *16th Cambridge Workshop on Cool Stars, Stellar Systems, and the Sun*, vol. 448 of *ASP Conf. Ser.*, pp. 617–624. San Francisco: Astronomical Society of the Pacific, 2011

Güdel, M., Skinner, S. L., Audard, M., Briggs, K. R., Cabrit, S. *A&A*, *478*, 797–807, 2008

Güdel, M., Skinner, S. L., Briggs, K. R., Audard, M., Arzner, K., Telleschi, A. *ApJ*, *626*, L53–L56, 2005

Güdel, M., Telleschi, A., Audard, M., Skinner, S. L., Briggs, K. R., Palla, F., Dougados, C. *A&A*, *468*, 515–528, 2007

Gueth, F., Guilloteau, S. *A&A*, *343*, 571–584, 1999

Guilloteau, S., Dutrey, A., Piétu, V., Boehler, Y. *A&A*, *529*, A105, 2011

Gullbring, E., Calvet, N., Muzerolle, J. M., Hartmann, L. *ApJ*, *544*, 927–932, 2000

Gullbring, E., Hartmann, L., Briceño, C., Calvet, N. *ApJ*, *492*, 323–341, 1998

Günther, H. M., Matt, S. P., Li, Z.-Y. *A&A*, *493*, 579–584, 2009

Hamann, F., Simon, M., Ridgway, S. T. *ApJ*, *326*, 859–864, 1988

Haro, G. *AJ*, *55*, 72, 1950

———. *ApJ*, *115*, 572, 1952

———. *ApJ*, *117*, 73, 1953

Hart, J., McGregor, P. J., Bloxham, G. In M. Iye, A. F. M. Moorwood, eds., *Instrument Design and Performance for Optical/Infrared Ground-based Telescopes*, vol. 4841 of *Proc. SPIE*, pp. 319–329. SPIE, 2003

Hartigan, P. M. *ApJ*, *339*, 987–999, 1989

Hartigan, P. M., Carpenter, J. M., Dougados, C., Skrutskie, M. F. *AJ*, *111*, 1278, 1996

Hartigan, P. M., Edwards, S., Ghandour, L. *ApJ*, *452*, 736–768, 1995

Hartigan, P. M., Frank, A., Foster, J. M., Wilde, B. H., Douglas, M., Rosen, P. A., Coker, R. F., Blue, B. E., Hansen, J. F. *ApJ*, *736*, 29, 2011

Hartigan, P. M., Frank, A., Varniére, P., Blackman, E. G. *ApJ*, *661*, 910–918, 2007

Hartigan, P. M., Heathcote, S., Morse, J. A., Reipurth, B., Bally, J. *AJ*, *130*, 2197–2205, 2005

Hartigan, P. M., Morse, J. A., Raymond, J. C. *ApJ*, *436*, 125–143, 1994

Hartigan, P. M., Morse, J. A., Tumlinson, J., Raymond, J., Heathcote, S. *ApJ*, *512*, 901–915, 1999

Hartigan, P. M., Raymond, J. C., Pierson, R. *ApJ*, *614*, L69–L71, 2004

Hartmann, L. *Accretion Processes in Star Formation*. Cambridge Astrophysics Series. Cambridge: Cambridge University Press, 1998

Hartmann, L., Kenyon, S. J. *ARAA*, *34*, 207–240, 1996

Hawley, J. F., Balbus, S. A. *ApJ*, *376*, 223–233, 1991

———. *ApJ*, *400*, 595–609, 1992

Hayashi, C. *ARAA*, *4*, 171–192, 1966

Helou, G., Walker, D. W. In *NASA RP-1190*. 1988

Herbig, G. H. *ApJ*, *111*, 11, 1950

———. *ApJ*, *113*, 697–699, 1951

———. In *Proceedings of a Conference at Vatican Observatory, Castel Gandolfo, May 20-28, 1957*, vol. 5 of *Ricerche Astronomiche*, p. 127. Amsterdam/New York: North-Holland/Interscience, 1958

———. *Adv. Astr. Astrophys.*, *1*, 47–103, 1962

———. In L. Detre, ed., *Non-Stable Phenomena in Variable Stars*, p. 75. Dordrecht: Reidel, 1969

———. *ApJ*, *217*, 693–715, 1977

Herbig, G. H., Petrov, P. P., Duemmler, R. *ApJ*, *595*, 384–411, 2003

Herbst, W., Herbst, D. K., Grossman, E. J., Weinstein, D. *AJ*, *108*, 1906–1923, 1994

Herczeg, G. J., Linsky, J. L., Walter, F. M., Gahm, G. F., Johns-Krull, C. M. *ApJS*, *165*, 256–282, 2006

Herriot, G., Morris, S., Roberts, S., Fletcher, J. M., Saddlemyer, L. K., Singh, G., Veran, J.-P., Richardson, E. H. In D. Bonaccini, R. K. Tyson, eds., *Adaptive Optical System Technologies*, vol. 3353 of *Proc. SPIE*, pp. 488–499. SPIE, 1998

Hessman, F. V., Guenther, E. W. *A&A*, *321*, 497–512, 1997

Hillenbrand, L. A., Strom, S. E., Vrba, F. J., Keene, J. *ApJ*, *397*, 613–643, 1992

Hirth, G. A., Mundt, R., Solf, J. *A&A*, *285*, 929–942, 1994a

———. *A&AS*, *126*, 437–469, 1997

Hirth, G. A., Mundt, R., Solf, J., Ray, T. P. *ApJ*, *427*, L99–L102, 1994b

Hoare, M. G., Kurtz, S. E., Lizano, S., Keto, E., Hofner, P. In B. Reipurth, D. Jewitt, K. Keil, eds., *Protostars and Planets V*, pp. 181–196. Tucson: University of Arizona Press, 2007

Hollenbach, D. J. In *Protostars & Planets II*, vol. 61 of *Icarus*, pp. 36–39. 1985

Hollenbach, D. J., Natta, A. *ApJ*, *455*, 133–144, 1995

Hoyle, F. *ApJ*, *118*, 513–528, 1953

Hughes, A. M., Hull, C. L. H., Wilner, D. J., Plambeck, R. L. *AJ*, *145*, 115, 2013

Hughes, J., Hartigan, P. M., Krautter, J., Kelemen, J. *AJ*, *108*, 1071–1090, 1994

Isella, A., Carpenter, J. M., Sargent, A. I. *ApJ*, *714*, 1746–1761, 2010

Jeans, J. H. *Astronomy and Cosmogony*. Cambridge: Cambridge University Press, 1929

Jenkins, E. B. *ApJ*, *700*, 1299–1348, 2009

Johns-Krull, C. M. *ApJ*, *664*, 975–985, 2007

Joy, A. H. *ApJ*, *102*, 168–195, 1945

Kajdič, P., Reipurth, B., Raga, A. C., Bally, J., Walawender, J. *AJ*, *143*, 106, 2012

Kenyon, S. J., Hartmann, L. *ApJS*, *101*, 117–171, 1995

Kepner, J., Hartigan, P. M., Yang, C., Strom, S. E. *ApJ*, *415*, L119–L121, 1993

Kirby, L. *ApJ*, *694*, 1056–1066, 2009

Kitamura, Y., Kawabe, R., Saito, M. *ApJ*, *457*, 277–286, 1996a

———. *ApJ*, *465*, L137–L140, 1996b

Klaassen, P. D., Juhasz, A., Mathews, G. S., Mottram, J. C., de Gregorio-Molsavo, I., van Dishoeck, E. F., Takahashi, S., Akiyama, E., Chapillon, E., Espada, D., Hales, A., Hogerheijde, M. R., Rawlings, M., Schmalzl, M., Testi, L. *A&A*, *555*, A73, 2013

Kofman, L., Raga, A. C. *ApJ*, *390*, 359–364, 1992

Königl, A., Pudritz, R. E. In V. Mannings, A. P. Boss, S. S. Russell, eds., *Protostars and Planets IV*, pp. 759–787. Tucson: University of Arizona Press, 2000

Königl, A., Salmeron, R. In P. J. V. Garcia, ed., *Physical Processes in Circumstellar Disks Around Young Stars*, chap. 7, pp. 283–354. Chicago: University of Chicago Press, 2011

Königl, A., Salmeron, R., Wardle, M. *MNRAS*, *401*, 479–499, 2010

Kraus, A. L., Hillenbrand, L. A. *ApJ*, *703*, 1511–1530, 2009

Kraus, A. L., Ireland, M. J., Martinache, F., Hillenbrand, L. A. *ApJ*, *731*, 8, 2011

Krist, J. E., Burrows, C. J., Stapelfeldt, K. R., Ballester, G. E., Clarke, J. T., Crisp, D., Evans, R. W., Gallagher III, J. S., Griffiths, R. E., Hester, J. J., Holtzman, J. A., Hoessel, J. G., Mould, J. R., Scowen, P. A., Trauger, J. T., Watson, A. M., Westphal, J. A. *ApJ*, *481*, 447–452, 1997

Krist, J. E., Stapelfeldt, K. R., Burrows, C. J., Hester, J. J., Watson, A. M., Ballester, G. E., Clarke, J. T., Crisp, D., Evans, R. W., Gallagher III, J. S., Griffiths, R. E., Hoessel, J. G., Holtzman, J. A., Mould, J. R., Scowen, P. A., Trauger, J. T. *ApJ*, *515*, L35–L38, 1999

Kristensen, L. E., Klaassen, P. D., Mottram, J. C., Schmalzl, M., Hogerheijde, M. R. *A&A*, *549*, L6, 2013

Krumholz, M. R. In J. S. Vink, ed., *Very Massive Stars in the Local Universe*. arXiv:1403.3417, 2014

Kuncic, Z., Bicknell, G. V. *ApJ*, *616*, 669–687, 2004

Kunz, M. W., Balbus, S. A. *MNRAS*, *348*, 355–360, 2004

Lada, C. J. *ARAA*, *23*, 267–317, 1985

———. In M. Peimbert, J. Jugaku, eds., *Star Forming Regions*, vol. 115 of *IAU Symp.*, pp. 1–18. Dordrecht: Reidel Publishing Co., 1987

Lada, C. J., Fich, M. *ApJ*, *459*, 638–652, 1996

Landau, L. D., Lifshitz, E. M. *Fluid Mechanics*, vol. 6 of *Course of Theoretical Physics*. Oxford: Elsevier, 2nd edn., 1987

Larson, R. B. *MNRAS*, *145*, 271–295, 1969

———. *MNRAS*, *194*, 809–826, 1981

———. *Rep. Prog. Phys.*, *66*, 1651–1697, 2003

———. *Rep. Prog. Phys.*, *73*, 14901, 2010

Launhardt, R., Stutz, A. M., Schmiedeke, A., Henning, T., Krause, O., Balog, Z., Beuther, H., Birkmann, S., Hennemann, M., Khanzadyan, T., Linz, H., Lippok, N., Nielbock, M., Pittan, J., Ragan, S., Risacher, C., Schmalzl, M., Shirley, Y. L., Stecklum, B., Steinacker, J., Tackenberg, J. *A&A*, *551*, A98, 2013

Lavalley, C., Cabrit, S., Ferruit, P., Dougados, C., Bacon, R. *A&A*, *327*, 671–680, 1997

Lavalley-Fouquet, C., Cabrit, S., Dougados, C. *A&A*, *356*, L41–L44, 2000

Lee, C.-F., Mundy, L. G., Reipurth, B., Ostriker, E. C., Stone, J. M. *ApJ*, *542*, 925–945, 2000

Lee, C.-F., Mundy, L. G., Stone, J. M., Ostriker, E. C. *ApJ*, *576*, 294–312, 2002

Leinert, C., Haas, M., Richichi, A., Zinnecker, H., Mundt, R. *A&A*, *250*, 407–419, 1991

Li, Z.-Y., Banerjee, R., Pudritz, R. E., Jorgensen, J. K., Shang, H., Krasnopolsky, R., Maury, A. In H. Beuther, R. S. Klessen, C. P. Dullemond, T. Henning, eds., *Protostars and Planets VI*. Tucson: University of Arizona Press, 2014

Li, Z.-Y., Krasnopolsky, R., Shang, H. *ApJ*, *738*, 180, 2011

Lim, A. J., Rawlings, J. M. C., Williams, D. A. *MNRAS*, *308*, 1126–1132, 1999

Liu, C.-F., Shang, H., Pyo, T.-S., Takami, M., Walter, F. M., Yan, C.-H., Wang, S.-Y., Ohashi, N., Hayashi, M. *ApJ*, *749*, 62, 2012

Livio, M. *Phys. Rep.*, *311*, 225–245, 1999

López-Cámara, D., Raga, A. C. *ApJ*, *723*, 449–456, 2010

Luhman, K. L., Stauffer, J. R., Muench, A. A., Rieke, G. H., Lada, E. A., Bouvier, J., Lada, C. J. *ApJ*, *593*, 1093–1115, 2003

Lynch, C., Mutel, R. L., Güdel, M., Ray, T. P., Skinner, S. L., Schneider, P. C., Gayley, K. G. *ApJ*, *766*, 53, 2013

Marconi, A., Axon, D. J., Capetti, A., Maciejewski, W., Atkinson, J., Batcheldor, D., Binney, J., Carollo, M., Dressel, L., Ford, H., Gerssen, J., Hughes, M. A., Macchetto, D., Merrifield, M. R., Scarlata, C., Sparks, W., Stiavelli, M., Tsvetanov, Z., van der Marel, R. P. *ApJ*, *586*, 868–890, 2003

Masson, C. R., Chernin, L. M. *ApJ*, *387*, L47–L50, 1992

———. *ApJ*, *414*, 230–241, 1993

Masunaga, H., Inutsuka, S.-i. *ApJ*, *531*, 350–365, 2000

Matsakos, T., Vlahakis, N., Tsinganos, K., Karampelas, K., Sauty, C., Cayatte, V., Matt, S. P., Massaglia, S., Trussoni, E., Mignone, A. *A&A*, *545*, A53, 2012

Matt, S., Pudritz, R. E. *ApJ*, *632*, L135–L138, 2005

———. In J. Bouvier, I. Appenzeller, eds., *Star-Disk Interaction in Young Stars*, vol. 243 of *IAU Symp.*, pp. 299–306. Cambridge: Cambridge University Press, 2007

Maurri, L., Bacciotti, F., Podio, L., Ray, T. P., Mundt, R., Locatelli, U., Coffey, D. *A&A*, *in print*, 2014

McGregor, P. J., Bloxham, G., Boz, R., Davies, J., Doolan, M., Ellis, M., Hart, J., Jones, D. J., Luvaul, L., Nielsen, J., Parcell, S., Sharp, R. G., Stevanovic, D., Young, P. J. In I. S. McLean, S. K. Ramsay, H. Takami, eds., *Ground-based and Airborne Instrumentation for Astronomy IV*, vol. 8446 of *Proc. SPIE*, p. 84461I. 2012

McGregor, P. J., Dopita, M. A., Wood, P., Burton, M. G. *PASA*, *18*, 41–57, 2001

McGregor, P. J., Hart, J., Conroy, P., Pfitzner, L., Bloxham, G., Jones, D., Downing, M., Dawson, M., Young, P. J., Jarnyk, M., van Harmelen, J. In M. Iye, A. F. M. Moorwood, eds., *Instrument Design and Performance for Optical/Infrared Ground-based Telescopes*, vol. 4841 of *Proc. SPIE*, pp. 1581–1591. SPIE, 2003

McGroarty, F., Ray, T. P. *A&A*, *420*, 975–986, 2004

McGroarty, F., Ray, T. P., Froebrich, D. *A&A*, *467*, 1197–1207, 2007

McKee, C. F., Ostriker, E. C. *ARAA*, *45*, 565–687, 2007

Melnikov, S. Y., Eislöffel, J., Bacciotti, F., Woitas, J., Ray, T. P. *A&A*, *506*, 763–777, 2009

Mestel, L., Spitzer, L. *MNRAS*, *116*, 503, 1956

Micono, M., Bodo, G., Massaglia, S., Rossi, P., Ferrari, A. *A&A*, *364*, 318–326, 2000

Mitchell, G. F., Hasegawa, T. I., Dent, W. R. F., Matthews, H. E. *ApJ*, *436*, L177–L180, 1994

Miura, A., Pritchett, P. L. *J. Geophys. Res.*, *87*, 7431–7444, 1982

Mohanty, S., Shu, F. H. *ApJ*, *687*, 1323–1338, 2008

Mundt, R., Fried, J. W. *ApJ*, *274*, L83–L86, 1983

Murillo, N. M., Lai, S.-P., Bruderer, S., Harsono, D., van Dishoeck, E. F. *A&A*, *560*, A103, 2013

Muzerolle, J. M., Hartmann, L., Calvet, N. *AJ*, *116*, 455–468, 1998

Najita, J. R., Carr, J. S., Mathieu, R. D. *ApJ*, *589*, 931–952, 2003

Najita, J. R., Edwards, S., Basri, G., Carr, J. S. In V. Mannings, A. P. Boss, S. S. Russell, eds., *Protostars and Planets IV*, pp. 457–484. Tucson: University of Arizona Press, 2000

Najita, J. R., Strom, S. E., Muzerolle, J. M. *MNRAS*, *378*, 369–378, 2007

Narayanan, G., Snell, R. L., Bemis, A. *MNRAS*, *425*, 2641–2667, 2012

Nguyen, D. C., Brandeker, A., van Kerkwijk, M. H., Jayawardhana, R. *ApJ*, *745*, 119, 2012

Nicholls, D. C., Dopita, M. A., Sutherland, R. S., Kewley, L. J., Palay, E. *ApJS*, *207*, 21, 2013

Nisini, B., Caratti o Garatti, A., Giannini, T., Lorenzetti, D. *A&A*, *393*, 1035–1051, 2002

Nordlund, A., Haugbolle, T., Küffmeier, M., Padoan, P., Vasileiades, A. In M. Booth, B. C. Matthews, J. R. Graham, eds., *Exploring the Formation and Evolution of Planetary Systems*, vol. 299 of *IAU Symp.*, pp. 131–135. Cambridge: Cambridge University Press, 2014

Ostriker, E. C., Shu, F. H. *ApJ*, *447*, 813–828, 1995

Ouyed, R., Clarke, D. A., Pudritz, R. E. *ApJ*, *582*, 292–319, 2003

Ouyed, R., Pudritz, R. E. *ApJ*, *419*, 255–267, 1993

Padgett, D. L., Brandner, W., Stapelfeldt, K. R., Strom, S. E., Terebey, S., Koerner, D. *AJ*, *117*, 1490–1504, 1999

Parkin, E. R., Pittard, J. M., Hoare, M. G., Wright, N. J., Drake, J. J. *MNRAS*, *400*, 629–645, 2009

Pech, G., Zapata, L. A., Loinard, L., Rodríguez, L. F. *ApJ*, *751*, 78, 2012

Pelletier, G., Pudritz, R. E. *ApJ*, *394*, 117–138, 1992

Pereyra, A., Girart, J. M., Magalhães, A. M., Rodrigues, C. V., de Araújo, F. X. *A&A*, *501*, 595–607, 2009

Pesenti, N., Dougados, C., Cabrit, S., Ferreira, J., Casse, F., Garcia, P. J. V., O'Brien, D. *A&A*, *12*, L9–L12, 2004

Pesenti, N., Dougados, C., Cabrit, S., O'Brien, D., Garcia, P. J. V., Ferreira, J. *A&A*, *410*, 155–164, 2003

Peters, T., Klaassen, P. D., Seifried, D., Banerjee, R., Klessen, R. S. *MNRAS*, *437*, 2901–2908, 2014

Petrov, P. P. *Astrophys.*, *46*, 506–529, 2003

Pineda, J. E., Arce, H. G., Schnee, S., Goodman, A. A., Bourke, T. L., Foster, J. B., Robitaille, T. P., Tanner, J., Kauffmann, J., Tafalla, M., Caselli, P., Anglada, G. *ApJ*, *743*, 201, 2011

Pineda, J. E., Maury, A. J., Fuller, G. A., Testi, L., García-Appadoo, D., Peck, A. B., Villard, E., Corder, S. A., van Kempen, T. A., Turner, J. L., Tachihara, K., Dent, W. *A&A*, *544*, L7, 2012

Piro, L., Costa, E., Feroci, M., Frontera, F., Amati, L., Dal Fiume, D., Antonelli, L. A., Heise, J., in't Zand, J., Owens, A., Parmar, A. N., Cusumano, G., Vietri, M., Perola, G. C. *ApJ*, *514*, L73–L77, 1999

Podio, L., Eislöffel, J., Melnikov, S. Y., Hodapp, K. W., Bacciotti, F. *A&A*, *527*, A13, 2011

Podio, L., Kamp, I., Codella, C., Cabrit, S., Nisini, B., Dougados, C., Sandell, G., Williams, J. P., Thi, W.-F., Testi, L., Woitke, P., Meijerink, R., Spaans, M., Aresu, G., Menard, F., Pinte, C. *ApJ*, *766*, L5, 2013

Podio, L., Medves, S., Bacciotti, F., Eislöffel, J., Ray, T. P. *A&A*, *506*, 779–788, 2009

Pradhan, A. K., Zhang, H. L. *ApJ*, *409*, 77–79, 1993

Protassov, R., van Dyk, D. A., Connors, A., Kashyap, V. L., Siemiginowska, A. *ApJ*, *571*, 545–559, 2002

Pudritz, R. E., Norman, C. A. *ApJ*, *274*, 677–697, 1983

Pudritz, R. E., Ouyed, R., Fendt, C., Brandenburg, A. In B. Reipurth, J. Jewitt, K. Keil, eds., *Protostars and Planets V*, pp. 277–294. Tucson: University of Arizona Press, 2007

Pyo, T.-S., Hayashi, M., Kobayashi, N., Tokunaga, A. T., Terada, H., Goto, M., Yamashita, T., Itoh, Y., Takami, H., Takato, N., Hayano, Y., Gaessler, W., Kamata, Y., Minowa, Y., Iye, M. *Ap&SS*, *287*, 21–24, 2003a

Pyo, T.-S., Kobayashi, N., Hayashi, M., Terada, H., Goto, M., Takami, H., Takato, N., Gaessler, W., Usuda, T., Yamashita, T., Tokunaga, A. T., Hayano, Y., Kamata, Y., Iye, M., Minowa, Y. *ApJ*, *590*, 340–347, 2003b

Qi, C., Öberg, K. I., Wilner, D. J., D'Alessio, P., Bergin, E., Andrews, S. M., Blake, G. A., Hogerheijde, M. R., van Dishoeck, E. F. *Science*, *341*, 630–632, 2013

Raga, A. C., Biro, S., Cantó, J., Binette, L. *Rev. Mex. A. A.*, *22*, 243–248, 1991

Raga, A. C., Cabrit, S. *A&A*, *278*, 267–278, 1993

Raga, A. C., Cabrit, S., Cantó, J. *MNRAS*, *273*, 422–430, 1995

Raga, A. C., Cantó, J. *Rev. Mex. A. A.*, *31*, 51–61, 1995

———. In E. F. van Dishoeck, ed., *Molecules in Astrophysics: Probes and Processes*, vol. 178 of *IAU Symp.*, pp. 89–101. Dordrecht: Kluwer Academic Publishers, 1997

Raga, A. C., Cantó, J., Binette, L., Calvet, N. *ApJ*, *364*, 601–610, 1990

Raga, A. C., Cantó, J., de Colle, F., Esquivel, A., Kajdic, P., Rodríguez-González, A., Velázquez, P. F. *Rev. Mex. A. A. (Ser. de Conf.)*, *36*, 186–192, 2009

Raga, A. C., De Colle, F., Kajdiuc, P., Esquivel, A., Cantó, J. *A&A*, *465*, 879–885, 2007

Raga, A. C., de Gouveia Dal Pino, E. M., Noriega-Crespo, A., Mininni, P. D., Velázquez, P. F. *A&A*, *392*, 267–276, 2002a

Raga, A. C., Noriega-Crespo, A. *Rev. Mex. A. A.*, *24*, 9–13, 1992

Raga, A. C., Rodríguez-González, A., Noriega-Crespo, A., Esquivel, A. *ApJ*, *744*, L12, 2012

Raga, A. C., Velázquez, P. F., Cantó, J., Masciadri, E. *A&A*, *395*, 647–656, 2002b

Raga, A. C., Williams, D. A., Lim, A. J. *Rev. Mex. A. A.*, *41*, 137–146, 2005

Ray, T. P. *Ap&SS*, *272*, 115–125, 2000

Ray, T. P., Dougados, C., Bacciotti, F., Eislöffel, J., Chrysostomou, A. In B. Reipurth, D. Jewitt, K. Keil, eds., *Protostars and Planets V*, pp. 231–244. Tucson: University of Arizona Press, 2007

Ray, T. P., Ershkovich, A. I. *MNRAS*, *204*, 821–831, 1983

Reipurth, B., Aspin, C. *AJ*, *114*, 2700–2707, 1997

———. *ApJ*, *606*, L119–L122, 2004

Reipurth, B., Bachiller, R. In W. B. Latter, ed., *CO: Twenty-Five Years of Millimeter-Wave Spectroscopy*, vol. 170 of *IAU Symp.*, pp. 165–174. Dordrecht: Kluwer Academic Publishers, 1997

Reipurth, B., Bally, J. *ARAA*, *39*, 403–455, 2001

Reipurth, B., Heathcote, S., Morse, J. A., Hartigan, P. M., Bally, J. *AJ*, *123*, 362–381, 2002

Reipurth, B., Raga, A. C., Heathcote, S. *A&A*, *311*, 989, 1996

Reipurth, B., Yu, K. C., Rodríguez, L. F., Heathcote, S., Bally, J. *A&A*, *352*, L83–L86, 1999

Rigliaco, E., Pascucci, I., Gorti, U., Edwards, S., Hollenbach, D. *ApJ*, *772*, 60, 2013

Robitaille, T. P., Whitney, B. A., Indebetouw, R., Wood, K. *ApJS*, *169*, 328–352, 2007

Rodríguez, L. F., Dzib, S. A., Loinard, L., Zapata, L. A., Raga, A. C., Cantó, J., Riera, A. *Rev. Mex. A. A.*, *48*, 243–249, 2012a

Rodríguez, L. F., González, R. F., Raga, A. C., Cantó, J., Riera, A., Loinard, L., Dzib, S. A., Zapata, L. A. *A&A*, *537*, A123, 2012b

Rodríguez-González, A., Esquivel, A., Raga, A. C., Cantó, J., Riera, A., Curiel, S., Beck, T. L. *AJ*, *143*, 60, 2012

Romanova, M. M., Long, M., Kulkarni, A. K., Kurosawa, R., Ustyugova, G. V., Koldoba, A. V., Lovelace, R. V. E. In J. Bouvier, I. Appenzeller, eds., *Star-Disk Interaction in Young Stars*, vol. 243 of *IAU Symp.*, pp. 277–290. Cambridge: Cambridge University Press, 2007

Romanova, M. M., Ustyugova, G. V., Koldoba, A. V., Lovelace, R. V. E. *MNRAS*, *399*, 1802–1828, 2009

Rossi, P., Bodo, G., Massaglia, S., Ferrari, A. *A&A*, *321*, 672–684, 1997

Rydgren, A. E., Schmelz, J. T., Zak, D. S. *Publ. US Naval Obs.*, *XXV*, Part 1, 1984

Ryu, D., Goodman, J. *ApJ*, *388*, 438–450, 1992

Safier, P. N. *ApJ*, *408*, 115–147, 1993

Salmeron, R. In W. Short, I. Cairns, eds., *Proceedings of the 8th Australian Space Science Conference*, Australian Space Science Conference Series, pp. 41–48. Sydney: National Space Society of Australia Ltd., 2009

Salmeron, R., Ireland, T. R. *EPSL*, *327-328*, 61–67, 2012

Salmeron, R., Königl, A., Wardle, M. *Ap&SS*, *311*, 81–85, 2007

Santiago-García, J., Tafalla, M., Johnstone, D., Bachiller, R. *A&A*, *495*, 169–181, 2009

Sauty, C., Tsinganos, K. *A&A*, *287*, 893–926, 1994

Schleuning, D. A. *ApJ*, *493*, 811, 1998

Schneider, P. C., Eislöffel, J., Güdel, M., Günther, H. M., Herczeg, G. J., Robrade, J., Schmitt, J. H. M. M. *A&A*, *550*, L1, 2013a

———. *A&A*, *557*, A110, 2013b

Schneider, P. C., Günther, H. M., Schmitt, J. H. M. M. *A&A*, *530*, A123, 2011

Schneider, P. C., Schmitt, J. H. M. M. *A&A*, *488*, L13–L16, 2008

Shang, H., Li, Z.-Y., Hirano, N. In B. Reipurth, D. Jewitt, K. Keil, eds., *Protostars and Planets V*, pp. 261–276. Tucson: University of Arizona Press, 2007

Shepherd, D. S. *Ap&SS*, *313*, 41–44, 2008

Shirley, Y. L. vol. 219 of *American Astronomical Society Meeting Abstracts*, p. #309.03. 2012

Shu, F. H. *ApJ*, *214*, 488–497, 1977

Shu, F. H., Adams, F. C., Lizano, S. *ARAA*, *25*, 23–81, 1987

Shu, F. H., Li, Z.-Y., Allen, A. *ApJ*, *601*, 930–951, 2004

Shu, F. H., Najita, J. R., Ostriker, E. C., Wilkin, F., Ruden, S. P., Lizano, S. *ApJ*, *429*, 781–796, 1994

Shu, F. H., Najita, J. R., Shang, H., Li, Z.-Y. In V. Mannings, A. P. Boss, S. S. Russell, eds., *Protostars and Planets IV*, pp. 789–813. Tucson: University of Arizona Press, 2000

Skinner, S. L., Audard, M., Güdel, M. *ApJ*, *737*, 19, 2011

Skrutskie, M. F., Meyer, M. R., Whalen, D., Hamilton, C. M. *AJ*, *112*, 2168–2183, 1996

Skumanich, A. *ApJ*, *171*, 565–567, 1972

Smith, M. D. *Astrophysical Jets and Beams*. Cambridge Astrophysics Series. Cambridge: Cambridge University Press, 2012

Snell, R. L., Loren, R. B., Plambeck, R. L. *ApJ*, *239*, L17–L22, 1980

Soker, N. *A&A*, *435*, 125–129, 2005

Solf, J., Böhm, K. H. *ApJ*, *410*, L31, 1993

Spruit, H. C. In R. A. M. J. Wijers, M. B. Davies, C. A. Tout, eds., *Evolutionary Processes in Binary Stars*, vol. 477 of *NATO ASIC Proc.*, pp. 249–286. 1996

Staff, J. E., Niebergal, B. P., Ouyed, R., Pudritz, R. E., Cai, K. *ApJ*, *722*, 1325–1332, 2010

Stahler, S. W. *ApJ*, *274*, 822–829, 1983

———. In D. P. Clemens, R. Barvainis, eds., *Clouds, Cores and Low Mass Stars*, vol. 65 of *ASP Conf. Ser.*, pp. 330–339. San Francisco: Astronomical Society of the Pacific, 1994a

———. *ApJ*, *422*, 616–620, 1994b

Stojimirović, I., Narayanan, G., Snell, R. L., Bally, J. *ApJ*, *649*, 280–298, 2006

Stutz, A. M., Launhardt, R., Linz, H., Krause, O., Henning, T., Kainulainen, J., Nielbock, M., Steinacker, J., André, P. *A&A*, *518*, L87, 2010

Stutz, A. M., Rubin, M., Werner, M. W., Rieke, G. H., Bieging, J. H., Kenne, J., Kang, M., Shirley, Y. L., Su, K. Y. L., Velusamy, T., Wilner, D. J. *ApJ*, *687*, 389–405, 2008

Stutz, A. M., Tobin, J. J., Stanke, T., Megeath, S. T., Fischer, W. J., Robitaille, T. P., Henning, T., Ali, B., Di Francesco, J., Furlan, E., Hartmann, L., Osorio, M., Wilson, T. L., Allen, L. E., Krause, O., Manoj, P. *ApJ*, *767*, 36, 2013

Sun, K.-F., Yang, J., Luo, S.-G., Wang, M., Deng, L.-C., Zhou, X., Chen, J.-S. *Chin. J. Astron. Astrophys.*, *3*, 458–468, 2003

Sutherland, R. S., Bicknell, G. V. *ApJS*, *173*, 37–69, 2007

Sutherland, R. S., Dopita, M. A. *ApJS*, *88*, 253–327, 1993

Suzuki, T. K., Inutsuka, S.-i. *ApJ*, *691*, L49–L54, 2009

Takami, M., Beck, T. L., Pyo, T.-S., McGregor, P. J., Davis, C. J. *ApJ*, *670*, L33–L36, 2007

Takami, M., Chrysostomou, A., Bailey, J., Gledhill, T. M., Tamura, M., Terada, H. *ApJ*, *568*, L53–L56, 2002

Takami, M., Chrysostomou, A., Ray, T. P., Davis, C. J., Dent, W. R. F., Bailey, J., Tamura, M., Terada, H. *A&A*, *416*, 213–219, 2004

Tan, J. C., Beltrán, M. T., Caselli, P., Fontani, F., Krumholz, M. R., McKee, C. F., Stolte, A. In H. Beuther, R. S. Klessen, C. P. Dullemond, T. Henning, eds., *Protostars and Planets VI*. Tucson: University of Arizona Press, 2014

Taylor, S. D., Raga, A. C. *A&A*, *296*, 823–832, 1995

Teixeira, P. S., McCoey, C., Fich, M., Lada, C. J. *MNRAS*, *384*, 71–76, 2008

Terebey, S., Shu, F. H., Cassen, P. *ApJ*, *286*, 529–551, 1984

Testi, L., Bacciotti, F., Sargent, A. I., Ray, T. P., Eislöffel, J. *A&A*, *394*, L31–L34, 2002

Tobin, J. J., Hartmann, L., Chiang, H.-F., Wilner, D. J., Looney, L. W., Loinard, L., Calvet, N., D'Alessio, P. *Nature*, *492*, 83–85, 2012

———. *ApJ*, *771*, 48, 2013

Trussoni, E. In S. Massaglia, G. Bodo, A. Mignone, P. Rossi, eds., *Jets from Young Stars III*, vol. 754 of *Lect. Notes. Phys.*, pp. 105–130. Berlin, Heidelberg: Springer-Verlag, 2008

Turner, N. J., Fromang, S., Gammie, C., Klahr, H., Lesur, G., Wardle, M., Bai, X.-N. In H. Beuther, R. S. Klessen, C. P. Dullemond, T. Henning, eds., *Protostars and Planets VI*. Tucson: University of Arizona Press, 2014

Urry, C. M., Padovani, P. *PASP*, *107*, 803, 1995

van Dishoeck, E. F., Jorgensen, J. K. *Ap&SS*, *313*, 15–22, 2008

Wagner, A. Y., Bicknell, G. V. *ApJ*, *728*, 29–37, 2011

Wagner, A. Y., Bicknell, G. V., Umemura, M. *ApJ*, *757*, 136, 2012

Walter, F. M., Brown, A., Mathieu, R. D., Myers, P. C., Vrba, F. J. *AJ*, *96*, 297–325, 1988

Ward-Thompson, D. *Science*, *295*, 76–81, 2002

Wassell, E. J., Grady, C. A., Woodgate, B., Kimble, R. A., Bruhweiler, F. C. *ApJ*, *650*, 985–997, 2006

Weaver, R., McCray, R., Castor, J., Shapiro, P., Moore, R. *ApJ*, *218*, 377–395, 1977

Westmoquette, M. S., Clements, D. L., Bendo, G. J., Khan, S. A. *MNRAS*, *424*, 416–456, 2012

Westmoquette, M. S., Exter, K. M., Smith, L. J., Gallagher, J. S. *MNRAS*, *381*, 894–912, 2007

White, M. C., Bicknell, G. V., McGregor, P. J., Salmeron, R. *MNRAS*, *442*, 28–42, 2014a

White, M. C., Bicknell, G. V., Salmeron, R., McGregor, P. J. *MNRAS*, *in review*, 2014b

White, M. C., McGregor, P. J., Bicknell, G. V., Salmeron, R., Beck, T. L. *MNRAS*, *441*, 1681–1707, 2014c

White, R. J., Ghez, A. M. *ApJ*, *556*, 265–295, 2001

White, R. J., Greene, T. P., Doppmann, G. W., Covey, K. R., Hillenbrand, L. A. In B. Reipurth, D. Jewitt, K. Keil, eds., *Protostars and Planets V*, pp. 117–132. Tucson: University of Arizona Press, 2007

White, R. J., Hillenbrand, L. A. *ApJ*, *616*, 998–1032, 2004

Wilkin, F. P., Stahler, S. W. *ApJ*, *590*, 917–931, 2003

Williams, J. P., Cieza, L. A. *ARAA*, *49*, 67–117, 2011

Woitas, J., Bacciotti, F., Ray, T. P., Marconi, A., Coffey, D., Eislöffel, J. *A&A*, *432*, 149–160, 2005

Woitas, J., Ray, T. P., Bacciotti, F., Davis, C. J., Eislöffel, J. *ApJ*, *580*, 336–342, 2002

Wootten, A., Thompson, A. R. *Proc. IEEE*, *97*, 1463–1471, 2009

Young, H. D., Freedman, R. A. *University Physics*. San Francisco: Addison Wesley, 11th edn., 2004

Zacharias, N., Urban, S. E., Zacharias, M. I., Wycoff, G. L., Hall, D. M., Germain, M. E., Holdenried, E. R., Winter, L. *CDS/ADC Collection of Electronic Catalogues*, *1289*, 2003

Zanni, C., Ferrari, A., Rosner, R., Bodo, G., Massaglia, S. *A&A*, *469*, 811–828, 2007

Zanni, C., Ferreira, J. *A&A*, *550*, A99, 2013

Zinnecker, H., McCaughrean, M. J., Rayner, J. T. *Nature*, *394*, 862–865, 1998

Appendices

APPENDIX A

The F-Test

This Appendix was originally presented as Appendix A to White et al. (2014c).

Formally, the F-test combines two different methods of computing a χ^2 statistic, and compares the results to determine if their relationship is reasonable. If two statistics following the χ^2 distribution have been determined, then the ratio of the reduced-χ^2 of those distributions is distributed according to the F-distribution (Bevington & Robinson 1992).

Given the additive nature of functions obeying χ^2 statistics, a new χ^2 statistic may be formed by taking the difference of two χ^2 statistics. In particular, consider fitting a model with m_1 free parameters (the simpler model) to N data points. Then, the corresponding chi-square value associated with the deviations about the regression χ_1^2 has $N - m_1$ degrees of freedom. Adding another term to the model, with an extra Δm free parameters such that $m_2 = m_1 + \Delta m$, will lead to a corresponding regression χ_2^2 with $N - m_2$ degrees of freedom (the more complex model). Forming the ratio of the difference in chi-square values to the more complex model reduced chi-squared forms a statistic that obeys the F-distribution,

$$F = \frac{(\chi_1^2 - \chi_2^2)/\Delta m}{\chi_2^2/(N - m_2)} = \frac{\Delta\chi^2/\Delta m}{\chi_2^2/(N - m_2)}. \tag{A.1}$$

This ratio is a measure of how much the additional term has improved the value of the reduced chi-squared, and should be small if the more complex model does not produce a fit significantly better than the simpler model (Bevington & Robinson 1992). The F-test determines if the improvement in χ^2 between the models warrants the loss of degrees of freedom. If the above ratio equation (A.1) is ~ 1, then the change in χ^2 is not significant when compared to the reduction in degrees of freedom, and the more complex model is therefore not a statistically significant improvement, and would be rejected as unjustified.

If the F-ratio is significantly greater than one, there are two possibilities. One is that the

more complex model is a statistically better fit to the data. However, it is also possible that, by coincidence, noise in the data has taken the form of an extra term to be fitted by the model. To estimate the probability of this, the F-distribution is used:

$$P_F(F, \nu_1, \nu_2) = \int_F^\infty P_f(f, \nu_1, \nu_2)\, \mathrm{d}f, \text{ where} \tag{A.2}$$

$$P_f(f, \nu_1, \nu_2) = \frac{\Gamma(\nu_1 + \nu_2/2)}{\Gamma(\nu_1/2)\Gamma(\nu_2/2)} \left(\frac{\nu_1}{\nu_2}\right)^{\nu_1/2} \times \frac{f^{1/(2(\nu_1-2))}}{(1 + f\nu_1/\nu_2)^{1/(2(\nu_1+\nu_2))}}, \tag{A.3}$$

where $\nu_1 = \Delta m$ and $\nu_2 = N - m_2$ are known as the degrees of freedom in the numerator, and degrees of freedom in the denominator, respectively, of equation (A.1). These values characterise the F-distribution that has been generated (Bevington & Robinson 1992; Westmoquette et al. 2007). This is then a test of whether the coefficient of the extra term in the more complex model is zero. In this formulation, if the probability $P_F(F, \nu_1, \nu_2)$ exceeds some test value (typically 5 per cent), then one may be fairly confident that the coefficient of the extra term is not zero, and hence the more complex model is a statistically significantly better fit to the data. Otherwise, it is rejected, and the simpler model is retained (Bevington & Robinson 1992).

A.1. Applicability

There are two necessary conditions for the proper use of F-statistics. The first is that the two models being compared must be nested. The simpler model must be the more complex model with some parameters set to special null values, typically one or zero. This is clearly satisfied when testing for the presence of extra spectral line components, as one may remove the extra line component from the more complex model by setting the component amplitude to zero. The other, less well-known condition, is that the null values of the additional parameters may not be on the boundary of the set of possible parameter values. This is violated when testing for extra emission line components, as the amplitude of the line may not be negative, and hence the boundary of the allowable values for the line amplitude is zero. This is the same as the null value. Hence, the test is being used outside of the formal mathematical definition, and so the underlying reference distribution of the statistic is unknown. One suggested alternative test is Bayesian model checking. However, this requires extensive Monte Carlo simulations to generate the test statistic (Protassov et al. 2002), which is not practicable for a large quantity of spectra.

The F-test will not necessarily produce incorrect results if used to detect extra spectral line components. Protassov et al. (2002) determined that model-checking with the F-test produces a false-positive rate of between 1.5 per cent and 31.5 per cent. Furthermore, as

an example, they re-analysed the detection of the Fe K line in a gamma-ray burst X-ray afterglow, GRB 970508, which had previously been claimed by Piro et al. (1999) based on an F-test. Re-analysis of the line detection with Bayesian statistics did not disprove the Piro et al. detection, but confirmed it with a higher significance. Protassov et al. also pointed out that the more sophisticated Bayesian methods have their own inherent flaws. Ultimately, there is no 'correct' test for all nested model situations; rather, a test appropriate to the particular model and context must be selected (Protassov et al. 2002).

APPENDIX B

Dynamical Calculations of a Turbulent Jet

This Appendix was originally presented as Appendix B to White et al. (2014c).

This Appendix was prepared by the candidate, based on a set of notes written by Professor Geoff Bicknell. The calculations based on this Appendix regarding the DG Tau jet (§2.4.1.5) were conducted by Professor Bicknell, based on data provided by the candidate.

We consider a dynamical model for the DG Tau jet, which we summarize here. The jet passes through a recollimation shock $\lesssim 50$ AU along the outflow channel. This produces a hot X-ray knot (Güdel et al. 2005, 2008, 2011; Schneider & Schmitt 2008; Günther et al. 2009) for the innermost streamlines, although a large fraction of the surrounding jet gas is also heated to $\sim 10^6$ K (§2.4.1.2). The jet rapidly cools to a few $\times 10^4$ K (Bacciotti 2002; Maurri et al. 2014), hence we see the jet mainly as an optical/infrared source. The supersonic jet interacts with the surroundings, becoming turbulent and entraining ambient gas (§§2.4.2, 3). Since the jet is supersonic, the amount of entrainment and related deceleration is modest. The turbulence associated with the entrainment produces the 50–100 km s^{-1} shocks observed in the DG Tau outflow (Lavalley-Fouquet et al. 2000). This turbulence also counteracts the radiative cooling of the jet, so the jet gas remains approximately isothermal. This, combined with the relatively flat density gradient within the jet, means the pressure gradient is also modest along the jet, and unable to cause acceleration (§2.4.1.5).

We now proceed to outline the calculations which support the above description. We adopt an ionization fraction, χ_e, of 0.3 for the jet (Bacciotti 2002; Maurri et al. 2014). We take a helium number density, $n_{\rm He} = X({\rm He}) n_{\rm H} = X({\rm He}) n_e \chi_e^{-1}$, where $X(He) \approx 0.085$ is the solar helium abundance with respect to hydrogen. Then, the total number density, $n = (1 + [1 + X({\rm He})]\chi_e^{-1}) n_e$, and the mass density, $\rho = (1 + 4X({\rm He}))\chi_e^{-1} n_e m$, where

m is the atomic mass unit. In the following, k is the Boltzmann constant, T is the gas temperature, and $\Lambda(T)$ represents the cooling function.

B.1. Cooling After the Recollimation Shock

The existence of the recollimation shock means that the jet comes into pressure equilibrium with the surroundings, so a model of a pressure-confined jet is feasible. The jet cools fairly rapidly following this shock, with a cooling length given by,

$$\begin{aligned} l_c &= \frac{3}{2}\,\frac{n}{n_e n_H}\,\frac{kT}{\Lambda(T)}\,v_{\rm jet} \\ &\approx 38\; n_{e,6}^{-1} T_{6.5} \Lambda_{-22.5} \left(\frac{v_{\rm jet}}{200\ {\rm km\ s^{-1}}}\right)\ {\rm AU}, \end{aligned} \tag{B.1}$$

where subscript numbers denote the quantity in exponential units of that power. When the temperature drops to $\sim 10^5$ K the cooling becomes even more rapid, so it is not surprising that the jet is seen at optical and infrared wavelengths with a temperature of a few $\times\, 10^4$ K.

B.2. Jet Turbulent Velocity

We now estimate the turbulent velocity within the jet. We take a cylindrical coordinate system, (r, ϕ, z), with z along the jet axis. Let $\bar{\rho}$, $\bar{p}$, $\tilde{v}_r$ and $\tilde{v}_z$, be the mean density, pressure and radial and axial velocity components along the jet direction (z), and let ϕ_g be the gravitational potential. For a jet subject to hydrodynamic turbulence, the z-momentum equation for the mean flow is

$$\frac{\partial(\bar{\rho}\tilde{v}_z^2)}{\partial z} + \frac{1}{r}\frac{\partial(r\bar{\rho}\tilde{v}_r\tilde{v}_z)}{\partial r} = -\frac{\partial \bar{p}}{\partial z} - \bar{\rho}\frac{\partial \phi_g}{\partial z} - \frac{1}{r}\frac{\partial(r\langle \rho v_r' v_z'\rangle)}{\partial z} \tag{B.2}$$

where $-\langle \rho v_r' v_z'\rangle$ is the Reynolds stress (§4.6; Bicknell 1984; Kuncic & Bicknell 2004), and angle brackets denote mass-weighted time-averaged quantities according to the Favre (1969) prescription. Primes are used to denote locally fluctuating quantities; bars and tildes denote time-averaged quantities.

For a jet in pressure equilibrium, $p(r, z) = p_{\rm ext}(z)$, the external pressure. For a stellar mass of 0.67 $M_\odot$ (Hartigan et al. 1995), the gravitational field is unimportant in the accelerating region. Let $R(z)$ be the jet radius. Then, for a jet which is spreading due to turbulence,

$$\langle \rho v_r' v_z'\rangle \approx \bar{\rho}\tilde{v}_z^2 \frac{{\rm d}R}{{\rm d}z} \tag{B.3}$$

$$\Rightarrow v' \approx 110\ {\rm km\ s^{-1}} \left(\frac{\tilde{v}_z}{200\ {\rm km\ s^{-1}}}\right)\left(\frac{{\rm d}R/{\rm d}z}{0.1}\right)^{0.5} \tag{B.4}$$

The observed value of $\mathrm{d}R/\mathrm{d}z \sim 0.05 - 0.1$ so that equation (B.4) agrees well with the turbulent velocity implied by both the HVC line widths (Fig. 2.6c) and the results of emission line modelling (Lavalley-Fouquet et al. 2000).

B.3. Turbulent Dissipation of Energy

The rate of production of turbulent energy per unit volume is given by:

$$\dot{\epsilon}_t = \langle \rho v_r' v_z' \rangle \, \tilde{v}_{z,r} \tag{B.5}$$

$$\approx \frac{\bar{\rho}\tilde{v}_z^3}{R} \frac{\mathrm{d}R}{\mathrm{d}z}. \tag{B.6}$$

This energy is dissipated and heats the plasma. For DG Tau, the amount of energy produced is of order 10^{-13}–10^{-12} erg s^{-1} cm^{-3}. By comparison, the rate of cooling in the jet, based on a nominal cooling function of $\Lambda(T) = 10^{-22}$ erg cm^3 s^{-1} as appropriate for a $\sim 10^4$ K plasma in collisional ionization equilibrium, is of order 10^{-14} erg s^{-1} cm^{-3}. The estimated heating exceeds the cooling rate, maintaining the jet temperature at $\sim 10^4$ K.

B.4. Pressure-Driven Jet Acceleration

We aim to determine if the acceleration of the DG Tau jet over the region 0.″5–1.″15 from the central star could be consistent with the inferred pressure gradient in the jet. There are two possible approaches. The first approach considers the momentum budget in the jet, while the second is based on a Bernoulli equation-type analysis. Both methods show that the pressure gradient in the DG Tau jet is incapable of providing acceleration.

B.4.1. Momentum Budget

Let us assume that the jet is in a steady state, and the observed increase in velocity in the jet is the result of acceleration by the pressure gradient. Integrating the momentum equation over the jet cross-section, neglecting the gravitational force, yields

$$\frac{\mathrm{d}}{\mathrm{d}z}\left[2\pi \int_0^\infty \bar{\rho}\tilde{v}_z^2 \, r \, dr\right] = -\frac{\mathrm{d}\bar{p}}{\mathrm{d}z} \times A(z), \tag{B.7}$$

where $A(z)$ is the jet cross-sectional area. This equation integrates to:

$$\rho_2 v_2^2 A_2 - \rho_1 v_1^2 A_1 \approx -\int_{z_1}^{z_2} \frac{\mathrm{d}\bar{p}}{\mathrm{d}z} A(z) \, \mathrm{d}z. \tag{B.8}$$

All quantities in this equation can be estimated from our observational data. The pressure may be estimated as $p = nkT$. For the DG Tau jet, over the region of increasing jet velocity,

the difference in momentum on the left-hand side of equation B.8, 1.1×10^{25} g cm s^{-1}, is two magnitudes of order higher than the average inferred pressure gradient along the jet multiplied by the average jet radius, 2.7×10^{23} g cm s^{-1}. Therefore, the pressure gradient cannot drive the observed momentum increase of the jet.

B.4.2. Bernoulli Equation-Type Analysis

Another way of deriving a similar result is to consider an approach related to the derivation of Bernoulli's equation. Take the scalar product of the momentum equation,

$$\bar{\rho}\frac{\partial \tilde{v}_i}{\partial t} + \bar{\rho}\tilde{v}_j\frac{\partial \tilde{v}_i}{\partial x_j} = -\frac{\partial \bar{p}}{\partial x_i} - \frac{\partial}{\partial x_j}\langle \rho v_i' v_j' \rangle, \tag{B.9}$$

with $\tilde{v}_i$,

$$\bar{\rho}\frac{\partial}{\partial t}\left(\frac{\tilde{v}^2}{2}\right) + \bar{\rho}\tilde{v}_j\frac{\partial}{\partial x_j}\frac{\tilde{v}^2}{2} = -\tilde{v}_i\frac{\partial \bar{p}}{\partial x_i} - \tilde{v}_i\frac{\partial}{\partial x_j}\langle \rho v_i' v_j' \rangle. \tag{B.10}$$

Equation (B.10) describes the increase of the quantity $\tilde{v}^2/2$ under the action of the pressure gradient, gravitational force and turbulent diffusion. The gravitational term and the turbulent term $-\tilde{v}_i(\partial/\partial x_j)\langle \rho v_i' v_j' \rangle$ reduce $\tilde{v}^2$ so that the most optimistic acceleration is described by

$$\bar{\rho}\frac{\mathrm{d}}{\mathrm{d}t}\left(\frac{\tilde{v}^2}{2}\right) = -\tilde{v}_i\frac{\partial \bar{p}}{\partial x_i} \tag{B.11}$$

$$\Rightarrow v_2^2 - v_1^2 \approx -2\int_{z_1}^{z_2}\frac{1}{\bar{\rho}}\frac{\partial \bar{p}}{\partial z}\,\mathrm{d}z. \tag{B.12}$$

The standard analysis of Bernoulli's equation assumes an equation of state for $p(\rho)$. In view of the complications of turbulent flow in this case, the relation between $\bar{p}$ and $\bar{\rho}$ would require a very detailed model. However, as with the momentum budget approach, all of the terms in equation (B.12) can be estimated from the data, and the integration of the right-hand side can be performed numerically. The end result is the same as for the analysis based on the momentum budget. The pressure gradient fails by approximately two orders of magnitude to produce the increase in jet velocity observed.

APPENDIX C

Acceleration of a Protostellar Jet by Embedded Magnetic Fields

This Appendix was originally presented as Appendix C to White et al. (2014c).

Consider the full expression for the energy flux density $\boldsymbol{F}_{\rm E}$ carried by the jet,

$$\boldsymbol{F}_{\rm E} = \left(\frac{1}{2}v^2 + h + \phi\right)\rho\boldsymbol{v} + \underbrace{\frac{B^2 v}{4\pi}\left(\hat{\boldsymbol{v}} - \hat{\boldsymbol{v}}\cdot\hat{\boldsymbol{B}}\hat{\boldsymbol{B}}\right)}_{\text{Poynting flux}}, \tag{C.1}$$

where ρ is the jet density, ϕ is the gravitational potential, $\boldsymbol{B}$ is the magnetic field, and hats denote unit vectors. Assuming a constant value of the jet energy flux across the jet cross-sectional area, $A_{\rm jet}$, the *total* jet power, $L_{\rm jet}$, is then given by

$$\begin{aligned} L_{\rm jet} &= \boldsymbol{F}_{\rm E}\cdot\hat{\boldsymbol{v}}A_{\rm jet} \\ &= \left[\left(\frac{1}{2}v^2 + h + \phi\right) + \frac{B^2}{4\pi\rho}\left(1 - (\hat{\boldsymbol{v}}\cdot\hat{\boldsymbol{B}})^2\right)\right]\rho v A_{\rm jet}. \end{aligned} \tag{C.2}$$

If one assumes, as a first approximation, that both the total jet power and the jet mass flux, $\dot{M} = \rho v A_{\rm jet}$, are constant[67], then one can form the equivalent of the Bernoulli equation for a hydromagnetic jet:

$$\left(\frac{1}{2}v^2 + h + \phi\right) + \frac{B^2}{4\pi\rho}\left(1 - (\hat{\boldsymbol{v}}\cdot\hat{\boldsymbol{B}})^2\right) = \frac{L_{\rm jet}}{\dot{M}} = \text{const.} \tag{C.3}$$

[67]Strictly speaking, the total jet power will not be constant, as some energy must be radiated away as observable emission. However, this would affect the enthalpy term of equation (C.1), which is typically negligible. Whilst this statement about enthalpy may not be true for post-shock regions in jet knots, it should be a good approximation for the non-shocked portion of the jet, which is the region observed to be accelerating.

We consider three extreme cases of equation (C.3). First, if the magnetic field is parallel to the jet velocity, then the Poynting flux term disappears, and equation (C.3) collapses back to the purely hydrodynamic Bernoulli equation, equation (2.6), which has already been argued to be incapable of driving coupled acceleration-expansion in this scenario (Appendix B). Secondly, if the magnetic field is perpendicular to the jet velocity, then $\hat{\boldsymbol{v}} \cdot \hat{\boldsymbol{B}} = 0$, and from the flux-freezing theorem, we deduce that the magnetic field of a self-similar jet evolves approximately as $B \propto 1/vR$, where R is the jet radius. We next choose a reference point in the flow, and denote the values of magnetic field, density, velocity and radius at that point with a subscript zero. The jet magnetic field and density will then evolve thus:

$$B = B_0 \left(\frac{v}{v_0}\right)^{-1} \left(\frac{R}{R_0}\right)^{-1}, \text{ and} \tag{C.4}$$

$$\rho = \rho_0 \left(\frac{v}{v_0}\right)^{-1} \left(\frac{R}{R_0}\right)^{-2}. \tag{C.5}$$

This leads to the expression

$$\frac{B^2}{4\pi\rho} = \frac{B_0^2}{4\pi\rho_0} \left(\frac{v}{v_0}\right)^{-1}, \tag{C.6}$$

which has no R dependence. Jet acceleration occurring in this regime would not show an increase in jet radius with jet velocity. Such an increase in radius is observed in the DG Tau jet (§2.4.1.4). Therefore, coupled acceleration-expansion cannot occur in this magnetic field configuration.

The third limiting case is that of a completely tangled magnetic field. Such a field behaves like a $\gamma = 4/3$ gas, where γ is the polytropic index of the gas, such that

$$\frac{B^2}{8\pi} \propto \rho^{4/3} \Rightarrow B^2 = B_0^2 \left(\frac{\rho}{\rho_0}\right)^{4/3} \tag{C.7}$$

(Kuncic & Bicknell 2004). The Poynting flux term in equation (C.3) may be evaluated by assuming the velocity is in the outflow-axis direction only, and then averaging over solid angle, such that

$$\langle 1 - (\hat{\boldsymbol{v}} \cdot \hat{\boldsymbol{B}})^2 \rangle = \frac{2}{3}. \tag{C.8}$$

Substituting the above into equation (C.3) yields the following equation relating quantities at a reference point, denoted by a subscript zero, to some other point along the outflow:

$$\left(\frac{v}{v_0}\right)^2 + \frac{2(h-h_0)}{v_0^2} + \frac{2(\phi-\phi_0)}{v_0^2} - 1 = \frac{B_0^2}{3\pi\rho_0 v_0^2} \left[1 - \left(\frac{v}{v_0}\right)^{-1/3} \left(\frac{R}{R_0}\right)^{-2/3}\right]. \tag{C.9}$$

The enthalpy and gravitational potential terms of equation (C.9) are generally unimportant in protostellar outflows at large distances from the central star.

APPENDIX D

Turbulent Mixing Layer Supplementary Calculations

This Appendix has been submitted as Appendix A to White et al. (2014b).

D.1. Characteristic Equations of MHD

For magnetohydrodynamic fluids with density ρ, velocity v, pressure p, viscous stress tensor t^v_{ij}, magnetic field $\boldsymbol{B}$ immersed in a gravitational potential ϕ_{G}, the equation of mass continuity can be written in Cartesian coordinate notation thus:

$$\frac{\partial \rho}{\partial t} + \frac{\partial (\rho v_i)}{\partial x_i} = 0. \tag{D.1}$$

Similarly, the equation of momentum conservation is written as

$$\frac{\partial (\rho v_i)}{\partial t} + \frac{\partial (\rho v_i v_j)}{\partial x_j} = -\rho \frac{\partial \phi_{\mathrm{G}}}{\partial x_i} - \frac{\partial p}{\partial x_i} + \frac{\partial t^B_{ij}}{\partial x_j} + \frac{\partial t^v_{ij}}{\partial x_j} \tag{D.2}$$

(Kuncic & Bicknell 2004).

Time-averaging equation (D.1) is trivial, yielding equation (3.6). Averaging the momentum conservation equation, equation (D.2), is more complex. The viscous stress tensor, t^v_{ij}, is disregarded, as it is unimportant to the transfer of momentum on large scales. The Reynolds stress tensor, t^R_{ij}, appears in equation (3.7) as a result of averaging the second term on the left-hand side of equation (D.2). This may then be combined with the magnetic stress tensor, t^B_{ij}, to form a single term encapsulating the total stress in the system, $t_{ij} = t^R_{ij} + t^B_{ij}$.

D.2. Dimensionless Functions

The dimensionless function $\mathcal{D}(\eta,\xi)$ in the mixing layer transverse velocity profile, equation (3.20), is given by

$$\mathcal{D}(\eta,\xi) = \int_{\xi_1}^{\xi} \xi' \frac{\mathrm{d}}{\mathrm{d}\xi'}\left(\frac{U(\xi')}{\eta+(1-\eta)S(\xi')}\right)\mathrm{d}\xi' \tag{D.3}$$

$$= \frac{\eta}{(\eta-1)^2}\left\{(\eta-1)\left[\frac{\xi}{(\eta-1)(\xi_1-\xi)+1}-\xi_1\right]+\log\left[(\eta-1)(\xi_1-\xi)+1\right]\right\}. \tag{D.4}$$

The dimensionless function $\mathcal{F}(\eta,\xi)$ in the mixing layer transverse turbulent stress profile, equation (3.22), is given by

$$\mathcal{F}(\eta,\xi) = \int_{\xi_1}^{\xi} -\xi' \frac{\xi'-\xi_1+1}{\eta+(1-\eta)(\xi'-\xi_1+1)} + \mathcal{D}(\eta,\xi')\,\mathrm{d}\xi'. \tag{D.5}$$

$$= \frac{1}{2(\eta-1)^3}\Big\{2\eta\left[(1-\eta)(\xi_1-\xi)-1\right]\log\left[(\eta-1)(\xi_1-\xi)+1\right]$$
$$-\left[(\eta-1)(2\eta-1)\xi_1-\eta(\xi-2)+\xi\right](\eta-1)(\xi-\xi_1)\Big\}. \tag{D.6}$$

D.3. Mixing Layer Transverse Velocity and Turbulent Stress Profiles

The transverse velocity profile across the mixing layer, $\tilde{v}_y(\eta,\xi)$, may be found by substituting the expression for $\xi_1(\eta)$, equation (3.23), in to equation (3.20):

$$\tilde{v}_y(\eta,\xi) = \frac{v_\mathrm{j}h'(x)\eta}{4(\eta-1)^6}\Big\{\left[\eta^2(2\log(\eta)-1)+1\right]\left[3\eta^2-2\eta^2\log(\eta)+2(\eta-1)^3\xi-4\eta+1\right]$$
$$-2(\eta-1)^2\left[\eta^2-2\eta^2\log(\eta)+2(\eta-1)^3\xi-1\right]$$
$$\times\log\left(-\frac{\eta^2(1-2\log(\eta))+2(\eta-1)^3\xi-1}{2(\eta-1)^2}\right)\Big\}. \tag{D.7}$$

The turbulent stress profile across the mixing layer, $t_{xy}(\eta,\xi)$, may be found in the same way, using equation (3.22):

$$\begin{aligned} t_{xy}(\eta,\xi) = \frac{\rho_\mathrm{j} v_\mathrm{j}^2 h'(x)}{8(\eta-1)^7}\Bigg\{ & 4\eta\Big[(\eta-1)^2\left[\eta^2(1-2\log(\eta))+2(\eta-1)^3\xi-1\right] \\ & \times\log\left(-\frac{\eta^2(1-2\log(\eta))+2(\eta-1)^3\xi-1}{2(\eta-1)^2}\right) \\ & +\eta\log(\eta)\Big(\eta\left(-4\eta^2-2(\eta-1)^3\xi+7\eta-4\right) \\ & +(2\eta-1)\eta^2\log(\eta)+1\Big)\Big] \\ & +(\eta-1)^2\Big[4(\eta-1)^4\xi^2+4\eta(\eta+1)(\eta-1)^2\xi \\ & +\eta(\eta(6\eta-5)+4)-1\Big]\Bigg\}. \end{aligned} \tag{D.8}$$

D.4. Calculation of the Mass Entrainment Rate

The mass entrainment rate is given by taking the x-derivative of equation (3.28),

$$\dot{M}'_\mathrm{ent} = \frac{\mathrm{d}}{\mathrm{d}x}\int_{\xi_2}^{\xi_1}\rho(\xi)v_x(x,\xi)h(x)\,\mathrm{d}\xi - \rho_\mathrm{j}v_\mathrm{j}h'(x)\xi_1(\eta) \tag{D.9}$$

$$\begin{aligned} &= \bar{\rho}(\xi_1)\tilde{v}_x(\xi_1)h(x)\frac{\mathrm{d}\xi_1}{\mathrm{d}x} - \bar{\rho}(\xi_2)\tilde{v}_x(\xi_2)h(x)\frac{\mathrm{d}\xi_2}{\mathrm{d}x} \\ &\quad + \int_{\xi_2}^{\xi_1}\frac{\mathrm{d}}{\mathrm{d}x}\left[\rho(\xi)v_x(x,\xi)h(x)\right]\,\mathrm{d}\xi - \rho_\mathrm{j}v_\mathrm{j}h'(x)\xi_1(\eta). \end{aligned} \tag{D.10}$$

The first two terms of the above are zero in (x,ξ)-space. The transformed equation of continuity, equation (3.19), may be written as

$$\frac{\partial}{\partial x}\left(\bar{\rho}\tilde{v}_x h(x)\right) = h'(x)\frac{\partial}{\partial\xi}\left(\xi\bar{\rho}\tilde{v}_x\right) - \frac{\partial}{\partial\xi}\left(\bar{\rho}\tilde{v}_y\right), \tag{D.11}$$

which reduces equation (D.10) to

$$\dot{M}'_\mathrm{ent} = h'(x)\left[\rho_\mathrm{j}v_\mathrm{j}\xi_1 - \rho_\mathrm{w}v_\mathrm{w}\xi_2\right] - \rho_\mathrm{J}\tilde{v}_y(x,\xi_1) + \rho_\mathrm{w}\tilde{v}_y(x,\xi_2) - \rho_\mathrm{j}v_\mathrm{j}\xi_1 h'(x). \tag{D.12}$$

Most of these terms are zero, or cancel, leaving

$$\dot{M}'_\mathrm{ent} = \rho_\mathrm{w}\tilde{v}_y(x,\xi_2) \tag{D.13}$$

$$= \rho_\mathrm{w}v_\mathrm{ent} \text{ by definition.} \tag{D.14}$$